



# COMSAT TECHNICAL REVIEW

## Volume 5 Number 1, Spring 1975

*Advisory Board* Joseph V. Charyk  
William W. Hagerty  
John V. Harrington  
Sidney Metzger

*Editorial Board* Pier L. Bargellini, Chairman  
Robert D. Briskman  
S. Browne  
S. J. Campanella  
William L. Cook  
Denis J. Curtin  
Joachim Kaiser  
R. W. Kreutel  
H. J. Meyerhoff  
Akos G. Revesz

*Editorial Staff* Larry G. Hastings  
MANAGING EDITOR  
Leonard F. Smith  
Margaret B. Jacocks  
TECHNICAL EDITORS  
Edgar Bolen  
PRODUCTION  
Michael K. Glasby  
CIRCULATION

The COMSAT TECHNICAL REVIEW is published twice a year by the Communications Satellite Corporation (COMSAT). Subscriptions including postage, \$5.00 U.S. per year; single copies, \$3.00 U.S. Bulk rates are available upon request. Remittances for subscriptions should be made payable to the Treasurer, COMSAT, and addressed to COMSAT TECHNICAL REVIEW, Room 5273, 950 L'Enfant Plaza, S. W., Washington, D.C. 20024, U.S.A.

- 1 EXPRESSIONS FOR THE TIME-VARYING TOPOCENTRIC DIRECTION OF A GEOSTATIONARY SATELLITE. **V. Slabinski**
- 15 INCLINATION CORRECTION STRATEGY WITH YAW SENSING VIA SUN ANGLE MEASUREMENT. **M. Kaplan**
- 29 DETECTION OF INTELSAT IV SPIN AXIS ANGULAR DISPLACEMENT INDUCED BY PROPELLANT SYSTEM MASS IMBALANCE. **A. Corio**
- 53 AIR BEARING PLATFORM TESTING OF A DOUBLE-GIMBALED MOMENTUM WHEEL ATTITUDE CONTROL SYSTEM. **A. Ramos**
- 73 INTELSAT IV-A TRANSMISSION SYSTEM DESIGN. **J. Dicks AND M. Brown, Jr.**
- 105 DIVEC, A COMBINED DIVERSITY AND ERROR CONTROL SCHEME. **R. Fang**
- 135 ATTENUATION AND PHASE SHIFT OF MICROWAVES DUE TO CANTED RAINDROPS. **D. Fang**
- 157 A LOW-LOSS MULTIPLEXER FOR SATELLITE EARTH TERMINALS. **R. Gruner AND A. Williams**
- 179 SUSPENDED SUBSTRATE STRIPLINE DIRECTIONAL FILTERS FOR RECEIVER DEMULTIPLEXING AT 4 GHz **C. Cotner**
- 199 TRANSLATIONS OF ABSTRACTS  
FRENCH 199  
SPANISH 205



**Index:** geostationary satellites, programmed drives,  
satellite tracking, celestial mechanics

***Expressions for the time-varying  
topocentric direction of a  
geostationary satellite***

V. J. SLABINSKI

(Manuscript received October 24, 1974)

***Abstract***

Programmed antenna drives have been proposed as a simple method for driving narrow-beam antennas at earth stations so that they track the changing direction of a nearly geostationary satellite. Antenna pointing information would be obtained from a minicomputer evaluation of simple algebraic expressions in the time domain. This paper shows that a suitable pointing expression would consist of a polynomial part, quadratic in time; a simple trigonometric part whose period is the sidereal day; and two Poisson terms. The error in such a pointing expression is less than  $0.015^\circ$  over a 28-day time interval. The trigonometric part need consist of only a sine and cosine term for orbit eccentricities less than 0.005 and inclinations less than  $1^\circ$ . Abbreviated forms of the expression give good accuracy over shorter time intervals. The practical evaluation of the expression on a minicomputer is also discussed.

---

This paper is based upon work performed at COMSAT partly under the joint sponsorship of the Communications Satellite Corporation (COMSAT) and the International Telecommunications Satellite Organization (INTELSAT). Views expressed in this paper are not necessarily those of INTELSAT.

## Introduction

Communications satellites are not kept perfectly stationary over the earth's surface. To allow for the changing direction of the satellite, a narrow-beam antenna at an earth station must be provided with tracking capability. Programmed antenna drives which obtain their pointing information for each coordinate from a minicomputer evaluation of a simple algebraic expression, called a *pointing expression*, have been proposed. This paper shows that a suitable form of the pointing expression for a coordinate  $f$  is given by the right side of the following *pointing equation*:

$$f(t') = B_0 + B_1 t' + B_2 (t')^2 + \sum_{i=1}^L (C_i \cos lwt' + S_i \sin lwt') + P_e t' \cos wt' + P_s t' \sin wt' \quad (1)$$

where  $t'$  is the difference in time,  $t$ , from some epoch  $t_0$ :

$$t' \equiv t - t_0 \quad (2)$$

Taking  $L = 1$  in equation (1) gives sufficient accuracy for a nearly geostationary satellite. One advantage of a programmed drive using this form of pointing equation is that less than 20 numerical parameters for the expressions must be transmitted to the station every few weeks in contrast to the present practice of sending an ephemeris for every two hours of time (24 numbers for each day).

The *fitting interval* is the time interval over which a pointing expression applies. An accuracy of  $\sim 0.015^\circ$  from the expression over its fitting interval is sufficient for communications antennas since this value is much less than the antenna beamwidth. For a transmitting frequency of 6 GHz (5-cm wavelength), the beamwidth (between half-power points) of a 32-m diameter dish is  $0.092^\circ$ , and smaller antennas have even larger beamwidths.

A rigorous demonstration of the accuracy of a pointing expression requires an analytic orbit theory for the satellite's motion; such a theory would also make it possible to obtain numerical values for the coefficients in equation (1) directly from the orbital elements and astrodynamical constants. Because a suitable theory is not yet available in finished form, numerically integrated orbits were used to compute exact values of the pointing coordinates spaced through the fitting interval. Numerical co-

efficients for the pointing expressions were obtained by a least-squares fit to the exact values.

This paper illustrates the pointing accuracy obtained with pointing expressions of different complexity. Graphs present the error in each pointing expression as a function of time to portray the character and magnitude of the pointing error. The errors portrayed should be within 20 percent of the worst-case error since the fits covered a time interval near solstice when perturbations to the orbit inclination were largest, and since satellites with moderate longitude drift rates were used to show that exact synchronism with the earth's rotation is not a prerequisite for a good fit.

## Error in various pointing expressions

### Expressions for the hour angle and declination

The apparent position of an object on the celestial sphere may be specified by its hour angle and declination, angular coordinates for the sky that are analogous to longitude and latitude on the earth. The hour angle gives the position of the object's projection onto the celestial equator, measured westward from the station's celestial meridian. The declination gives the object's angular distance north or south of the celestial equator, with north taken positive. A more detailed discussion can be found in any textbook on spherical astronomy [1].

The hour angle and declination are the most convenient coordinates for discussing the apparent angular motion of a nearly geostationary satellite as viewed from an earth station; the satellite motion in longitude appears to the station primarily as a motion in hour angle, while the satellite motion in latitude appears primarily as a motion in declination. A change in the satellite's geocentric distance results in a comparatively small change in the apparent angular coordinates.

For a nearly geostationary satellite, the satellite motion in latitude is a nearly sinusoidal oscillation about the equator with an orbit period,  $P$ , due to the orbit inclination. The motion in longitude is a nearly sinusoidal oscillation with the same period, due to the orbit eccentricity, about a mean position that moves along the equator linearly with time. These observations suggest pointing equations of the form

$$H = H_0 + H_1 t' + C_H \cos wt' + S_H \sin wt' \quad (3)$$

$$\delta = \delta_0 + C_\delta \cos wt' + S_\delta \sin wt' \quad (4)$$

for the hour angle,  $H$ , and declination,  $\delta$ , where

$$w = 2\pi \text{ rad}/P \quad (5)$$

The parameters  $H_0$ ,  $H_1$ ,  $C_H$ ,  $S_H$ ,  $\delta_0$ ,  $C_\delta$ ,  $S_\delta$ , and  $P$  are taken to be constant throughout the fitting interval.

Figure 1 illustrates the accuracy of these pointing expressions over a 7-day interval for a satellite with a  $0.4^\circ$  inclination, nearly zero eccentricity, and a longitude drift rate of  $\sim 0.05^\circ/\text{day}$ . The period,  $P$ , was taken as one sidereal day (1,436.068 min) and the remaining parameters in equations (3) and (4) were obtained by a least-squares fit to exact values over the interval. The largest error,  $0.014^\circ$ , occurred in the declination coordinate near the beginning and end of the interval.

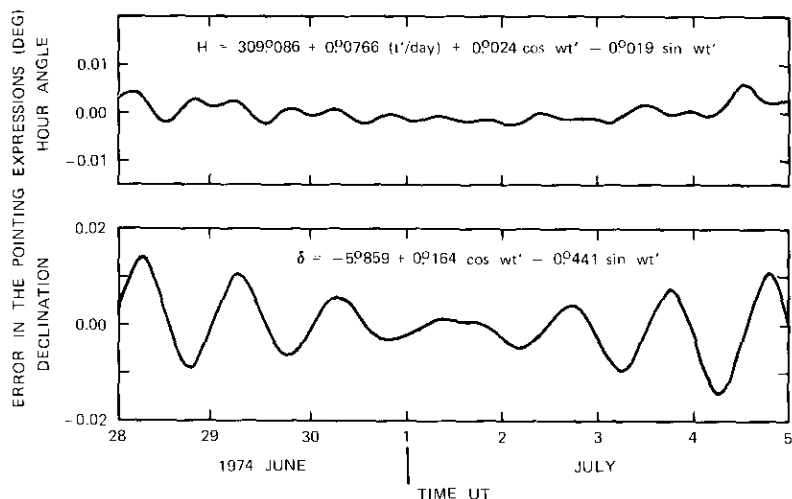


Figure 1. Error in the Stated Hour Angle and Declination Pointing Expressions (exact value minus expression value) over Their 7-Day Fitting Interval (The pointing expressions are for INTELSAT IV F-7 near  $330^\circ\text{E}$  longitude as seen from Clarksburg, Maryland, at  $282.7^\circ\text{E}$  longitude,  $39.2^\circ\text{N}$  latitude with  $t_0 = 1974 \text{ July } 1.^{\text{d}}490 \text{ UT}$ .)

Figure 2 shows the error which results from using these pointing equations for the same satellite over a 14-day interval. The hour angle error has a parabolic trend which arises from the acceleration of the satellite in longitude due to the  $J_{2,2}$  gravitational harmonic. The declination error

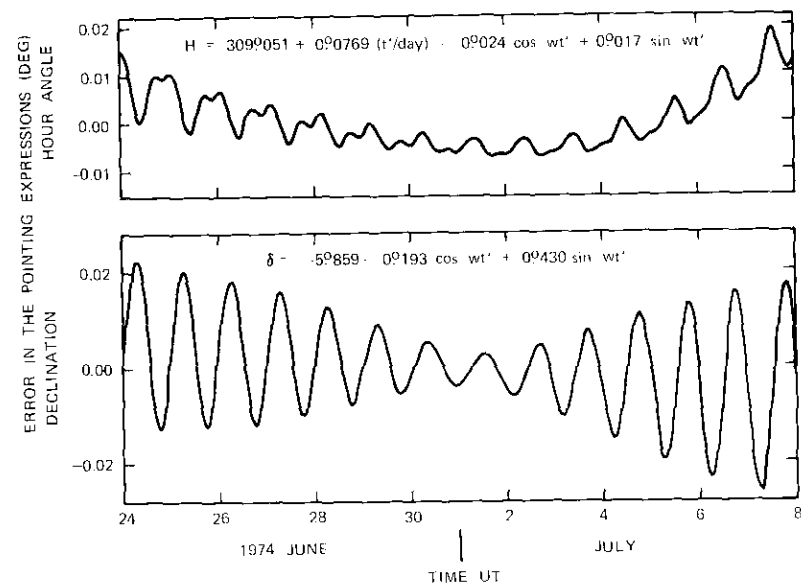


Figure 2. Error in the Stated Hour Angle and Declination Pointing Expressions (exact value minus expression value) over Their 14-Day Fitting Interval (The pointing expressions are for INTELSAT IV F-7 near  $330^\circ\text{E}$  longitude as seen from Clarksburg, Maryland, at  $282.7^\circ\text{E}$  longitude,  $39.2^\circ\text{N}$  latitude with  $t_0 = 1974 \text{ June } 30.^{\text{d}}981 \text{ UT}$ .)

has a 24-hour oscillation whose amplitude increases roughly linearly with time from the midpoint of the fitting interval and whose phase undergoes a  $180^\circ$  change near the midpoint. This oscillation indicates that the amplitudes  $C_\delta$  and  $S_\delta$  of the 24-hour trigonometric terms have a significant linear change with time. These observations suggest pointing equations of the form

$$H = H_0 + H_1 t' + H_2 (t')^2 + C_H \cos wt' + S_H \sin wt' \quad (6)$$

$$\delta = \delta_0 + (C_\delta + P_{\delta c} t') \cos wt' + (S_\delta + P_{\delta s} t') \sin wt' \quad (7)$$

which involve the additional parameters  $H_2$ ,  $P_{\delta c}$ , and  $P_{\delta s}$ , for fitting intervals of the order of 14 days.

Figure 3 shows that equations (6) and (7) give a good fit over an interval of almost 28 days. The hour angle error has a 14-day oscillation from a corresponding oscillation in the satellite's mean longitude caused by the moon, but the extreme error in the fit is only 0.011°. However, the declination error exceeds 0.015° on the first and last day of the interval. This declination error can be reduced by including a term linear in time in equation (7) to allow for the small change in declination as the satellite drifts in longitude. For a fitting interval of the order of 28 days, equation (6) is satisfactory for the hour angle, but the declination pointing equation should have the form

$$\delta = \delta_0 + \delta_1 t' + (C_\delta + P_{\delta c} t') \cos wt' + (S_\delta + P_{\delta s} t') \sin wt' \quad (8)$$

which involves the additional parameter  $\delta_1$ . Figure 4 shows that equation (8) gives a very good fit for the declination over an interval of 30 days with an extreme error of only 0.008°.

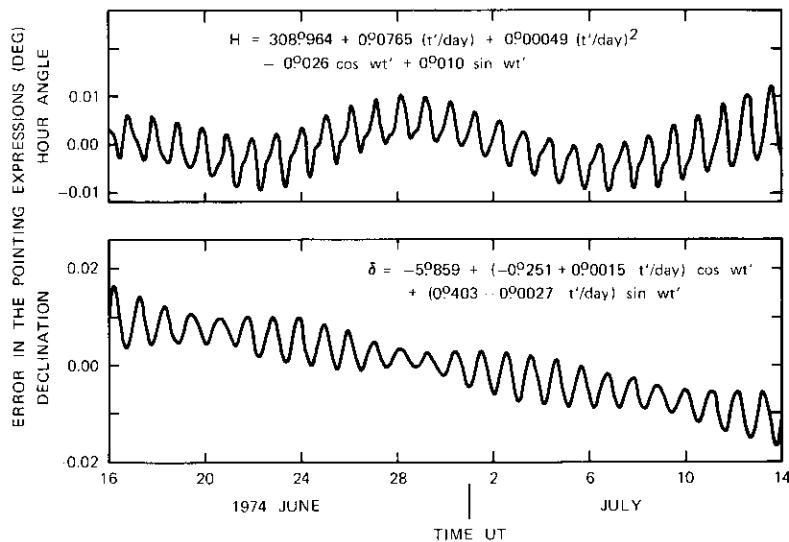


Figure 3. Error in the Stated Hour Angle and Declination Pointing Expressions (exact value minus expression value) over Their 28-Day Fitting Interval (The pointing expressions are for INTELSAT IV F-7 near 330°E longitude as seen from Clarksburg, Maryland, at 282.7°E longitude, 39.2°N latitude with  $t_0 = 1974$  June 29.4962 UT.)

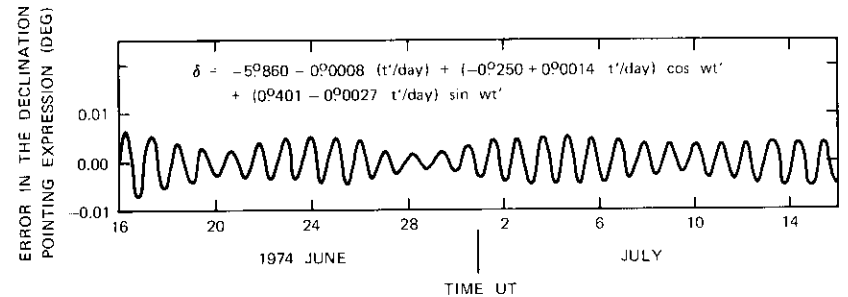


Figure 4. Error in the Stated Declination Pointing Expression (exact value minus expression value) over Its 30-Day Fitting Interval (The pointing expressions are for INTELSAT IV F-7 near 330°E longitude as seen from Clarksburg, Maryland, at 282.7°E longitude, 39.2°N latitude with  $t_0 = 1974$  June 30.4959 UT.)

**Poisson terms**

Terms such as  $P_{\delta c} t' \cos wt'$  and  $P_{\delta s} t' \sin wt'$  in equations (7) and (8), which involve a sine or cosine term multiplied by a polynomial in the independent variable, are called Poisson terms in celestial mechanics. They have been introduced into the declination fit for two reasons:

- a. they allow for the amplitude change in the diurnal declination variation as the orbit inclination changes due to the gravitational attractions of the sun and moon,
- b. they allow for a small error in  $w$  which results from assigning  $P$  the same fixed value for all fits.

A fixed value of  $P$  eliminates the need to transmit this parameter to the earth stations without increasing the complexity of the fit, since the contribution of  $b$  is usually small compared to the contribution of  $a$ .

To show that an assigned  $P$  value results in Poisson terms, assume that the value  $w$  obtained from equation (5) using the assigned period differs from the true value,  $w_t$ , by a small quantity,  $\Delta w$ :

$$w_t = w + \Delta w \quad (9)$$

A term which should be represented as  $C \cos w t'$  would be represented by terms with angular frequency  $w$  as

$$\begin{aligned} C \cos w t' &= C \cos (\Delta w t') \cos w t' - C \sin (\Delta w t') \sin w t' \\ &\simeq C \cos w t' - \{C \Delta w\} t' \sin w t' \end{aligned} \quad (10)$$

where a Taylor series expansion in  $\Delta w t'$  has been made and powers greater than 1 omitted. The second term on the right side of equation (10) is a Poisson term.

To put a bound on the coefficient  $C \Delta w$  for operational INTELSAT IV satellites, note that these satellites have orbit inclinations,  $i$ , less than  $0.5^\circ$  and longitude drift rates which do not exceed  $0.06^\circ/\text{day}$ . The latter value gives  $|\Delta w| < 10^{-3}$  rad/day for  $P = 1$  sidereal day.  $C$  is generally largest for declination fits in which its value is  $\sim i$ ; hence,  $|C \Delta w| < 5 \times 10^{-4}$  deg/day. This value is small compared to the contribution from the inclination change,  $\sim 3 \times 10^{-3}$  deg/day. However,  $C \Delta w$  can be comparatively large for larger orbit inclinations or longitude drift rates. For such cases the declination pointing expression requires Poisson terms for fitting intervals of even a few days.

#### Expressions for other coordinates

For discussion purposes assume that expressions for other antenna pointing coordinates (such as azimuth and elevation, or the rail coordinates of a movable feed horn) are obtained from the  $H$  and  $\delta$  equations by a rotation of axes about the  $(H_0, \delta_0)$  direction. This procedure transforms terms from both the hour angle and declination equations into each of the new coordinates. Specifically, if a particular type of term, such as a Poisson term, appears in either the  $H$  or  $\delta$  equation, that type of term will generally appear in the pointing equations for *both* new coordinates. Thus, the form of the pointing equation will generally be the same for both of the new coordinates, and will contain all of the term types needed in the corresponding  $H$  and  $\delta$  equations.

Figure 5 illustrates this use of the same pointing expression for both coordinates in an azimuth-elevation application. In practice, coefficients for the pointing expressions are not obtained from a coordinate transformation of the  $H$  and  $\delta$  expressions, but from a least-squares fit to exact values computed for the new coordinate system.

#### Expressions for large inclinations and eccentricities

Nearly geostationary satellites with inclinations less than  $0.5^\circ$  and eccentricities less than 0.001 require only trigonometric terms of frequency

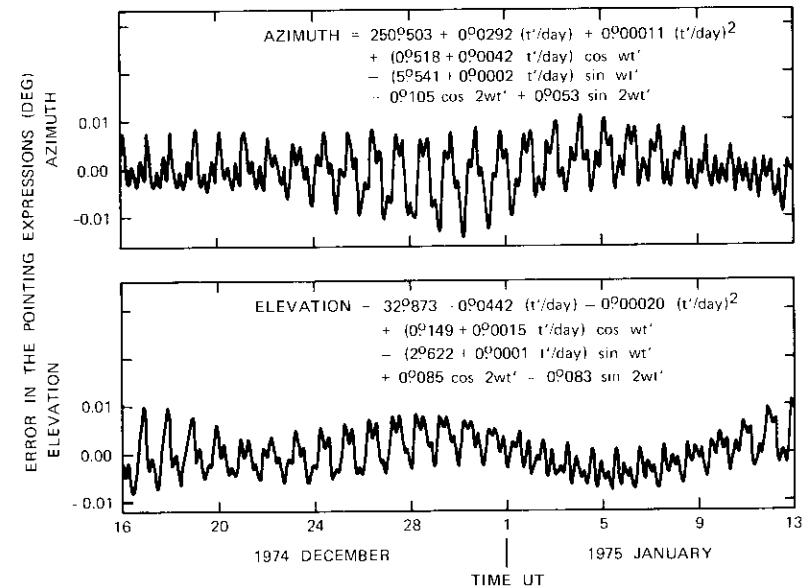


Figure 5. Error in the Stated Azimuth and Elevation Pointing Expressions (exact value minus expression value) over Their 28-Day Fitting Interval (The pointing expressions are for INTELSAT II F-2 near  $156^\circ\text{E}$  longitude as seen from Paumalu, Hawaii, at  $202.0^\circ\text{E}$  longitude,  $21.7^\circ\text{N}$  latitude with  $t_0 = 1974 \text{ Dec } 29.4962 \text{ UT}$ .)

$w$  in their pointing expressions. For  $i > 1^\circ$ , terms of frequency  $2w$  become important since they represent the 12-hour oscillation of the satellite in longitude, with an amplitude of  $\sim 0.0044^\circ (i/\text{deg})^2$ , due to the width of the figure eight pattern of the satellite ground trace. Figure 5 illustrates the accuracy obtained with pointing expressions which include constant amplitude terms of frequency  $2w$  for a satellite with  $i$  near  $5^\circ$ . The orbit eccentricity is very small and the longitude drift rate is  $\sim -0.05^\circ/\text{day}$ . The error in the pointing expressions is less than  $0.014^\circ$  over a 28-day fitting interval. A definite oscillation with frequency  $3w$  is present in the error, indicating that trigonometric terms of this frequency should be included in the pointing expressions for inclinations greater than  $5^\circ$ .

Trigonometric terms of frequency  $2w$  are also important if the orbit eccentricity exceeds 0.005, since the eccentricity introduces a 12-hour oscillation in longitude with an amplitude of  $\sim 72^\circ e^2$ . However, present communications satellites do not have such high eccentricities.

## Practical evaluation of the pointing expressions

### Time interval between antenna pointing adjustments

The pointing of programmed track antennas is not adjusted continuously but at discrete time intervals,  $\Delta t$ . To minimize the pointing error due to satellite motion between adjustments, the antenna should be pointed at the position computed for a time midway to the next adjustment; that is, the pointing expressions should be evaluated with

$$t' = \left( t_e + \tau + \frac{\Delta t}{2} \right) - t_0 \quad (11)$$

where  $t_e$  is the time at the start of computation and  $\tau$  is the time delay between computation and antenna adjustment.  $\tau$  is usually a negligible delay. This pointing refinement is most simply implemented by having the minicomputer take  $t_e$  from a local clock at the start of computation and using

$$t' = t_e - t_{0,d} \quad (12)$$

to compute  $t'$ , where

$$t_{0,d} \equiv t_0 - \tau - \frac{\Delta t}{2} \quad (13)$$

is a parameter supplied to the minicomputer in place of  $t_0$ .

The time interval,  $\Delta t$ , between antenna pointing adjustments depends upon the tracking accuracy required and the apparent angular velocity,  $\dot{\theta}$ , of the satellite with respect to the antenna base. The error budget for antenna pointing must allow for an error,  $\epsilon_d$ , resulting from the discrete times of adjustment (in addition to the error in the pointing expressions, discussed in the preceding section, and errors from other sources). It is desired that

$$\dot{\theta}_{\max} \frac{\Delta t}{2} \leq \epsilon_d \quad (14)$$

The largest apparent angular motion of the satellite usually comes from the orbit inclination,  $i$ , which gives a diurnal variation in declination of approximately  $i \sin \omega(t - t_N)$ , where  $t_N$  is the time of a nodal crossing. The maximum angular rate in declination, which occurs when the satellite orbit has its maximum inclination,  $i_{\max}$ , is  $\simeq i_{\max} \omega$ . This product gives an

upper bound on  $\dot{\theta}_{\max}$  so that the last inequality yields

$$\Delta t \leq 2 \frac{\epsilon_d}{i_{\max} \omega} \quad (15)$$

if a fixed value of  $\Delta t$  is to be used. For a nearly geostationary satellite,  $\omega \simeq 2\pi \text{ rad}/1,436 \text{ min}$  so that this inequality gives

$$\Delta t \leq 457 \text{ min} \left( \frac{\epsilon_d}{i_{\max}} \right) \quad (16)$$

for  $\epsilon_d$  and  $i_{\max}$  in the same units. For  $\epsilon_d = 0.01^\circ$  and  $i_{\max} = 0.5^\circ$ ,  $\Delta t \leq 9 \text{ min}$ .

### Evaluation of the trigonometric functions

Direct evaluation of a sine or cosine function by means of a series expansion or other rational polynomial approximation is the most costly part of the pointing expression evaluation in terms of both minicomputer core storage and execution time. Thus, it is desirable to minimize the number of direct trigonometric function evaluations required. An antenna adjustment generally involves two direct evaluations to obtain the values  $\cos \omega t'$  and  $\sin \omega t'$ . If the higher frequency functions  $\cos l\omega t'$  and  $\sin l\omega t'$  with  $l > 1$  are included in the pointing expressions, they may be obtained very simply from these values through the trigonometric identities

$$\begin{aligned} \cos l\omega t' &= \cos [(l-1)\omega t'] \cos \omega t' \\ &\quad - \sin [(l-1)\omega t'] \sin \omega t' \end{aligned} \quad (17)$$

$$\begin{aligned} \sin l\omega t' &= \sin [(l-1)\omega t'] \cos \omega t' \\ &\quad + \cos [(l-1)\omega t'] \sin \omega t' \end{aligned} \quad (18)$$

starting with  $l = 2$ .

If only one sine and one cosine term appear in each pointing expression, they may be combined into a single sine term with an amplitude  $A$  and phase angle  $\beta$  replacing the parameters  $C$  and  $S$ . For example, a mathematically equivalent form of equations (3) and (4) is

$$H = H_0 + H_1 t' + A_H \sin(\omega t' + \beta_H) \quad (19)$$

$$\delta = \delta_0 + A_\delta \sin(\omega t' + \beta_\delta) \quad (20)$$

Either form may be evaluated with equal efficiency since only two direct evaluations of trigonometric terms are required in either case. [The pointing expressions in equations (19) and (20) were adopted for the rail coordinates of the movable antenna feed in the unattended earth terminal project.]

There are alternatives to the direct evaluation of even two trigonometric functions. For example, the feed positioner of the unattended earth terminal obtains its trigonometric function values from a sine table stored in a read only memory (ROM).

Another possibility is to store the values of  $\cos(w \Delta t)$  and  $\sin(w \Delta t)$  in the minicomputer and require that the epoch for the fitting equations be the start time for using the pointing expressions. For the expression evaluation at this start time,  $t' = 0$  so that  $\cos wt' = 1$  and  $\sin wt' = 0$ . For the  $n$ th subsequent evaluation at a time  $t_n$  given by

$$t_n = t_0 + n \Delta t \quad (21)$$

for which

$$t'_n = t_n - t_0 = n \Delta t = t'_{n-1} + \Delta t \quad (22)$$

the trigonometric function values are obtained from the values found at the previous evaluation by using

$$\cos wt'_n = (\cos wt'_{n-1}) \cos(w \Delta t) - (\sin wt'_{n-1}) \sin(w \Delta t) \quad (23)$$

$$\sin wt'_n = (\sin wt'_{n-1}) \cos(w \Delta t) + (\cos wt'_{n-1}) \sin(w \Delta t) \quad (24)$$

For  $\Delta t = 9$  min, the minicomputer would iterate the last two equations 1,120 times during a fitting interval of only one week. Usually a smaller  $\Delta t$  value would be used so that the number of iterations would be greater. This large number of iterations requires consideration of the accumulated roundoff error. The computation can be discussed in terms of complex numbers since the values  $\cos wt'_n$  and  $\sin wt'_n$  are the real and imaginary parts of  $R^n$ , respectively, where

$$R \equiv \exp^{jw\Delta t} \quad (25)$$

and  $j = \sqrt{-1}$ . The  $(n - 1)$ th iteration does not give  $R^{n-1}$  exactly, but a slightly different number,  $P_{n-1}$ , due to roundoff error. The intended computation of  $R^n$  from  $P_{n-1} R$  gives

$$P_n = P_{n-1} R + \epsilon_n = R^n + \sum_{k=1}^N R^{n-k} \epsilon_k \quad (26)$$

where  $\epsilon_n$  is the roundoff error introduced in the  $n$ th iteration. The summation represents the total roundoff error. Since the magnitude of  $R^{n-k}$  is 1, an upper bound on the error is  $n|\epsilon_{\max}|$ . The trigonometric function values should be accurate to  $5 \times 10^{-4}$  to avoid introducing significant error into the pointing expression evaluation; hence,  $|\epsilon_{\max}|$  must be less than  $5 \times 10^{-4}/n_{\max}$ . As a numerical example, consider  $\Delta t = 9$  min and a fitting interval of four weeks so that  $n_{\max} = 4,480$  and  $|\epsilon_{\max}| < 10^{-7}$ , which requires that a fixed-point minicomputer work to seven decimal places if this iteration scheme for evaluating the trigonometric functions is used.

### Conclusion

The fairly simple pointing expressions developed in this paper give adequate pointing accuracy for fitting intervals as long as 28 days even for large orbit inclinations. In practical applications each expression involves only seven parameters in addition to  $w$  and the epoch time. The best form of the pointing expressions for use in a given application depends on the eccentricity and inclination of the satellite orbit, the longitude drift rate, the pointing coordinates used, the pointing accuracy desired, and the time interval over which the pointing expressions must hold. An appropriate form for the pointing expressions may be selected from the examples in this paper.

### Acknowledgment

*This paper extends an unpublished study performed by Dr. James C. Su of COMSAT Laboratories. Dr. Su first showed that pointing expressions given by equation (1) of this paper, without the two Poisson terms, would give a pointing accuracy of 0.01° over a 7-day fitting interval.*

### Reference

- [1] W. M. Smart, *Text-Book on Spherical Astronomy*, 5th ed., Cambridge: University Press, 1962, Chap. 2, pp. 25-30.



*Victor J. Slabinski received a B.S. in Physics from Case Institute of Technology in 1961. He was a part-time instructor with the Physics Department at Case Western Reserve University until he received his Ph.D. in 1970. He then became a member of the technical staff of COMSAT's Astrodynamics Department, where he is concerned primarily with problems of satellite orbital and attitude mechanics and prediction.*

*Dr. Slabinski is a member of Tau Beta Pi, Sigma Xi, and the American Astronomical Society.*

**Index: sun sensors, yaw; attitude control, slope**

## ***Inclination correction strategy with yaw sensing via sun angle measurement***

M. H. KAPLAN

(Manuscript received August 19, 1974)

### ***Abstract***

During high thrust and impulse inclination corrections of a nonspinning synchronous satellite, significant attitude torques may be generated due to misalignment of the thrust vector and uncertainty in the center of mass position. If a bias momentum wheel is used for accurate attitude control and sized for solar pressure torques, it cannot provide yaw holding to prescribed values during these orbit maneuvers. Thus, yaw angle data must be provided through additional sensors and/or techniques.

Sun sensors can presently provide yaw information during certain times of the day, depending on the time of year. The work reported here considers the use of these sensors on a year-round basis. A technique for executing orbit inclination corrections so that yaw information is available during all maneuvers is presented. Technical aspects and operational procedures are discussed. The use of this technique may involve a slight increase in propellant utilization for given inclination control requirements. Maximum propellant penalties have been estimated for sun sensor fields of view with half angles between  $45^\circ$  and  $60^\circ$ , and for inclination holding limits of  $0.06^\circ$  to  $0.1^\circ$ .

---

This paper is based upon work performed in COMSAT Laboratories under the sponsorship of the International Telecommunications Satellite Organization (INTELSAT). Views expressed in this paper are not necessarily those of INTELSAT.

## Introduction

Body-stabilized communications satellites are likely to replace present generation spacecraft in synchronous orbit. Such configurations will present unique problems in many areas. Of particular interest here is the interaction of inclination control impulses with attitude sensors and holding performance. High pointing accuracy must be maintained throughout such maneuvers. However, these vehicles will probably employ momentum bias devices and hydrazine propulsion. Anticipated thrust misalignment torques due to inclination thrusters are expected to exceed solar pressure torques, which are the basis for sizing bias momentum devices. This will result in excessive yawing unless direct yaw sensing is provided.

Several techniques for measuring yaw error have been proposed. These include the use of rate gyros, direct yaw sensing by star tracking, and RF methods employing associated ground equipment. There are techniques which do not require direct yaw measurement, such as the use of smaller and more frequent impulses for inclination correction or increasing momentum wheel stiffness through increased angular momentum. In addition, sun sensors can provide yaw information when the satellite is near the dawn and evening terminators. However, a yaw sensing technique, which can be used at any point in the orbit, is costly in terms of complexity, weight, and operations. Alternate methods which avoid direct yaw sensing are also costly and tend to counteract the advantages of using bias momentum wheels and hydrazine thrusters.

Since the basic attitude control system does not nominally require direct yaw information, it seems advantageous to consider a yaw sensing technique that requires a minimum of complexity, weight, and added operations during inclination corrections. Thus, if yaw measurement is required only for short intervals of time, a simple device which can operate during those times is quite desirable. This motivation has led to a technique for using sun sensors so that yaw requirements are satisfied. In other words, the part-time capability of sun sensors has been matched to inclination correction operations by considering the orbital geometry and mission requirements.

The work reported here considers the use of these sensors on a year-round basis. Technical aspects and operational procedures are presented. The use of this technique may involve a slight increase in propellant utilization for given inclination control requirements. Maximum propellant

penalties have been estimated for sun sensor fields of view with half angles between  $45^\circ$  and  $60^\circ$ , and for inclination holding limits of  $0.06^\circ$  to  $0.1^\circ$ .

## Orbit normal drift and solar geometry

For synchronous orbits with inclinations less than about  $5^\circ$ , the orbit normal vector is a more convenient representation than "inclination" and "node position." This vector has components of inclination,  $i$ , and azimuth position, and is usually represented by its projection onto the equatorial plane [1].

Figure 1 illustrates zones of desirable normal vector position immediately after an inclination correction. Perturbative forces generally tend to precess this vector toward the First Point of Aries,  $\Upsilon$ , i.e., in the direction of the sun on March 21 (vernal equinox). The azimuthal position of the orbit normal lags the ascending node position by  $90^\circ$ .

Allan [2] has pointed out that it is possible to maximize the time interval between successive inclination corrections for a given tolerance. As shown in Figure 1, which also indicates the sun's position at different times of the year, this generally requires positioning the orbit normal away from  $\Upsilon$ . Since the ideal firing points on the orbits are the nodes, "solstice periods" are associated with a very poor geometry for yaw sensing with sun sensors. The lengths of these periods, which are centered around June 21 and December 21, correspond to the sensor field of view, which is  $\pm 45^\circ$  in Figure 1. Note that these periods can be narrowed somewhat without incurring a propellant penalty by firing slightly off node. The angular momentum change vector,  $\vec{\Delta h}$ , represents  $\Delta v$  requirements per unit mass. The impulse per unit mass is merely the quantity of  $\Delta v$  imparted. Since this quantity is applied as a torque to the orbit plane, the associated value of  $\Delta v$  is

$$\Delta v = v \left( \frac{\Delta h}{h} \right) = v \sqrt{i_f^2 + i_0^2 - 2i_f i_0 \cos \Delta \Omega}$$

- where
- $i_f$  = inclination immediately before the impulse is applied
  - $i_0$  = inclination immediately after the impulse is applied
  - $v$  = orbital velocity = 3,070 m/s
  - $h$  = orbital angular momentum  
=  $v/\omega_0 = 1.20 \times 10^{11}$  m<sup>2</sup>/s
  - $\Delta \Omega$  = azimuthal shift of the orbit normal vector and the shift in the node line.

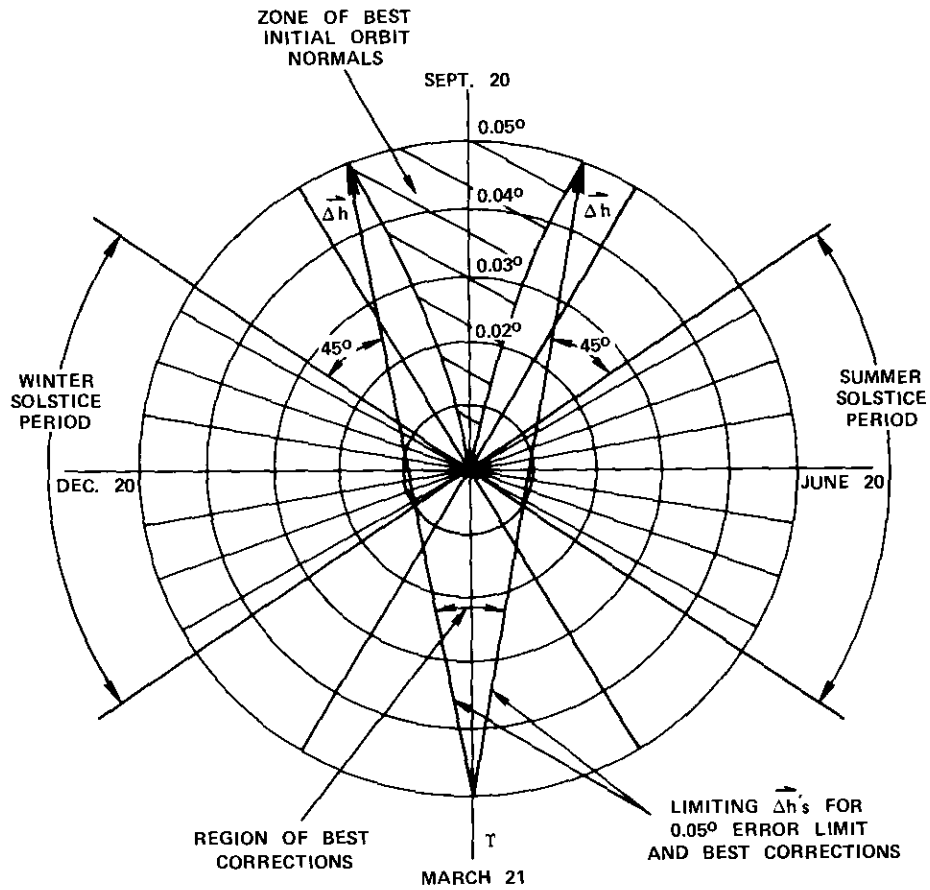


Figure 1. Qualitative Plot of Orbit Normal Situation for  $0.05^\circ$  Limit and  $\pm 45^\circ$  Field of View

Note that the thruster firing position is always  $\pm 90^\circ$  azimuthally away from the corresponding  $\Delta h$ . Qualitative limits on  $\Delta h$  for a  $0.05^\circ$  inclination holding value and for best propellant use are also depicted in Figure 1. Normals to all  $\Delta h$  vectors which correspond to ideal propellant utilization fall into the solstice zones, indicating that sun sensors cannot give yaw information during these intervals if optimum inclination corrections are required. Thus, the problem is to determine alternate procedures for use during these two periods of each year.

Figure 2 shows the orbit normal precession process over several weeks for different initial azimuth positions, but the same initial inclination of

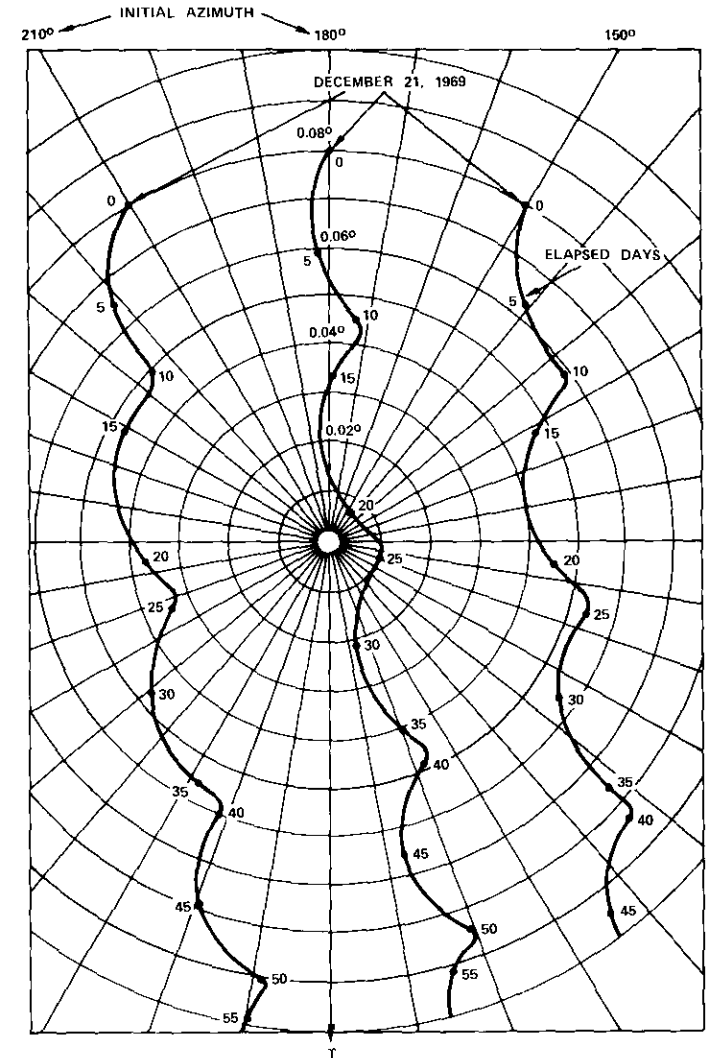


Figure 2. Examples of Orbit Normal Precession for an Inclination Limit of  $0.08^\circ$

$0.08^\circ$ . The starting date of December 21, 1969, has been selected because the lunar-solar effects are maximum at that time. Initial conditions corre-

spend to those immediately after N-S thruster firing. The maximum time between corrections for a  $0.08^\circ$  limit is about 48 days under worst-case conditions. This interval is generally longer and varies due to the cyclic precessional motion of the lunar orbit, with a period of 18.6 years.

**Thrusting strategy**

The objective of minimizing propellant penalty while using sun sensors for yaw information is realized through a series of off-node thrust impulses during each solstice period. The exact strategy and timing depend on the sensor field of view and inclination holding limit. For example, consider a situation in which inclination must be held to  $0.08^\circ$  with a sensor field of view of  $\pm 45^\circ$ . An optimized summer solstice sequence is depicted in Figure 3. The following is a list of events for 1974, which is a year of average inclination precession activity:

- a. May 7 is the last day to apply thrust at the nominal node position with yaw sensing. The orbit normal must be brought to point 1 from its drift position on that day.
- b. On May 30, to ensure that the orbit normal is kept near the line of precession,  $\Upsilon$ , symmetrical firings with regard to the sun's position about the node line are planned. This period fortunately corresponds to the time between corrections, or about 41 days in this case. Thus, the orbit normal is again moved upward.
- c. On July 12, the inclination limit is reached and another impulse is applied. The sun is now leaving the solstice region and the orbit normal can be brought to point 3, which is very close to the ideal point 1.

Figure 4 shows the path of the orbit normal over this period.

If the availability of yaw sensing were independent of sun position, then the reference propellant situation would be established. Computer simulations were used to determine propellant usage for a limited number of cases with and without yaw sensing constraints. The sequence described for 1974 indicated that the difference in velocity increments was only 0.30 m/s for the entire summer solstice interval. For an 810-kg satellite with a thruster of 200-second specific impulse, the propellant penalty was 0.124 kg; for all of 1974, it would be 0.248 kg. A similar sequence of thrusts was applied to years of high and low inclination precession, 1969 and 1978, respectively. An average of these data resulted in a 7-year propellant penalty estimate of 1.61 kg (0.1 percent of the propellant load)

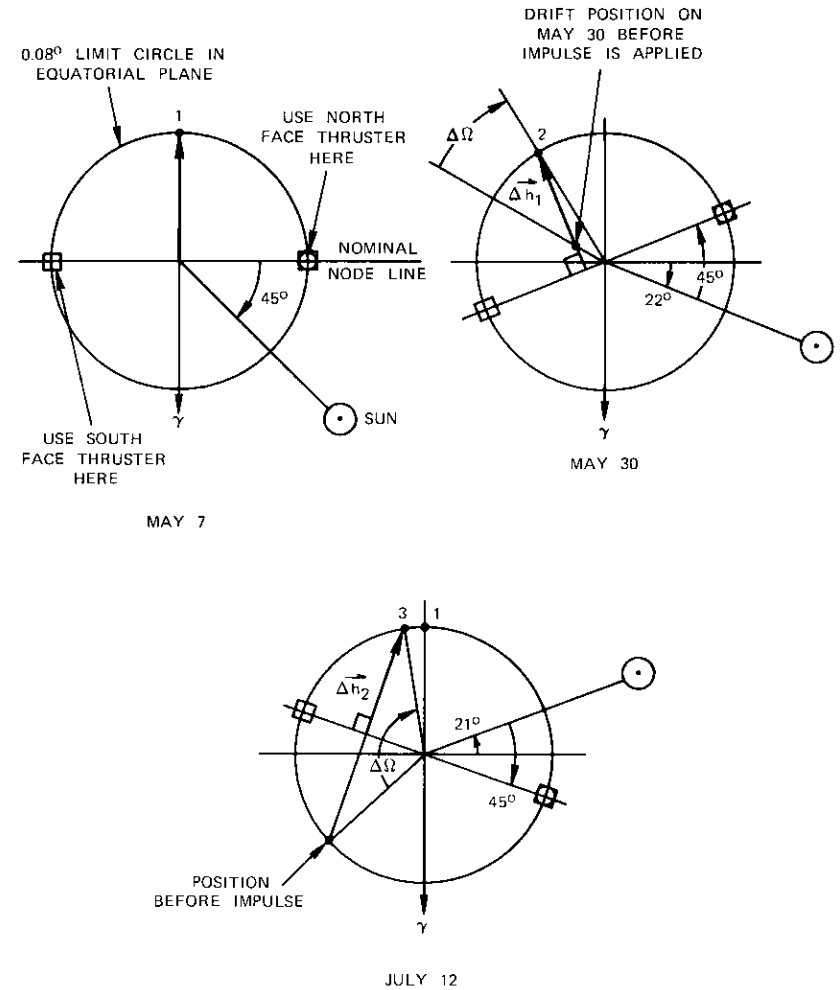


Figure 3. Basic Thrusting Strategy for a Sensor Field of View of  $\pm 45^\circ$

for the aforementioned satellite. A similar strategy was used for selected cases with fields of view up to  $\pm 60^\circ$  and inclination limits of  $0.06^\circ$  to  $0.1^\circ$ .

Because of the  $1^\circ$  per day motion of the sun, the thrusting strategy becomes more complicated when the maximum number of days between corrections is less than approximately 90 minus the number of degrees

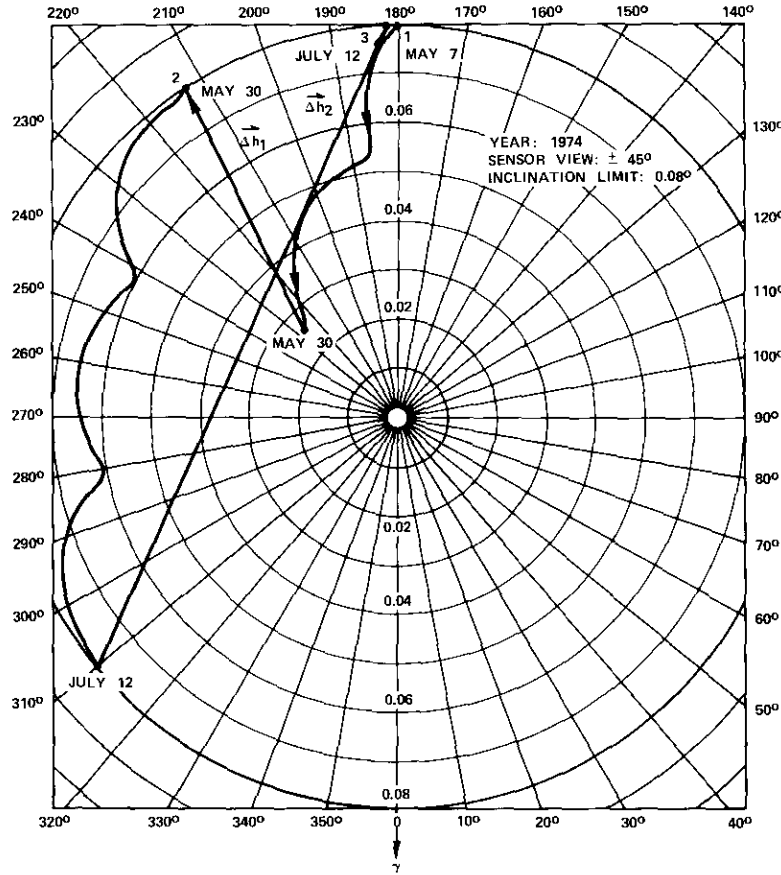


Figure 4. Example of Orbit Normal History

in the sensor field of view. For example, in the preceding case, the number of degrees is 45. Thus, the associated strategy is relatively simple because the maximum time between corrections is 47 days.

The maximum number of days between corrections is a function of perturbation magnitude and inclination holding limit. Solar-lunar attraction precesses the orbit normal at an average rate of about 0.003° per day. Thus, a sensor field of view of ±45° implies thrusting strategy increases in complexity for inclination holding limits below about 0.07°. For example, consider a holding limit of 0.06° with this sensor field of view during 1969, a year of maximum orbit normal precession.

Figure 5 illustrates the precession and correction history. It is important to note that some of the applied impulses are used to move the orbit normal only a partial distance away from the limit circle. These maneuvers are essential to permit more time for the sun to leave the solstice region and thus return the strategy to normal. In the case shown in Figure 5, the basic strategy can be used after August 14. Associated penalties are significantly higher for such cases. Thus, complicated strategies should be avoided through increased inclination holding limits and/or increased sensor fields of view.

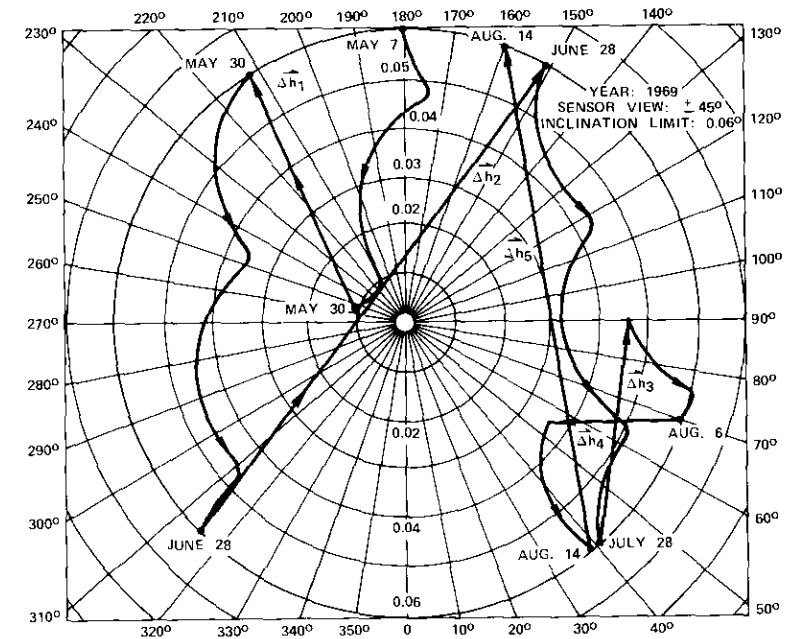


Figure 5. Example of Complicated Strategy

**Propellant penalties**

Propellant penalties for optimum situations can be determined by using the simulation procedure outlined in the preceding section. This procedure should be used for the years of expected orbital life and for various fields of view and inclination holding limits; however, each data point requires a substantial amount of time. To obtain conservative penalty figures,

a simplified method, developed by Dr. G. Gordon of COMSAT Laboratories, was used to determine near-optimum values.

The perturbation is modeled by a steady drift of  $0.003^\circ$  per day toward  $\Upsilon$ . Figure 6 illustrates the simplified procedure for a sensor field of view

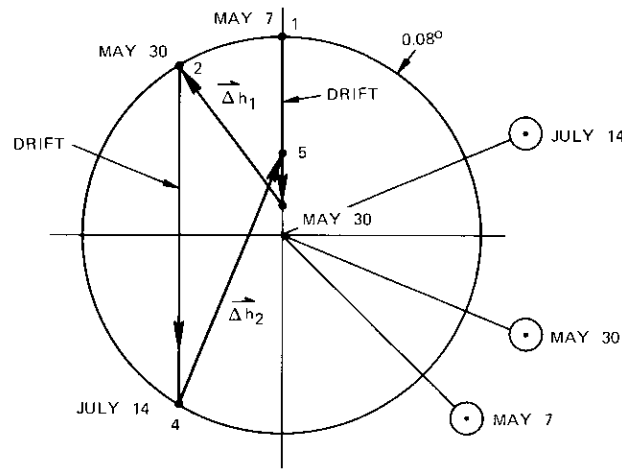


Figure 6. Simplified Strategy for Penalty Calculations

of  $\pm 45^\circ$  and inclination limit of  $0.08^\circ$ . On May 7 a maneuver brings the orbit normal back to point 1. Drift is permitted until May 30, when another impulse is applied and point 2 is reached. Drift is again permitted (in this case, for 45 days) until point 4 is reached on July 14. An impulse then brings the orbit normal back to the centerline at point 5. Further maneuvers do not result in propellant penalties until late fall. The difference in velocity increments is  $0.15$  m/s as opposed to  $0.082$  m/s for the optimum case in 1974. Thus, this simplified technique yields conservative estimates of propellant penalties.

The results of calculations performed by G. Gordon for inclination limits of  $0.06^\circ$  to  $0.1^\circ$  and a sensor field of view of  $\pm 45^\circ$  are shown in Figure 7. An 810-kg satellite and thrusters with 200-second specific impulse have been assumed. The result of similar calculations for an inclination limit of  $0.08^\circ$  and varying fields of view, between  $\pm 45^\circ$  and  $\pm 60^\circ$ , are plotted in Figure 8. These two figures confirm that penalties are minimized for larger inclination limits and sensor fields of view.

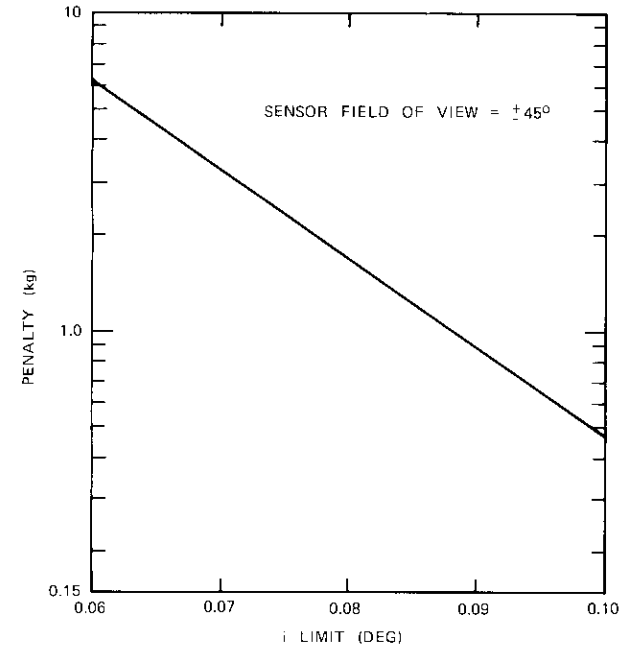


Figure 7. Effect of Inclination Limit on Propellant Penalty (field of view =  $\pm 45^\circ$ )

### Sensor requirements

During solstice periods, the declination of the sun is between  $20^\circ$  and  $23.5^\circ$ . Thus, the technique described here employs the projection of the sun onto the equatorial plane. The deviation in the expected declination has itself been proposed for use in measuring yaw error. However, sensitivity is poor and high pointing accuracy is not possible during the solstice periods. During spring and fall months, sun sensor application to yaw measurement is straightforward. Of course, sensor alignment accuracy and sensitivity must be compatible with year-round operations.

### Conclusions

A unique combination of geometry, impulsive thrust, and perturbation characteristics makes the off-node technique practical and attractive. The cost of implementation is negligible in most realistic cases. Propellant

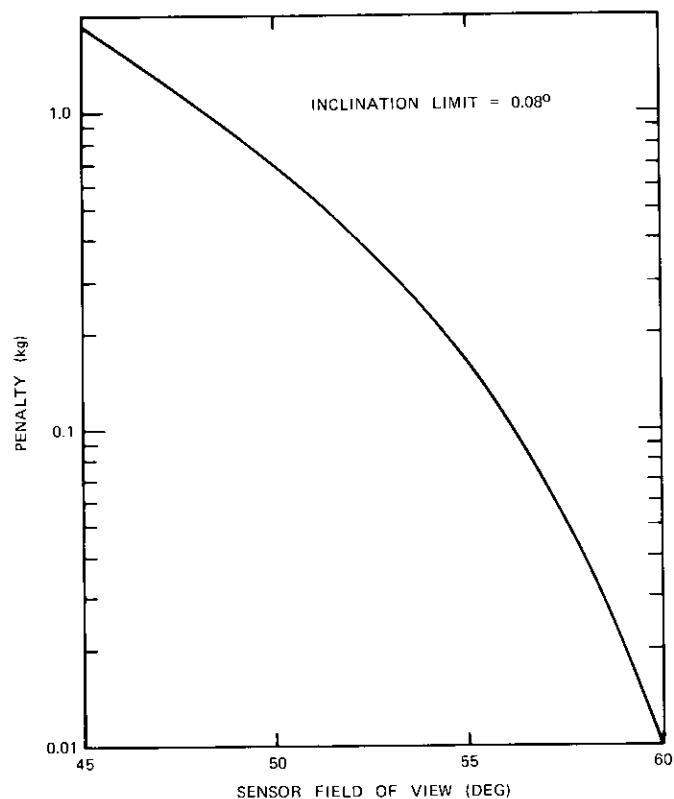


Figure 8. *Effect of Sensor Field of View on Propellant Penalty*  
(*i limit = 0.08°*)

penalties depend on the sun sensor field of view and specified inclination limits. Hardware requirements include a minimum of one sun sensor and associated logic if both north and south facing thrusters are available. Otherwise, two sun sensors are necessary. Thus, this method offers a simple inexpensive way to satisfy mission objectives.

Off-node firing with minimum propellant penalty may be useful for applications other than minimization of the yaw measurement problem. For example, the solar array orientation may interfere with thruster operations at the solstice points. Thus, it may be essential to align the arrays with the yaw axis during inclination corrections while using the arrays to supply 50 to 70 percent of normal power. The strategy used here

for a sensor field of view of  $\pm 60^\circ$  would be appropriate for supplying 50 percent of normal power, and that for a sensor field of view of  $\pm 45^\circ$  would provide 70.7 percent of normal power. Obviously, there may be other situations in which this strategy would prove advantageous.

### Acknowledgment

The author would like to thank the several COMSAT personnel who assisted in this work. In particular, appreciation is extended to A. Ramos for initiating this study, to W. D. Kinney for supplying computer programs and suggestions on thrusting strategy, and to G. D. Gordon for helping to optimize the strategy.

### References

- [1] A. A. Satterlee, Private Communication, April 1973.
- [2] R. R. Allan, "Perturbations of a Geostationary Satellite, 2) Lunisolar Effects," Royal Aircraft Establishment, Technical Note No. SPACE 47, September 1963.

Marshall H. Kaplan is Associate Professor of Aerospace Engineering at the Pennsylvania State University and a consultant to COMSAT Laboratories on satellite dynamics and control. His teaching and research interests include astrodynamics, spacecraft autopilots, propulsion, and planetary gravity analysis. Recently, he has published papers on the use of electric thrusters for complete satellite control, retrieval of spinning objects from orbit, and modeling of the lunar gravity field. Dr. Kaplan received a B.S. in aeronautical engineering from Wayne State University, an S.M. in aeronautics and astronautics from M.I.T., and a Ph.D. in aeronautics and astronautics from Stanford University. He is an Associate Fellow of AIAA, a member of Sigma Xi, and a Founder Member of the American Academy of Mechanics.



***Detection of INTELSAT IV spin axis angular displacement induced by propellant system mass imbalance***

A. J. CORIO

(Manuscript received June 13, 1974)

***Abstract***

Following an orbital inclination change maneuver of INTELSAT IV F-3 on February 14, 1973, unexpected changes were observed in data from attitude sensors. Analysis of the changes indicated a spin axis angular displacement caused by a propellant system mass imbalance attributed to a bubble trapped in the connecting manifold. This same problem was later noted in F-4 and F-5.

This paper presents the analysis techniques and their application to INTELSAT IV F-5. The angular displacement was found to be  $0.15^\circ$ , induced by a mass imbalance of about 7.4 kg (16 lb). The analysis of angular displacement is an exact geometric formulation using sun and earth sensor alignments and measurements. The mass imbalance is analyzed as the removal of a point mass which causes a principal axis rotation.

Bubbles were successfully expelled from F-3, F-4, and F-5 using short firings of the system A radial thrusters. The phenomenon of bubble trapping is not discussed in this paper, but is the subject of continuing investigation by COMSAT and the Hughes Aircraft Company.

---

This paper is based on work performed under the sponsorship of the International Telecommunications Satellite Organization (INTELSAT). Views expressed in this paper are not necessarily those of INTELSAT.

## Introduction

The 2-body INTELSAT IV communications satellite is a rotating cylindrical drum (rotor) from which an antenna platform is mechanically despun. The longitudinal principal axis of the satellite coincides with the bearing axis joining the bodies so that the rotating satellite does not wobble. Any nutation induced by disturbing torques is damped by platform-mounted nutation dampers. A rotor mass imbalance angularly displaces the longitudinal principal axis from the bearing axis, and the satellite wobbles in synchronism with the spin rate.

The inertial attitude of the spin axis (angular momentum vector) is determined from measurements made by rotor-mounted sensors scanning the sun and earth. When the rotor becomes unbalanced, the sensor scans relative to the new principal axis, resulting in measurement changes which are used to calculate the magnitude and direction of the principal axis angular displacement. The best values of these changes are obtained by comparing sensor measurement biases computed in attitude determinations before and after the rotor becomes unbalanced.

On February 14, 1973, an orbital inclination change maneuver was performed on INTELSAT IV F-3 using the system A axial thruster. Routine processing of attitude data after the maneuver revealed unexpected changes in sun and earth sensor measurement biases. An angular displacement of the spacecraft's spin axis was suspected and investigated. The results showed a spin axis shift of about  $0.13^\circ$  in the plane containing the bearing axis and the two diametrically opposed tanks of propellant system A (see Figure 1). This was confirmed by calculating the angular shift of the spin axis caused by drawing propellant from only one of the two tanks.

The failure to draw propellant from one of the tanks was caused by a bubble trapped in an expansion loop of the connecting manifold and was demonstrated with a mock-up at COMSAT Laboratories [1]. Members of the Spacecraft Laboratory analyzed the imbalance and recommended a short continuous burn from the system A radial thruster to draw the bubble out of the loop and expel it. Following the burn on April 5, 1973, expulsion of the bubble was confirmed by spin speed changes and restoration of sun and earth sensor biases to their values prior to the inclination maneuver as the propellant redistributed to a symmetrical configuration. This same type of mass imbalance occurred in F-4 and F-5 following inclination maneuvers in the summer of 1973; the trapped bubbles were successfully expelled the following winter.

The following sections contain derivations of the analysis techniques

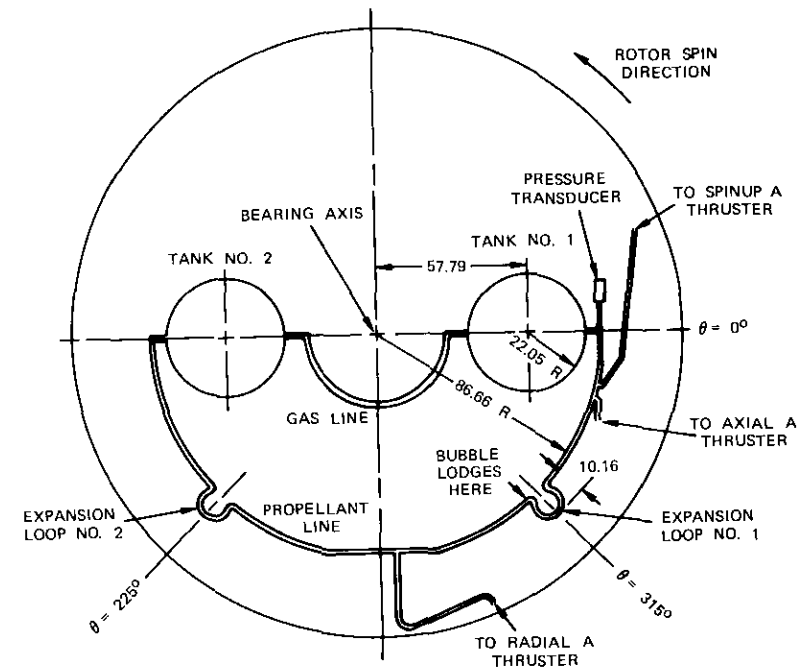


Figure 1. Rotor Showing Positioning and Orientation System As Viewed Along the Spin Axis from the Despun Antenna Platform (dimensions are in centimeters)

and their application to the mass imbalance of INTELSAT IV F-5, whose large measurement changes provide a convincing case. The analysis is presented in two sections. The first derives equations for computing the magnitude and direction of the spin axis angular displacement from changes in sun and earth sensor biases. The second section derives equations for determining the rotor mass imbalance in terms of spacecraft mass properties and angular displacement of the spin axis.

## Analysis of spin axis displacement from sensor data

Figure 2 shows the angular alignment of sensors and some other equipment in the rotor's spin plane (normal to the bearing axis) viewed from above. The system A propellant tanks (not shown) are located at  $0^\circ$  and  $180^\circ$ .

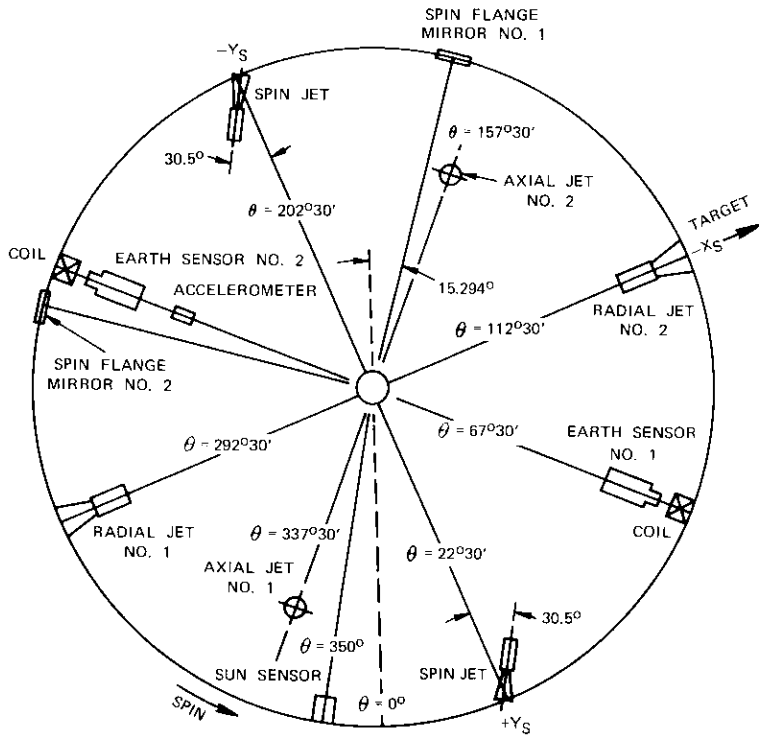


Figure 2. Spin Location of Sun and Earth Sensors

Figure 3 shows the sun sensor, which consists of two fan-beam-shaped planar slits, each capable of detecting the sunlight entering it once per spacecraft rotation. The  $\psi_1$  slit plane contains the spin axis so that detection in this slit always occurs at the same spacecraft rotational phase. The  $\psi_2$  slit is located  $35^\circ$  ( $\lambda$ ) later in rotation and is canted by  $35^\circ$  ( $\xi$ ) from the local meridian so that it detects sunlight at a rotational phase dependent upon the sun angle. The spacecraft rotational angle,  $\psi$ , measured from  $\psi_1$  to  $\psi_2$  detection is used with  $\xi$  and  $\lambda$  to calculate the sun angle.

The north and south earth sensors are mounted diametrically opposite each other, with the lines of sight elevated  $6.2^\circ$  above and below the spin plane, respectively. As the spacecraft rotates, each sensor's line of sight sweeps across the earth and produces a pulse at each horizon crossing. The earth angle is the spacecraft rotation angle between the enter-earth and exit-earth pulses.

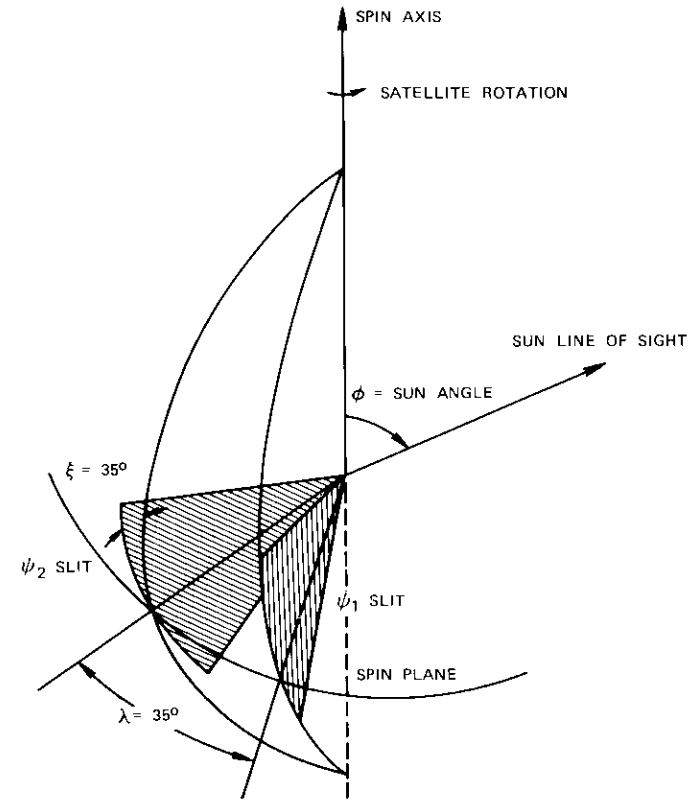


Figure 3. Sun Sensor Design

The effects of a rotor mass imbalance on sensor measurements are best visualized in an idealized situation; the mass imbalance occurs instantaneously and does not alter the inertial direction of the spin axis (the angular momentum vector). After the mass imbalance occurs, the rotor wobbles in synchronism with the spin rate, causing a change in the sensor alignment with the spin axis. Changes in sun and earth sensor measurements taken immediately before and after the mass imbalance are physically attributable only to this realignment.

Although the mass imbalance may occur within a short period of time, it is always associated with propulsion which slightly disturbs the direction of the angular momentum. This problem is overcome by using measurement biases calculated by the attitude determination computer program.

Spin axis attitude is determined by a least-squares method using sun and earth sensor measurements. A sensor bias is, in effect, the typical difference between the actual sensor measurement and the corresponding measurement computed from the best estimate of the attitude. Separate attitude determinations are made during 24-hour data spans preceding and following the mass imbalance, and the changes in sensor biases are used to compute the spin axis displacement in the rotor.

These biases depend on the sun and earth angles and, for the earth sensors, seasonal variations. The satellite operates in geosynchronous orbit with the spin axis oriented normal to the coincident orbital and equatorial planes. In any 48-hour period,  $\phi$  changes directly with the sun's declination (a maximum of  $0.8^\circ$ ), and small perturbations cause a small amplitude (less than  $0.5^\circ$ ) sinusoidal diurnal variation of  $\eta$  about  $90^\circ$ .

This slow variation in sun and earth angles ensures that changes in measurement biases are equivalent to the idealized measurement changes. Also, since the subsequent analysis is concerned with change and does not require absolute accuracy in the reference values,  $\eta$  is assumed to be  $90^\circ$  and a single representative value of  $\phi$  is chosen.

When the spacecraft's position and spin axis attitude are known with respect to the earth and sun, the sun angle and earth angle are calculated as follows:

$$\text{ctn } \phi = \text{ctn } \xi \sin (\psi - \lambda) \quad (1)$$

$$\cos q = \frac{\cos H - \cos \eta \cos G}{\sin \eta \sin G} \quad (2)$$

where  $\phi$  = sun angle (Figure 3)  
 $\lambda$  = separation angle (Figure 3)  
 $\xi$  = cant angle (Figure 3)  
 $\psi$  = spacecraft rotation angle from  $\psi_1$  to  $\psi_2$  detection  
 $q$  = half earth angle measured in the spin plane  
 $H$  = half angular width of the earth as seen by the satellite  
 $\eta$  = angle between the spin axis and the line of sight to the earth's center  
 $G$  = angle between the spin axis and the earth sensor's line of sight.

Figure 4 is a vectorial abstraction of the sun sensor and north earth sensor in spacecraft rotor coordinates. The  $XY$  plane is the spin plane of Figure 2 with the  $X$  axis along  $\theta = 0^\circ$ , and the  $Z$  axis along the bearing

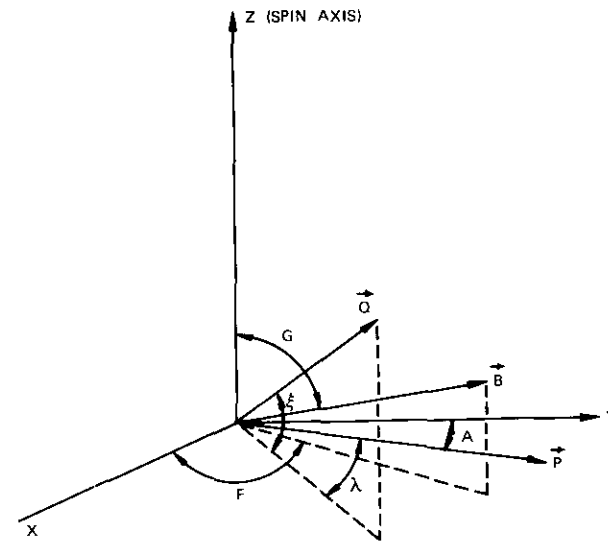


Figure 4. *Vector Representation of Sun and Earth Sensors*

axis. Unit vectors  $\vec{P}$  and  $\vec{Q}$  are normal to the  $\psi_1$  and  $\psi_2$  sun sensor slits, respectively. Vector  $\vec{B}$  through the north earth sensor's line of sight has a length equal to the distance from the satellite to the circumference of the visible earth disk. The south earth sensor is geometrically redundant. Any angular displacement of the spin axis within the rotor can be defined by the sequence of coordinate rotations in Figure 5. The  $Z'$  axis is the new spin axis and the  $X'Y'$  plane is the new spin plane.

After the mass imbalance, the sun and earth sensor measurements change, but  $\phi$  and  $\eta$  do not change since they relate to the inertial spin axis. The altered sensor measurements are designated as  $\psi'$  and  $q'$ .

The coordinate rotation of a vector from unprimed to primed coordinates is

$$\begin{bmatrix} V_{X'} \\ V_{Y'} \\ V_{Z'} \end{bmatrix} = \begin{bmatrix} \cos \alpha \cos \beta & \cos \alpha \sin \beta & -\sin \alpha \\ -\sin \beta & \cos \beta & 0 \\ \sin \alpha \cos \beta & \sin \alpha \sin \beta & \cos \alpha \end{bmatrix} \begin{bmatrix} V_X \\ V_Y \\ V_Z \end{bmatrix} \quad (3)$$

where  $\vec{V}$  is any vector. Since the  $Z'$  axis is the physical spin axis, the rotating line-of-sight vectors to the sun's and earth's centers are defined by components in the primed coordinate system:

$$\vec{N}_1 = \begin{bmatrix} \sin \phi \cos \psi'_1 \\ \sin \phi \sin \psi'_1 \\ \cos \phi \end{bmatrix} \quad (4)$$

$$\vec{N}_2 = \begin{bmatrix} \sin \phi \cos \psi'_2 \\ \sin \phi \sin \psi'_2 \\ \cos \phi \end{bmatrix} \quad (5)$$

$$\psi' = \psi'_1 - \psi'_2 \quad (6)$$

where  $\vec{N}_1$  = unit vector to the sun at detection through the  $\psi_1$  slit  
 $\vec{N}_2$  = unit vector to the sun at detection through the  $\psi_2$  slit  
 $\phi$  = sun aspect angle to the spin axis  
 $\psi'_1$  = spin plane angle of  $\vec{N}_1$  at detection through the  $\psi_1$  slit  
 $\psi'_2$  = spin plane angle of  $\vec{N}_2$  at detection through the  $\psi_2$  slit  
 $\psi'$  = rotation angle of the spacecraft from  $\psi'_1$  to  $\psi'_2$  detection.

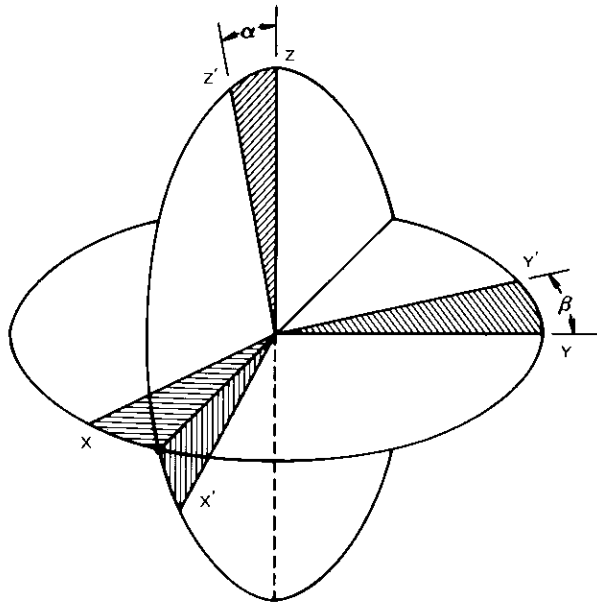


Figure 5. Coordinate Rotations for Analyzing Spin Axis Displacements

The components of  $\vec{P}$  and  $\vec{Q}$  in the primed coordinate system are obtained by using equation (3):

$$\vec{P} = \begin{bmatrix} \cos \alpha \cos \beta & \cos \alpha \sin \beta & -\sin \alpha \\ -\sin \beta & \cos \beta & 0 \\ \sin \alpha \cos \beta & \sin \alpha \sin \beta & \cos \alpha \end{bmatrix} \begin{bmatrix} \sin A \\ \cos A \\ 0 \end{bmatrix} \quad (7)$$

$$\vec{P} = \begin{bmatrix} \cos \alpha \sin (\beta + A) \\ \cos (\beta + A) \\ \sin \alpha \sin (\beta + A) \end{bmatrix} \quad (8)$$

$$\vec{Q} = \begin{bmatrix} \cos \alpha \cos \beta & \cos \alpha \sin \beta & -\sin \alpha \\ -\sin \beta & \cos \beta & 0 \\ \sin \alpha \cos \beta & \sin \alpha \sin \beta & \cos \alpha \end{bmatrix} \begin{bmatrix} \cos \xi \sin (\lambda + A) \\ \cos \xi \cos (\lambda + A) \\ \sin \xi \end{bmatrix} \quad (9)$$

$$\vec{Q} = \begin{bmatrix} \cos \alpha \cos \xi \sin (\beta + \lambda + A) - \sin \alpha \sin \xi \\ \cos \xi \cos (\beta + \lambda + A) \\ \sin \alpha \cos \xi \sin (\beta + \lambda + A) + \cos \alpha \sin \xi \end{bmatrix} \quad (10)$$

Equations relating the effect of spin axis displacements on sun sensor measurements are formed in terms of these vectors. Sunlight detections through the  $\psi_1$  and  $\psi_2$  slits occur when the sun line-of-sight vectors are normal to  $\vec{P}$  and  $\vec{Q}$ , respectively:

$$\vec{N}_1 \cdot \vec{P} = 0 \quad (11)$$

$$\vec{N}_2 \cdot \vec{Q} = 0 \quad (12)$$

Equations (4)-(6) are used with equations (8) and (10) to yield

$$C_1 \cos \psi'_1 + S_1 \sin \psi'_1 = T_1 \quad (13)$$

$$C_2 \cos \psi'_1 + S_2 \sin \psi'_1 = T_2 \quad (14)$$

$$\text{where } C_1 = \sin \phi \cos \alpha \sin (\beta + A) \quad (15)$$

$$S_1 = \sin \phi \cos (\beta + A) \quad (16)$$

$$T_1 = -\cos \phi \sin \alpha \sin (\beta + A) \quad (17)$$

$$C_2 = \sin \phi \{ \cos \psi' [\cos \alpha \cos \xi \sin (\beta + \lambda + A) - \sin \alpha \sin \xi] - \sin \psi' \cos \xi \cos (\beta + \lambda + A) \} \quad (18)$$

$$S_2 = \sin \phi \{ \sin \psi' [\cos \alpha \cos \xi \sin (\beta + \lambda + A) - \sin \alpha \sin \xi] + \cos \psi' \cos \xi \cos (\beta + \lambda + A) \} \quad (19)$$

$$T_2 = -\cos \phi [\sin \alpha \cos \xi \sin (\beta + \lambda + A) + \cos \alpha \sin \xi] \quad (20)$$

and  $A$  is the angular location of the  $\psi_1$  slit in the spin plane.

Equations (13) and (14) contain three unknowns:  $\alpha$ ,  $\beta$ , and  $\psi_1$ . Combining these equations eliminates  $\psi_1$ :

$$(T_1 S_2 - T_2 S_1)^2 + (C_1 T_2 - C_2 T_1)^2 - (C_1 S_2 - C_2 S_1)^2 = 0 \quad (21)$$

Equation (21), the generalized sun angle equation, relates the spin axis displacement angles  $\alpha$  and  $\beta$  to known values of  $\phi$  and  $\psi'$ . If  $\alpha$  and  $\beta$  are set to zero, it reduces to equation (1). The values of  $\alpha$  and  $\beta$  are not unique, but the solution line can be plotted on polar graph paper in the region of  $\alpha = 0$  (at the pole of the projected unit sphere).

A similar procedure determines the locus of spin axis angular displacements for earth sensor measurements. The components of  $\vec{B}$  are expressed in the primed coordinate system using the alignment angles of Figure 4 and equation (3):

$$\vec{B} = \begin{bmatrix} \cos \alpha \cos \beta & \cos \alpha \sin \beta & -\sin \alpha \\ -\sin \beta & \cos \beta & 0 \\ \sin \alpha \cos \beta & \sin \alpha \sin \beta & \cos \alpha \end{bmatrix} \begin{bmatrix} B \sin G \cos F \\ B \sin G \sin F \\ B \cos G \end{bmatrix} \quad (22)$$

$$\vec{B} = \begin{bmatrix} B \cos \alpha \sin G \cos (\beta - F) - B \sin \alpha \cos G \\ -B \sin G \sin (\beta - F) \\ B \sin \alpha \sin G \cos (\beta - F) + B \cos \alpha \cos G \end{bmatrix} \quad (23)$$

If  $F'$  and  $G'$  are angles analogous to  $F$  and  $G$ , but defined in the primed coordinate system, then the components of  $\vec{B}$  are expressed as follows:

$$\vec{B} = \begin{bmatrix} B \sin G' \cos F' \\ B \sin G' \sin F' \\ B \cos G' \end{bmatrix} \quad (24)$$

Therefore, from equations (23) and (24),

$$\cos G' = \sin \alpha \sin G \cos (\beta - F) + \cos \alpha \cos G \quad (25)$$

Let  $\vec{D}$  be the vector from the satellite to the earth's center when  $\vec{B}$  intersects the horizon of the earth's disk. Since the spin axis is aligned with the orbit normal,  $\vec{D}$  lies in the spin plane at angle  $K$ :

$$\vec{D} = \begin{bmatrix} D \cos K \\ D \sin K \\ 0 \end{bmatrix} \quad (26)$$

Let  $\vec{R}$  be the earth's radius vector from the earth's center to the point of horizon intersection by  $\vec{B}$ . Then,

$$\vec{R} = \vec{B} - \vec{D} \quad (27)$$

Since  $\vec{R}$  is normal to the earth's surface and  $\vec{B}$  is tangent to it,  $\vec{B}$  and  $\vec{R}$  are orthogonal to each other. Therefore,

$$\cos H = \frac{B}{D} \quad (28)$$

and

$$B D \cos H = \vec{B} \cdot \vec{D} \quad (29)$$

Hence, from equations (24) and (26),

$$\cos H = \sin G' \cos (F' - K) \quad (30)$$

where  $(F' - K)$  is the angle between  $\vec{D}$  and the projection of  $\vec{B}$  in the spin plane, and is just half of the earth angle measured by the earth sensor. Then, from equation (30),

$$\cos G' = + \sqrt{1 - \left( \frac{\cos H}{\cos q'} \right)^2} \quad (31)$$

$$q' = F' - K \quad (32)$$

Combining equations (25) and (31) yields

$$\sin \alpha \sin G \cos (\beta - F) + \cos \alpha \cos G = + \sqrt{1 - \left(\frac{\cos H}{\cos q'}\right)^2}. \quad (33)$$

Equation (33) for the earth sensor is analogous to equation (21). When  $\alpha$  and  $\beta$  are zero, equation (33) reduces to equation (2) evaluated at  $\eta = 90^\circ$ .

Similar to the sun sensor equation, the solution line for  $\alpha$  and  $\beta$  can be plotted on polar graph paper. The intersection of the two lines is, of course, the common solution for the spin axis displacement. Equations (21) and (33) may also be solved simultaneously by iteration.

Before the spin axis is displaced, the measurement angles,  $\psi$  and  $q$ , are calculated from  $\phi$  and  $\eta$  using equations (1) and (2). After the spin axis displacement by  $\alpha$  and  $\beta$ , the measurement angles become  $\psi'$  and  $q'$ . They are related to  $\phi$  and  $\eta$  by equations (21) and (33), which account for the spin axis displacement.

The value of the earth half-angle,  $q'$ , after the displacement is found by adding the observed change in measurement bias to the value of  $q$  before the displacement. The value of  $\psi'$  must be obtained indirectly, since its bias is not determined. The attitude determination program uses values of  $\phi$  calculated from  $\psi$  measurements as "measurement" variables and determines a bias for  $\phi$ . The post-displacement  $\phi'$  is the sum of  $\phi$  during the displacement and the bias change. The value of  $\psi'$  is calculated from  $\phi'$  using equation (1), and represents the sun sensor's measurement after displacement of the spin axis. These values of  $\psi'$  and  $q'$  are used with  $\phi$  and  $\eta$  ( $90^\circ$ ) in equations (21) and (33) to calculate  $\alpha$  and  $\beta$ .

The preceding analysis was applied to the balance restoring bubble expulsion of INTELSAT IV F-5. The presence of a trapped bubble was confirmed after an inclination maneuver in the summer of 1973, but expulsion was delayed until the following winter to refine expulsion calculations [1] and to exploit the sun sensor's greater geometric sensitivity at large sun angles (see Figure 6). In any case, the delay did not jeopardize the integrity of the spacecraft.

Expulsion restored balance to the spacecraft; it was the geometric inverse of the inclination maneuver which caused the imbalance.

Attitude determinations were run using 24-hour data spans immediately before and after the bubble expulsion. The biases and their changes are listed in Table 1. The changes show that, after expulsion, the sun sensor measured smaller sun angles and the earth sensor larger earth angles. These differences, along with their upper and lower bounds, were used to

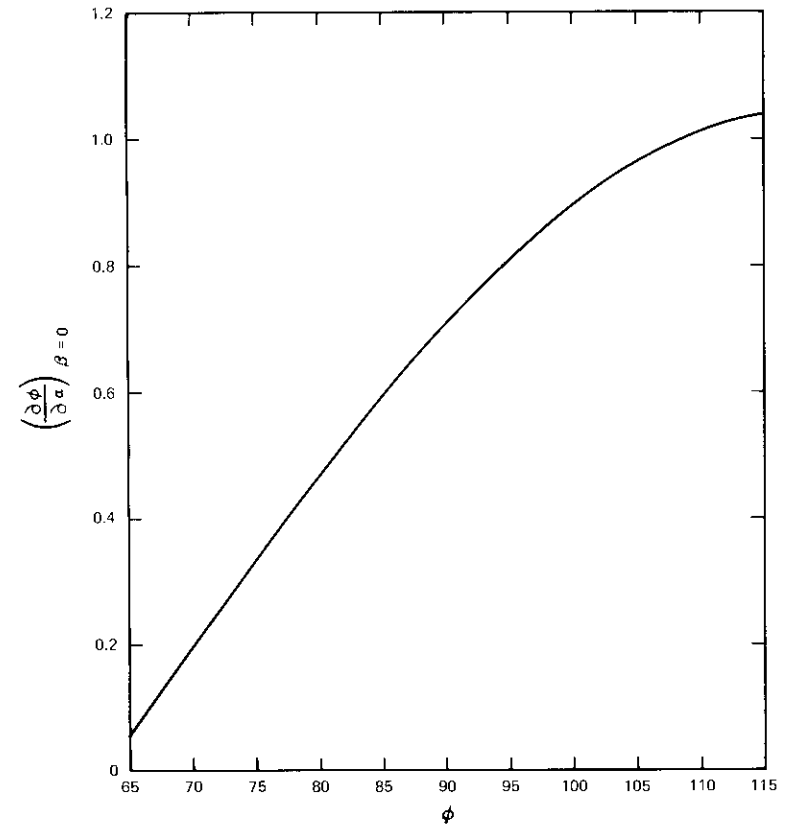


Figure 6. Rate of Change of Calculated Sun Angle with Respect to Spin Axis Displacement in Plane of Propellant System A for All Sun Angles

obtain values for equations (21) and (33). The solution and its bounds are plotted in Figure 7.

TABLE 1. BIAS CHANGES

	$\phi$ Bias	$q$ (south earth sensor) Bias
Before Bubble Expulsion	+0.1338 $\pm$ 0.010	-0.1116 $\pm$ 0.010
After Bubble Expulsion	-0.0105 $\pm$ 0.010	-0.0489 $\pm$ 0.010
Change	-0.1443 $\pm$ 0.014	+0.0627 $\pm$ 0.014

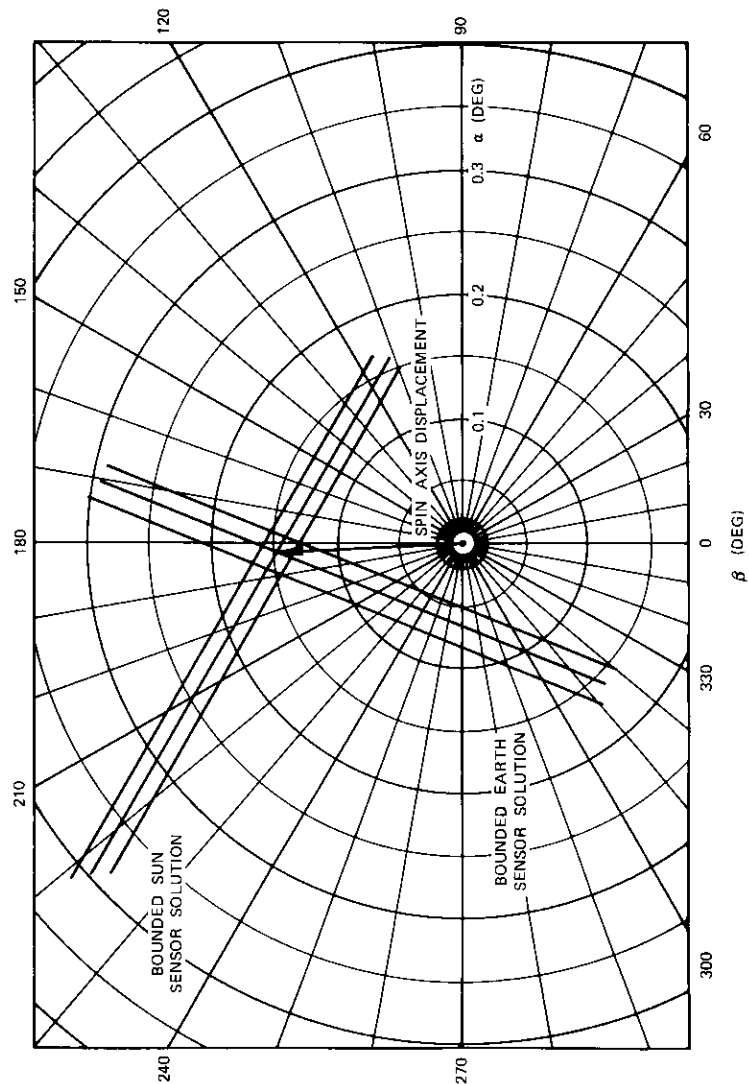


Figure 7. Graphical Solution for Spin Axis Displacement

The solution occurs when  $\alpha$  equals  $0.147^\circ$  and  $\beta$  equals  $183^\circ$ , indicating a spin axis displacement in the plane containing the system A propellant tanks ( $0^\circ \rightarrow 180^\circ$ ) and the original spin axis.

**Estimation of mass imbalance**

The magnitude of the system A propellant mass imbalance is estimated from the spacecraft's mass properties and the principal axis displacement determined above. Figure 8 shows the location of the system A propellant tanks in spacecraft coordinates. The left tank is closer to the axial thruster. During thrusting, unequal amounts of propellant are drawn, with the greater amount coming from the left tank. The difference is represented by the shaded area, which is the propellant deficiency after the maneuver. It is approximated as a point mass  $u$  at a distance  $X_u$  from the spin axis and  $Z_u$  from the X axis.

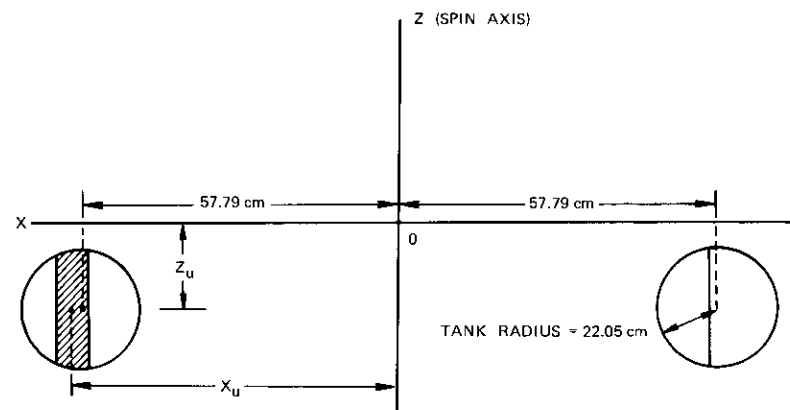


Figure 8. Propellant Tank Locations in the Satellite

Figure 9 shows the effects of removing  $u$  on the spacecraft's coordinate system. Initially, the spacecraft's center of mass is located at 0, with the Z axis as the spin axis and the Y axis pointing directly out of the paper. The following assumptions are made for the analysis:

- a. before  $u$  is removed, X, Y, and Z are principal axes of the spacecraft with the spin axis along Z;
- b. the X and Y (transverse) moments of inertia are equal;

c. the platform of the spacecraft is inertially despun so that only the rotor's mass contributes to the Z moment of inertia even after removal of  $u$ ;

d. after  $u$  is removed, the spacecraft spins about a new principal axis.

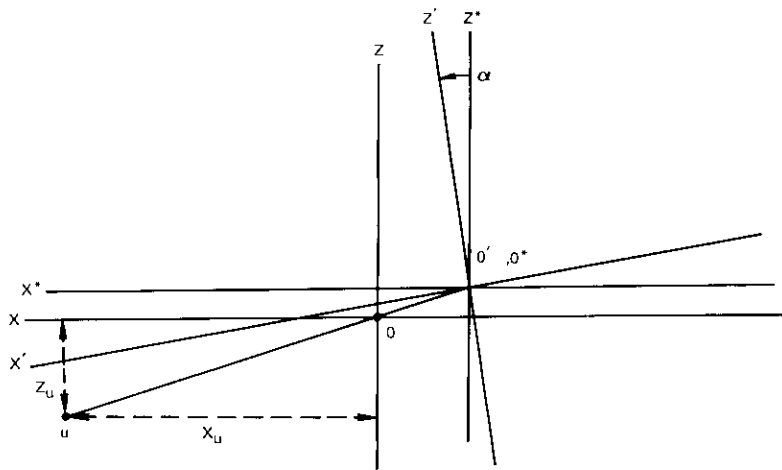


Figure 9. Coordinate Transformations Resulting from Propellant Mass Removal

Removing  $u$  from the spacecraft produces two effects. First, the center of mass is displaced from  $0$  to  $0^*$ . Second, the principal axes shift through an angle  $\alpha$  to  $X', Z'$ . The angle  $\alpha$  is attributable solely to the  $XZ$  product of inertia induced by the point mass removal, and  $Z'$  becomes the new spin axis.

The mass properties of the spacecraft are defined in the context of Figure 10. Any point mass  $m_i$  is located by a vector  $\vec{r}_i$  in pre-maneuver spacecraft coordinates. After  $u$  is removed, the spacecraft's center of mass displacement is  $\vec{S}$ , and the relative point mass location is  $\vec{r}_i^*$ . The initial moments and products of inertia for  $N$  point masses are

$$I_{XX} = \sum_{i=1}^N m_i(r_i^2 - X_i^2) \tag{34}$$

$$I_{YY} = \sum_{i=1}^N m_i(r_i^2 - Y_i^2) \tag{35}$$

$$I_{ZZ} = \sum_{i=1}^N m_i(r_i^2 - Z_i^2) \tag{36}$$

$$I_{XY} = I_{YX} = -\sum_{i=1}^N m_i X_i Y_i \tag{37}$$

$$I_{YZ} = I_{ZY} = -\sum_{i=1}^N m_i Y_i Z_i \tag{38}$$

$$I_{ZX} = I_{XZ} = -\sum_{i=1}^N m_i Z_i X_i \tag{39}$$

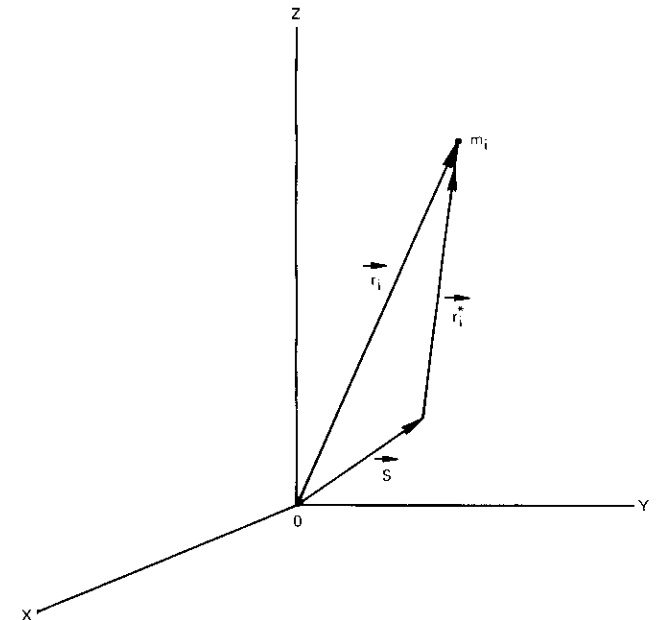


Figure 10. Mass Point Location in Spacecraft Coordinates

The following constraints result from the assumptions:

$$I_{XX} = I_{YY} \tag{40}$$

$$I_{XY} = I_{YZ} = I_{ZX} = 0 \tag{41}$$

When the point mass  $u$  is removed, the center of mass is displaced to  $\vec{S}$ :

$$\vec{S} = \frac{-u\vec{r}_u}{M - u} \tag{42}$$

$$M = \sum_{i=1}^N m_i \tag{43}$$

where  $\vec{r}_u$  is the location of  $u$ . The mass properties of the spacecraft with  $u$  removed are now expressed with respect to the new center of mass in the  $X^*Y^*Z^*$  coordinates of Figure 9:

$$I_{XX}^* = \sum_{i=1}^N m_i(r_i^{*2} - X_i^{*2}) - u(r_u^{*2} - X_u^{*2}) \tag{44}$$

$$I_{YY}^* = \sum_{i=1}^N m_i(r_i^{*2} - Y_i^{*2}) - u(r_u^{*2} - Y_u^{*2}) \tag{45}$$

$$I_{ZZ}^* = \sum_{i=1}^N m_i(r_i^{*2} - Z_i^{*2}) - u(r_u^{*2} - Z_u^{*2}) \tag{46}$$

$$I_{XY}^* = I_{YX}^* = -\sum_{i=1}^N m_i X_i^* Y_i^* + u X_u^* Y_u^* \tag{47}$$

$$I_{YZ}^* = I_{ZY}^* = -\sum_{i=1}^N m_i Y_i^* Z_i^* + u Y_u^* Z_u^* \tag{48}$$

$$I_{ZX}^* = I_{XZ}^* = -\sum_{i=1}^N m_i Z_i^* X_i^* + u Z_u^* X_u^* \tag{49}$$

From Figure 10 and equation (42),

$$\vec{r}_i^* = \vec{r}_i - \vec{S} = \vec{r}_i + \left(\frac{u}{M - u}\right) \vec{r}_u \tag{50}$$

$$\vec{r}_u^* = \vec{r}_u - \vec{S} = \left(\frac{M}{M - u}\right) \vec{r}_u \tag{51}$$

When equations (50) and (51) are used in equations (44)-(49),

$$I_{XX}^* = I_{XX} - \left(\frac{uM}{M - u}\right) (r_u^2 - X_u^2) \tag{52}$$

$$I_{YY}^* = I_{YY} - \left(\frac{uM}{M - u}\right) (r_u^2 - Y_u^2) \tag{53}$$

$$I_{ZZ}^* = I_{ZZ} - \left(\frac{uM}{M - u}\right) (r_u^2 - Z_u^2) \tag{54}$$

$$I_{XY}^* = I_{YX}^* = I_{XY} + \left(\frac{uM}{M - u}\right) X_u Y_u \tag{55}$$

$$I_{YZ}^* = I_{ZY}^* = I_{YZ} + \left(\frac{uM}{M - u}\right) Y_u Z_u \tag{56}$$

$$I_{ZX}^* = I_{XZ}^* = I_{ZX} + \left(\frac{uM}{M - u}\right) Z_u X_u \tag{57}$$

Using equations (40) and (41) along with  $Y_u = 0$  (because of the tank location) yields

$$I_{XX}^* = I_{XX} - Z_u^2 \left(\frac{uM}{M - u}\right) \tag{58}$$

$$I_{YY}^* = I_{XX} - \left(\frac{uM}{M - u}\right) (X_u^2 + Z_u^2) \tag{59}$$

$$I_{ZZ}^* = I_{ZZ} - X_u^2 \left(\frac{uM}{M - u}\right) \tag{60}$$

$$I_{XY}^* = I_{YZ}^* = 0 \tag{61}$$

$$I_{ZX}^* = \left(\frac{uM}{M - u}\right) Z_u X_u \tag{62}$$

The principal axis locations are obtained by finding that coordinate rotation of  $X^*, Y^*, Z^*$  axes for which all products of inertia are zero.

Since only the  $X^*Z^*$  product of inertia is nonzero, a rotation about the  $Y^*$  axis suffices. This rotation angle is  $\alpha$  in Figure 9, and the rotation is defined as follows:

$$Z'_i = Z_i^* \cos \alpha + X_i^* \sin \alpha \quad (63)$$

$$X'_i = -Z_i^* \sin \alpha + X_i^* \cos \alpha \quad (64)$$

$$Z'_u = Z_u^* \cos \alpha + X_u^* \sin \alpha \quad (65)$$

$$X'_u = -Z_u^* \sin \alpha + X_u^* \cos \alpha \quad (66)$$

The  $Z'X'$  product of inertia must be zero so that

$$I'_{ZX} = -\sum_{i=1}^N m_i Z'_i X'_i + u Z'_u X'_u = 0 \quad (67)$$

When the transformation equations are applied to equation (67), the angle  $\alpha$  is obtained as

$$\alpha = \frac{1}{2} \arctan \frac{-2I_{ZX}^*}{I_{XX}^* - I_{ZZ}^*} \quad (68)$$

This in turn becomes

$$\alpha = \frac{1}{2} \arctan \frac{-2[uM/(M-u)]Z_u X_u}{(I_{XX} - I_{ZZ}) + [uM/(M-u)](X_u^2 - Z_u^2)} \quad (69)$$

Equation (69) expresses the angular displacement of the spin axis in terms of parameters measured in the pre-maneuver coordinates.

The values for INTELSAT IV F-5 prior to the inclination maneuver are as follows:

$$\begin{aligned} I_{XX} &= 691.8 \text{ kg } m^2 \text{ (510.3 slug } ft^2) \\ I_{ZZ} &= 239.0 \text{ kg } m^2 \text{ (176.3 slug } ft^2) \\ M &= 707.5 \text{ kg (48.48 slugs)} \\ Z_u &= -0.264 \text{ m (-10.4 in.)} \\ X_u &= 0.596 \text{ m (23.45 in.)} \\ \alpha &= 0.147^\circ \pm 0.020^\circ. \end{aligned}$$

The value of  $X_u$  has been obtained from Slabinski's [1] calculations of propellant levels. Since the propellant level is near the center of the spherical tank, it varies almost linearly with propellant mass. The inclination maneuver used 16.24 kg (35.8 lb) from system  $A$ . If the tanks were initially balanced and this propellant were drawn equally from both, then the propellant levels would be 0.596 m (23.45 in.) from the bearing axis in both tanks. If the propellant were drawn unequally, then the levels would be above and below this value by an equal amount so that, regardless of the size of the mass imbalance,  $X_u$  would be 0.596 m. In this range of values, equation (69) is well approximated by

$$\alpha \approx \frac{-uZ_u X_u}{I_{XX} - I_{ZZ}} \quad (70)$$

since

$$\frac{M}{M-u} \approx 1 \quad (71)$$

$$(I_{XX} - I_{ZZ}) \gg u(X_u^2 - Z_u^2) \quad (72)$$

$$(I_{XX} - I_{ZZ}) \gg uZ_u X_u \quad (73)$$

Equation (70) is plotted in Figure 11 with  $u$  as a function of  $x_u$  for the best estimate of  $\alpha$  and its bounds. For  $X_u = 0.596$  m,  $u \approx 7.39 \pm 0.91$  kg (16.3  $\pm$  2.0 lb). This estimate agrees well with Slabinski's [1] 6.8 kg to 7.7 kg based on the spin speed change during propellant redistribution following the bubble expulsion.

The value of  $\alpha$  computed in equation (70) is positive since  $u$  and  $X_u$  are positive and  $Z_u$  is negative. It indicates a spin axis shift of the  $Z^*$  axis toward the  $X^*$  axis, as shown in Figure 9. In terms of the previous sensor analysis angles,  $\beta$  equals  $0^\circ$  instead of  $180^\circ$ . This is entirely consistent because complementary effects are analyzed; the point mass removal applies to the inclination maneuver (mass imbalance induced), and the sensor analysis applies to bubble expulsion (mass balance restored).

## Conclusion

The routine processing of attitude data and systematic recording of the results are effective ways of monitoring the spacecraft's dynamic balance. Analysis of the data following an inclination maneuver of INTELSAT IV F-3

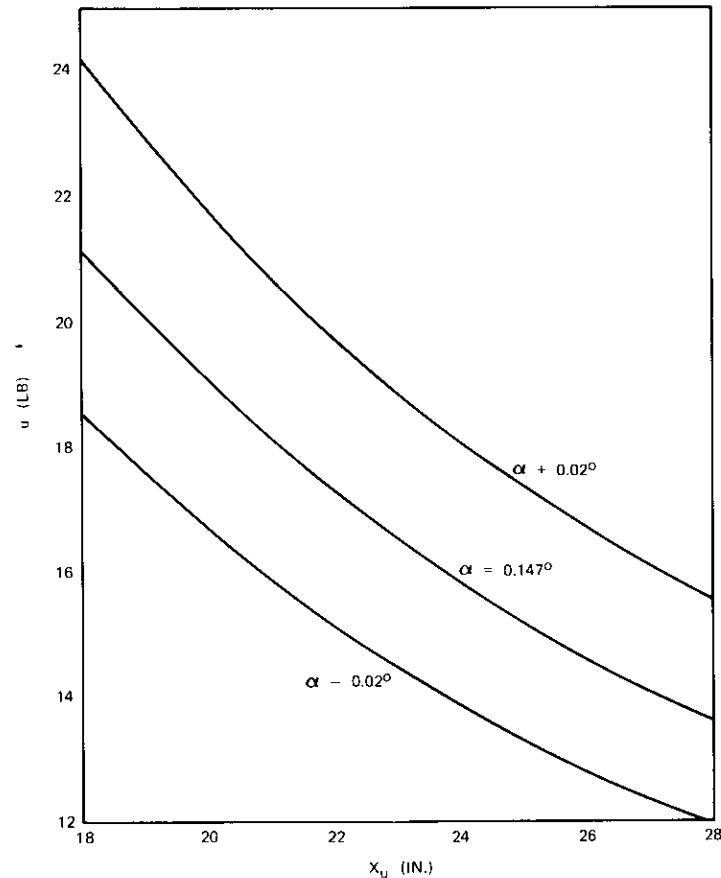


Figure 11. Mass Imbalance vs Propellant Level

on February 14, 1973, quickly established the existence of a mass imbalance in propellant system A. This paper contains the derivations of the analysis methods and their application to the mass imbalance of INTELSAT IV F-5.

The occurrence of a mass imbalance changes the direction of angular momentum so that sensor measurements before and after the imbalance cannot be used directly to calculate angular displacement. However, the equivalent information has been obtained from measurement biases computed from attitude determinations before and after the imbalance.

The mass imbalance was analyzed as a point mass removal which caused

a principal axis rotation. The calculated imbalance agreed well with an independent determination [1].

The cause of the induced mass imbalance, bubbles trapped in the manifold, has not been discussed. It is, however, the subject of a continuing investigation by COMSAT [1] and Hughes Aircraft Company.

### Reference

- [1] G. D. Gordon, G. R. Huson, and V. J. Slabinski, "Blocking Bubbles in the INTELSAT IV Fuel Lines," *COMSAT Technical Review*, Vol. 4, No. 2, Fall 1974.



Anthony J. Corio received a B.S. in Physics from Manhattan College in 1959 and an M.S. in Physics from Syracuse University in 1965. Since 1967 he has been a Member of the Technical Staff in COMSAT's Astrodynamics Department. His duties include development of mathematical methods for determining and controlling satellite orbital and attitude motion. He was previously employed by Melpar, Inc. and General Electric.

Index: attitude control, analog simulation, digital simulation, stabilized platforms, gimbals.

## ***Air bearing platform testing of a double-gimbaled momentum wheel attitude control system***

A. RAMOS

(Manuscript received August 26, 1974)

### ***Abstract***

An attitude control system whose central components are a double-gimbaled momentum wheel (DGMW) and an onboard digital computer was tested on the COMSAT Laboratories air bearing platform. Tests were performed to evaluate its performance in terms of stability, accuracy, and speed of response in two different modes, the track mode (including momentum dumping and simulated stationkeeping) and acquisition, and in mode transitions. These tests, which were supported by digital and analog computer simulations, also allowed evaluation of operational procedures associated with the combination of DGMW and digital computer. They demonstrated that a DGMW system is a feasible solution for achieving high roll and pitch accuracy in geostationary communications satellites. Equally as important, they demonstrated that yaw accuracy compatible with the roll and pitch accuracy required for spot beams is achievable without a yaw sensor.

---

This paper is based upon work performed under the sponsorship of the International Telecommunications Satellite Organization (INTELSAT). Views expressed in this paper are not necessarily those of INTELSAT.

## Introduction

A double-gimbaled momentum wheel (DGMW) attitude control system was tested for potential application to INTELSAT spacecraft using COMSAT Laboratories' air bearing platform. The testing was supported and verified by analyses and digital and analog computer simulations.

Part of the hardware and software for the system was designed, fabricated, and tested by TRW under contract. The hardware consisted of a ball-bearing momentum wheel mounted on two external rotary gimbals, associated power and transducer electronics, an onboard programmable digital computer, voltage regulators, and cold gas thrusters. The software consisted of the control and mode logic program, an assembler, and other support programs.

The testing had two primary objectives. The first was to evaluate the performance of the system in two different modes, the track mode (including momentum dumping and simulated stationkeeping) and acquisition, and in mode transitions. Performance measures of interest were stability, accuracy, speed of response, and parameter sensitivity. The second objective was to evaluate operational procedures associated with the combination of DGMW and digital computer. The testing included procedures for switching modes, updating parameters, and dumping momentum by ground command.

## Background

It is important to study methods for body stabilization because it offers high attitude and pointing accuracy and it is compatible with oriented solar arrays. A prime candidate for achieving body stabilization is a hybrid system composed of a double-gimbaled momentum wheel system and a mass expulsion system. A biased momentum wheel with its spin axis directed along the pitch axis is the source of angular momentum. The wheel speed is varied to provide pitch control torque, while gimbals along the roll and yaw axes are driven to provide yaw and roll control torques. The mass expulsion system is used for momentum dumping and other tasks. In this type of system yaw attitude need not be sensed directly. This is a characteristic common to biased momentum systems such as the double-gimbaled system.

Integrated circuits and memories which are sufficiently fast, low-power, small, and lightweight permit the use of a spaceborne programmable digital computer as the control logic unit. Advantages of this implementation

are flexibility and potentially enhanced reliability.

Related work on air bearing platform testing of double-gimbaled momentum wheel attitude control systems has been reported [1], [2]. Lebsack et al. [1] arranged the pitch axis so that it was parallel to the earth's spin axis; hence, the test orbit rate was equal to the earth's rate. However, the tests were limited to roll and pitch transient response, and no results were given for long-term performance, yaw response, or simulated stationkeeping. Kalley and Mork [2] described the basic tests performed at TRW on the equipment delivered to INTELSAT. These tests—transient response and long-term performance for small gimbal angles—were reproduced at COMSAT and served as the basis for more extensive testing.

## Test description

As shown in Figure 1, which also indicates the simulated geostationary orbit quantities, the local vertical frame with the pitch axis down was used as a reference. Orbiting was simulated by having the yaw axis of the air bearing platform (ABP) track a rotating arm on which the pitch and roll target was mounted. The axis of rotation of the arm was vertical. For simulation, its velocity was  $0.2^\circ$  per second counterclockwise looking down, which represents an increase in speed of 48 times the earth orbit rate. The speed accuracy was 0.5 percent, with wow and flutter of about 0.25 percent. The air bearing platform could be tilted by as much as  $45^\circ$  from the vertical and had unlimited rotation about the vertical.

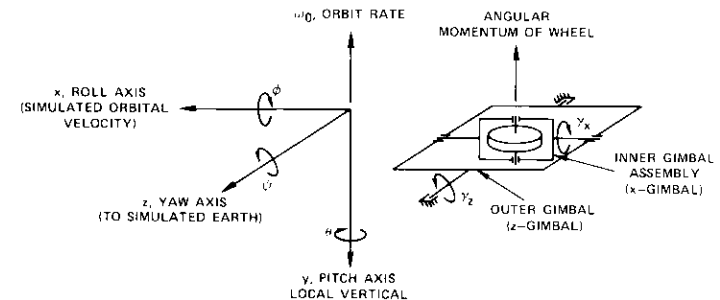


Figure 1. Reference Frame and Double Gimbaled Momentum Wheel

The angular momentum of the DGMW is 40 N-m-s. Each gimbal can rotate as much as  $\pm 20^\circ$ . These figures are a compromise between the parameters required to meet the disturbance torque environment of air bearing platform testing and the generally smaller figures expected for typical flight applications. The momentum wheel has an operating speed range of  $\pm 10$  percent about the bias speed of 5,000 rpm.

The onboard digital computer is designed to meet the requirements of a range of attitude control systems. To enhance its reliability, hardware design features have been simplified at the expense of more complicated software programming. The resulting design has a word length of 16 bits, an instruction repertoire of 38 instructions, an add time of  $7 \mu\text{s}$ , and a multiply time of about  $80 \mu\text{s}$ . A 512-word semiconductor random-access memory is used for scratchpad and working storage. For storage of the program, constants, and baseline parameters, the semiconductor read-only memory is simulated by a 3,072-word alterable program memory. The program segment related to control and testing takes up one-half of this memory capacity; the rest is used by the teletypewriter subroutine.

The heart of the air bearing platform is a 25-cm ball of hardened aluminum. In addition to the test article, the air bearing platform contains a 23-Ah, 28-V nickel-cadmium battery; a coulombmeter; two nitrogen gas tanks connected through a common line to a pressure regulator; a PCM/FSK/FM command receiver and decoder; an FM telemetry transmitter; balance wheels and micrometer heads; and the all-optical and analog attitude sensor complement consisting of a pitch-roll sensor, a yaw sensor, and a wide-angle pitch-yaw sensor. The ground support equipment comprises battery chargers, an external power supply, the controller for the air bearing platform, telemetry and command equipment, a stripchart recorder, a magnetic tape recorder, and a minicomputer. The minicomputer is used to select, scale, and convert real-time or played back telemetry data, and to synthesize 32-bit words which are sent through the command system as data.

Figure 2 is a block diagram of the attitude control system.

### Balancing procedures

The center of mass of the air bearing platform must be sufficiently close to the center of pressure of the air ball to keep the balance torques within acceptable limits, which are of the order of 0.001 N-m. The air bearing platform was first manually balanced to about 0.02 N-m. It was found that, after a 2-hour warm-up period, the balance changed by 0.04 N-m about

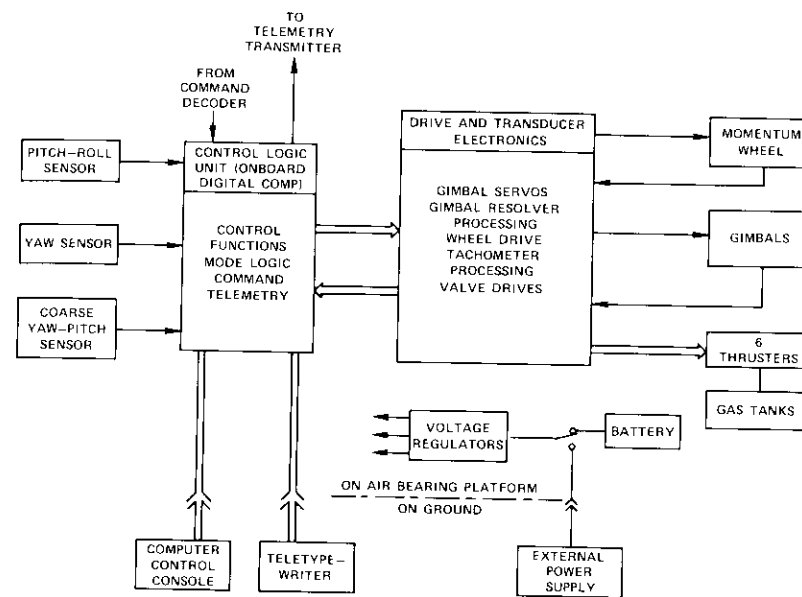


Figure 2. Block Diagram of Attitude Control System

the roll axis and by 0.012 N-m about the yaw axis. Therefore, it was necessary to compensate for these biases.

The attitude control system in the 3-sensor mode was used for further balancing. The gimbal rates (after compensation for the earth rate effect) provided a good measure of roll and yaw imbalance torques. Vertical imbalance was measured by using a yaw sensor target which was off vertical by about  $16^\circ$ . Thus, the component of the vertical imbalance seen about the roll-yaw plane led to the vertical imbalance itself. This precise balancing procedure, which is an adaptation of one used in the gyroscope industry, was required before each run.

### Concepts

The performance and operation of the attitude control system were evaluated on the basis of a set of concepts considered vital to DGMW systems. These concepts will be discussed briefly in the following subsections.

**Basic 2-axis sensing and 3-axis control**

Attitude control systems which are characterized by a substantial amount of angular momentum (so-called biased momentum systems) do not require a yaw sensor for basic operation. This is a major advantage because it is difficult to make accurate yaw sensors for geostationary orbit. Hence, it is important to study the basic stability and accuracy of such a concept. The DGMW system which has been tested can operate in the 2-sensor mode, i.e., 3-axis control (control torques applied by the DGMW about all three axes) realized with 2-axis sensing (roll and pitch). It can also operate in the 3-sensor mode; i.e., 3-axis control realized with 3-axis sensing. This latter mode has also been studied.

**Disturbance torque modeling**

The effects of external disturbance torques, especially yaw disturbance torque, are significant in the 2-sensor mode because the achievable yaw bandwidth, which is closely related to the orbit rate, is small compared to the roll and pitch bandwidths.

**EARTH ROTATION**

The earth's rotation can be represented as an inertially fixed torque with magnitude  $\omega_e H \cos \lambda = 0.0023$  N-m. This is a large but calibrated effect which can be offset by the attitude control functions. Hence, with the exception of residuals due to computational error, it does not represent a disturbance. Compensation was always used during testing.

**ORBIT RATE DECOUPLING**

Precession torques due to the fast orbit are relatively large for large gimbal angles. These torque terms, which were viewed as disturbances, occur because the angular momentum of a momentum-conservative system must remain fixed in inertial space and therefore oscillate with respect to the spacecraft. This can be achieved by including so-called orbit rate decoupling terms in the control functions. These terms force the gimbals to oscillate at the orbit rate so that roll and yaw angular momentum are interchanged in the proper manner. Hence, no attitude errors are generated.

Without these orbit rate decoupling terms, attitude errors are incurred. These errors are sinusoidal, with yaw (or roll) amplitude approximately equal to

$$\frac{H_t \tau^2 \omega_0}{I} \quad (1)$$

where  $I$  = yaw (or roll) moment of inertia

$H_t$  = angular momentum stored in the roll-yaw plane

$\tau$  = yaw (or roll) equivalent lead time constant

$\omega_0$  = orbit rate.

For the test application, this represents 0.0023-N-m disturbance torque for each degree of wheel tilt and hence  $0.01^\circ$  peak roll error, which is acceptable, but  $1^\circ$  yaw error, which is too large. Therefore, orbit rate decoupling was mandatory during the testing.

**IMBALANCE DRIFT**

During long runs it was found that the disturbance torque on the air bearing platform changed consistently. The yaw torque changed by 0.004 to 0.005 N-m, and the roll torque by about  $-0.003$  N-m. These figures were obtained by observing the yaw angle and by matching performance with an analog computer simulation. Although the exact causes of these drifts are unknown, a probable dominant factor is differential thermal bending or air currents. As previously stated, precise balancing was done only after the equipment was warmed up. However, to protect the flexible lead capsules of the gimbals, the gimbals were not energized during the long warm-up period.

In the 2-sensor mode, in which disturbance torques of the magnitude cited above markedly affect yaw error, compensating terms in the control functions were updated by ground command on the basis of the telemetered yaw angle. This was an artifice which would not be possible in a flight application because yaw is not expected to be measured.

Two approaches to the estimation of disturbance torques have been developed and will be reported later. Since the roll disturbance torque can be estimated, it can be used in the control to reduce roll error. Although the yaw disturbance torque cannot be estimated as a separate variable, it is shown that the yaw attitude angle can be estimated to within an unobservable value  $\bar{\psi}$ , where

$$\bar{\psi} = \frac{T_{dz}}{\omega_0 H} \quad (2)$$

and

$T_{dz}$  = yaw disturbance torque

$H$  = bias angular momentum.

### Compensation during momentum dumping

The simplest scheme of momentum dumping (or unloading) is to pulse a thruster and, through the action of the control system, to null the resulting attitude error, thereby achieving the desired correction in angular momentum. This same scheme may be used to correct wheel speed, i.e., magnitude of angular momentum, or z-gimbal angle, i.e., direction of angular momentum. Note that attitude error is induced. A novel method of reducing the peak error is to command the wheel speed or the gimbal angle toward the desired operating point and then, after a calculated delay, to pulse the thruster. The angular impulse command to drive the z-gimbal at the maximum rate (or the wheel at maximum acceleration) must be equal to the roll (or pitch) thruster impulse. This technique reduces the peak error because the predictive command and the thruster pulse are impulses of opposite sign.

The thruster unload pulse can be considered to be an impulsive driving function into the system. From a single-axis analysis without unload compensation, the response is

$$\alpha(t) = \frac{A}{Ib} e^{-at} \sin bt \quad (3)$$

where  $\alpha$  = attitude angle

$A$  = torque impulse

$I$  = moment of inertia

$a$  = magnitude of the real part of the dominant root of the characteristic equation

$b$  = magnitude of the imaginary part of the dominant root of the characteristic equation.

For critical damping,  $a = b$ . Then the peak attitude error,  $\alpha_{\max}$ , is given by

$$\alpha_{\max} = \frac{A}{Ib} e^{-\pi/4} \sin \frac{\pi}{4} = \frac{0.33A}{Ib} \quad (4)$$

As an example, for gimbal unloading, roll thrusters are used. Hence, consider the roll channel, in which

$$A = 0.5 \text{ N-m} \times 0.1 \text{ s} = 0.05 \text{ N-m-s}$$

$$I = 70 \text{ kg-m}^2$$

$$a = b = 0.28 \text{ rad/s.}$$

In this case  $\alpha_{\max} = 0.05^\circ$ , while tests yield  $0.06^\circ$ .

Analysis shows that the peak error with unload compensation can be reduced to about 25 percent of that without compensation.

### Performance with large gimbal angles

Operation at large gimbal angles allows less frequent momentum dumping to correct the gimbal angle. Since most of the stored angular momentum is due to secular rather than cyclic inertial torque, momentum dumping is also more efficient so that less propellant is required. However, as gimbal angles become large, the cross-axis coupling becomes more significant. For example, wheel reaction torque has components not only about the pitch axis but also about the roll and yaw axes. These become larger as gimbal angles grow. It is important to verify the amount of coupling and its effect on performance, and to investigate the level at which the gimbals can be operated.

### Delta-V mode sequences and control

Current design criteria for sizing the bias momentum lead toward designs which require 3-axis sensing because of the high-level disturbance torques caused by delta-V maneuvers. However, the type of control to be used (DGMW or thruster with DGMW caged electrically), sequences of mode switching between the 2-sensor track mode and the 3-sensor mode, and preferred direction of disturbance torque must still be selected. Furthermore, if the thrusters are to be used for control, the concept of off pulsing, or turning off a roll thruster that normally would be turned on, to achieve simultaneous delta-V and attitude control is important.

### Acquisition

During acquisition and reacquisition, the procedure used to switch from one mode to the next is just as important as the performance of the system. The tested procedure consists of sending ground commands to the onboard digital computer to progress through the different modes. A special point of interest is the wheel spin-up at the end of acquisition. This is significant for several reasons, but the one of interest here is that the

gimbals can only be caged electrically, i.e., commanded to null by means of the gimbal servos.

**Onboard digital computer**

Analyses and comparative studies have shown that the use of an onboard digital computer enhances the performance and operation of DGMW systems, especially in the 2-sensor mode. The system characteristics for which a digital computer is particularly useful are the multiplicity of operating modes, the several channels associated with 3-axis control, the complexity of the control functions, and the need for high resolution in certain terms in the control functions. It is important to verify by dynamic testing the control function synthesis as it has been implemented on a digital computer.

*A fortiori*, testing of a DGMW system is more convenient and flexible if a digital computer is part of the system. All locations in the random-access memory are accessible through the teletypewriter or the command system. Thus, parameters and modes are easily changed. Also, any variable in the random-access memory can be chosen for insertion in the telemetry signal stream simply by patching the control program.

**Discussion of test results**

**Speed of response and parameter estimation**

Preliminary runs, augmented by calculation and digital and analog computer simulations, led to estimates of the mass properties of the air bearing platform. The moments of inertia were derived from the transient responses in the 3-sensor mode using the DGMW only and the thrusters only (see Figures 3 and 4). The coupling between roll and yaw that becomes apparent when the vertical scale of Figure 3 is magnified is due to a nonzero product of inertia,  $I_{xz}$ , whose value was deduced from digital computer simulations. The resulting inertia matrix of the air bearing platform is

$$\begin{bmatrix} 70 & 0 & -5 \\ 0 & 95 & 0 \\ -5 & 0 & 80 \end{bmatrix} \text{ kg-m}^2$$

with about  $\pm 10$ -percent accuracy.

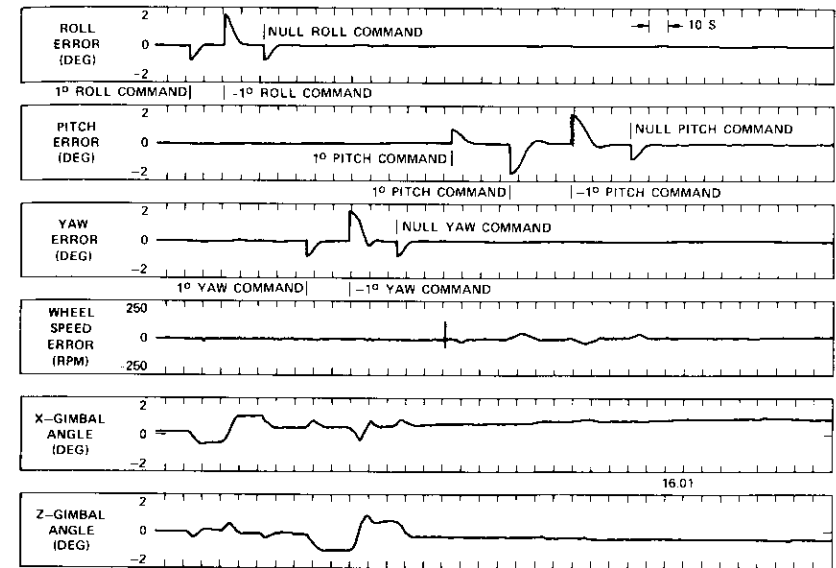


Figure 3. Transient Response of DGMW Attitude Control System in 3-Sensor Mode

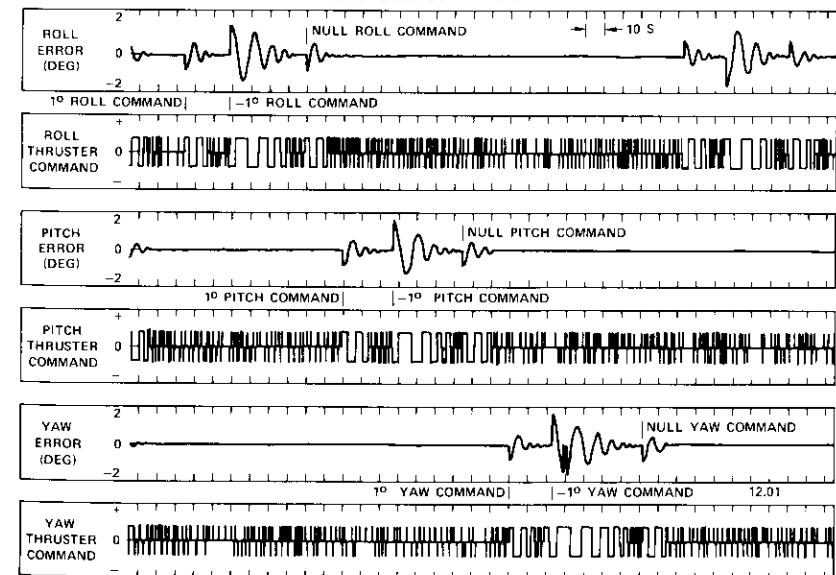


Figure 4. Transient Response of Thruster Attitude Control System in 3-Sensor Mode

Telemetry of the sensor noise showed that the noise content of the sensor signals below 2 Hz was  $0.06^\circ$  peak-to-peak or about  $0.01^\circ$  rms. Even though the sensors were optical sensors which are essentially noiseless, noise from the operation of other equipment such as the wheel spin motor was added to their outputs. The resulting noise approximated the characteristics of "real" spacecraft sensors.

Figure 3 shows the transient response of the DGMW attitude control system in the 3-sensor mode (thrusters off). This test proved the basic integrity of the control system. In this, as in all other runs in which the pitch-roll target was fixed, it was placed north of the origin of the reference system, i.e., the center of the air bearing. The net linear growth in the gimbals corresponded to imbalance torques of  $-0.002$  N-m about the yaw axis and about  $0.0005$  N-m about the roll axis. Therefore, the major portion of the growth in the z-gimbal angle was due to the earth rate.

Figure 4 shows the transient response of the thruster attitude control system in the 3-sensor mode (DGMW off). It also proved the basic integrity of the thruster control system. The dead zone was  $0.04^\circ$  for all channels. This small value resulted in hard "limit cycling" at a high frequency. The choice of thruster torque level was not predicated upon the desire to achieve a level low enough to decrease the number of pulses. Instead, for adequate unloading, it was considered more important in this testing program to employ the level actually used ( $0.5$  N-m). Otherwise the amount of torque would have been insufficient to eliminate the effect of the earth rate, which is equivalent to a comparatively large inertially fixed torque during long runs.

#### Basic 2-sensor mode

Figure 5, which shows one 30-minute orbit in the DGMW 2-sensor mode with unloading inhibited, demonstrates the stability, accuracy, and speed of response of the basic 2-sensor mode in pitch, roll, and yaw. In this, as in all other runs in which the pitch-roll target was moving, earth rate compensation and orbit rate decoupling were used in the control functions. Also, similar to all other 2-sensor mode tests, the run was started in the 3-sensor mode and then switched at about 30 seconds to the 2-sensor mode after transients had settled out. Roll and pitch remained less than  $0.05^\circ$ . Yaw, which was not used in the control but was nevertheless measured, increased to  $4^\circ$ . This large value was due to the drift in imbalance torque mentioned earlier, which was not offset by the control functions in this run. Note that the gimbals achieved large values, with peaks of  $6^\circ$  in both cases.

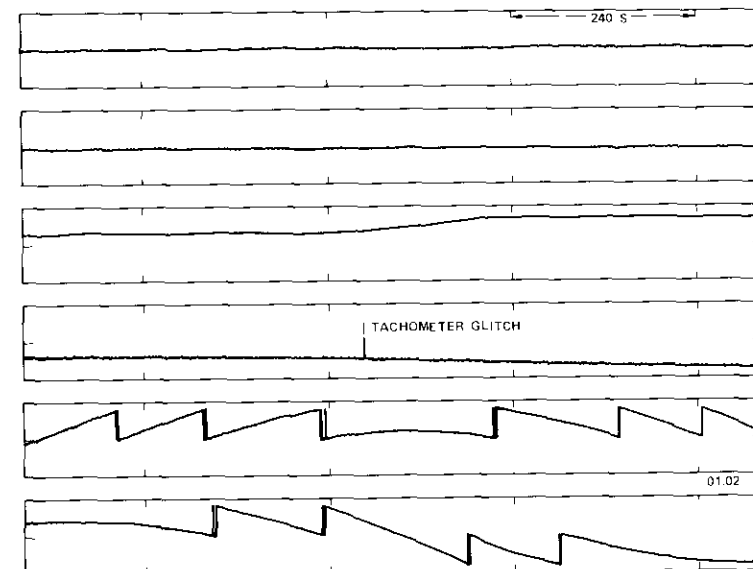
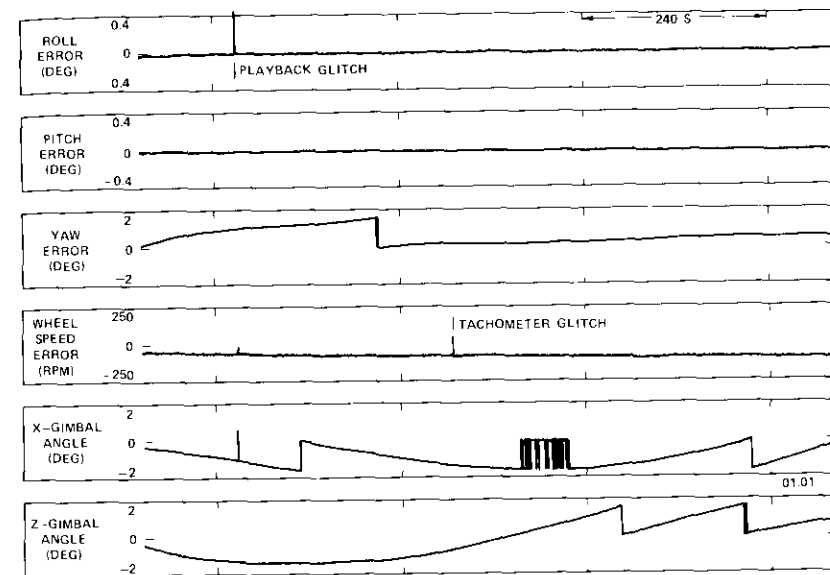


Figure 5. DGMW 2-Sensor Mode with Unloading Inhibited

### Momentum unloading and disturbance compensation

Unloading in the 2-sensor mode is shown in Figure 6. For this run, which was one and one-half orbits long, the gimbal unloading sequence was ini-

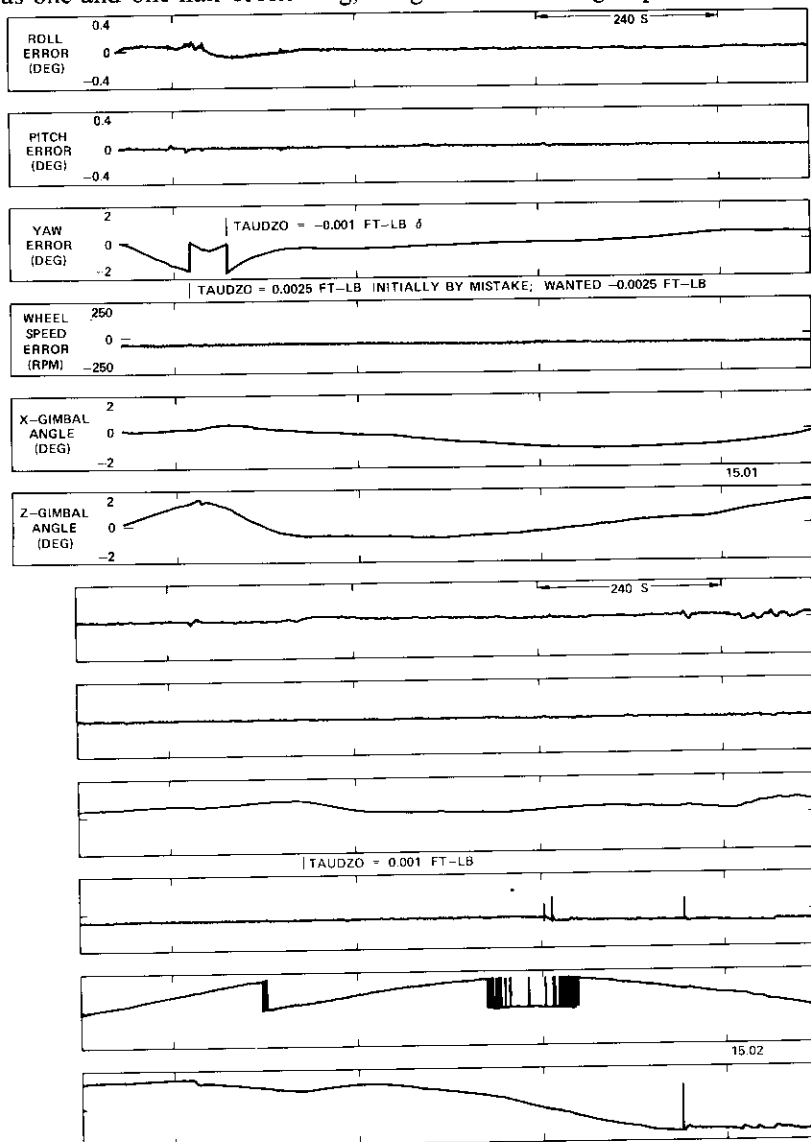


Figure 6. DGMW 2-Sensor Mode with Unloading

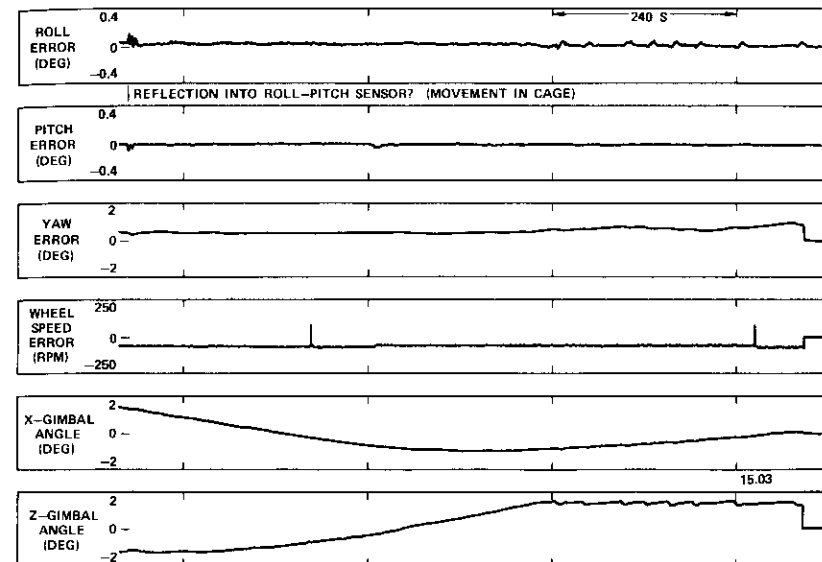


Figure 6. (continued)

tiated when the z-gimbal exceeded  $1.9^\circ$ , and unload compensation was used. It can be seen that the peak roll error was  $0.06^\circ$  and that the gimbal angle was reduced by  $0.3^\circ$  in each unload sequence. A smaller decrement could be chosen to decrease the roll transient peak. However, as stated earlier, it was necessary to remove enough angular momentum to keep up with the earth rate torque. The test suggested that both gimbals are maintained at small values even if unloading is based on the z-gimbal angle alone. The yaw error was maintained at less than  $1^\circ$  by updating the yaw disturbance torque compensation (TAUDZO) by ground command.

Proper pitch unloading sequences occurred at the 1,850- and 2,270-second marks. The wheel speed was unloaded when the magnitude of speed error exceeded 100 rpm. It can be seen that the peak pitch error associated with an unloading pulse is  $0.06^\circ$ . The corresponding change in wheel speed is 25 rpm.

High-speed detail of gimbal unloading sequences showed the predictive motion of the z-gimbal resulting from the compensation command, the delayed and narrower roll thruster command, and the bucking effects on the roll error.

### Simulated delta-V mode sequences and control

Figure 7 shows some simulated delta-V maneuvers. Both the positive and negative roll thrusters are commanded to fire at the same time. Hence, only torques due to misalignment and thrust imbalance are exerted on the air bearing platform. In the first sequence, the DGMW is kept in the control. The sequence of events is as follows. Control is switched to the 3-sensor mode (mode 33). The large roll transient due to the large yaw correction is attributable to a nonzero product of inertia, as discussed earlier. This can be avoided by holding the yaw at its initial value rather than controlling to null. After transients have settled out (settling time is typically 30 seconds), the opposed roll thrusters are fired for 25 seconds. It can be seen that the DGMW control system maintains attitude accuracy while the thrusters are on. The thrusters are then turned off, and after an interval for the transients to settle out, control is switched back to the 2-sensor mode (mode 31). Note the smooth yaw response.

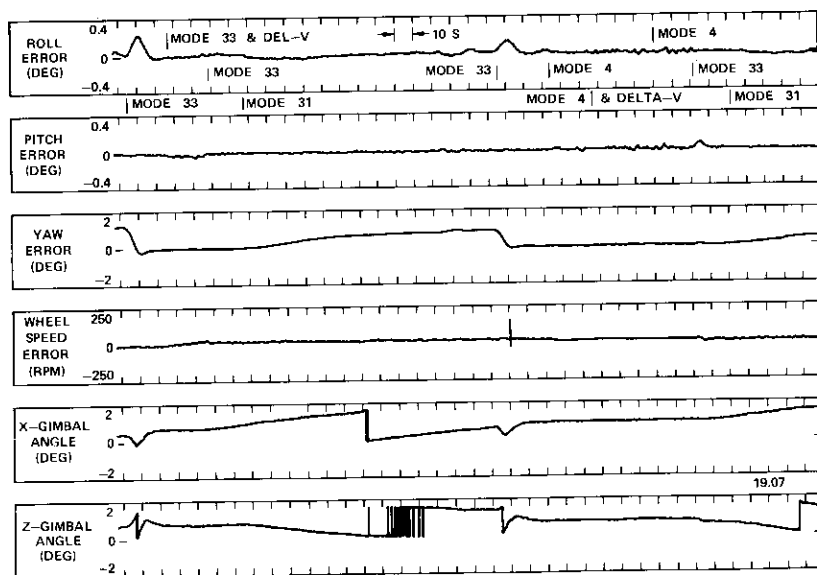


Figure 7. Delta-V Mode Sequences and Control

In the second sequence, the thrusters are in control, whereas the gimbals and wheel are electrically caged (mode 4). That is, gimbal angles and wheel speed are maintained at their initial values upon entering the mode. The

sequence starts by switching control to the 3-sensor mode (mode 33). After transients have settled out, control is switched to mode 4. The control channels have relatively small dead zones of  $0.04^\circ$  in this mode. Hence, there is much thruster activity at this time, although attitude accuracy is maintained. The roll thrusters are then simultaneously commanded on to simulate the delta-V maneuver. Roll control torques are obtained at this stage by off pulsing. Control is then returned to the DGMW in the 3-sensor mode (mode 33). Note the relatively large pitch transient; a large roll transient might also result upon switchover from thruster to DGMW control. Finally, control is switched to the 2-sensor mode (mode 31). As in the previous sequence, this last transition is smooth. An increase in the vertical scale would show that in mode 4 the gimbals remain within  $0.04^\circ$  of the set points.

Figure 7 illustrates the salient features of delta-V sequencing and control. However, it does not show a large change in angular momentum because the thrusters could not be turned on for a long period; propellant usage upset the balance of the air bearing platform. Hence, supplementary tests were performed in which the disturbance torque associated with delta-V maneuvers was obtained by placing a small weight on the platform. The results of these tests were close to the predictions.

### Initial wheel run-up

Figures 8 and 9 show a critical stage in a possible acquisition sequence. The air bearing platform is under 3-sensor thruster control. Yaw is derived from the wide-angle sensor. The gimbals are electrically commanded to null. Initially, the wheel is not running. Thirty seconds into the run, the wheel is turned on by ground command. The tachometer signal is initially bad, but improves as the magnetic picker signal grows with increasing wheel speed. After 240 seconds, the gimbal servos are automatically switched from direct to precession control. Note that the attitude, the wheel speed, and the gimbals all remain under proper control during this stage of the acquisition sequence.

### Conclusions

The primary purpose of this work was to test the performance of the combination DGMW and onboard digital computer in the 2-sensor mode. The testing demonstrated that this is a feasible system for achieving high roll and pitch accuracy in geostationary communications satellites. Equally as important, it demonstrated that yaw accuracy compatible with the roll

and pitch accuracy required for spot beams is achievable without a yaw sensor. As a corollary, it can be stated that high accuracy in yaw, roll, and pitch can be achieved in the 3-sensor mode.

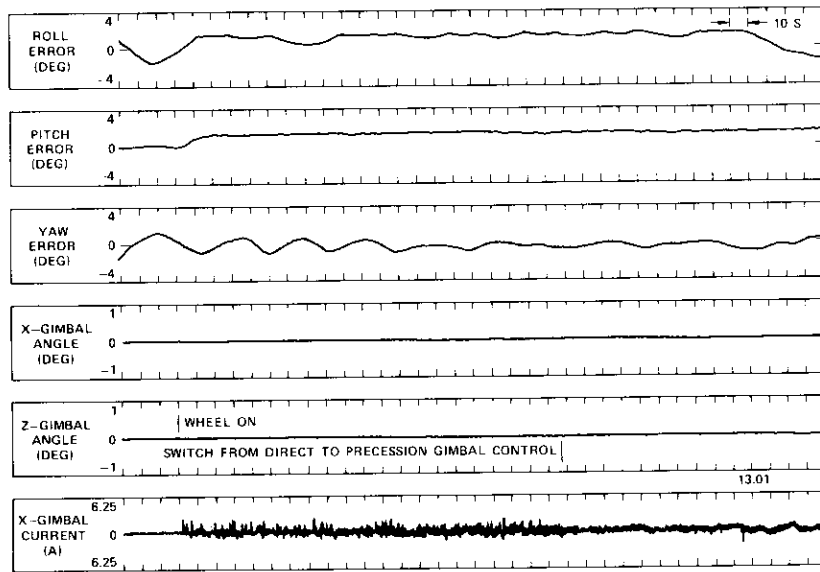


Figure 8. Initial Segment of Wheel Run-up under Thruster Attitude Control (part a)

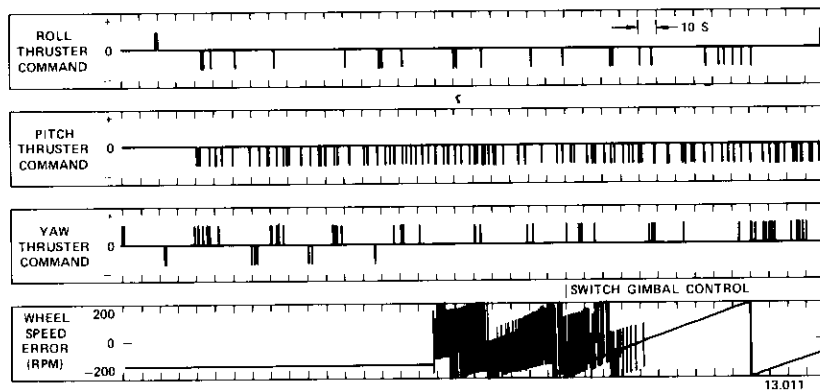


Figure 9. Initial Segment of Wheel Run-up under Thruster Attitude Control (part b)

It has been found that stability, accuracy, speed of response, and other results obtained in the tests are close to those derived from analyses and simulations if the effects of imbalance drift are properly considered.

Certain concepts are vital to the validity of the main conclusions. These are summarized in the following paragraphs.

The question of whether or not orbit rate decoupling is required for flight is answered in parametric form; hence, it depends on the specific application. Equation (1) should be useful for this determination.

For flight application, the results of the estimation problem provide a solution at two conceptual levels to the problem of modeling long-term disturbance torque. The brute force solution starts by fixing the maximum allowable yaw error and calculating the yaw torque. From these values, the minimum value of bias momentum can be found. The more elegant solution is to estimate the residuals that result from a proposed estimation method. Since these are smaller than the yaw torque itself, with compensation in the control functions the maximum yaw error is less for the same size wheel, or a smaller wheel can be used for the same maximum yaw error. Therefore, it can be seen that there is no single value of bias momentum because the answer is provided parametrically.

The necessity of using unload compensation for flight depends on the application of performance equation (4). Hence, no single answer is generally applicable. An example of this logic is the air bearing platform testing, in which it has been proven that unload compensation is required for the test application.

The testing and computer simulation have demonstrated that operation of the gimbal angles at values as large as  $8^\circ$  yields satisfactory performance. At this level, the control functions are still valid because they are based on linearization. It can be stated as a general rule that conditions are more benign in the flight case than in the test case. For example, the orbit rate is 50 times smaller and moments of inertia are an order of magnitude larger in the flight case. The bias momentum value is of the same order of magnitude. Hence, whereas all of the stated concepts are critical to the test, during the design it may be found that some are unnecessary on the basis of the parameters of the specific flight application.

The tests show that delta-V maneuvers are performed more effectively with the DGMW in control because the attitude rates are smaller than they would be if attitude control were provided by the thrusters. In both cases attitude angular errors can be kept within accuracy limits. The exception is the case in which the disturbance torque is larger than that permitted in the design. Since thruster control has higher loop gains than DGMW

control, attitude errors will be smaller if thruster control is used.

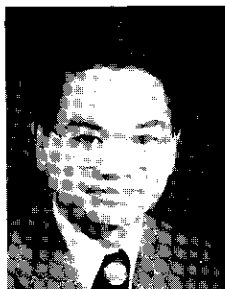
By judicious placement of thrusters used for delta-V maneuvers it is possible to minimize the expected roll disturbance torque compared to the expected yaw torque, or vice versa. Thus, it is important to determine whether there is a preferred direction of disturbance torque, which must exist in any case. The tests show that a disturbance torque which is biased in the yaw axis is preferable because the resulting attitude error is in yaw rather than in roll. Hence, the communications mission is affected less adversely.

### **Acknowledgment**

*The author wishes to acknowledge the help of T. C. Patterson, who performed the balancing and calculated the moments of inertia of the air bearing platform.*

### **References**

- [1] K. L. Lebsack, H. R. Flanders, and J. J. Rodden, "Simulation and Testing of a Double-Gimballed Momentum Wheel Stabilization System for Communications Satellites," *Journal of Spacecraft and Rockets*, Vol. 11, No. 6, June 1974, pp. 395-400.
- [2] J. J. Kalley and H. L. Mork, "Development and Air Bearing Test of a Double-Gimballed Momentum Wheel Attitude Control System," *AIAA 5th Communications Satellite Systems Conference*, Los Angeles, California, April 22-24, 1974 (Paper No. 74-488).



*Alberto Ramos received a B.S. degree in electrical engineering from the University of the Philippines in 1958, and an M.S. degree in electrical engineering from Purdue University in 1961. In October 1967 he joined COMSAT, where he is presently a member of the technical staff of the Spacecraft Laboratory. He is a member of the IEEE and the IEEE Control System Society.*

**Index:** INTELSAT IV-A, transmission impairments, frequency-division multiplexing, multiple access, co-channel interference (spatial isolation)

## **INTELSAT IV-A transmission system design**

J. DICKS AND M. BROWN, JR.

(Manuscript received October 3, 1974)

### **Abstract**

The INTELSAT IV-A satellite is expected to be ready for launch in mid-1975. This 20-transponder satellite will achieve greater capacity than the INTELSAT IV through frequency reuse by spatial separation of its east and west antenna beams. Transmission planning is more complex than that of INTELSAT IV due to the effects of cochannel interference, as well as adjustments made in communications performance for the normally encountered signal impairments: earth station RF out-of-band emission, satellite group-delay and dual path distortion, adjacent transponder intermodulation interference, and crosstalk. This paper discusses preliminary INTELSAT IV-A transmission design in terms of these impairments.

### **Introduction**

Due to the rapid growth of international telecommunications traffic in the Atlantic Ocean region, a new generation INTELSAT satellite series

The basic text of this paper was presented at the AIAA 5th Communications Satellite Systems Conference, Los Angeles, California, on April 22-24, 1974 (AIAA paper no. 74-474). It has been updated for publication in the COMSAT Technical Review. This paper is based upon work performed at COMSAT under the sponsorship of the International Telecommunications Satellite Organization (INTELSAT). Views expressed in this paper are not necessarily those of INTELSAT.

will be required to replace the existing INTELSAT IV system in the 1976 time frame. As is true of most technology, the new series, designated INTELSAT IV-A, has retained many of the proven characteristics of its predecessor while introducing new concepts as a step toward achieving expanded capacity with a launch vehicle of the same size, the Atlas-Centaur.

Spatial separation of east and west antenna beams will be used on the INTELSAT IV-A in order to reuse the frequencies emanating from west and east hemispheres. As illustrated in Figures 1 and 2, frequency reuse will

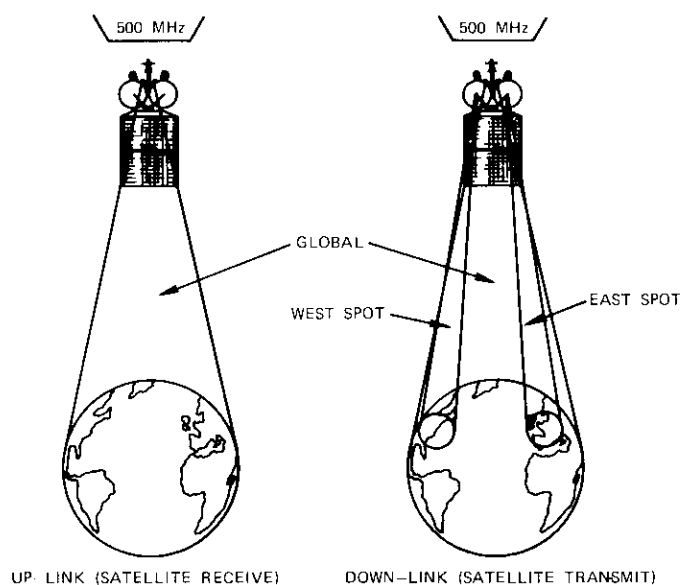


Figure 1. INTELSAT IV *Antenna Coverage Capability*

enable the INTELSAT IV-A to almost double the 500-MHz bandwidth which had been available to the INTELSAT IV. Although the fundamental transponder configuration of the INTELSAT IV will be preserved, there have been many changes necessary in individual subsystems to provide a suitable tradeoff among weight, transmission performance, and new technology. This paper will focus on the transmission performance characteristics of the INTELSAT IV-A and the difference between these characteristics and those of INTELSAT IV.

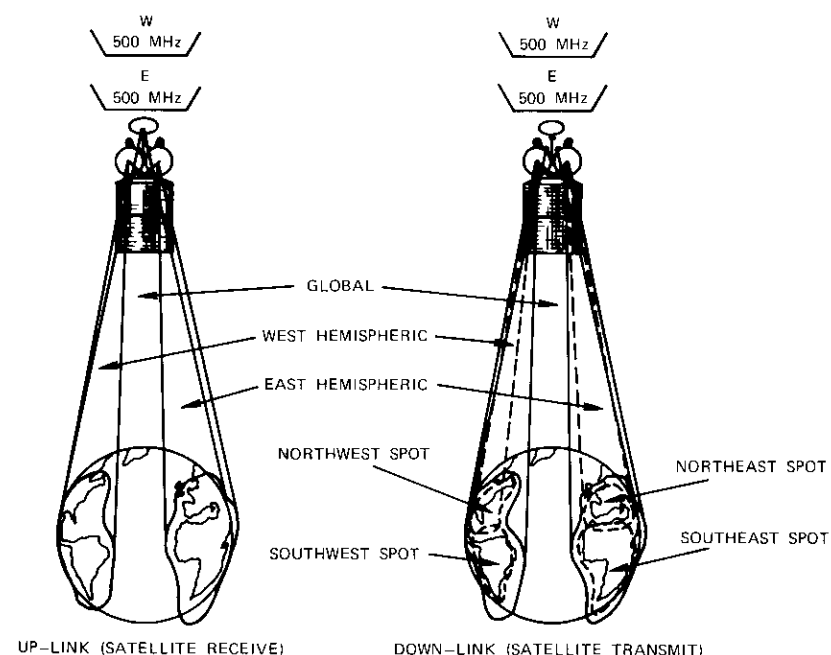


Figure 2. INTELSAT IV-A *Antenna Coverage Capability*

### **Satellite communications configuration**

#### **Traffic distribution patterns**

The cross-connectivity requirements for the INTELSAT IV-A satellite were initially based on meeting the traffic distribution pattern of the Atlantic Ocean region. Later, in the planning stages, the usefulness of this satellite in the other operating regions, i.e., the Pacific and Indian Oceans, was also considered. Consequently, the satellite has undergone a number of configuration modifications and is now capable of providing service in all three ocean regions until the early 1980s. It is capable of being used with all existing and presently proposed modulation and access techniques.

Figure 3 shows the basic traffic distribution pattern in the Atlantic Ocean region. It should be recognized, however, that, although most of the traffic can be represented in this manner, there are many small links which do not fit this pattern and therefore require a global-beam capability.

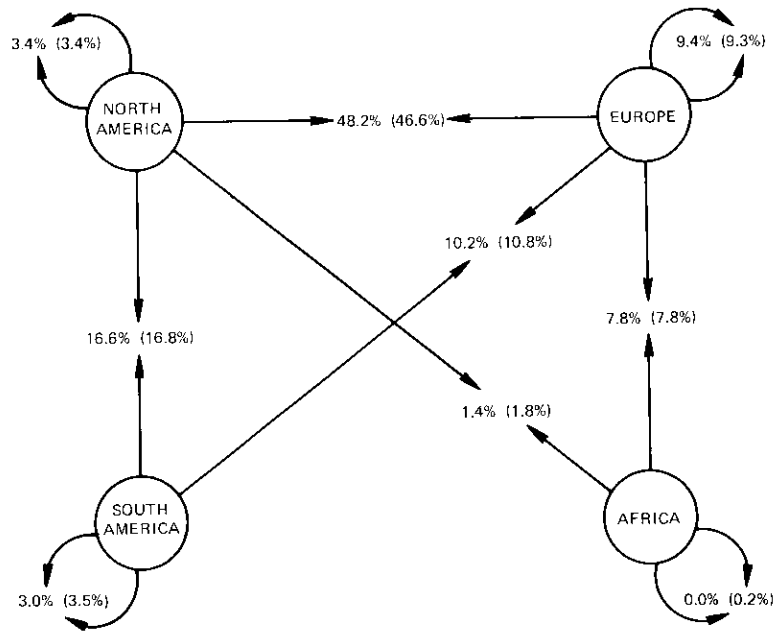


Figure 3. Typical Atlantic Primary Traffic Distribution for 1977 and 1978 (figures for 1978 are in parentheses)

#### Antenna patterns and transponder connectivity

From an analysis of the required coverage regions, it is apparent that frequency reuse in the east and west hemispheres provides the maximum spatial separation and at the same time encompasses most of the land mass in both the Atlantic and Pacific Ocean areas. Initially, it was considered undesirable to include a global-beam capability since this would allow a frequency to be used only once. Geographic locations which tended to fall generally between the east and west beams were therefore to be serviced by "secondary coverage" beams. These would be either separate offset antenna feeds or carefully defined areas on the slope of the main beam with specifically defined parameters (e.g., antenna gain, satellite G/T, and saturation flux density). Examples of such coverage requirements are Canary Island, Ascension Island, and Senegal in the Atlantic, and New Zealand and Indonesia in the Pacific.

When this satellite was later evaluated for use in the Indian Ocean region, it was considered necessary to incorporate global beams, since

large areas of land mass with fairly large traffic requirements fall between the two main beams. In operational use, it is expected that the secondary coverage capability will be utilized where possible since it allows greater overall channel capacity than the use of global-beam transponders. The resulting antenna pattern is depicted in Figure 2.

To provide flexible connectivity between transponders to meet the traffic patterns of Figure 3, transponders were made available for operation in either the hemispheric or spot-beam modes. Careful consideration of all operating modes in each ocean area resulted in the switching connections shown in Figure 4.

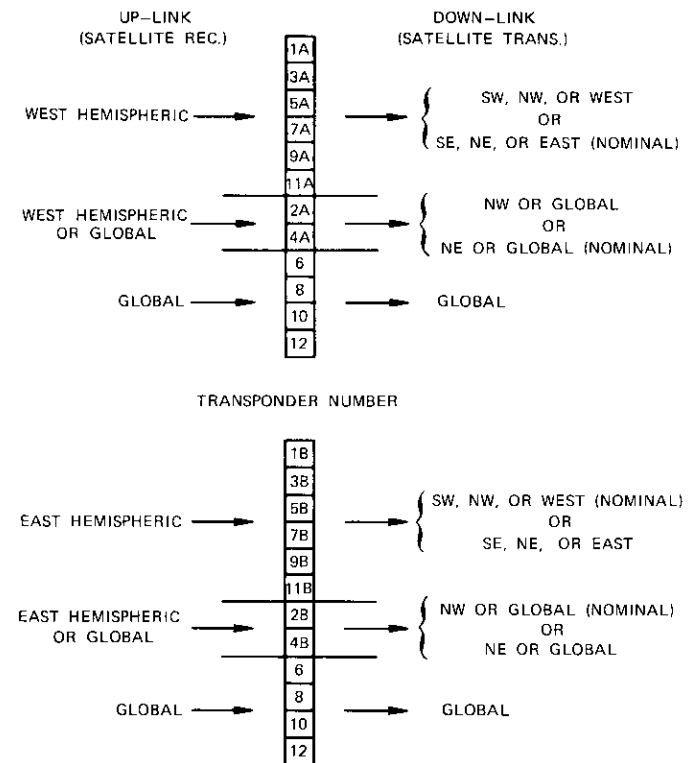


Figure 4. Switching Connections Available on INTELSAT IV-A

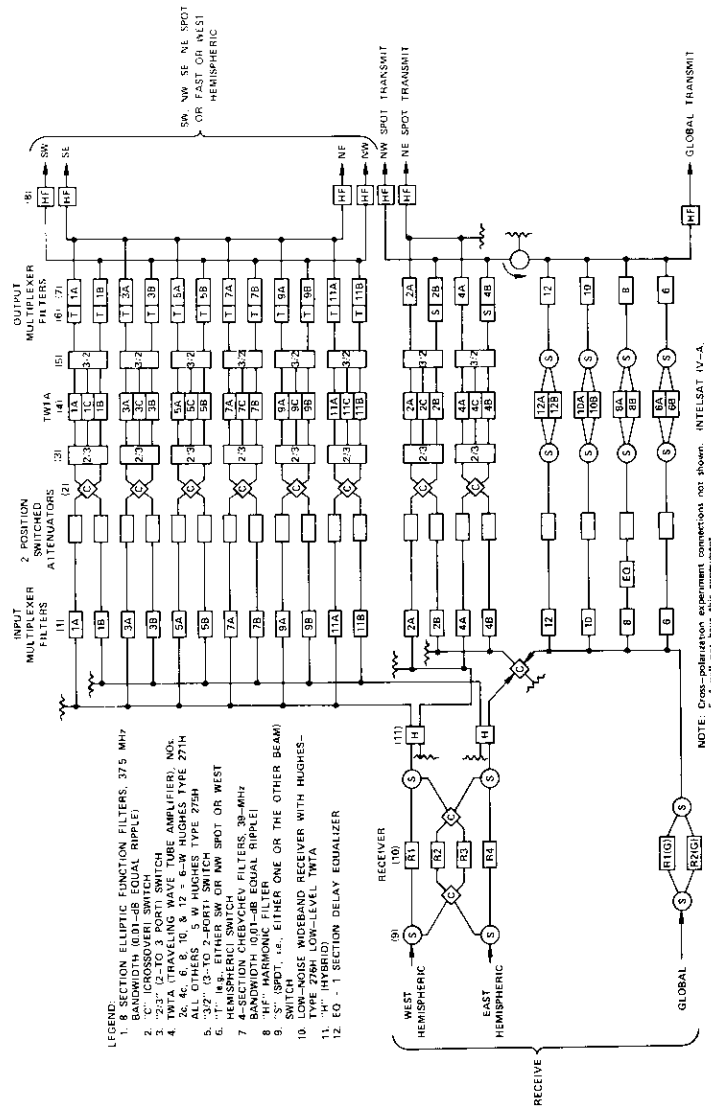


Figure 5. INTELSAT IV-A Block Diagram

In the block diagram (Figure 5),\* note that three different switch designations have been applied. Each of these switches is used to select the desired antenna mode as follows:

a. *C switches.* These are connected to the input of each transponder pair and provide the facility for cotransponders to be interchanged between east or west down-link beams.

b. *S and T switches.* The output of each transponder is connected to either an S or a T switch. For even-numbered transponders 2 and 4, the S switch is used to select either a north spot beam or the global mode of operation. On odd-numbered transponders 1 through 11, the T switch connects transponders to either north or south spot beams and also permits two spot beams to be combined into a composite hemispheric beam by paralleling the appropriate north and south beam antenna.

The T switch is physically located just in front of the output 4-section Chebyshev circular waveguide directional filter. Because of the directional property of these filters, if a signal is coupled into the filter as either left- or right-hand circular polarization, it will propagate in a specified direction through the output manifold and into the appropriate antenna feeds. Switching between the three transmit modes is accomplished by launching right, left, or both right and left circular polarized waves through a circular iris of the directional filter. The T switch itself consists of a linear mode launcher and a rotatable tuned phase shifter. The launcher is a balanced-type launcher with two opposing probes excited out of phase. Right-hand, left-hand, or any mix of both polarizations can be achieved by properly orienting the polarizer with respect to the linear input mode. The polarizer orientation is controlled by a commandable stepping motor.

As saturation is approached, maximum channel capacity will be required and therefore more spot-beam transponders will be placed in service. There will be circumstances, however, in which a transponder switched to the south mode may be only partially filled, while those in the north are fully saturated. Switching this unfilled transponder to the T (hemispheric)

\*This diagram applies to the first flight model (i.e., INTELSAT IV F-1) only. Subsequent models will have an added dual polarization experiment in transponders 2 and 4 when they are switched to the global mode. The communications capability of these channels will be unaffected by this modification. A brief description of the purpose of the experiment is provided in the appendix.

mode will still allow it to fulfill its south traffic requirements while its unfilled portion can also be utilized for more north beam traffic.

### Satellite transmission characteristics

One of the primary considerations in the development of the INTELSAT IV-A satellite was an attempt to minimize its impact on earth stations during its introduction into service, while also obtaining the maximum channel capacity available. Accordingly, the transmission characteristics were selected to closely reflect those of the INTELSAT IV satellite (but within any constraints dictated by actual INTELSAT IV-A development).

#### Transmission link parameters

Since the output power of the global-beam transponders in the INTELSAT IV-A satellite is similar to that of INTELSAT IV, the satellite receive G/T and saturation flux densities are also similar. For the INTELSAT IV, the G/T is specified as  $-18.6$  dB/K and the single-carrier saturation flux density ( $\psi_s$ ) is specified as  $-73.7$  dBW/m<sup>2</sup> (for single-carrier operation) and  $-68.7$  dBW/m<sup>2</sup> (for multiple-carrier operation). In the INTELSAT IV-A, the saturation flux density is specified as  $-75.0$  dBW/m<sup>2</sup> and  $-67.5$  dBW/m<sup>2</sup>, respectively. The minor differences between the two specifications result from compensation necessary to mate with values selected for INTELSAT IV-A hemispheric-beam antenna gain.

On INTELSAT IV, all transponders are connected to the global receive antenna; therefore they have the same satellite G/T for both spot- and global-beam modes. On INTELSAT IV-A, the receive antenna for the spot/hemispheric transponders is a hemispheric-beam antenna, one each for the west and east hemispheres. Since the coverage area has been decreased, the antenna has an increased gain of about 6 dB over the global beam with a specified G/T (at beam edge) of  $-11.6$  dB/K. This improved sensitivity will provide sufficient up-link carrier-to-noise performance while employing the same saturation flux densities of  $-75.0$  dBW/m<sup>2</sup> for single-carrier saturation and  $-67.5$  dBW/m<sup>2</sup> for multiple-carrier operation. On the basis of these specifications, typical link parameters have been developed as shown in Table 1.

With the exception of the effects of cochannel interference, transponder optimization of the INTELSAT IV-A satellite is carried out in the same manner as for the INTELSAT IV by using a tradeoff between down-link noise and transponder intermodulation as a function of transponder input backoff [1].

TABLE 1. TYPICAL INTELSAT IV-A LINK PARAMETERS

Item	Spot Beam		Hemispheric Beam		Global Beam
	Single Carrier	Multi-carrier	Single Carrier	Multi-carrier	Multi-carrier
e.i.r.p., Beam Edge (dBW)	29.0	29.0	26.0	26.0	22.0
Backoff <sub>in</sub> (dB)	—	-12.0	—	-11.0	-10.0
Backoff <sub>out</sub> (dB)	—	-7.0	—	-6.0	-4.2
Usable Bandwidth (MHz)	36.0	32.4	36.0	32.4	32.4
Usable Bandwidth (dB-Hz)	75.5	75.1	75.5	75.1	75.1
Saturation Flux Density (dBW/m <sup>2</sup> )	-75.0	-67.5	-75.0	-67.5	-67.5
Satellite G/T (dB/K)	-11.6	-11.6	-11.6	-11.6	-17.6
C/N <sub>up-link</sub> (dB)	29.0	24.9	29.0	25.9	20.9
C/N <sub>intermod</sub> (dB)	—	23.5	—	21.8	18.9
C/N <sub>down-link</sub> , including 0.6-dB Geographic Advantage (dB)	26.7	20.1	23.7	18.1	15.9
C/N <sub>total</sub> (dB)	24.7	17.6	22.6	16.1	13.3
Loss Due to Cochannel Interference, C/I = 24 dB (dB)	~1.5	~0.8	~1.5	~0.8	—
C/N <sub>available</sub> (dB)	23.2	16.8	21.1	15.3	13.3
Typical Number of Channels per Transponder	1,300	700	1,100	600	450

#### Beam isolation

Since the same frequencies are used in both the east and west beams, the degree of isolation needed to keep cochannel interference within acceptable levels is quite important. The present specification requires 27-dB isolation between one beam and its interfering sidelobe component in the other beam. This number applies to both the up-link and the down-link. Since the spectrum of an FM signal has a nonuniform distribution, it cannot be treated as thermal noise. As a result, two carriers located at the same frequency will cause greater mutual interference than two carriers offset in frequency. Based on an analysis of a number of frequency plans, it is estimated that, with 27-dB isolation and the types and sizes of carriers involved, the interference per carrier can be kept in the region of 500-1000 pW0p. A more detailed description of this analysis is presented in a later section on cochannel interference.

**Impact on earth stations**

Transmission design for the INTELSAT IV-A system has been developed to minimize the transition of earth stations presently configured for INTELSAT IV operation. Accordingly, with the possible exception of the addition of a few new carriers to the existing list found in INTELSAT document ICSC-45-13 (Rev. 1) [2], carrier sizes will not change when the new system is implemented.

Although the INTELSAT IV-A will have a 6 dB better G/T than the INTELSAT IV, the maximum earth station power levels presently used as guidelines in ICSC-45-13 (Rev. 1) have remained unchanged in the INTELSAT IV-A earth station document, BG-11-40, with the exception of a few high-density carrier sizes. There are several reasons for this:

- a. The gain stability of the INTELSAT IV-A has been specified to be  $\pm 2$  dB over its operating lifetime. Toward the end of the satellite design life, earth station power may be required to offset a change in sensitivity.
- b. Cochannel interference will be a factor which must be offset by power adjustment. Small carrier sizes paired with large carriers may need from 1 to 2 dB more power to compensate for this impairment.
- c. As many as six global-beam transponders can be placed in service, particularly in the Pacific and Indian Ocean regions. Since the global beam on the INTELSAT IV-A is essentially the same as that on the INTELSAT IV, carriers in these transponders will need the same power levels as the present system.

Other areas which may have an impact on earth stations are summarized below:

- a. With the modified filter specifications on the INTELSAT IV-A, transmission impairments such as crosstalk and group delay will require equalization at the earth stations for a few large carrier sizes.
- b. Earth station RF out-of-band emission may be a potential problem in the INTELSAT IV-A system and may have a direct impact on earth station high-power amplifier (HPA) size and operation. (This item is discussed in the section on earth station RF out-of-band emission.)
- c. The concept of frequency reuse will mean that more smaller carriers must be transmitted from most earth stations because of the physical separation of geographic locations by spot and hemispheric

beams. For example, in the Atlantic Ocean region, approximately 60 percent of the earth stations will transmit from two to three carriers. This will mean the addition of one or two more up-converter chains at some earth stations.

- d. All existing INTELSAT IV e.i.r.p. monitoring facilities in the Atlantic Ocean region are located above the equator. Two new monitoring earth stations are therefore required to control carriers which can be viewed only in the SW and SE spot beams.

**Transmission impairments**

The INTELSAT IV-A satellite will be affected more by transmission impairments than the INTELSAT IV, not only because of the introduction of cochannel interference but due to modifications in filter requirements. Each of the following INTELSAT IV-A impairments will therefore be discussed separately:

- a. cochannel interference (due to beam isolation requirements),
- b. earth station RF out-of-band emission,
- c. satellite group-delay and dual path distortion,
- d. adjacent transponder interference (due to intermodulation),
- e. satellite and earth station crosstalk.

**Cochannel Interference**

Because of the wide geographic dispersal of earth stations accessing INTELSAT satellites and variations in the electromagnetic environment surrounding those stations, careful frequency coordination is necessary. Extensive use of multidestinational carriers (to minimize the number of carriers in the system) requires that a single carrier frequency be cleared with as many as 12 to 20 different earth station locations. Since there is also a wide range of carrier sizes, INTELSAT IV-A frequency plans show carriers with large variations in capacity and power density located throughout the satellite band. In a typical frequency plan, the maximum interference is expected to result from the carrier with the largest power density interfering with the carrier with the smallest power density if they happen to be cochannel (or nearly cochannel). The overall problem reduces to a search for a plan in which a certain amount of flexibility in distributing the capacity, power density, and frequency locations is retained within the constraints of the available isolation between the two cochannel beams.

Another important requirement of such a frequency plan is that the

interference between the two systems should remain within certain specified bounds irrespective of the carrier loading (i.e., whether the carrier is carrying the full "busy hour load" for its nominal capacity or whether it has a light load with an energy dispersal signal applied). When carriers are nearly cochannel, the interference on one carrier actually increases with decreasing load on the other carrier.

The method used to develop frequency plans is to manually lay out all the carriers assigned to each of the cochannel transponders so that carrier frequency offsets are maximized. In practice, each transponder is initially brought to its optimum operating condition and then adjusted for co-channel interference [3]. A system model is presently under development to automate this evaluation by employing computerized techniques.

Figure 6 shows a typical representation of the variation of interference between carriers as a function of the carrier offset.

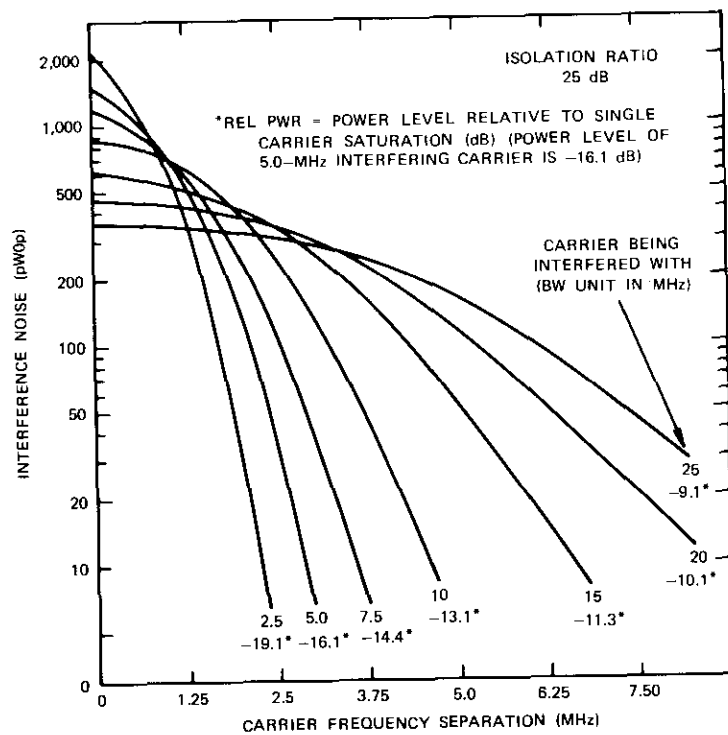


Figure 6. Cochannel Interference Noise (effect of 5.0-MHz-bandwidth carrier on other carriers)

### Earth station RF out-of-band emission

Of the total per channel system noise budget, 500 pW0p has been allocated to earth station RF out-of-band emission.\* There is a tradeoff between usable transmitter output power and the amount of emission noise which the satellite transmission system can tolerate. When a high-power wideband TWT is operated at saturation, its full output power can be realized; however, it will also produce severe intermodulation emission with multiple-carrier transmission. In the INTELSAT IV system, it was determined that an output backoff of approximately 7 dB would still allow the system to be operated within the 500-pW0p allowance. For a 12-kW TWT this would mean a loss of 9.6 kW, or a usable output power of 2.4 kW, just to compensate for the effects of out-of-band emission.

The determination of an output backoff of 7 dB was in itself a compromise. Depending on the carrier arrangement, it was determined that an emission product in excess of 26 dBW/4 kHz could be produced by a transmitter operating with a 7-dB output backoff [4]. With the particular link budget of carriers adjusted in the INTELSAT system, this could equate to as much as 4,000 pW0p of emission noise; the amount of noise would depend on the size of the affected carrier. Therefore, even with a 7-dB output backoff, there would be no guarantee that a 500-pW0p system noise budget could be met unless another alternative were available. In this respect, it was noted that, if the affected carrier were to increase its up-link power level, the amount of emission noise could be reduced back down to 500 pW0p. It was felt that this "give and take method" would permit a 7-dB output backoff to be applied and at the same time keep emission noise within the system noise budget of 500 pW0p.

The tradeoff between transmitter output power and up-link adjustment has worked favorably in the INTELSAT IV system because there has been sufficient power margin in the satellite transponders to allow the up-link of some carriers to be increased, followed by a reoptimization of the remaining carriers for the best transponder intermodulation structure and

\*The phrase "RF out-of-band emission" may require clarification. In this paper, it refers to the unwanted radiation generated by the intermodulation of carriers within an earth station's wideband HPA. When transmitted, these intermodulation products may fall within the satellite frequency band or outside of the satellite band. RF out-of-band emission is therefore meant to indicate RF emission which is out of the wanted carrier's band. (Intermodulation products falling under the generating earth station's carriers are considered in another specification for C/I.)

carrier performance. However, as the transponders become more heavily loaded, it is more difficult to increase the up-link power without upsetting the delicate power balance of the other carriers in that transponder. Hence, in a fully loaded system it will be necessary to limit earth station out-of-band emission to 500 pW0p through some means other than up-link power adjustment. This can be accomplished by methods such as careful frequency planning, larger TWTs (and thus lower input backoff), or multiplexed narrowband klystrons.

A typical out-of-band emission environment expected for the west up-link of the INTELSAT IV-A system in 1976 is shown in Figure 7. In general, most of the products are about 8 dB below the INTELSAT IV criterion of 26 dBW/4 kHz. This is because the large number of small carrier sizes transmitted from each earth station tends to spread the total emission spectrum out over the 500-MHz band instead of concentrating it in peaks.

The INTELSAT IV-A system will not be as flexible in terms of up-link power adjustment to overcome the effects of out-of-band emission as the INTELSAT IV system. As has been discussed in the section on cochannel interference, an intricate balance in power levels will be needed just to ensure that cochannel interference is minimized. Introducing another factor, such as out-of-band emission, may make it difficult to maintain this balance, especially if contingency carriers are transmitted on an intermittent basis. Following a detailed analysis of this subject, INTELSAT has lowered the RF out-of-band emission limit for the INTELSAT IV-A system to 23 dBW/4 kHz [5].

#### **Satellite group-delay and dual path distortion**

Since the INTELSAT IV-A system will be configured primarily as an FDM/FM/FDMA network, it was felt that the input and output filter specifications could be modified with respect to those of INTELSAT IV to permit a weight reduction. INTELSAT IV filters and group-delay equalizers were designed with the expectation that high-capacity low-modulation-index FM carriers would be used extensively. Due to a somewhat different course in system development, INTELSAT IV-A transponders will employ many relatively small capacity carriers and will be able to accept up to 4-phase 60-Mbps TDMA transmission without group-delay equalizers.\*

\* With the exception of transponder 8, which includes a 1-section equalizer TDMA for field trial testing.

To permit weight and space reduction, the INTELSAT IV-A will be configured with an 8-section pseudo-elliptic [6] function Invar filter instead of the 10-section Chebychev input filter used on INTELSAT IV. The output filter will be a 4-section Chebychev, whereas a 6-section Chebychev filter had been chosen for INTELSAT IV. A comparison of INTELSAT IV and INTELSAT IV-A filter specifications is shown in Figures 8 and 9.

Near the band edges of each transponder, where the skirts of the input and output filters overlap those of adjacent transponders, a carrier may travel through an indirect path and be recombined at a receiving earth station. Thus a dual path is available to a carrier when it can be transmitted in part through the adjacent channel. This type of distortion is principally a function of the following conditions:

- a. gain difference between paths due to input satellite flux density and transmit antenna gain,
- b. phase difference between paths,
- c. filter rejection characteristics.

Dual path distortion is generated primarily by the linear components of the combined group-delay response and gives rise to second-order intermodulation products. When measured, the combined group-delay response is due to both the direct (intrinsic) and the indirect paths which the signal will follow. The dual path distortion under discussion is coherent; that is, it is the vector sum of the voltage of each path. At the frequency at which transmission gain through both paths is equal, the resulting distortion may be zero if the paths are out of phase. Conversely, if the paths are in phase, the maximum distortion will be 6 dB. As the relative gain between the paths increases, distortion can be greater than 6 dB.

Distortion due to intrinsic group delay and dual path is expected to be held to a 500-pW0p allocation in the INTELSAT IV-A system noise budget. Two typical examples are shown in Figures 10 and 11.\* The gain difference between these transponders can be readily seen in Figure 12, which shows the relative gain for each of the 20 transponders in a typical INTELSAT

\*These figures represent the results of a computer system model developed by COMSAT under INTELSAT sponsorship to simulate the effects of distortion due to dual path. The program has been compared with measured results under various study contracts and is believed to be a reliable model. A discussion can be found in Reference 7.



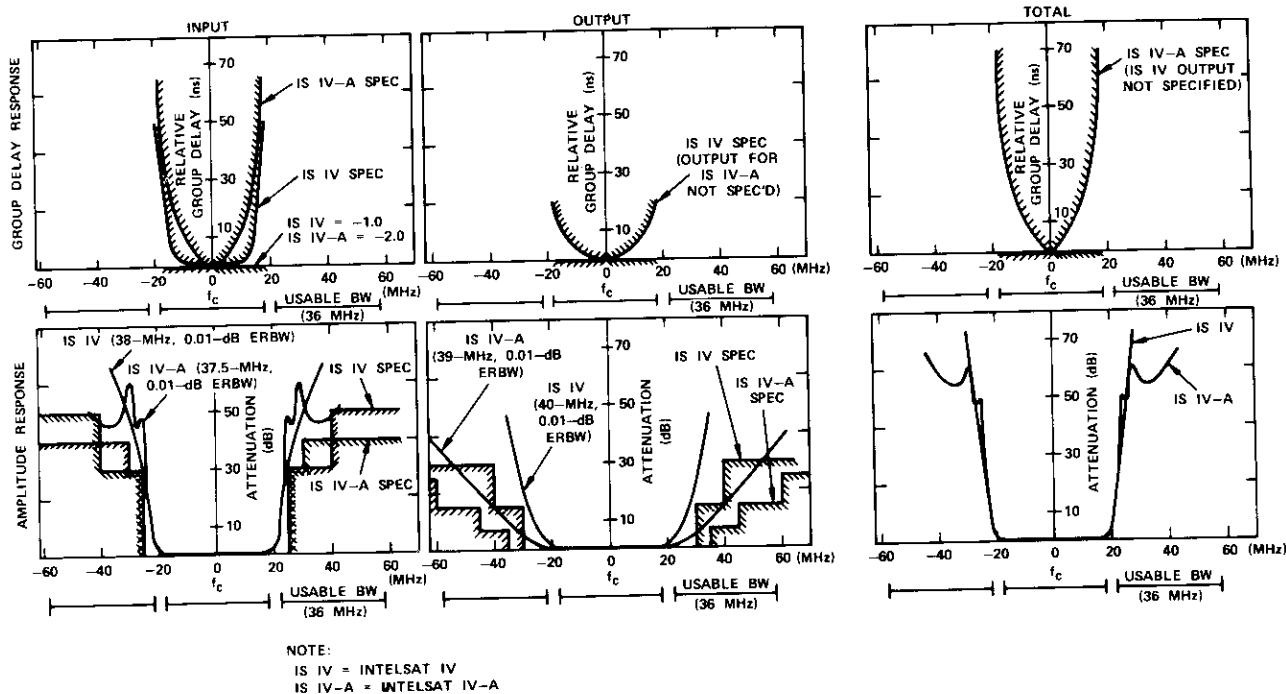


Figure 8. General Comparison of INTELSAT IV and INTELSAT IV-A Input and Output Filters

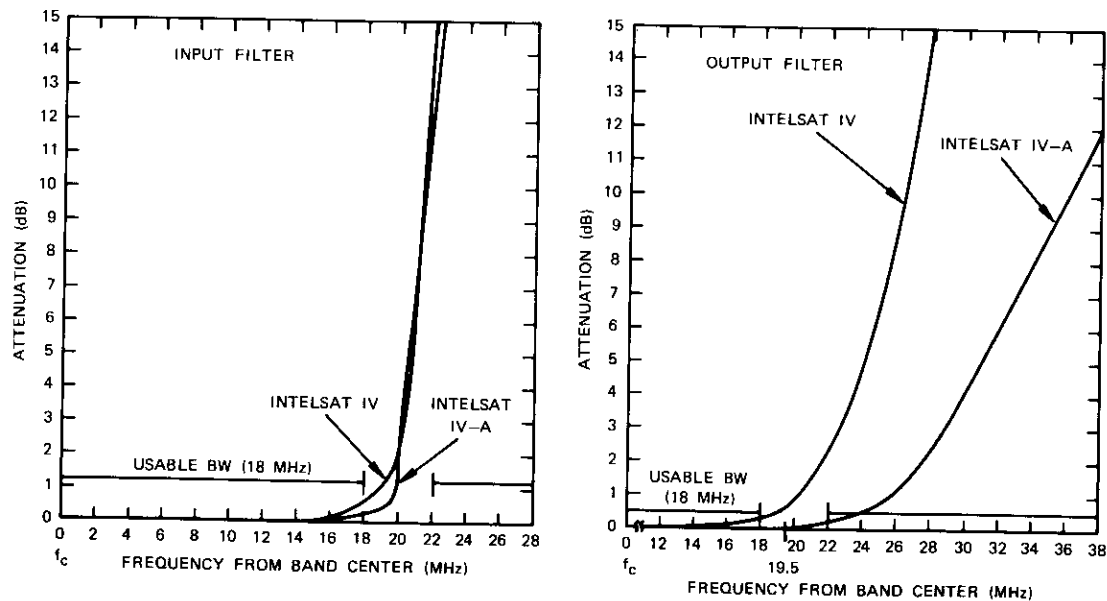


Figure 9. Detailed Comparison of INTELSAT IV and INTELSAT IV-A Input and Output Filters

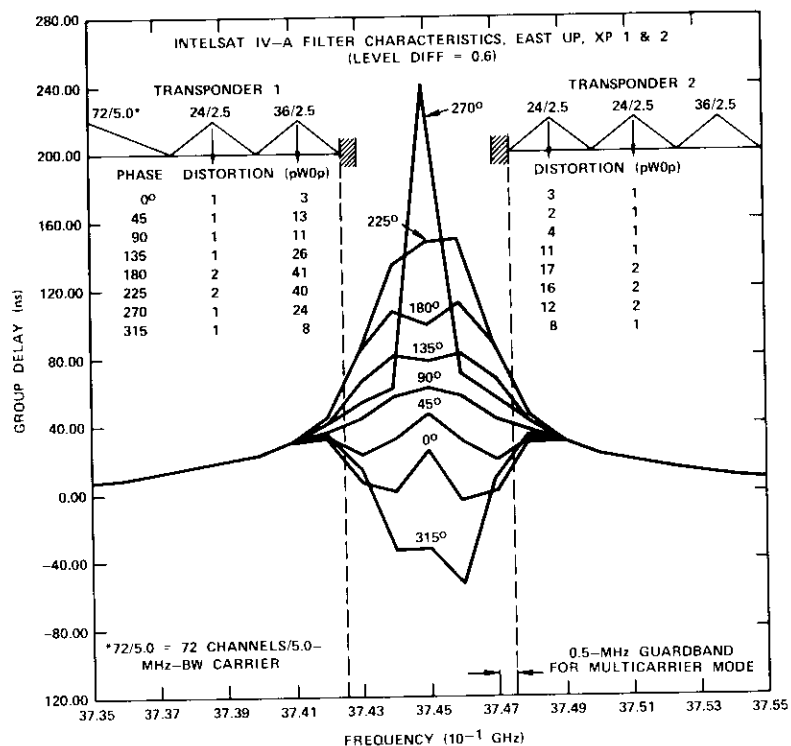


Figure 10. Typical Small Carrier Group-Delay and Dual Path Distortion (INTELSAT IV-A)

IV-A frequency plan. In each example, values have been determined for the total distortion with C.C.I.R. emphasis used in the transmission chain and for a variety of phase possibilities.

As has been mentioned previously, one factor which has permitted a reduction of the group-delay specification in the INTELSAT IV-A system is the requirement for only a few large carrier sizes. In general, carrier sizes with bandwidth units in the range 2.5, 5.0, and 10.0 MHz will be in the majority. Group-delay and dual path distortion for carrier sizes in this category (at band edge) are shown in Figure 10. There are some cases, however, in which larger carrier sizes will be placed into operation. For example, the effect of locating a 432-channel/17.5-MHz carrier at band edge is shown in Figure 11. The deviation of such a large carrier is expected to produce a distortion level greater than the budgeted 500 pWOp. Alter-

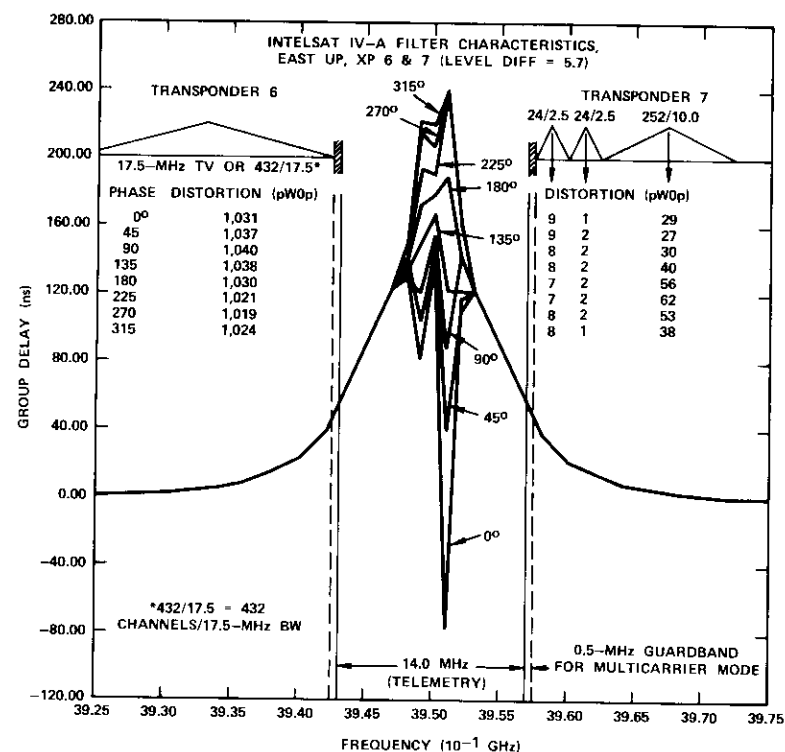
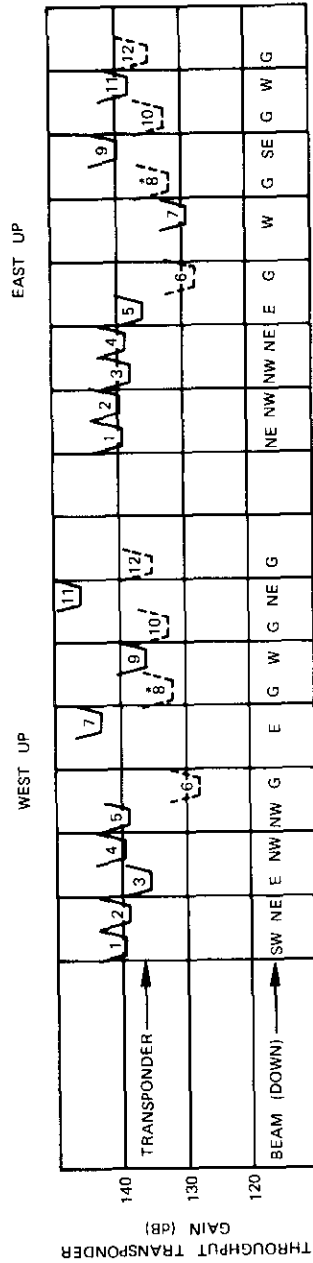


Figure 11. Typical Large Carrier Group-Delay and Dual Path Distortion (INTELSAT IV-A)

natives to this problem are simply relocation of the carrier toward the center of the transponder or, if relocation is not feasible, use of equalization at the earth station. Since there are relatively few of these situations, the INTELSAT IV-A system is expected to be able to meet the system noise budget of 500 pWOp for group delay and dual path in all cases, even with a less restrictive filter specification than that of INTELSAT IV.

#### Adjacent transponder interference (due to intermodulation)

When satellite transponders are operated in the multicarrier mode (accessed by many carriers), intermodulation products are generated in the output TWT and transmitted together with the desired signals. Although the out-of-band products are attenuated by the output filter, their magnitude can, in some cases, be sufficient to cause considerable



NOTE:

1. 8° USED FOR SPADE AND POSSIBLY TDMA FIELD TRIALS. ONLY THIS TRANSPONDER HAS SPECIAL GROUP-DELAY EQUALIZATION.
2. G = GLOBAL BEAM.
3. SW, NE & NW = DOWN-LINK SPOT BEAM.
4. E & W = DOWN-LINK HEMISPHERIC BEAM.
5. = GLOBAL BEAM (CAN BE ACCESSED ON EITHER E OR W UP-LINK)
6. \*\* REFERENCE INTELSAT IVA FREQUENCY PLAN IN FIGURE 14.

Figure 12. INTELSAT IV-A Transponder Gain Differences (dual path considerations)

interference with signals transmitted from adjacent transponders. For example, when the two television signals in Figure 14 are transmitted through global-beam transponder 12, the TWT is operated very close to saturation. Of the two third-order intermodulation products generated (types 2A-B and 2B-A), the center frequency of the lower product falls 5.75 MHz inside of transponder 11. The output filter attenuation at this point is approximately 1.8 dB. The other product falls out of the satellite frequency band.

Since transponder 12 is operated in the global-beam mode, its intermodulation is received at all earth stations. The effect of this interference is twofold:

- a. stations located in the northeast spot beam (Figure 14) and receiving the large carrier transmitted from the western hemisphere will experience interference with their reception,
- b. stations located in the western hemisphere and receiving the large carrier transmitted from the eastern hemisphere will experience interference with their reception.

The magnitude of the interference depends on the configurations of both the interfering transponder and the transponder experiencing interference. In this case, when satisfactory TV performance requires that transponder 12 be operated at or near its saturation point, the placement of large carriers in the adjacent transponder helps to minimize the amount of interference.

It should be noted that intermodulation products generated by global-beam transponders always cause interference with some carriers in adjacent spot-beam transponders. However, since the global transponders have the lowest e.i.r.p., while carriers emanating from spot-beam transponders generally have the highest power levels, this interference can be kept to a minimum. On the other hand, intermodulation products generated by spot- or hemispheric-beam transponders adjacent to global-beam transponders do not always interfere with the global-beam carriers. This will depend on which spot or hemispheric beam is activated and on the destination of the global carriers.

Although the actual interference values will depend on the individual transponder frequency plans, the range of interference values expected is summarized in Table 2. In comparison, adjacent transponder intermodulation has not been detectable in the INTELSAT IV system.

TABLE 2. INTELSAT IV-A INTERFERENCE DUE TO ADJACENT TRANSPONDER INTERMODULATION

Example No.	Case	Interference in Adjacent Carriers (pW0p)
1	2 TV signals (global beam) adjacent to large carrier in multicarrier mode (transponder 12 into transponder 11)	—
2	Multicarrier (hemisphere) adjacent to multicarrier global (transponder 7 into transponder 8)	≈500–1,000
3	Multicarrier (spot) adjacent to multicarrier (spot) (transponder 2 NW into transponder 3 NW)	≈1,000–1,500

### Crosstalk

When FDM/FM carriers are applied to a multicarrier satellite repeater, intelligible crosstalk is produced by a transmission versus frequency deviation, followed by an amplitude to phase conversion. That is, as the carrier passes through the TWTA, its phase is changed as a function of any amplitude modulation which may be present. Another carrier passing through the TWTA will also vary in phase at the same rate as the amplitude modulation and thereby pick up intelligible information from its neighboring carrier.

The crosstalk objective in the INTELSAT system conforms to the Geneva C.C.I.T.T. recommendation (Geneva 1964, Vol. III) for intelligible crosstalk of  $-58$  dB or better. In preparation for the INTELSAT IV satellite system, extensive laboratory testing and modeling was conducted to ensure that this objective could be met through appropriate specifications [7]. Later field tests on the actual system indicated that even worse situations did not produce detectable crosstalk levels. There was therefore reasonable assurance that the crosstalk specifications for the INTELSAT IV-A could be modified due to the different usage envisioned for this satellite. Through supportive modeling and calculations, an INTELSAT IV-A contract specification for intelligible crosstalk 6 dB lower than that of INTELSAT IV was established. This in turn meant that the gain slope tolerance of an 8-section elliptic function input filter would be compatible with overall system objectives.

There are some reservations, however, concerning the feasibility of a crosstalk level of  $-58$  dB in the few rare instances in which two carriers with large bandwidth units are placed side by side in the same transponder. It is felt that situations in this category can be overcome by ensuring that

proper safeguards are applied in the frequency planning process. At the time of this writing, further investigations are proceeding to determine if there may still be some large carrier cases in which corrective measures in the form of gain slope equalization before the input of the HPA are needed at the earth station. There are limitations to this approach in that crosstalk can also be produced in the earth station HPA. In any case, it is expected that crosstalk can be held within the C.C.I.T.T. intelligible crosstalk recommendation. If necessary, the INTELSAT IV-A frequency plan will be altered to overcome the few potential problems due to crosstalk.

### *Intelsat IV-A frequency planning*

Frequency planning for the INTELSAT IV-A system is more complex than for the INTELSAT IV system because of the additional transmission constraints resulting from frequency reuse techniques. A rough visual approximation of the magnitude of this difference can be seen by comparing typical frequency plans for both systems in Figures 13 and 14.

Figures 1 and 2 present a further comparison of the INTELSAT IV and INTELSAT IV-A systems. For the INTELSAT IV-A there are two possible up-link modes: hemispheric (E and W) and global. The down-link has three modes: hemispheric (E and W), spot (NW, NE, SW, and SE), and global. In the INTELSAT IV, only global access is employed on the up-link, and either global or spot can be chosen for the down-link.

To provide such services as SPADE,\* TDMA, TV, and telephony to earth stations outside the normal hemispheric coverage zones, four transponders have been designated as global-beam channels in the INTELSAT IV-A. With some constraints,† the remaining eight cotransponder pairs (16 transponders) can be switched to either a hemispheric or spot beam on the down-link. That is, of the potential 1,000-MHz bandwidth made available by frequency reuse techniques, 160 MHz (40 MHz/transponder  $\times$  4) will be lost to provide unique services on a global scale. Within these bounds, the 20-transponder INTELSAT IV-A is expected to be configured to handle 12,000–12,500 voice grade channels (plus one TV and one SPADE transponder) for a typical Atlantic primary satellite frequency plan configuration. By comparison, an INTELSAT IV Atlantic primary satellite can

\*SPADE is an acronym for single-channel-per-carrier, pulse-code-modulation, multiple-access, demand-assignment equipment.

†Transponders 2 and 4 of the eight cotransponder pairs can also be switched to the global mode of operation.

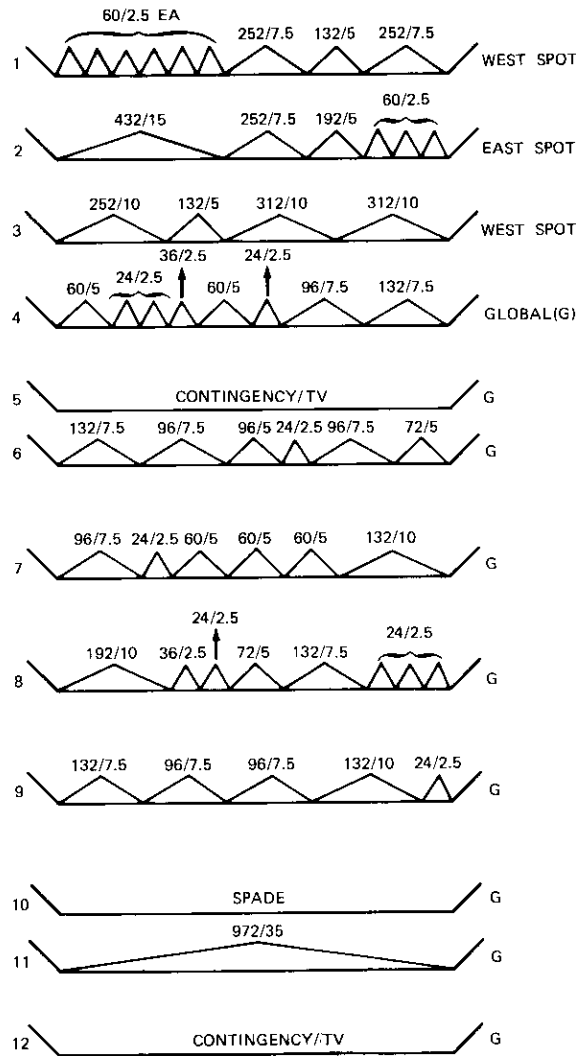


Figure 13. Typical INTELSAT IV Frequency Plan (12 transponders)

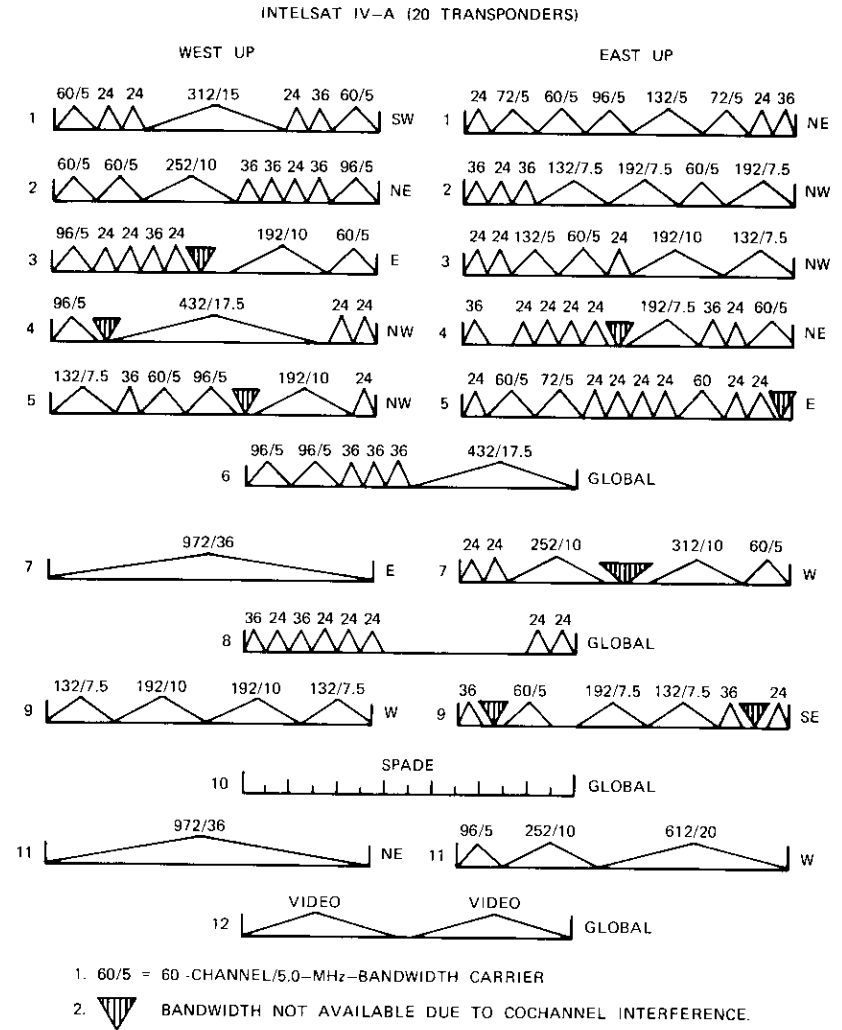


Figure 14. Typical INTELSAT IV-A Frequency Plan (20 transponders)

be configured for 7,500 channels (plus one TV and one SPADE transponder). The net capacity increase of the INTELSAT IV-A will be approximately 5,000 channels.

Several technical considerations must be taken into account in INTELSAT IV-A frequency planning to achieve maximum channel capacity in a frequency reuse environment. A brief explanation of some of these constraints is provided in the paragraphs that follow.

#### **Cochannel interference**

To minimize interference, the same carrier center frequency should not be assigned to two carriers in the same cochannel set. In addition, spot and hemispheric beams should be paired together only as a last resort. Interference from the spot into the hemispheric transponder will be increased by 3 dB if this configuration is employed.

#### **Adjacent transponder interference (due to intermodulation)**

The output filter skirts on the INTELSAT IV-A are much wider than those on the INTELSAT IV and therefore do not offer as much rejection to adjacent transponder intermodulation. In some cases judicious frequency planning can resolve the problem. For example, in Figure 14 the two large intermodulation products produced by the dual video carriers in transponder 12 will create a minimum amount of interference because one of the products will fall out of the satellite band, while the other will fall under the large carriers in transponder 11. Frequency planning should also attempt to use different down-link beams for adjacent transponders.

#### **Dual path and crosstalk**

With the particular multisection input and output filters used in the INTELSAT IV-A system, group delay at the transponder band edge will be more serious than in INTELSAT IV. As a frequency planning criterion, carriers with large bandwidth units should not be placed at band edge where they are more susceptible to distortion due to group delay and its associated dual path impairment. The gain difference between transponders is also greater in INTELSAT IV-A than in INTELSAT IV due to spot/global interleaving and will produce greater dual path distortion. To reduce severe crosstalk possibilities, large carrier sizes should not be placed in the same transponder.

Connectivity requirements in the spot and hemispheric beams will mean that each earth station will transmit several small carrier sizes. For the frequency plan shown in Figure 14, approximately three-fourths of the total carriers have bandwidth units of 5.0 MHz or less. Having a large

number of small carrier sizes in the system results in less group-delay and crosstalk distortion, and a lower overall RF out-of-band emission environment.

Obviously, frequency planning is becoming more complicated with each generation of the INTELSAT satellite system. In an effort to expedite technical evaluations of the many carrier arrangements that are proposed before a final plan is approved, computer system models have been developed to simulate many of the impairments mentioned above and automatically balance power levels for the best performance. A system model is currently in use for the INTELSAT IV satellites and has worked very well over the past three years [1].

#### **Conclusions**

Transmission design for the INTELSAT IV-A satellite has been developed around a concept which will create a minimum change in present-day earth station equipment and operation. In addition, the satellite must possess the channel capacity necessary to fulfill international satellite traffic requirements in the Atlantic Ocean region from 1975 through 1980. To achieve these goals while retaining the use of an Atlas-Centaur launch vehicle, frequency reuse by spatial separation of west and east hemispheric beams will be employed.

Theoretically, frequency reuse should double the available satellite bandwidth allocation and thereby double the number of available channels. In practice, however, a typical INTELSAT IV-A Atlantic primary satellite will fall short of this objective by about 20 percent. Several factors account for this loss:

- a. The requirement to provide global-beam coverage for special services such as SPADE and TV, secondary coverage zones, and application versatility have resulted in the elimination of four transponders which could have been employed with frequency reuse. This accounts for 160 MHz of bandwidth, or 16 percent of the total 1,000 MHz initially available.
- b. With the exception of cochannel interference, the transmission impairments discussed in this paper (adjacent transponder interference, group-delay and dual path distortion, crosstalk, and earth station RF out-of-band emission) can be held within the normal INTELSAT system noise budget apportionment either by careful frequency planning or by appropriate countermeasures at the earth

stations. On the other hand, cochannel interference, which results from the coupling between spatially isolated beams, will add a new 500- to 1,000-pW0p contribution to the noise budget. This impairment will cause some carriers to be intentionally omitted from certain cotransponder configurations just to minimize its effects.

c. Frequency reuse will require the utilization of many small carrier sizes. Approximately three-quarters of the carriers in a typical Atlantic primary frequency plan will have bandwidth units of 5.0 MHz or less. Maximum channel capacity can be achieved when a transponder is operated with a large single carrier near saturation; this provides the best down-link e.i.r.p. and does not produce harmful TWT intermodulation. As more carriers are added, intermodulation increases and the transponder channel capacity decreases.

d. The size of large single carriers will be limited by the amount of interference they will create in a cotransponder. To minimize this interference, up-link power must be restricted, which in turn reduces the maximum channel capacity the carrier might otherwise have been able to attain.

While frequency planning for INTELSAT IV-A will be more intricate than for INTELSAT IV due to the restraints mentioned in the previous paragraphs, automated techniques are presently under development to keep pace with the demands of day-to-day system operation. Although there are limiting factors, INTELSAT IV-A is expected to achieve its goal of handling the Atlantic Ocean region traffic until the early 1980s using the Atlas-Centaur launch vehicle with minimum earth station disruption. When configured as an Atlantic primary satellite, INTELSAT IV-A is expected to have a capacity of approximately 12,000–12,500 voice grade channels (plus one TV and one SPADE transponder), or a net increase of about 5,000 channels over a similarly configured INTELSAT IV.

### References

- [1] J. L. Dicks, P. H. Schultze, and C. H. Schmitt, "INTELSAT IV System Planning," *COMSAT Technical Review*, Vol. 2, No. 2, Fall 1972.
- [2] "Performance Characteristics of Earth Stations in the INTELSAT IV Systems," ICSC-45-13 (Rev. 1), 23 June 1973.
- [3] B. A. Pontano, J. C. Fuenzalida, and N. K. Chitre, "Interference into Angle-Modulated Systems Carrying Multi-Channel Telephony," *IEEE Transactions on Communications*, June 1973.

- [4] M. P. Brown, Jr., "Review of INTELSAT Earth Station RF Out-of-Band Emission Criteria," *COMSAT Technical Review*, Vol. 4, No. 1, Spring 1974.
- [5] "Performance Characteristics of Earth Stations in the INTELSAT IV-A System," BG-11-40, September 1974.
- [6] A. E. Atia and A. E. Williams, "New Types of Waveguide Bandpass Filters for Satellite Transponders," *COMSAT Technical Review*, Vol. 1, No. 1, Fall 1971.
- [7] *COMSAT Technical Review*, Vol. 2, No. 2, Fall 1972, pp. 489–561.

### Appendix A. INTELSAT IV-A dual polarization experiment

Exploitation of frequency reuse by dual polarization in the INTELSAT network would permit broader system alternatives. The major drawback at present is the requirement for additional propagation data to provide a better understanding of depolarization effects and possibly the development of a means of depolarization compensation. It is also necessary to demonstrate the performance of both satellite and earth station antenna on a systems basis as well as to establish estimates of cost, technical performance, and earth station modifications for this type of operation. The dual polarization experiment on the INTELSAT IV-A will be used in conjunction with other projects to supply this information.

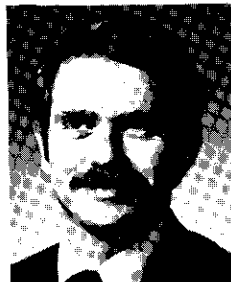
Basically, the experiment will involve newly developed global transmit and receive antennas with ports for both right- and left-hand circularly polarized signals. When propagation measurements are conducted, both of the global receivers shown in Figure 5 will be employed, one for each polarization. Transponders 2A and 4A will be used for right-hand circular polarization and transponders 2B, 4B, 6, 8, 10, and 12 for normal left-hand circular polarization. (The output of transponders 2A and 4A will be connected to the left-hand port of the transmit antenna and the remaining six transponders to the normal right-hand circular polarization port.) A 1-kHz keying modulator will be added to the new signal path to permit identification of signals passed through it. The discrimination provided by the global antenna in transponders 2 and 4 will be at least 32 dB and that provided by the remaining global transponders will be at least 29 dB.



*Jack L. Dicks received his B.S. in Mathematics and Engineering Physics from Sir George Williams College in Montreal, Canada. Before joining COMSAT, he was on the engineering staff of the Canadian Overseas Telecommunications Corporation, where he was involved in planning, installation, and testing of equipment associated with the CANTAT and COMPAC submarine telephone cables and the Mill Village earth station. Since he joined COMSAT in 1968, he has been primarily*

*involved in transmission planning for the INTELSAT IV and IV-A satellite systems. He is presently Director of Transmission Engineering in the International Systems Division.*

*Martin P. Brown, Jr. received his B.E.E. from Georgia Institute of Technology in 1966. Before entering the service, he worked with IBM at Cape Kennedy on the Saturn V launch vehicle. From 1967 to 1971, he served as an engineering communications officer with the U.S. Air Force. He joined COMSAT Laboratories in 1971 and is presently a Sr. Communications Engineer with the International Systems Division studying multi-carrier satellite transmission impairments.*



*Mr. Brown is active in C.C.I.R. Study Group IV, the Aerospace and Electronics Systems Group of IEEE, a member of the AIAA, and a registered professional engineer.*

**Index:** telecommunications, fading, diversity, error control, TDMA, feedback communication, soft-decision modem

## ***DIVEC, a combined diversity and error control scheme***

R. J. F. FANG

(Manuscript received August 29, 1974)

### ***Abstract***

This paper describes a combined diversity and error control scheme called DIVEC, which can lead to a reduction of the system margin required to achieve a specified performance for communications over fading channels. The new scheme uses selection and burst switching spatial diversity in the up-link and spatial diversity with probabilistic and algebraic error control in the down-link. Because of its inherent redundancy, diversity itself can be regarded as a trivial repetitive coding technique in terms of information theory. Improved performance and hence a reduced system margin can be obtained by exploiting the code structure to provide error detection or correction. It is shown that for certain applications DIVEC offers an advantage of 2.8 and 2.6 dB over selective spatial diversity and triple diversity, respectively. Its hardware implementation is straightforward.

### ***Introduction***

The capacity of communications satellites in the present INTELSAT system is essentially bandwidth limited. Increased capacity through additional available bandwidth could be provided as follows:

- a. by frequency reuse through multiple-beam and/or dual polarization satellites;

- b. by using higher carrier frequencies, such as 11/14 or 20/30 GHz, where additional bandwidth has been allocated to satellite communications.
- c. by using a combination of these two approaches.

The assigned capacity of a multiple-beam satellite depends upon the traffic patterns, and in general a high degree of connectivity is required between the multiple beams. Satellite-switched [1] and transponder-hopping time-domain multiple-access (SS/TDMA and TH/TDMA, respectively), which can provide the desired connectivity, appear to be promising access techniques for future multiple-beam satellites. However, at frequencies as high as 20/30 GHz, deep fades may be experienced in some areas when heavy precipitation is present. Consequently, large system margins may have to be provided unless some kind of diversity is used. With conventional diversity techniques, the needed system margin may still be excessive.

This paper addresses itself to the problem of providing additional decibels of system margin for SS/TDMA or TH/TDMA multiple-beam systems with spatial diversity and high frequencies such as 20/30 GHz. It is assumed that these systems will use quaternary coherent phase-shift-keying [4-phase CPSK] modulation at bit rates around 1 Gbps over 500-MHz-bandwidth transponders.

A combined *diversity* and *error control* scheme called DIVEC is proposed in this paper. This scheme uses selection and burst-switching spatial diversity in the up-link and spatial diversity with probabilistic and algebraic error control in the down-link. Due to the inherent redundancy of any diversity system, diversity itself can be regarded as a trivial repetitive coding technique in terms of information theory.\* System performance can be improved and hence the required system margin can be reduced by exploiting this code structure to provide error detection or correction. This paper also shows that in some applications DIVEC has an advantage of 2.8 and

\* Diversity receptions can be viewed as identical messages received from *separate* channels regardless of whether the actual diversity is achieved by space, polarization, mode, angle, frequency, or time. For example, if spatial diversity is used, the same message is received at different geographical locations. Effectively, the same message has been repeated over separate channels. Thus, diversity can be viewed as a trivial form of repetitive coding. For a  $\kappa$ th-order diversity system, the same message is repeated over  $\kappa$  channels. If the  $\kappa$  channels are regarded as  $\kappa$  time slots represented by  $\kappa$  bits, then  $\kappa - 1$  of the  $\kappa$  bits are obviously redundant. It is this inherent redundancy that permits the DIVEC scheme to provide the desired error control.

2.6 dB over conventional selective, spatial, dual diversity and triple diversity techniques, respectively. In addition, the hardware implementation of DIVEC appears straightforward.

### **Description of the DIVEC scheme**

Under the assumption that the input data are already in the form of a bit stream, the even and odd bits of this bit stream are separately encoded by some efficient systematic code, convolutional or block, such as the single parity check, rate-9/10, block code (10, 9). This systematically encoded bit stream is fed to the 4-phase PSK modulator and transmitted in the form of TDMA bursts. If differential encoding is used to resolve phase ambiguity in the 4-phase CPSK modem, then the separate encoding of even and odd bits can prevent the reduction of error correction capability due to the presence of the characteristic pairwise error patterns [2]. If, on the other hand, the digital transmission system already has some codec [coder-decoder] equipment, this equipment may be sufficient.\*

The modulated burst signal can be sent to the satellite by transmitter A at the switch center if diversity is not needed (see Figure 1). If dual diversity is used, it may be sent by transmitter AA at the switch center or by transmitter BB at a diversity site connected to the switch center by terrestrial facilities. In heavy precipitation areas, triple diversity may be used. That is, the signal may be sent via transmitter AAA at the switch center or via transmitter BBB or transmitter CCC at the diversity sites. The site chosen to transmit the signal in the case of dual or triple diversity depends upon the state of the switch in Figures 2 and 3, which is controlled by the unit labeled "control logic." The function of this control unit will be described in the following.

### **Dual diversity**

#### **UP-LINK STRATEGY**

For an SS/TDMA system it is conceivable that the frame synchronization signal will be sent back or "looped back" to the transmitting station. The carrier-to-noise ratio, C/N, of the signal can be used for monitoring

\* Since the duration of serious fades at 20/30 GHz is of the order of seconds or minutes, and since the data rate is nearly 1 Gbps, the attenuation due to precipitation can be assumed to be constant over the code length for all practical purposes.

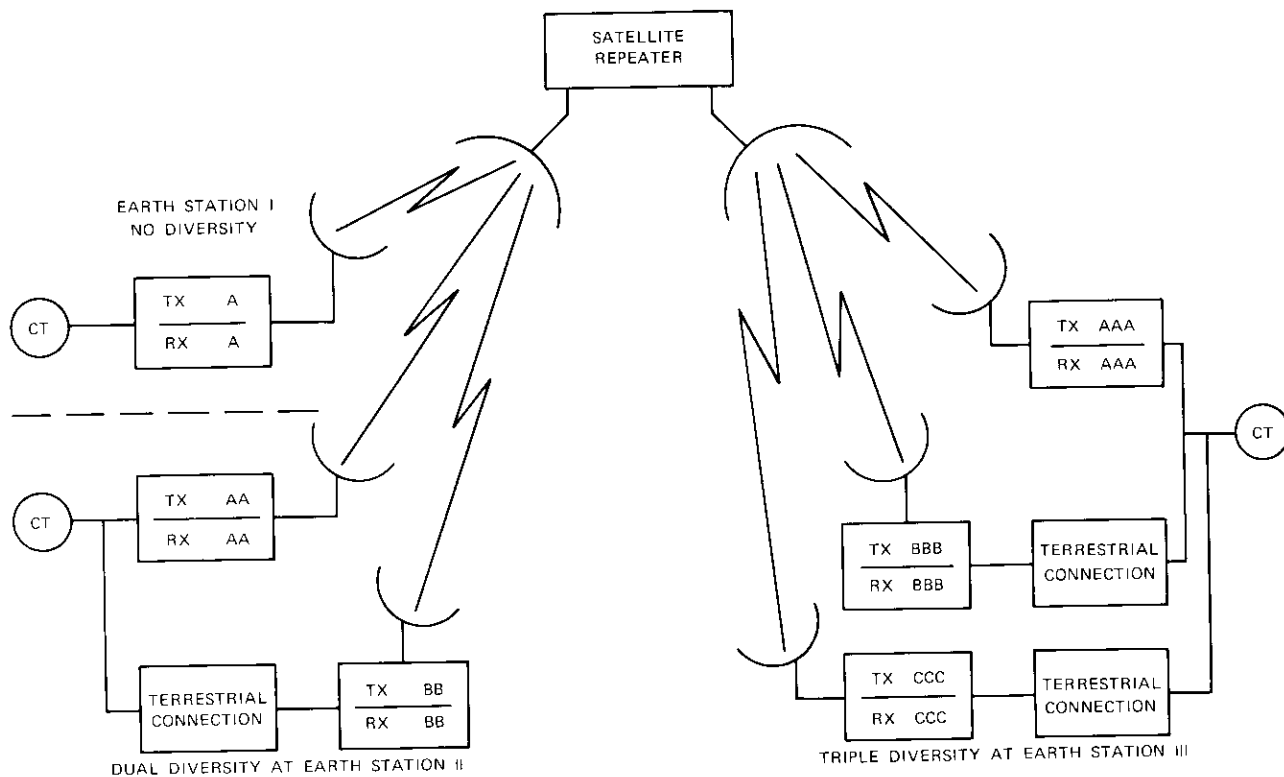


Figure 1. Diversity Configurations in Multiple-Beam SS/TDMA or TH/TDMA Systems

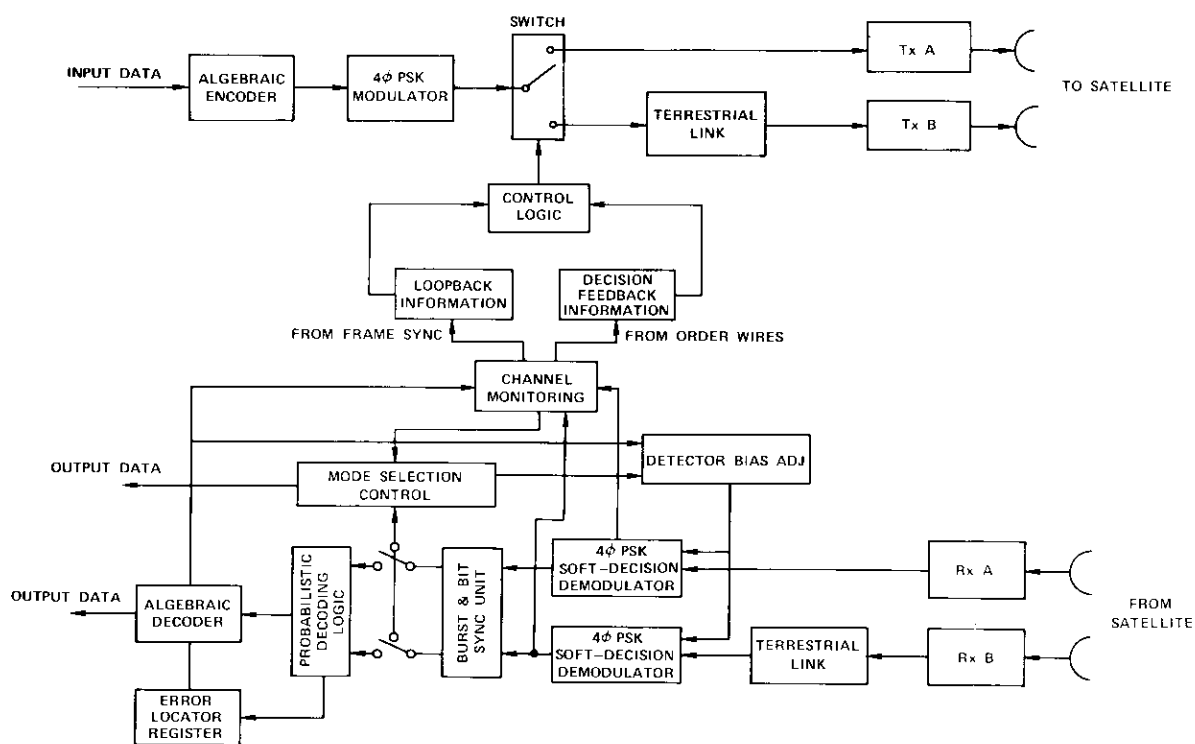


Figure 2. Block Diagram of DIVEC for Dual Diversity Case

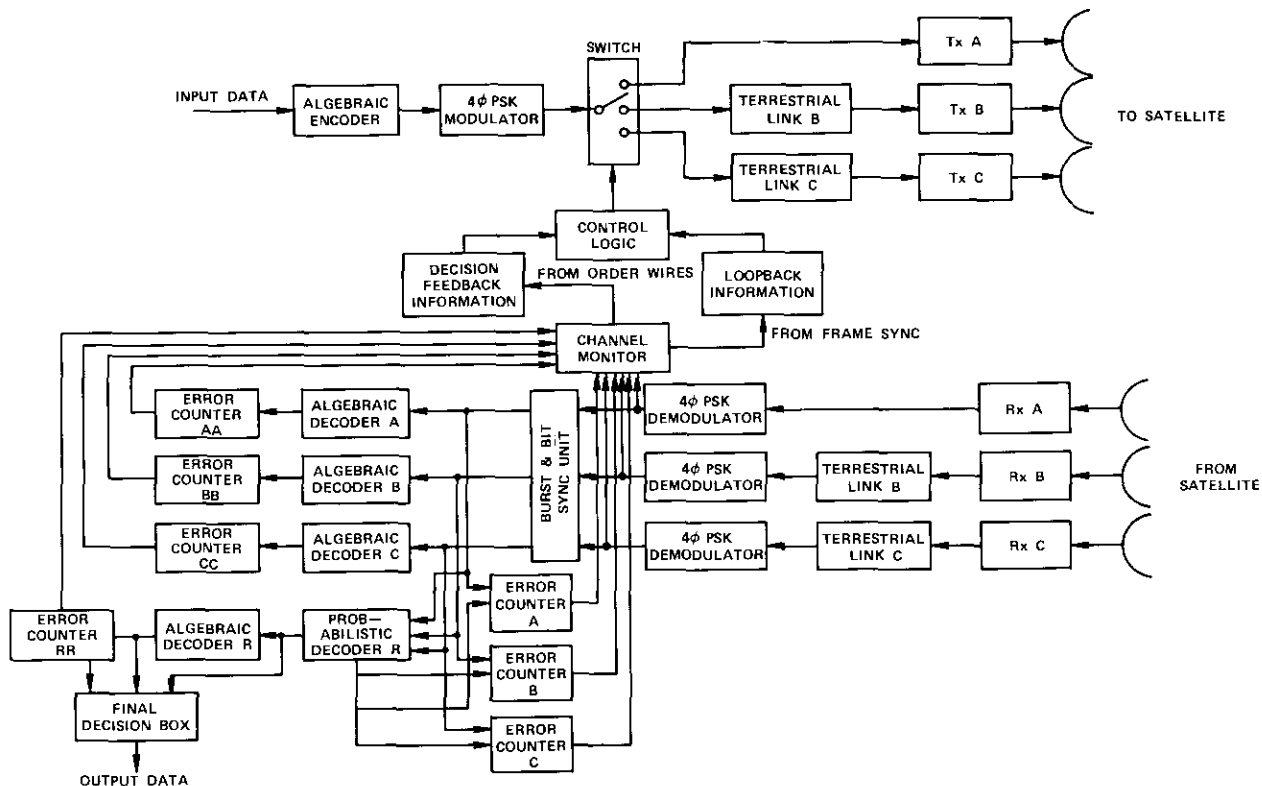


Figure 3a. Block Diagram of a Triple Diversity DIVEC System

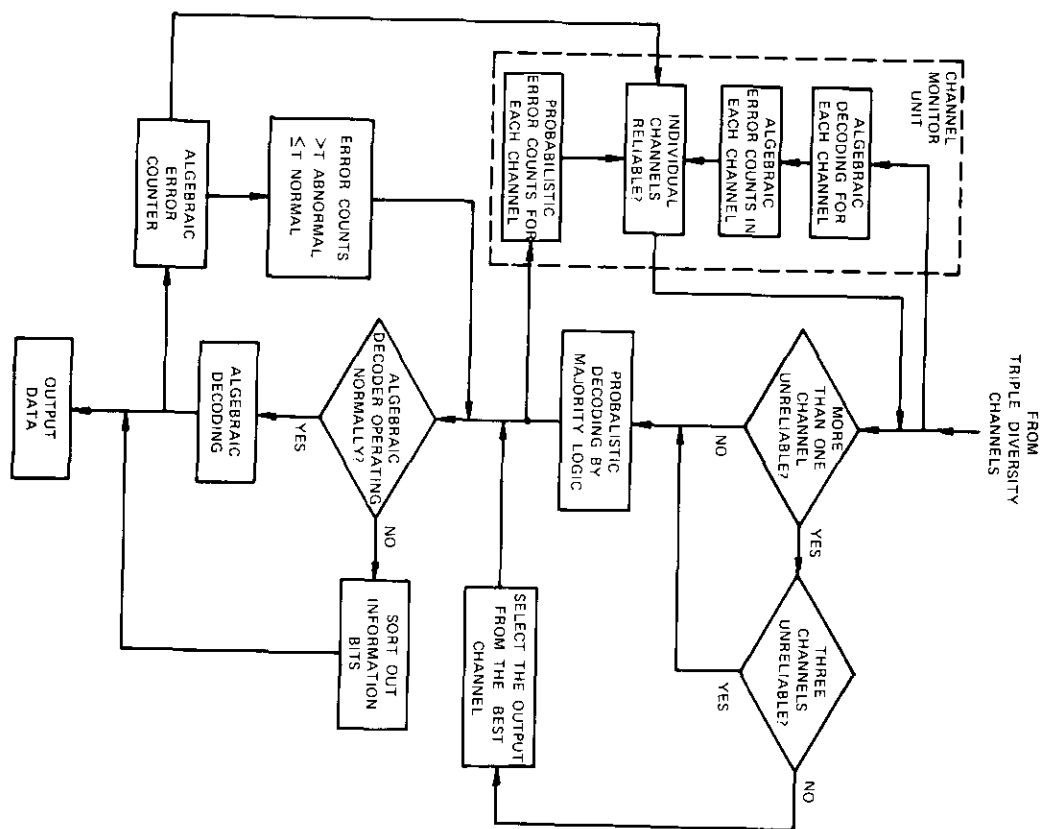


Figure 3b. A Simplified Error Control Algorithm for a Triple Diversity DIVEC System

the precipitation attenuation in the up-link. The control logic unit in Figure 2 enforces the following rules:

- a. It always uses the better up-link to transmit if the precipitation attenuation in this link is less than a certain threshold,  $T_1$ .\*
- b. If the precipitation attenuation in both up-links is greater than threshold  $T_1$ , but less than threshold  $T_3$  ( $T_3 > T_1$ ) so that initial acquisition and burst synchronization are still possible, then TDMA bursts will be transmitted alternately from the two sites [3] until the attenuation in one of the two paths becomes less than threshold  $T_1$ . The strategy of selecting the better path will then be resumed.
- c. If either link has an attenuation larger than  $T_3$ , the other link will be selected. However, if both links have attenuation greater than  $T_3$ , an up-link outage occurs.

When the attenuation in both up-links is between thresholds  $T_1$  and  $T_3$ , alternate transmission of TDMA bursts from the two sites will allow a very important advantage. That is, since most stations in TDMA systems are transmitting as well as receiving multidestination bursts, the earth stations at the destinations can help to monitor the up-link fades at the source stations. For example, if a destination receives bursts with small error probabilities from all but a few of its sources, then it is very likely that the up-links of these few sources have experienced fades. Such unique status information can be fed back very *reliably* via the order wires in the return paths to these particular transmitting stations since it is only necessary to feed back this status information very infrequently and since the required data rate is very low. At these transmit stations, the fed-back status, or the "decision feedback" information [4], [5], can be utilized to monitor the quality of individual up-links.

Knowing that a dual diversity station transmitted bursts alternately from its two sites, the destination stations can easily tell the source station which up-link of the two sites is better by simply comparing the error rates of the unique word bits in the odd and even bursts. Hence, rule *b* can be refined as follows:

If the attenuation in both up-links is greater than threshold  $T_1$  but less than threshold  $T_3$  ( $T_3 > T_1$ ) so that initial acquisition and burst

\* If the merit of rule *a* does not warrant the additional equipment complexity involved, it can be combined with rule *b*. In this case  $T_1$  should be set equal to 0 dB in *a* and *b*.

synchronization are still possible, then TDMA bursts will be transmitted alternately from the two sites until the attenuation in one of the two links becomes less than threshold  $T_1$ , or the majority of the destination stations notify this source station, via the order wires in the return links, of the best up-link. In either of these two cases, the strategy of selecting the best up-link will be resumed.

#### DOWN-LINK STRATEGY

The signals at the two diversity receivers will be detected into the baseband coherently\* and *separately* by a 4-phase PSK demodulator with soft decision. These two baseband digital streams can be synchronized bit by bit without much difficulty by using two compression and expansion buffers. The two bursts, which are received from two different diversity links, can be written into the buffers at different times and read out simultaneously; hence, they are synchronized bit by bit.†

Now consider the soft-decision 4-phase PSK demodulator. In addition to the original decision boundaries 1 and 2 of the hard-decision demodulator shown in Figure 4a, two extra boundaries are introduced in both the in-phase and quadrature-phase components (see boundaries 1', 1'', 2', and 2'' in Figure 4b). Each boundary corresponds to a binary detector with a certain bias.

The six decision boundaries, 1, 1', 1'', 2, 2', and 2'', can be easily implemented by simply changing the biases of the six detectors. The received signal sample at the demodulator can fall into any of the 16 decision regions, as shown in Figure 4b. Each of these regions is uniquely associated with a 4-bit symbol in this soft-decision demodulator as opposed to a regular 4-phase PSK hard-decision demodulator in which there are only four decision regions, each associated with a 2-bit symbol. Therefore, the weakly received signal samples, which are most likely to fall into the shaded regions of Figure 4b, are not given a 0 or 1 "hard" decision. Instead, a soft decision is given to indicate where they belong in the shaded areas.

If the C/N of one or both receivers stays above threshold  $\Delta$ , which

\* If other digital modulation techniques such as DPSK are employed, this term should be changed accordingly.

† Since the data rate is nearly 1 Gbps, other conventional combining techniques for achieving bit-by-bit synchronization are extremely difficult to implement.

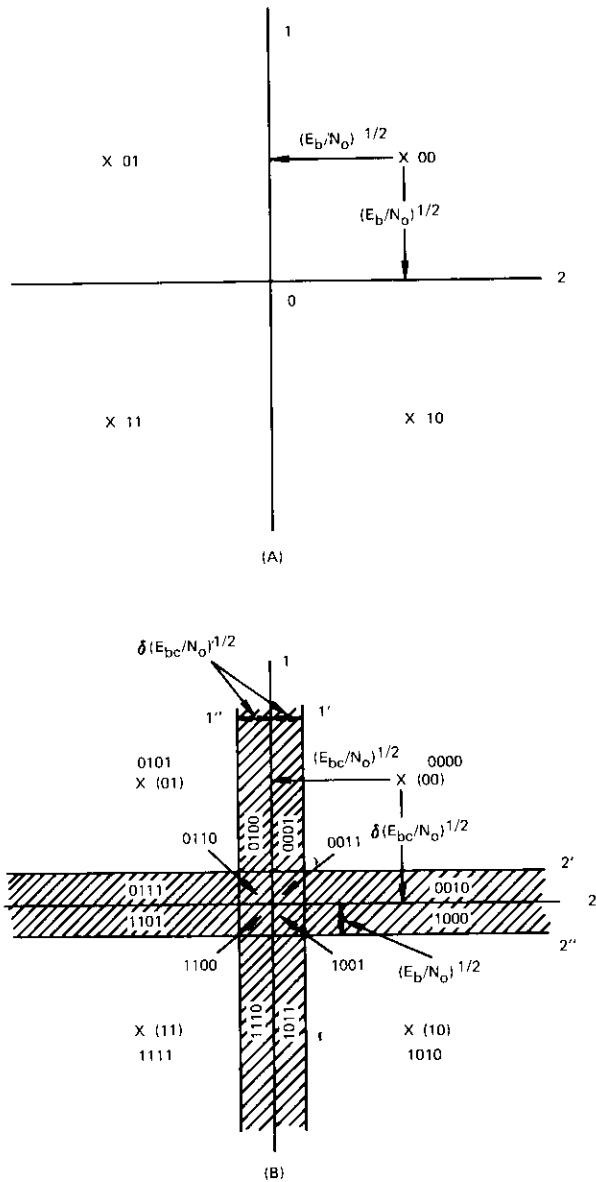


Figure 4. Decision Regions for 4-Phase PSK Demodulators

TABLE 1. RULES OF PROBABILISTIC DECODING FOR TRANSFORMING FROM 4-BIT SYMBOLS OF THE TWO DIVERSITY LINKS TO 2-BIT SYMBOLS (horizontal and vertical coordinates are received 4-bit symbols from the two sites)

	0000	0010	0101	0111	1010	1000	1111	1101		
	0001	0011	0100	0110	1011	1001	1110	1100		
0000	0	0	0	0	0	0	0	0	x	0
0001	0	0	0	0	0	0	0	0	0	0
0010	0	0	0	0	0	0	0	0	0	0
0011	0	0	0	0	0	0	0	0	0	0
0101			0	1	0	1	0	1	x	0
0100			0	1	0	1	1	0	x	0
0111			0	1	0	1	1	1	x	0
0110			0	1	0	1	0	1	0	x
1010					1	0	1	0	1	0
1011					1	0	1	0	1	1
1000					1	0	1	1	0	1
1001					1	0	1	1	1	1
1111							1	1	1	1
1110							1	1	1	1
1101							1	1	1	1
1100							1	1	1	1

THE LOW TRIANGLE IS SYMMETRIC TO THE UPPER TRIANGLE

corresponds to a  $10^{-4}$  bit-error rate, then the output of the channel with the higher C/N will be chosen until both are below  $\Delta$ . That is, only the outputs of the detectors corresponding to boundaries 1 and 2 will be used, and the outputs of the other four detectors corresponding to boundaries 1', 1'', 2', and 2'' will not be used. Otherwise, after bit-by-bit synchronization at the compression and expansion buffers, 2-bit symbols\* are generated from the 4-bit symbol pairs received from the two soft-decision demodulators according to the rule provided in Table 1. This rule is essentially the maximum-likelihood (ML) rule for 4-bit symbols from both links.

Those entries in Table 1 with the letter "x" represent cases in which the ML rule would result in very uncertain decisions because of unacceptable error rates. Hence, they are "erased." When such a situation occurs, a potential error is detected and its location recorded into an "error locator"

\* The letter "x" in Table 1 is either a 0 or a 1 as determined by the algebraic decoder. Therefore, although there are three kinds of letters, 0, 1, and x in Table 1, the pairs 00, 01, 10, 0x, x0, 1x, and x1 are still considered to be 2-bit symbols.

register. For example, suppose that the 2-bit symbol 00 corresponding to the angle  $\pi/4$  has been sent and the received signal samples at the two diversity sites fall into the regions represented by 0001 and 1000, respectively. Then, it is more likely that 00 has been sent. Hence, in Table 1 the 2-bit symbol 00 is chosen. On the other hand, if 0001 and 0100 are received from the two links, it is equally probable that either the 2-bit symbol 00 or the 2-bit symbol 01 has been sent. Naturally the first bit of the transmitted 2-bit symbol is more likely to be a 0, whereas the second bit is very uncertain. Thus, it is erased and replaced by an erasure  $x$  in Table 1.

The probabilistically decoded letters of 0, 1, and  $x$  are sent to an algebraic decoder, where the erasures are replaced by either a 1 or a 0. Whenever any replacements cause the codec to decode meaning parity checks, these replaced bits are considered to be the correct bits since the bit stream with this particular replacement becomes a code word.

Without loss of generality, suppose that the  $C/N$ s in both links are below  $\Delta$ , that (00 00 00 00 00 00 00 00 00 00) is the sequence of 2-bit symbols transmitted as a result of separately encoding the odd and even bits of the 18-bit message sequence (000000000000000000) with a rate-9/10 single parity check code, and that (0100 0000 0000 0000 0000 0100 0001 0010 0000 0010) and (0001 0000 0000 0000 0000 0010 1000 0011 0000 1000) are the 4-bit symbols received from soft-decision modems A and B, respectively. Then, from Table 1, the probabilistically decoded symbols are (0x 00 00 00 00 00 00 00 00 x0). In other words, the odd and even bit sequences are (000000000x) and (x000000000), respectively. If these two sequences are sent into the algebraic decoder, which in this case simply performs parity checking, the decoder easily determines that (00 00 00 00 00 00 00 00 00 00) is the transmitted sequence and (000000000000000000) is the 18-bit message sequence.

Note that, if the hard-decision demodulator were used instead of the soft-decision demodulator, the sequences (01 00 00 00 00 01 00 00 00 00) and (00 00 00 00 00 00 10 00 00 10) would be received from receivers A and B, respectively. In this case both the odd and even bit sequences would have two bits in error and the high-efficiency, rate-9/10, single parity check code simply could not detect any of the errors. On the other hand, the DIVEC scheme, with soft decision and probabilistic decoding, could correct these errors simply with a single parity check code.

The quantitative performance of a dual diversity DIVEC scheme will be analyzed in a subsequent section, where it will be shown that DIVEC can reduce the required system margin of the TDMA system.

### Triple diversity

#### UP-LINK STRATEGY

As in the dual diversity case, the carrier-to-noise ratios of the TDMA looped back signals for frame synchronization and the "decision feedback information" from the destination stations can be utilized to rank the three available up-links (see Figure 3a). The best link can be selected at the command of the control logic to transmit TDMA bursts under normal operation. However, if the best link has an attenuation higher than a certain threshold  $T_2$ , the other two links are compared. If the other two are clearly higher, the best link is chosen by the control logic. If the other two are not clearly much higher, however, the bursts are transmitted alternately between the better two or among the three.

For example, if all three links are worse than  $T_2$ , but at least two links are better than another threshold  $T_4$  ( $T_4 > T_2$ ) so that initial acquisition and burst synchronization are still achievable, then the series of bursts 1, 2, 3, 4, 5, . . . is transmitted as follows: (1,A), (2,B), (3,C), (4,A), (5,B), etc., or (1,A), (2,A), (3,B), (4,B), (5,C), (6,C), (7,A), (8,A), etc., where the notation ( $i,L$ ) denotes that the burst number  $i$  is transmitted via link  $L$ . When any link becomes better than threshold  $T_2$ , this link is chosen for transmission. If all three links are higher than  $T_2$  and only one link is lower than  $T_4$ , this better link will be selected unless the majority of the destination stations tell the source station to select a particular link. If all three links are higher than  $T_4$ , then an outage is encountered.

#### DOWN-LINK STRATEGY

The received signals from the three diversity sites are coherently and separately detected into the baseband by a hard-decision demodulator (although soft-decision demodulators may also be used). The three baseband bursts can be synchronized bit by bit with compression and expansion buffers. Suppose that all three links are reliable or unreliable, as defined by the probabilistic and algebraic error counts in Figure 3b. Then the resultant output bit from the buffer is chosen to be the same as the majority of the three bits at the same location in these three bursts. That is, if (1, 0, 1) is the snap shot of the three bursts in the buffers at the  $i$ th instant, than 1 is assumed to be the bit that was transmitted since 1 is more probable than 0. This resultant burst is compared with the burst from each individual link and the disagreements are counted. For example, if (0111000), (0100111), and (0010110) are the received bursts from links

A, B, and C, respectively, the resultant burst is (0110110). The number of disagreements between the resultant burst and those from A, B, and C are 3, 2, and 1, respectively. Therefore, link A is worse than B and C. If this error count is tracked for each link, the quality of the transmission channels in the three down-links can be monitored. (Of course, the overall C/N can also be monitored.)

The resultant burst is sent to an algebraic decoder for error detection or correction. Meanwhile each burst from the three individual links is also algebraically decoded by its associated decoders, and the number of detected errors or corrected errors is counted (Figure 3). These error counts plus the error counts resulting from the probabilistic decoding described in the preceding paragraph can determine whether the resultant burst is reliable and whether a particular link is reliable.

When two of the three links are considered to be unreliable, only the output of the remaining link will be chosen. The burst from this link will be taken as the resultant burst. This mode of operation is maintained either until the algebraic decoder greatly exceeds its supposed detection/correction capability indicated by the error detectability/correctability of the algebraic code or until another link becomes reliable again. In either case, the mode of operation is switched back to normal. That is, instead of using the output of one link only, the outputs of all three links will be utilized and probabilistic majority decoding will be resumed.

If all three links are unreliable and if the algebraic decoder for the resultant burst fails to decode (i.e., if it exceeds its detection/correction capability), then the raw information bits at the output of the probabilistic decoder will be taken as the final output bit stream. The bit stream from the algebraic decoder will not be taken as the final output bit stream since the decoder fails to decode.

Prior to the analysis of the performance of the DIVEC scheme for dual and triple diversity, it should be noted that diversity may not be needed at every earth station in an SS/TDMA or TH/TDMA system. Depending on the precipitation statistics at given locations, no diversity, dual diversity, or triple diversity may be needed, and the proposed DIVEC scheme is clearly compatible with any situation. Thus, the DIVEC scheme will work for any of the eight possible combinations of earth station diversity usage listed in Table 2.

TABLE 2. POSSIBLE COMBINATIONS OF EARTH STATION DIVERSITY USAGE IN TDMA SYSTEMS

DOWN-LINK \ UP-LINK	NO DIVERSITY, 1	DUAL DIVERSITY, 2	TRIPLE DIVERSITY, 3
NO DIVERSITY, 1	DIVEC NOT NEEDED	1 → 2	1 → 3
DUAL DIVERSITY, 2	2 → 1	2 → 2	2 → 3
TRIPLE DIVERSITY, 3	3 → 1	3 → 2	3 → 3

### Performance Analysis

A mathematically rigorous analysis of the DIVEC scheme is impossible at this stage because it involves the solution of two fundamental unsolved problems in communications theory. One is an error rate analysis of continuous digital transmissions over an arbitrary nonlinear channel with intersymbol interference, multiplicative noise due to fading, and additive thermal noise both before and after the arbitrary nonlinear element. The other is a performance analysis of the synchronization circuits of the digital system operated in this environment, especially when the digital system is operated in a burst mode. However, such a rigorous performance analysis is not needed to demonstrate the advantages of DIVEC over conventional diversity techniques.

#### Dual diversity

According to the strategy presented in the preceding section, it suffices to consider only the case in which the overall carrier-to-noise ratios in both links are below the previously defined threshold  $\Delta$ . Otherwise, the bit-error rate would certainly be better than  $10^{-4}$  because of the way in which

the threshold  $\Delta$  was chosen. If the various transmission losses, impairments, and margins are excluded, then it is necessary to consider only the case in which the available  $E_b/N_o$  (energy per channel bit over noise power density) in both links is below a threshold of 8.4 dB, which is the value required to achieve a  $10^{-4}$  bit-error rate [6] (see Figure 5).

Suppose that, for a given availability, the dual spatial diversity with link selection strategy in both the up-link and the down-link can provide a bit-error rate of only  $3.5 \times 10^{-3}$  with the usual 4-phase PSK hard-decision

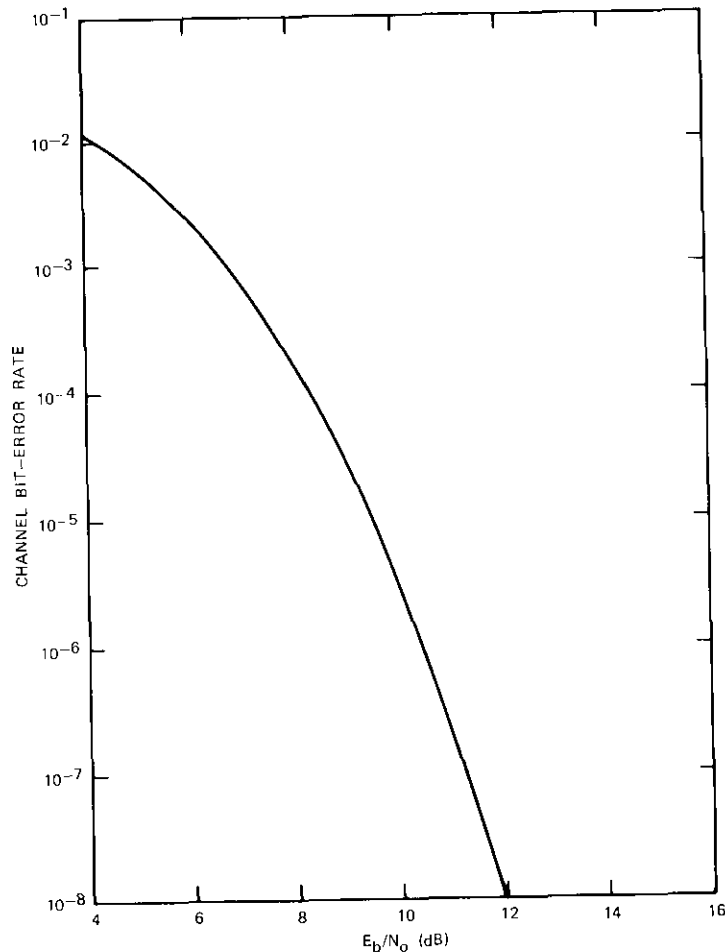


Figure 5. Channel Bit-Error Rate versus  $E_b/N_o$  for a 4-Phase PSK System

demodulator. Namely, suppose that the available  $(E_b/N_o)_1$  at the demodulator in the better path is only 5.6 dB after considering various transmission losses, impairments, and system margins (see Figure 5). Then an additional margin of  $8.4 - 5.6 = 2.8$  dB will be required to achieve a threshold bit-error rate of  $10^{-4}$ . In the following it will be shown that the dual diversity DIVEC scheme with soft decisions can provide this additional 2.8-dB system margin when fading in the two links is highly correlated.

As an example, assume that the simple single parity check code (10, 9) of rate 9/10 is used to separately encode the in-phase and quadrature-phase components of an SS/TDMA 4-phase PSK system. Then, since the transmission rate over the channel is now 10/9 times faster than it would be if no such code were being used, the available energy per transmitted channel bit over noise density is only

$$(E_{bc}/N_o)_i = (E_b/N_o)_i + \log_{10} R, \quad i = 1, 2 \quad (1)$$

where

$i$  = link number

$R$  = code rate

$(E_{bc}/N_o)_i, (E_b/N_o)_i$  = energy per channel bit over noise density in the  $i$ th link for the coded and uncoded cases, respectively.

Since  $(E_b/N_o)_1$  equals 5.6 dB and  $R$  equals 9/10, it follows from equation (1) that  $(E_{bc}/N_o)_1 = 5.1$  dB. This  $(E_{bc}/N_o)_1$  can just support a channel bit-error rate of  $5 \times 10^{-3}$ , as can be seen in Figure 5. It appears then that coding would be undesirable because  $(E_{bc}/N_o)_1$  can support a bit-error rate of only  $5 \times 10^{-3}$ , whereas  $(E_b/N_o)_1$  can support a rate of  $3.5 \times 10^{-3}$ . However, as mentioned at the beginning of this paper, diversity itself has inherent redundancy and can be viewed as a simple repetitive code. This coding structure plus the algebraic rate-9/10 single parity check code can provide an error correction capability so that the error performance can be significantly better than  $3.5 \times 10^{-3}$ .

For  $i = 1, 2$ , let

$$x_i = \frac{1}{2} \operatorname{erfc} [(1 - \delta_i) \sqrt{(E_{bc}/N_o)_i}] \quad (2)$$

$$y_i = \frac{1}{2} \operatorname{erfc} [\sqrt{(E_{bc}/N_o)_i}] \quad (3)$$

$$z_i = \frac{1}{2} \operatorname{erfc} [(1 + \delta_i) \sqrt{(E_{bc}/N_o)}] \quad (4)$$

where  $\delta_i$  is as defined by  $\delta$  in Figure 4b, and

$$\operatorname{erfc}(x) = \frac{2}{\pi} \int_x^\infty \exp(-t^2) dt. \quad (5)$$

Then, when the symbol 00 is transmitted, the following conditional probabilities of receiving the 16 possible 4-bit symbols in the  $i$ th path can be obtained:

$$\begin{aligned} p_0^i &\equiv p^i(0000|00) = (1 - x_i)^2 \\ p_1^i &\equiv p^i(0001|00) = (1 - x_i)(x_i - y_i) = p^i(0010|00) \equiv p_2^i \\ p_3^i &\equiv p^i(0011|00) = (x_i - y_i)^2 \\ p_4^i &\equiv p^i(0101|00) = z_i(1 - x_i) = p^i(1010|00) \equiv p_8^i \\ p_6^i &\equiv p^i(0100|00) = (1 - x_i)(y_i - z_i) = p^i(1000|00) \equiv p_{10}^i \\ p_8^i &\equiv p^i(0111|00) = z_i(x_i - y_i) = p^i(1011|00) \equiv p_9^i \\ p_7^i &\equiv p^i(0110|00) = (x_i - y_i)(y_i - z_i) = p^i(1001|00) \equiv p_{11}^i \\ p_{12}^i &\equiv p^i(1111|00) = z_i^2 \\ p_{13}^i &\equiv p^i(1110|00) = z_i(y_i - z_i) = p^i(1101|00) \equiv p_{14}^i \\ p_{15}^i &\equiv p^i(1100|00) = (y_i - z_i)^2 \end{aligned} \quad (6)$$

where the superscript  $i$  of  $p_j^i$  simply denotes the probability  $p_j$  in the  $i$ th link and should not be interpreted as the power of  $p_j$ . According to Table 1, the channel bit-error rate at the output of the demodulator as a result of an incorrect probabilistic decision is

$$\begin{aligned} p &= p_1^1[p_4^2 + p_6^2 + p_8^2 + 2p_{12}^2 + p_{14}^2] + p_2^1[p_4^2 + p_8^2 + p_9^2 + 2p_{12}^2 \\ &+ p_{13}^2] + p_3^1[p_4^2 + p_5^2 + p_6^2 + p_8^2 + p_9^2 + p_{10}^2 + 2p_{12}^2 + p_{13}^2 \\ &+ 2p_{14}^2] + p_4^1[p_4^2/2 + p_5^1[p_5^2 + p_6^2 + p_7^2 + p_9^2 + p_{10}^2 + p_{11}^2 + p_{12}^2 \\ &+ p_{13}^2 + p_{14}^2 + p_{15}^2] + p_5^1[p_5^2/2 + p_5^1[p_6^2 + p_7^2 + p_8^2 + p_{11}^2 + 2p_{12}^2 \\ &+ p_{13}^2 + p_{14}^2 + p_{15}^2] + p_6^1[p_6^2/2 + p_6^1[p_7^2 + p_8^2 + 2p_9^2 + p_{11}^2 + 2p_{12}^2 \\ &+ p_{13}^2 + p_{14}^2 + p_{15}^2] + p_7^1[p_7^2/2 + p_7^1[p_8^2 + p_9^2 + p_{11}^2 + 2p_{12}^2 \\ &+ p_{13}^2 + p_{14}^2 + p_{15}^2] + p_8^1[p_8^2/2 + p_8^1[p_9^2 + p_{10}^2 + p_{11}^2 + 2p_{12}^2 \\ &+ p_{13}^2 + p_{14}^2 + p_{15}^2] + p_9^1[p_9^2/2 + p_9^1[p_{10}^2 + p_{11}^2 + 2p_{12}^2 + p_{13}^2 \\ &+ p_{14}^2 + p_{15}^2] + p_{10}^1[p_{10}^2/2 + p_{10}^1[p_{11}^2 + 2p_{12}^2 + p_{13}^2 + p_{14}^2 + p_{15}^2] \\ &+ p_{12}^1[p_{12}^2/2 + p_{12}^1[2p_{13}^2 + 2p_{14}^2 + 2p_{15}^2] + p_{13}^1[p_{13}^2 + p_{14}^2 + 2p_{15}^2] \\ &+ p_{14}^1[p_{14}^2/2 + p_{14}^1[p_{15}^2 + p_{15}^2]. \end{aligned} \quad (7)$$

$$\begin{aligned} &+ 2p_{13}^2 + p_{14}^2 + p_{15}^2] + p_7^1[p_7^2/2 + p_7^1[p_8^2 + p_9^2 + p_{10}^2 + 2p_{12}^2 \\ &+ 2p_{13}^2 + 2p_{14}^2 + p_{15}^2] + p_8^1[p_8^2/2 + p_8^1[p_9^2 + p_{10}^2 + p_{11}^2 + p_{12}^2 \\ &+ p_{13}^2 + p_{14}^2 + p_{15}^2] + p_9^1[p_9^2/2 + p_9^1[p_{10}^2 + p_{11}^2 + 2p_{12}^2 + p_{13}^2 \\ &+ 2p_{14}^2 + p_{15}^2] + p_{10}^1[p_{10}^2/2 + p_{10}^1[p_{11}^2 + 2p_{12}^2 + p_{13}^2 + p_{14}^2 + p_{15}^2] \\ &+ p_{12}^1[p_{12}^2/2 + p_{12}^1[2p_{13}^2 + 2p_{14}^2 + 2p_{15}^2] + p_{13}^1[p_{13}^2 + p_{14}^2 + 2p_{15}^2] \\ &+ p_{14}^1[p_{14}^2/2 + p_{14}^1[p_{15}^2 + p_{15}^2]. \end{aligned} \quad (7)$$

The channel erasure probability,  $q$ , i.e., the average probability of the  $x$ 's in Table 1, can be found in a similar fashion:

$$\begin{aligned} q &= \sum_{i=1}^4 [p_{i-1}^1(p_{i+3}^2 + p_{i+7}^2 + 2p_{i+11}^2) \\ &+ p_{i+3}^1(2p_{i+7}^2 + p_{i+11}^2) + p_{i+7}^1 p_{i+11}^2]. \end{aligned} \quad (8)$$

The channel bit-error rate,  $p$ , and the channel erasure probability,  $q$ , of equations (7) and (8) have been computed for the case in which the attenuation values in the two paths are highly correlated. That is,  $(E_{bc}/N_o)_1 \doteq (E_{bc}/N_o)_2 = E_{bc}/N_o$  and  $\delta_1 = \delta_2 = \delta$ . The results for various values of  $E_{bc}/N_o$  and  $\delta$  are plotted in Figure 6b. The corresponding equivalent discrete channel model before the decoder is the well-known erasure channel [7] shown in Figure 6a, in which  $p$  and  $q$  are as given in equations (7) and (8), respectively.

The decoder accepts a block of  $N$  letters of 0, 1, or  $x$  (in this case, 10 letters) and determines the correct  $(N - 1)$  information bits (in this case, 9 bits). If there is an  $x$  in the block of  $N$ , the decoder simply replaces it with either a 0 or a 1 and computes the parity. The decoder determines that the  $(N - 1)$  bits with the correct parity are the correct  $(N - 1)$  informa-

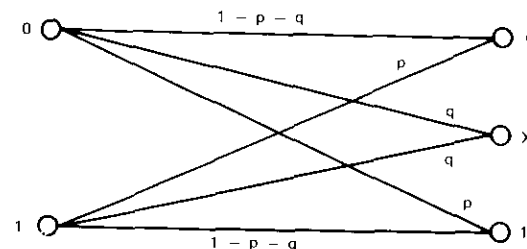


Figure 6a. Equivalent Channel Model for the Decoder

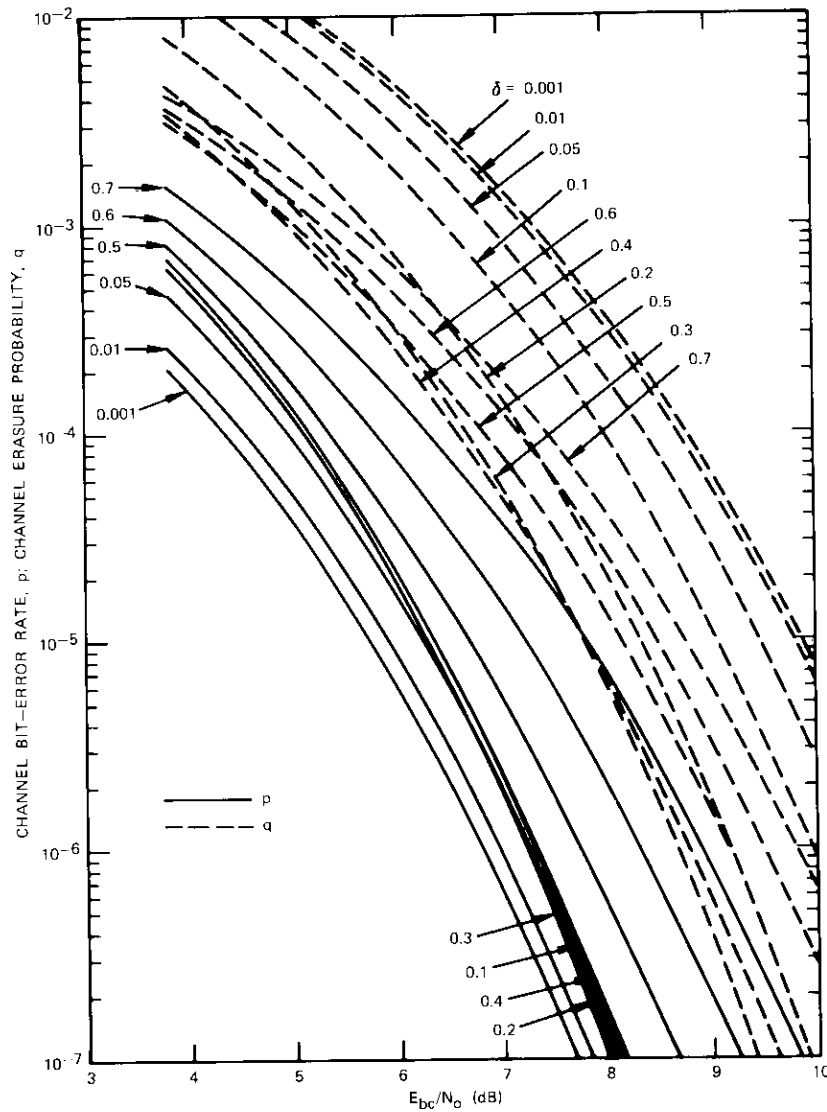


Figure 6b. Bit-Error Rate,  $p$ , and Erasure Probability,  $q$ , as Functions of  $E_{bc}/N_o$

tion bits. This decision rule will provide correct answers whenever there is only one erasure in the block of  $N$ . Therefore, the overall "coded" bit-error rate,  $P_b$ , can be found as follows:

$N \cdot P_b \equiv$  average number of erroneous bits that are not correctable by using the single parity check code in a block of length  $N$

$$\begin{aligned} &\leq \sum_{\substack{k,l \\ (k \geq 1, l > 2)}} \frac{N!}{k!l!(N-k-l)!} (k+l)p^kq^l(1-p-q)^{N-k-l} \\ &= \sum_{k,l} \frac{N!}{k!l!(N-k-l)!} (k+l)p^kq^l(1-p-q)^{N-k-l} \\ &\quad - Nq(1-p-q)^{N-1} \end{aligned} \quad (9)$$

However, from equation (A5) of Appendix A,

$$\sum_{k,l} \frac{N!}{k!l!(N-k-l)!} (k+l)p^kq^l(1-p-q)^{N-k-l} = N(p+q) \quad (10)$$

Substituting equation (10) into equation (9) yields the desired overall bit-error rate,

$$\begin{aligned} P_b &= (p+q) - q(1-p-q)^{N-1} \\ &= p + q[1 - (1-p-q)^{N-1}] \\ &= p + q[(p+q)\{1 + (p+q) + (p+q)^2 + \dots + (p+q)^{N-2}\}] \\ &\leq p + q(p+q) \min [(N-1), (1-p-q)^{-1}]. \end{aligned} \quad (11)$$

This "coded" bit-error rate has been computed and is given in Figure 7 as a function of  $E_{bc}/N_o$  with  $\delta$  as a parameter.

For a given "coded" bit-error rate,  $P_b$ , the required values of  $E_{bc}/N_o$  can be obtained from Figure 7 as functions of  $\delta$  so that the optimum  $\delta$  can be determined. For example, the values of  $E_{bc}/N_o$  required to achieve overall bit-error rates of  $10^{-4}$  and  $10^{-5}$  can be obtained from Figure 7 and are plotted in Figure 8a as functions of  $\delta$ . It can be seen that, for  $\delta$  in the range of 0.3 to 0.4, the  $E_{bc}/N_o$  required to achieve a  $10^{-4}$  overall bit-error rate is approximately 5.1 dB. If this  $E_{bc}/N_o$  is substituted into equation (1),

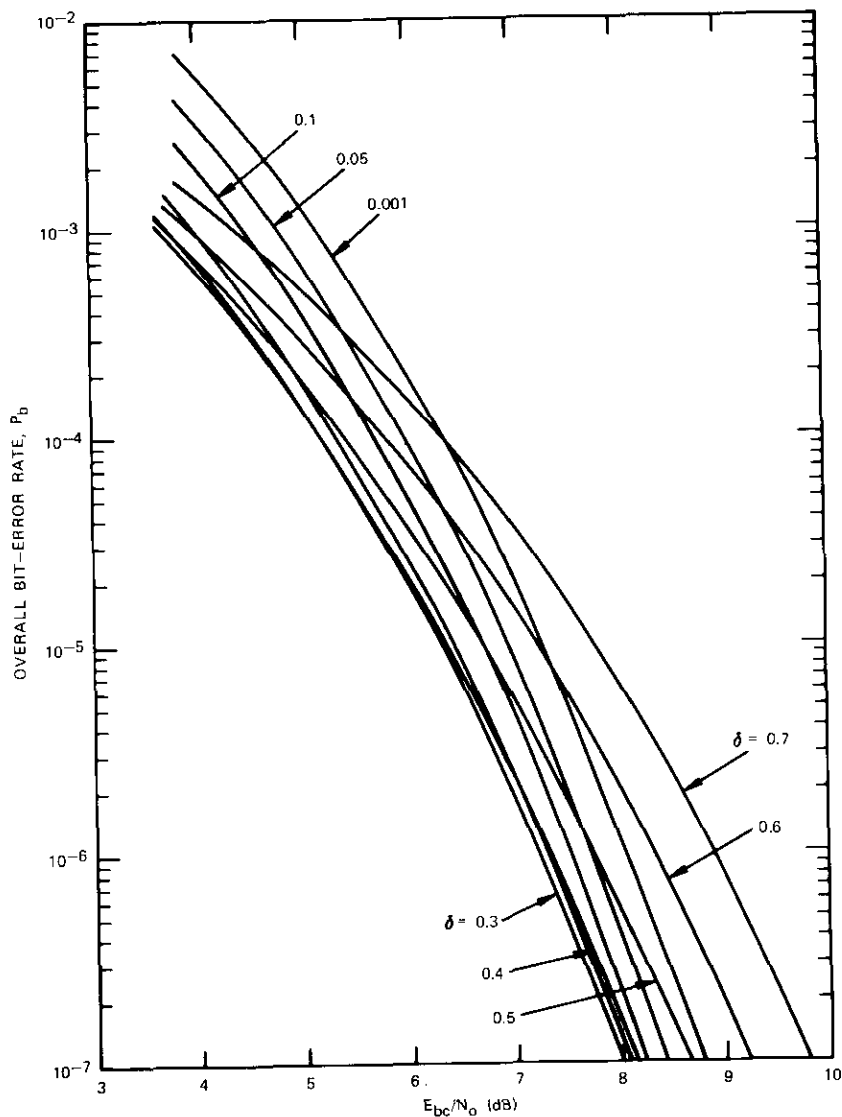


Figure 7. Coded Bit-Error Rate,  $P_b$  as a Function of  $E_{bc}/N_o$

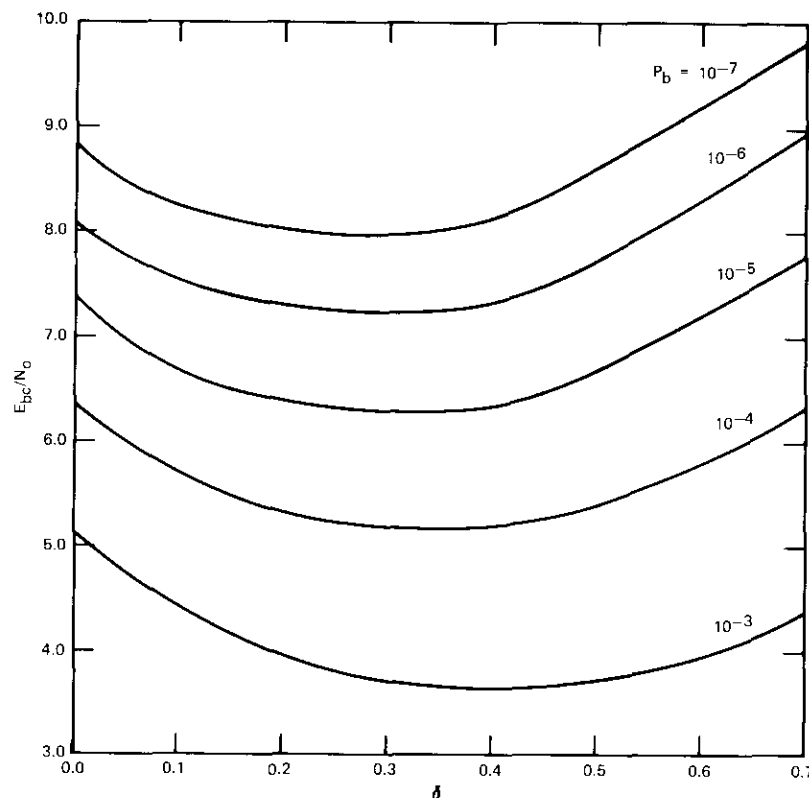


Figure 8a. Required  $E_{bc}/N_o$  as a Function of Bias,  $\delta$

it follows that an uncoded  $(E_b/N_o)_1 = (E_b/N_o)_2 = E_b/N_o$  of 5.6 dB will be sufficient to achieve an overall bit rate of  $10^{-4}$ . Hence, the system margin has been extended for at least  $8.4 - 5.6 = 2.8$  dB at an overall bit-error rate of  $10^{-4}$  by using the dual diversity DIVEC scheme with soft decisions. This margin improvement holds for all desired bit-error rates less than  $10^{-3}$ , as can be seen in Figure 8b.

Observe that, as  $\delta$  approaches zero, the required  $E_{bc}/N_o$  is about 6.4 dB. Therefore, the dual diversity DIVEC scheme with hard decisions can also improve the system margin by  $8.4 - (6.4 + 0.5) = 1.5$  dB, but not by 2.8 dB.

It should be noted that the optimal combining technique *without* coding for dual diversity can provide an improvement of no more than 3 dB\*

\* This figure should not be misinterpreted as the limit when coding is used.

over the selective combining technique. DIVEC has already achieved an improvement of more than 2.8 dB. In fact, when the number of quantization levels for soft decisions becomes large, the improvement should approach 3 dB or even more, especially if a more powerful code is used.

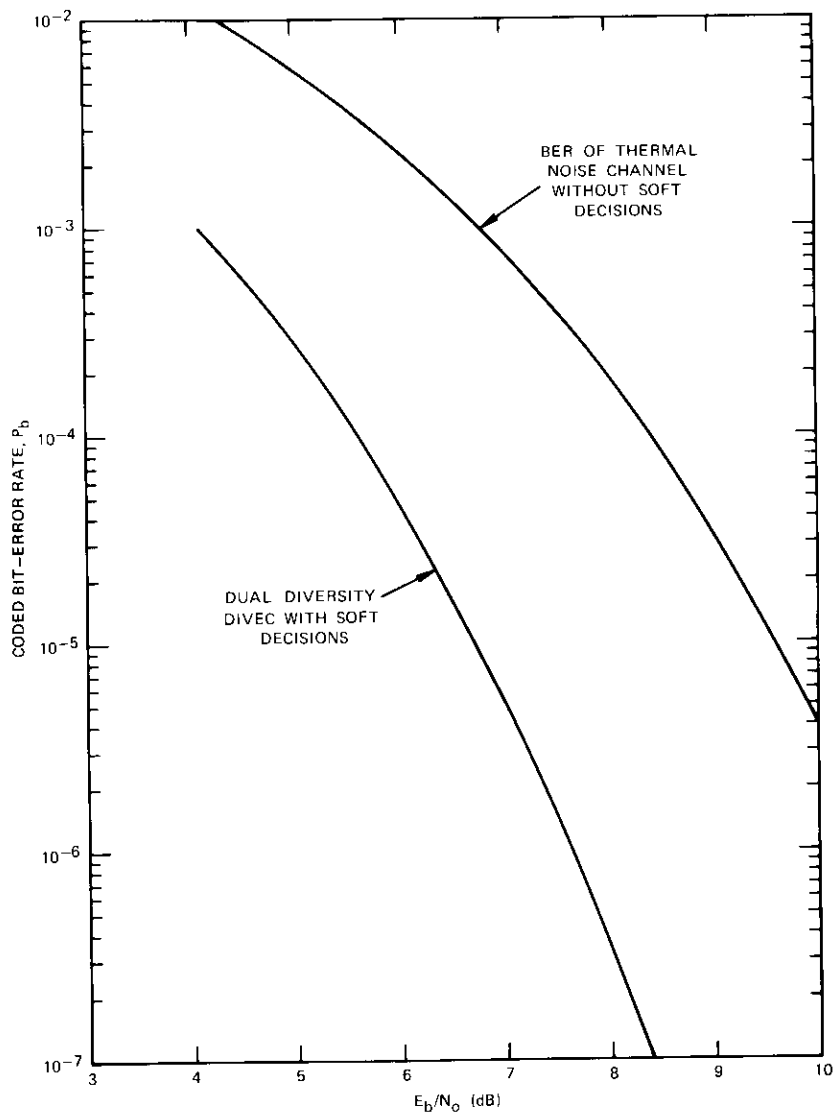


Figure 8b. Coded Bit-Error Rate vs  $E_b/N_0$ .

### Triple diversity

For a desired availability, suppose that the usual triple diversity with link selection strategy in both the up-link and the down-link can achieve a bit-error rate of only  $3 \times 10^{-3}$  by employing 4-phase PSK hard-decision modems. Then the available  $(E_b/N_0)_1$  at the demodulator in the best link is only 5.8 dB after considering various transmission losses, impairments, and system margins. Hence, an additional margin of  $8.4 - 5.8 = 2.6$  dB is needed if a threshold bit-error rate of  $10^{-4}$  is desired.

Assume that, as in the dual diversity case, the single parity check, rate-9/10, block code (10, 9) is used. Because of this coding, the available  $(E_{bc}/N_0)_1$  is then only  $5.8 + 10 \log_{10} (9/10) = 5.3$  dB instead of 5.8 dB. Clearly, the channel bit-error rate has increased from  $3 \times 10^{-3}$  to  $4.2 \times 10^{-3}$ . However, this bit-error rate can be improved to  $10^{-4}$  by using DIVEC, which exploits the inherent redundancy of triple diversity reception.

A link is defined as unreliable if its bit-error rate exceeds  $10^{-4}$ , or equivalently if the total loss including attenuation, noise, and other impairments is higher than a certain threshold. Then, according to the DIVEC scheme, when only two of the three links are unreliable the reliable link is selected and the bit-error rate in this case is certainly better than  $10^{-4}$ .

On the other hand, if all three links are unreliable or if more than one link is reliable, then according to the DIVEC scheme, majority logic bit-by-bit decoding will be used on the bit streams from all three links. Clearly if it can be shown that all three links are unreliable and yet the DIVEC scheme can achieve a bit-error rate of  $10^{-4}$ , the proof is complete since the other case has been discussed in the preceding paragraph.

Note that the DIVEC scheme with triple diversity can be viewed as a trivial rate-1/3 repetitive code. When bit-by-bit majority decoding is applied to the outputs from the three links, any single bit error can be corrected, but double or triple errors cannot. For example, if 0 is the transmitted bit and if (0, 1, 0) are the three received bits from links A, B, and C, respectively, then the majority decision is 0. Even though there is a single bit error in the bit from path B, it has been corrected by the majority decision process. On the other hand, if (0, 1, 1) or (1, 1, 1) are the received bits from links A, B, and C, respectively, then the majority decision is 1. Hence, decision errors are made in either case. Suppose that the attenuation values in the three links are fully correlated and that the additive thermal noises are independent, namely,  $(E_{bc}/N_0)_i = E_{bc}/N_0$  for  $i = 1,$

2, 3. Then, the average *channel* bit-error rate after the "probabilistic" majority decoding can be bounded from above by

$$P = 3 \times (4.2 \times 10^{-3})^2(1 - 4.2 \times 10^{-3}) + (4.2 \times 10^{-3})^3 \\ \leq 5.3 \times 10^{-5} < 10^{-4} .$$

Since the algebraic decoder is simply an error detector, it will not affect the information bit-error rate. Therefore, the bit-error rate of the decoded information bits is less than  $10^{-4}$ , and for the case of fully correlated attenuation, DIVEC can effectively reduce the margin by 2.6 dB.

### Concluding remarks

In the case of triple diversity DIVEC, only a hard-decision 4-phase PSK demodulator was used and the worst link was not discarded. If a soft-decision demodulator were used and the worst link discarded, then the bit-error rate would be improved and the performance could be improved whether or not the link attenuation values were correlated. The analysis would be similar to that in the dual diversity DIVEC case but more complicated.

Synchronization of up-link transmissions from all diversity sites is essential because burst switching is employed in the up-link. However, synchronization would not be a problem if a slow switching rate were maintained by increasing the number of bursts (or frames) between switching intervals.

The regulation of up-link power to obtain acceptable levels of cochannel interference and other impairments seems essential for any frequency reuse SS/TDMA or even TH/TDMA systems experiencing heavy fading including, of course, the applications of DIVEC. This subject warrants further study.

In this paper, performance has been analyzed only for the cases in which attenuation in the diversity links is highly correlated. Future work should include other cases. However, knowledge of the joint distribution of the attenuation in the diversity links as a function of site separation and rainfall statistics is required to more accurately assess the system margin improvement for DIVEC as opposed to conventional diversity schemes.

In the dual diversity case, a soft-decision demodulator was used to provide some "channel measurement" information with which the effectiveness of the particular code employed could be extended [8]-[11]. On the other hand, the DIVEC scheme also utilizes the "inherent redundancy"

of diversity systems to perform error control. Various applications of the concept of using the inherent redundancy of communications systems to perform error control can be found in the literature [8]-[14]. The problem of how to best combine coding, modulation, diversity, and accessing techniques for fading multiple-access channels seems to be a very promising research topic.

### Acknowledgment

The author is indebted to Drs. L. Golding and T. Muratani for stimulating discussions. The constructive criticism of Dr. P. Bargellini, Mr. R. Davis, and Dr. H. Meyerhoff during the preparation of this paper is deeply appreciated.

### References

- [1] W. Schmidt, "Satellite-Switched TDMA: Transponder-Switched or Beam-Switched," AIAA paper no. 74-460, 1974.
- [2] J. Salz and B. R. Salzberg, "Double Error Rates in Differentially Coherent Phase Systems," *IEEE Transactions on Communication Technology*, COM-12, June 1964, pp. 202-205.
- [3] T. Muratani, H. Saito, and T. Watanabe, "Control System for Diversity Transmission in a Terrestrial Station of Satellite Communication," U.S. Patent Filed, No. 329,026, February 2, 1973.
- [4] P. E. Green, "Feedback Communication Systems," *Lectures on Communication System Theory*, New York: McGraw Hill, 1961, pp. 345-368.
- [5] R. J. F. Fang, "On Coding for Channels with Feedback," Ph.D. dissertation, Report SU-SEL-68-025, Stanford University, Stanford, California, 1968 (also available from University Microfilms, Ann Arbor, Michigan).
- [6] W. R. Bennett and J. R. Davey, *Data Transmission*, New York: McGraw-Hill, 1965, p. 211.
- [7] J. M. Wozencraft and I. M. Jacobs, *Principles of Communications Engineering*, New York: Wiley, p. 401.
- [8] H. Kobayashi, "Correlation Level Coding and Maximum-Likelihood Decoding," *IEEE Transactions on Information Theory*, IT-17, No. 5, September 1971, pp. 586-594.
- [9] G. D. Forney, Jr., "Maximum Likelihood Sequence Estimation of Digital Sequences in the Presence of Intersymbol Interference," *IEEE Transactions on Information Theory*, IT-18, May 1972, pp. 363-378.
- [10] D. Chase, "A Class of Algorithms for Decoding Block Codes with Channel

Measurement Information," *IEEE Transactions on Information Theory*, IT-18, No. 1, January 1972, pp. 170-182.

- [11] D. Chase, "A Combined Coding and Modulation Approach for Communication over Dispersive Channels," *IEEE Transactions on Communication Technology*, COM-21, No. 3, March 1973, pp. 159-174.
- [12] S. Browne, P. J. Bartholome, and I. Vogt, "VHF Communications: New Design Concepts and Experimental Results," NATO SHAPE Air Defence Technical Centre, Den Haag, the Netherlands, Technical Memorandum TM-56, June 1963.
- [13] H. Kobayashi, "Application of Probabilistic Decoding to Digital Magnetic Recording Systems," *IBM Journal of Research and Development*, Vol. 15, January 1971, pp. 64-71.
- [14] G. D. Forney, Jr., "Error Correction for Partial Response Modems," *1970 International Symposium on Information Theory*, Noordwijk, the Netherlands, June 15-19, 1970.

### Appendix A. Derivation of equation (10)

The quantity

$$\sum_{k,l} \frac{N!}{k!l!(N-k-l)!} (k+l) p^k q^l (1-p-q)^{N-k-l} \quad (\text{A1})$$

can be interpreted as the expected value of  $(x+y)$ , where  $x$  and  $y$  are multinomial random variables according to the following probability mass function [A1]:

$$\frac{N!}{x!y!(N-x-y)!} p^x q^y (1-p-q)^{N-x-y} \quad (\text{A2})$$

Note that

$$[(1-p-q) + sp + tq]^N = \sum_{k,l} \frac{N!}{k!l!(N-k-l)!} \cdot p^k q^l (1-p-q)^{N-k-l} s^k t^l \quad (\text{A3})$$

It follows by differentiating both sides of equation (A3) with respect to  $s$  and  $t$  separately and adding them together that

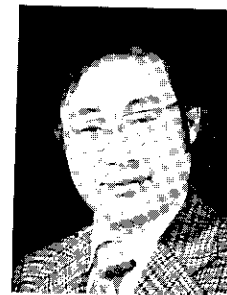
$$N[(1-p-q) + sp + tq]^{N-1} (p+q) = \sum_{k,l} \frac{N!}{k!l!(N-k-l)!} p^k q^l (1-p-q)^{N-k-l} (ks^{k-1} + lt^{l-1}) \quad (\text{A4})$$

Setting  $s$  and  $t$  equal to unity immediately yields the desired equation (10):

$$N(p+q) = \sum_{k,l} \frac{N!}{k!l!(N-k-l)!} (k+l) p^k q^l (1-p-q)^{N-k-l} \quad (\text{A5})$$

### Reference

- [A1] S. S. Wilks, *Mathematical Statistics*, New York: Wiley, 1962, p. 139.



Russell J. F. Fang is Manager, Communications Systems Analysis Department at COMSAT Laboratories, where he is engaged in research on advanced transmission systems for satellite communications, networking via satellites, and signal processing. Born in Chungking, China, he received a B.S. in electrical engineering from the National Taiwan University (1962), M.S. and Ph.D. in electrical engineering from Stanford University (1964 and 1968). Before joining COMSAT in 1968, Dr. Fang was employed by Stanford Electronics Laboratories (1965-1968), Stanford Research Institute (1964-1965), and the Chinese Air Force Electronics and Ordnance Division, Taiwan (1962-1963). He is a member of the IEEE.

# ***Attenuation and phase shift of microwaves due to canted raindrops***

D. J. FANG

(Manuscript received January 2, 1975)

## ***Abstract***

This paper discusses the results of a quantitative estimation of changes in propagation parameters, i.e., attenuation and phase shift, due to the canting of raindrops for both horizontal and vertical polarizations. These results show that the difference in propagation behavior between satellite-earth paths (i.e., slant paths) and terrestrial paths is significant if raindrops are canted. In many cases, the canting effect produces large amplitude and phase variations which are important even for propagation studies concerning a single polarized transmitter-receiver channel.

## ***Introduction***

It is known that raindrops are usually tilted with respect to the local vertical. The tilting is random in the case of light precipitation. In heavy rainstorms, however, the wind and turbulence will in many instances cause the raindrops to tilt collectively, on an averaged basis, toward a preferred direction. This is called canting.

The parameter that describes the statistics of canting is the canting angle distribution. A few attempts were made to determine the parameter by photographing the raindrops under various meteorological and experimental conditions. However, only one study, based on observations

of 463 raindrops in two different storms, is known to have resulted in a postulated distribution [1]. In the absence of definitive information and to simplify the model, researchers [2]-[4] have assumed a unique direction distribution for performing first-order studies of canting.

In studies of centimeter and millimeter waves propagating through hydrometeors, the effect of canting is usually considered only in assessing the depolarization. Analyses [1]-[4] have been made by modeling a terrestrial propagation path in the presence of raindrops tilting in a vertical plane perpendicular to the path in the belief that such a model would yield the greatest variations in amplitude and phase for the two linear orthogonally polarized channels.

The purpose of this paper is to study the effect of canting angles on propagation characteristics in a more general sense. It is intended to show that the canting effect results in amplitude and phase variations which in turn cause fading and depolarization in turbulent rainstorms. This is particularly true of satellite-earth propagation, for which the effect of canting angles differs significantly from that of the terrestrial case.

**General approach for uncanted raindrops**

The geometry for forward scattering analysis of an uncanted single raindrop is shown in Figure 1a. The axis of symmetry of the drop is denoted as  $\vec{i}_c$ , which is aligned along the vertical axis  $z$ . The  $x$  axis is chosen so that the incident wave normal lies in the  $x$ - $z$  plane, making an angle  $\psi$  with the  $z$  axis. The unit vector for wave propagation  $\vec{i}_k$  is given by

$$\vec{i}_k = -\vec{i}_z \cos \psi - \vec{i}_x \sin \psi \quad (1)$$

A general incident wave field,  $\vec{E}_o$ , is treated as a vector combination of horizontally and vertically polarized fields  $\vec{E}_H$  and  $\vec{E}_V$ . The sense of polarization is such that the respective unit vectors  $\vec{i}_H$  and  $\vec{i}_V$  are specified by

$$\vec{i}_H = \vec{i}_y \quad (2a)$$

$$\vec{i}_V = -\vec{i}_z \cos \psi + \vec{i}_x \sin \psi \quad (2b)$$

The scattering amplitudes  $f_H(\psi)$  and  $f_V(\psi)$ , shown in Figure 1a, have been the subject of many extensive analytical and numerical studies [5]-[9]. Tabulations for selected frequencies are available, almost all at  $\psi = 90^\circ$ .

The total forward scattering field at  $r \rightarrow \infty$  due to the many drops

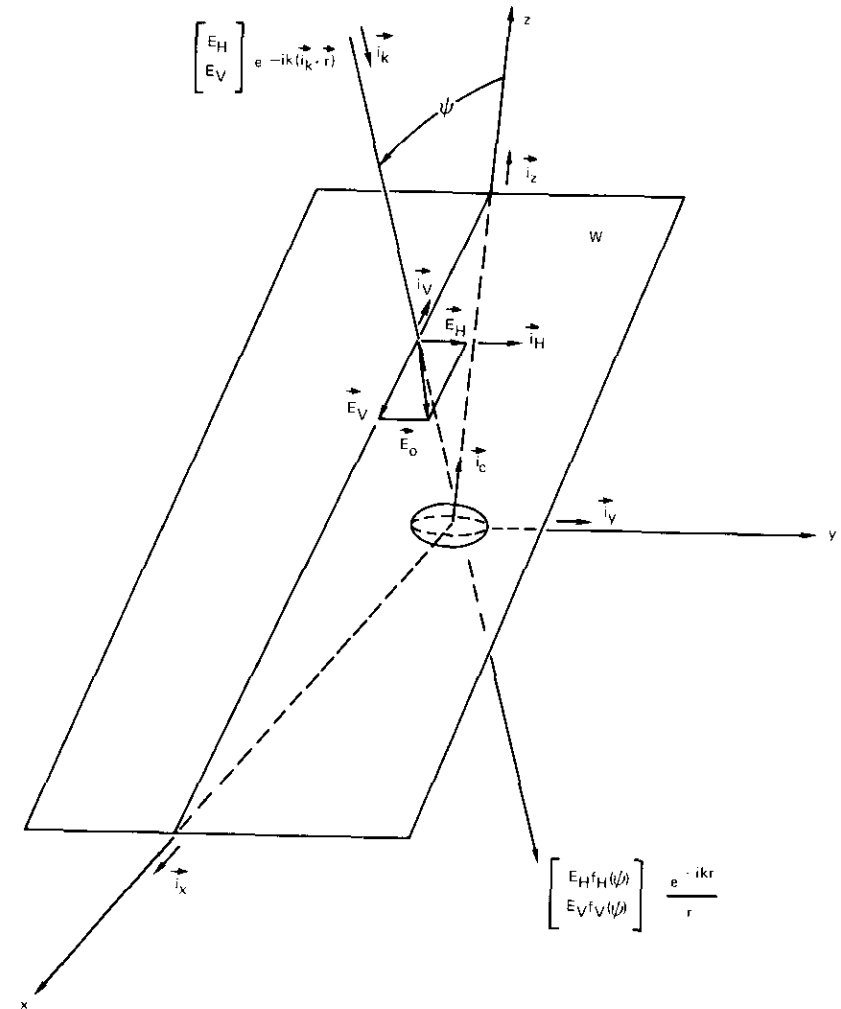


Figure 1a. Geometry for a Plane Wave Penetrating a Raindrop: Uncanted Drop with Its Symmetric Axis ( $\vec{i}_c$ ) Aligned along the Vertical Axis (A general incident field  $\vec{E}_o$  can be decomposed into horizontally and vertically polarized fields  $\vec{E}_H$  and  $\vec{E}_V$  for separate forward scattering analysis.)

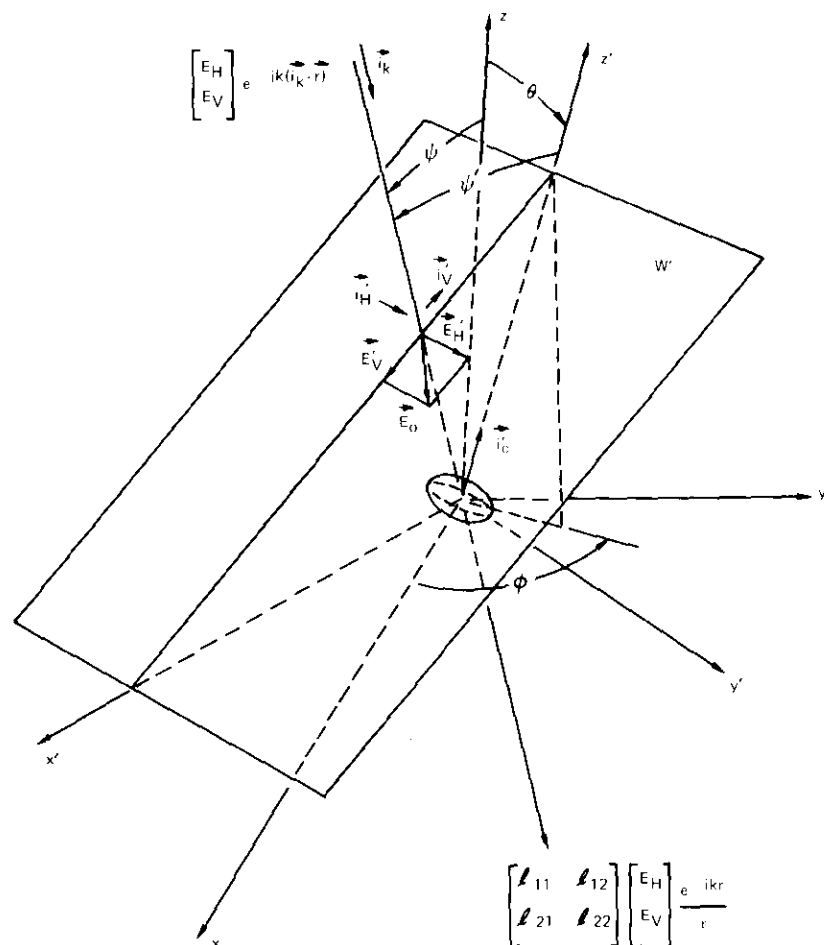


Figure 1b. Geometry for a Plane Wave Penetrating a Raindrop: Canted Drop with  $\vec{i}_c$  Making  $\theta$  and  $\phi$  Polar Angles with Respect to the Original Coordinates (Forward scattering analysis can be made via  $\vec{E}'_H$  and  $\vec{E}'_V$ ).

which constitute an actual rain cloud is usually evaluated by assuming that the cloud is a stratified layer with a uniform spatial drop distribution. The concept of Fresnel zone diffraction across a thin layer is then applied [10], [11] to convert the spherical wave factors  $f_{H,V}(1/r) e^{-ikr}$  into equivalent plane wave factors  $e^{-ik_{H,V}r}$ , where

$$K_H(\psi) = k + \frac{2\pi}{k} \int f_H(\psi) n(a) da \quad (3a)$$

$$K_V(\psi) = k + \frac{2\pi}{k} \int f_V(\psi) n(a) da \quad (3b)$$

and  $n(a) da$  is the number of drops in a unit volume with radii, corresponding to an equivalent spherical volume, lying between  $a$  and  $a + da$ . Equivalent wave numbers  $K_H$  and  $K_V$  are complex numbers containing negative imaginary parts. It follows that

$$A_H(\psi) = 8.686 \text{Im}[K_H(\psi)] \quad (4a)$$

$$A_V(\psi) = 8.686 \text{Im}[K_V(\psi)] \quad (4b)$$

$$\Phi_H(\psi) = \frac{180}{\pi} \text{Re}[K_H(\psi)] \quad (5a)$$

$$\Phi_V(\psi) = \frac{180}{\pi} \text{Re}[K_V(\psi)] \quad (5b)$$

where  $A$  is the attenuation in dB/km and  $\Phi$  is the phase shift in deg/km. Again, for  $\psi = 90^\circ$ , values of  $A_H$ ,  $A_V$ ,  $\Phi_H$ , and  $\Phi_V$  are tabulated for selected frequencies in the literature [4]-[8]. Values of  $A$  and  $\Phi$  for  $\psi \neq 90^\circ$  are rarely available.

### Modified approach for canted raindrops

As shown in Figure 1b, for a single raindrop canted so that its axis of symmetry,  $\vec{i}_c$ , makes canting angles  $\theta$  and  $\phi$  with respect to the original  $x$ - $y$ - $z$  coordinates, a new coordinate system  $x'$ - $y'$ - $z'$  can be established. The general approach described in the preceding section can be duplicated in the primed system after the incident field is resolved into vectors  $\vec{E}'_H$  and  $\vec{E}'_V$  along the directions specified by unit vectors:

$$\begin{aligned}\vec{i}_H' &= \vec{i}_V' \\ &= \frac{1}{\sin \psi'} [\vec{i}_z \sin \theta \sin \phi \cos \psi \\ &\quad + \vec{i}_y (\cos \theta \sin \psi - \sin \theta \cos \phi \cos \psi') \\ &\quad - \vec{i}_z \sin \theta \sin \phi \sin \psi] \quad (6)\end{aligned}$$

$$\begin{aligned}-\vec{i}_V' &= -\vec{i}_z \cos \psi' + \vec{i}_z' \sin \psi' \\ &= \frac{1}{\sin \psi'} [\vec{i}_z \cos \psi (\cos \psi \sin \theta \cos \phi - \sin \psi \cos \theta) \\ &\quad + \vec{i}_y \sin \theta \sin \phi \\ &\quad - \vec{i}_z \sin \psi (\cos \psi \sin \theta \cos \phi - \sin \psi \cos \theta)] \quad (7)\end{aligned}$$

where  $\psi'$  is such that  $\cos \psi' = \sin \psi \sin \theta \cos \phi + \cos \psi \cos \theta$ . It follows that the scattering field at  $r \rightarrow \infty$  along the  $\vec{i}_H'$  and  $\vec{i}_V'$  directions is given by

$$\frac{1}{r} e^{-ikr} \begin{bmatrix} E_H' f_H(\psi') \\ E_V' f_V(\psi') \end{bmatrix} = \frac{1}{r} e^{-ikr} \begin{bmatrix} f_H(\psi') & 0 \\ 0 & f_V(\psi') \end{bmatrix} \begin{bmatrix} \vec{i}_H \cdot \vec{i}_H' & \vec{i}_H \cdot \vec{i}_V' \\ \vec{i}_V \cdot \vec{i}_H' & \vec{i}_V \cdot \vec{i}_V' \end{bmatrix} \begin{bmatrix} E_H \\ E_V \end{bmatrix} \quad (8)$$

To obtain the scattering field resolved along the original  $\vec{i}_H$  and  $\vec{i}_V$  directions, one more rotation is required. The required rotation matrix,  $[J]$ , given in Figure 1b, is

$$\begin{aligned}[J] &= \begin{bmatrix} \vec{i}_H \cdot \vec{i}_H' & \vec{i}_H \cdot \vec{i}_V' \\ \vec{i}_V \cdot \vec{i}_H' & \vec{i}_V \cdot \vec{i}_V' \end{bmatrix} \begin{bmatrix} f_H(\psi') & 0 \\ 0 & f_V(\psi') \end{bmatrix} \begin{bmatrix} \vec{i}_H \cdot \vec{i}_H' & \vec{i}_H \cdot \vec{i}_V' \\ \vec{i}_V \cdot \vec{i}_H' & \vec{i}_V \cdot \vec{i}_V' \end{bmatrix} \\ &= \begin{bmatrix} f_H(\psi') & 0 \\ 0 & f_V(\psi') \end{bmatrix} + [f_H(\psi') - f_V(\psi')] \frac{\sin^2 \theta \sin^2 \phi}{\sin^2 \psi'} \begin{bmatrix} -1 & 0 \\ 0 & 1 \end{bmatrix} \\ &\quad - [f_H(\psi) - f_V(\psi')] \frac{\sin \theta \sin \phi}{\sin^2 \psi'} \\ &\quad \cdot (\sin \psi \cos \theta - \cos \psi \sin \theta \cos \phi) \begin{bmatrix} 0 & 1 \\ 1 & 0 \end{bmatrix} \quad (9)\end{aligned}$$

As indicated in equation (9), canting contributes three different effects:

- the change of effective zenith angle from  $\psi$  to  $\psi'$  given in the first matrix,
- the change of effective spheroidicity given in the second matrix,
- the cross-polarization effect which is evident as a result of the off-diagonal terms in the third matrix.

The changes in attenuation and phase shift for a canted drop with respect to an uncanted drop are due to effects *a* and *b*. Consider a single linearly copolarized transmitter and receiver pair transmitting and receiving electromagnetic waves penetrating through a rain cloud containing canted raindrops. The equivalent plane wave number, either  $K_H'$  for horizontal polarization or  $K_V'$  for vertical polarization, is given by

$$K_H' = k + \frac{2\pi}{k} \int \left\{ f_H(\psi) + [f_H(\psi') - f_H(\psi)] - [f_H(\psi') - f_V(\psi')] \right. \\ \left. \cdot \frac{\sin^2 \theta \sin^2 \phi}{\sin^2 \psi'} \right\} n(a) P_a(\theta, \phi) da d\theta d\phi \quad (10a)$$

$$K_V' = k + \frac{2\pi}{k} \int \left\{ f_V(\psi) + [f_V(\psi') - f_V(\psi)] + [f_H(\psi') - f_V(\psi')] \right. \\ \left. \cdot \frac{\sin^2 \theta \sin^2 \phi}{\sin^2 \psi'} \right\} n(a) P_a(\theta, \phi) da d\theta d\phi \quad (10b)$$

where  $P_a(\theta, \phi)$  is the canting angle distribution function for canting at  $\theta$  and  $\phi$  at equivolumic drop radius  $a$ . The changes in wave numbers  $K_H' - K_H$  and  $K_V' - K_V$  due to a rain cloud containing canted drops are therefore

$$\Delta K_H = \frac{2\pi}{k} \int \left\{ f_H(\psi') - f_H(\psi) - [f_H(\psi') - f_V(\psi')] \frac{\sin^2 \theta \sin^2 \phi}{\sin^2 \psi'} \right\} \\ \cdot n(a) P_a(\theta, \phi) da d\theta d\phi \quad (11a)$$

$$\Delta K_V = \frac{2\pi}{k} \int \left\{ f_V(\psi') - f_V(\psi) + [f_H(\psi') - f_V(\psi')] \frac{\sin^2 \theta \sin^2 \phi}{\sin^2 \psi'} \right\} \\ \cdot n(a) P_a(\theta, \phi) da d\theta d\phi \quad (11b)$$

If  $P_a(\theta, \phi)$  is independent of  $a$ , this equation can be simplified to yield

$$\Delta K_H = \int \left\{ K_H(\psi') - K_H(\psi) - [K_H(\psi') - K_V(\psi')] \frac{\sin^2 \theta \sin^2 \phi}{\sin^2 \psi'} \right\} \\ \cdot P_a(\theta, \phi) d\theta d\phi \quad (11c)$$

$$\Delta K_V = \int \left\{ K_V(\psi') - K_V(\psi) + [K_H(\psi') - K_V(\psi')] \frac{\sin^2 \theta \sin^2 \phi}{\sin^2 \psi'} \right\} \cdot P_a(\theta, \phi) d\theta d\phi \quad (11d)$$

and the changes in attenuation and phase shift are

$$\Delta A_H(\psi) = 8.686 \operatorname{Im}(\Delta K_H) \quad (12a)$$

$$\Delta A_V(\psi) = 8.686 \operatorname{Im}(\Delta K_V) \quad (12b)$$

$$\Delta \Phi_H(\psi) = \frac{180}{\pi} \operatorname{Re}(\Delta K_H) \quad (13a)$$

$$\Delta \Phi_V(\psi) = \frac{180}{\pi} \operatorname{Re}(\Delta K_V) \quad (13b)$$

Equations (11) through (13) are the definitive equations relating propagation parameters to the canting angle distribution. Once density function  $P_a(\theta, \phi)$  and scattering amplitude functions  $f_H$  and  $f_V$  at  $\psi \neq 90^\circ$  become available, propagation parameters can be readily evaluated.

### **First-order estimation of attenuation and phase shift based on values of $\psi = 90^\circ$**

A first-order estimation of the changes in attenuation and phase shift can be made on the basis of the following assumptions:

- Raindrops are canted only along a single direction so that the  $P_a(\theta, \phi) d\theta d\phi$  integration can be disregarded.
- The  $A_H$ ,  $A_V$ ,  $\Phi_H$ , and  $\Phi_V$  values for uncanted raindrops can be modeled as

$$A_H(\psi) = U(\psi) A_S + \frac{1}{2} [A_H(90) - A_V(90)] \sin^2 \psi \quad (14a)$$

$$A_V(\psi) = U(\psi) A_S - \frac{1}{2} [A_H(90) - A_V(90)] \sin^2 \psi \quad (14b)$$

$$\Phi_H(\psi) = V(\psi) \Phi_S + \frac{1}{2} [\Phi_H(90) - \Phi_V(90)] \sin^2 \psi \quad (15a)$$

$$\Phi_V(\psi) = V(\psi) \Phi_S - \frac{1}{2} [\Phi_H(90) - \Phi_V(90)] \sin^2 \psi \quad (15b)$$

with the following boundary conditions:

$$U(0) = V(0) = 1 \quad (16)$$

$$U(90) = \frac{1}{2A_S} [A_H(90) + A_V(90)] \quad (17)$$

$$V(90) = \frac{1}{2\Phi_S} [\Phi_H(90) + \Phi_V(90)] \quad (18)$$

Assumption *a* is based on the common supposition that a rain cloud containing canted raindrops should show an average effective canting direction which can be specified by polar angles  $\theta$  and  $\phi$ . Assumption *b*, which is simply a scaling approach with scale factors  $U(\psi)$  and  $V(\psi)$ , is necessary because values of  $f_H$  and  $f_V$  at  $\psi \neq 90^\circ$  are generally not available. At  $\psi = 0$ , values of  $A_H$  and  $A_V$  and  $\Phi_H$  and  $\Phi_V$  should be identical to the values for spherical drops, i.e.,  $A_S$  and  $\Phi_S$ , respectively. For  $\psi$  between  $0^\circ$  and  $90^\circ$ , the difference between  $A_H - A_V$  and between  $\Phi_H - \Phi_V$  should be proportional to  $\sin^2 \psi$  with proportionality constants equal to  $A_H(90) - A_V(90)$  and  $\Phi_H(90) - \Phi_V(90)$ , respectively [4], [12].

The simplest scaling of  $U$  and  $V$  is linear. From the data available at 4, 6, 11, 15, and 30 GHz [13], it can be shown that the frequency dependence of  $U$  and  $V$  is not significant, that

$$U(\psi) = \frac{1}{90} [U(90) - U(0)] \psi + U(0) \simeq 1 \quad (19)$$

and that

$$V(\psi) = \frac{1}{90} [V(90) - V(0)] \psi + V(0) \simeq 1 - \frac{1}{9} \times 10^{-2} \psi \quad (20)$$

are good approximations of the behavior of  $A$  and  $\Phi$  as functions of  $\psi$ . Representative curves are shown in Figure 2.

It is now possible to evaluate  $\Delta A$  and  $\Delta \Phi$ . The final equations are

$$\Delta A_H(\psi) = [A_H(90) - A_V(90)] D(\theta, \phi, \psi) \quad (21a)$$

$$\Delta A_V(\psi) = -[A_H(90) - A_V(90)] D(\theta, \phi, \psi) \quad (21b)$$

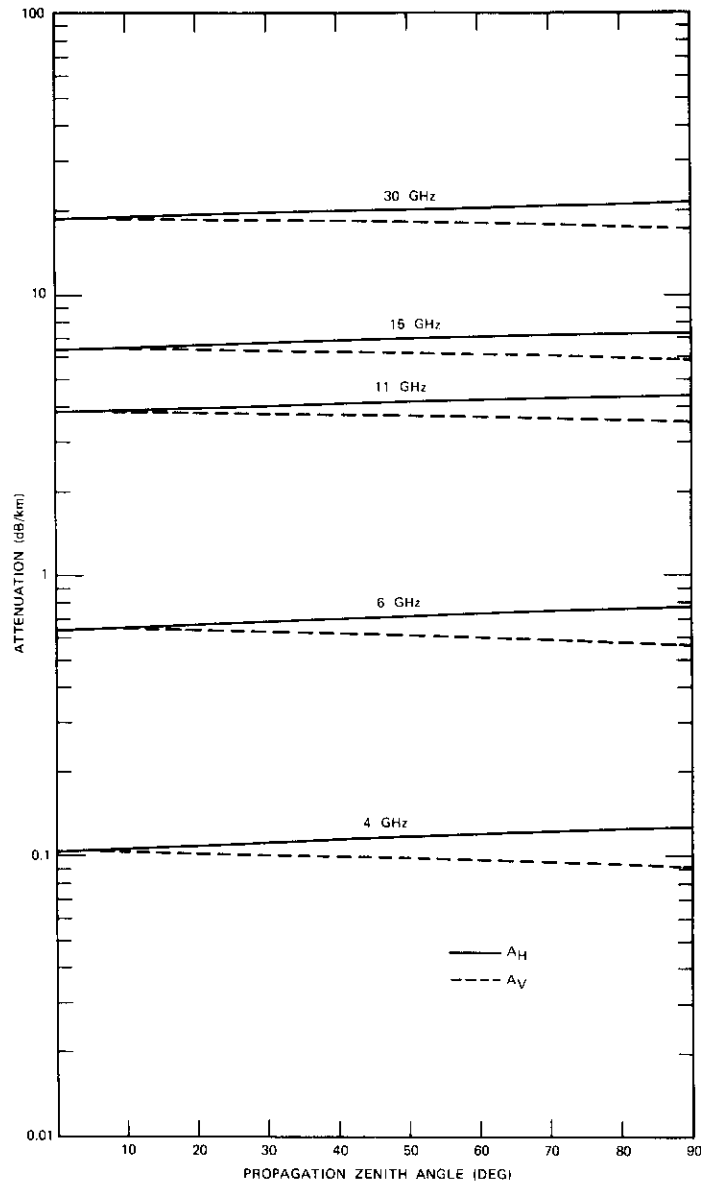


Figure 2. Linear Scaling of Attenuation and Phase Shifts versus Zenith Angle,  $\psi$

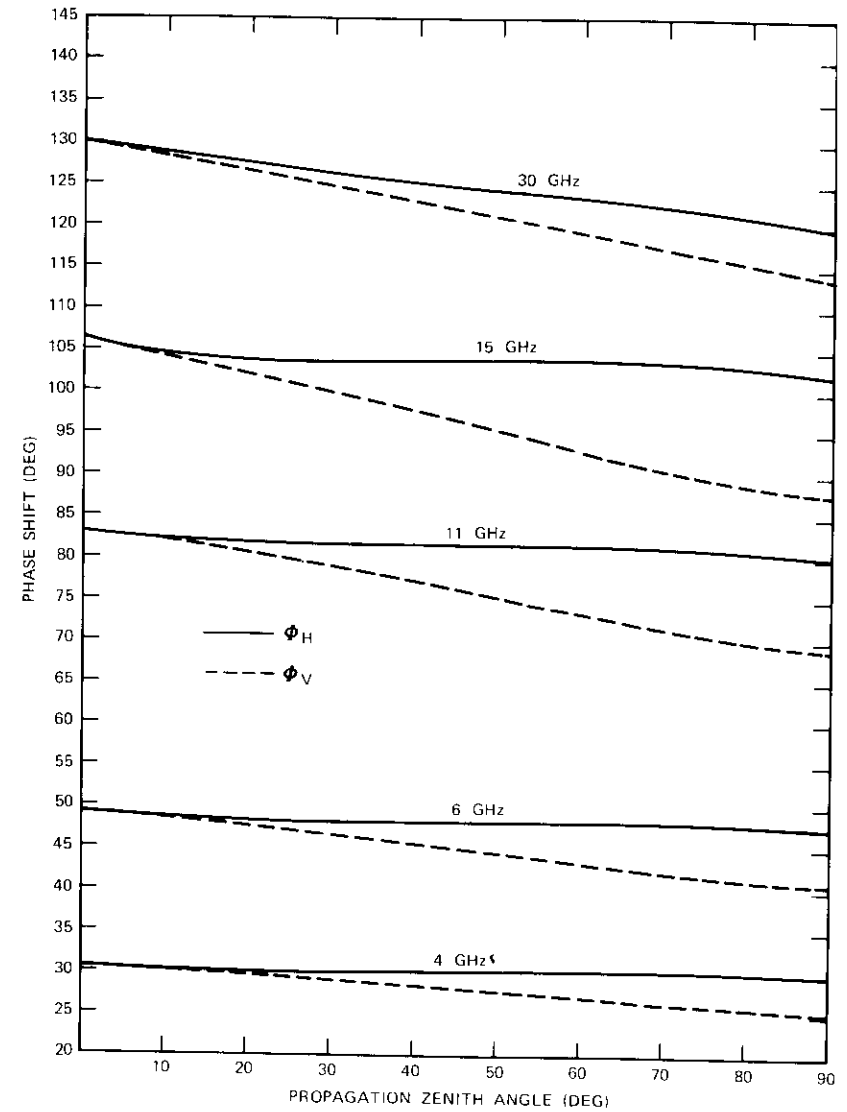


Figure 2. (Continued)

$$\Delta\Phi_H(\psi) = \frac{1}{9} \times 10^{-2} E(\theta, \phi, \psi) \Phi_S + [\Phi_H(90) - \Phi_V(90)] D(\theta, \phi, \psi) \quad (22a)$$

$$\Delta\Phi_V(\psi) = \frac{1}{9} \times 10^{-2} E(\theta, \phi, \psi) \Phi_S - [\Phi_H(90) - \Phi_V(90)] D(\theta, \phi, \psi) \quad (22b)$$

$$\text{where } D(\theta, \phi, \psi) = \frac{1}{2} (\sin^2 \psi' - \sin^2 \psi) - \sin^2 \theta \sin^2 \phi \quad (23)$$

$$E(\theta, \phi, \psi) = \psi - \psi' \quad (24)$$

These equations are available for detailed numerical calculations.

### Discussion

Equations (14) through (24) are engineering formulas for the evaluation of attenuation and phase shift. For example, terrestrial propagation analysis [13] has indicated that, at a frequency of 30 GHz and a rain rate of 150 mm/hr, the values of attenuation and phase shift are

$$\begin{aligned} A_H &= 28.87, & A_V &= 23.19 & \text{dB/km} \\ \Phi_H &= 166.16, & \Phi_V &= 160.75 & \text{deg/km} \end{aligned}$$

with  $A_S = 27.61$  and  $\Phi_S = 177.0$ . If the propagation path is instead  $30^\circ$  in elevation ( $\psi = 60^\circ$ ), the values will be changed to

$$\begin{aligned} A_H &= 29.74, & A_V &= 25.48 & \text{dB/km} \\ \Phi_H &= 167.23, & \Phi_V &= 163.17 & \text{deg/km} \end{aligned}$$

in accordance with equations (14) and (15).

If the turbulence and wind system of the storm are such that raindrops are canted with averaged canting angles  $\theta = 45^\circ$  from the zenith and  $\phi = 90^\circ$  from the plane of wave normal to the zenith, additional changes will result from equations (21) and (22):

$$\begin{aligned} \Delta A_H &= -2.64, & \Delta A_V &= 2.64 & \text{dB/km} \\ \Delta \Phi_H &= -2.53, & \Delta \Phi_V &= 2.52 & \text{deg/km} \end{aligned}$$

When these changes are taken into consideration, the actual attenuation and phase shift should be

$$\begin{aligned} A'_H &= 27.10, & A'_V &= 28.12 & \text{dB/km} \\ \Phi'_H &= 164.71, & \Phi'_V &= 165.17 & \text{deg/km} \end{aligned}$$

indicating that raindrops scatter electromagnetic energy in a manner similar to spheres. This is rather obvious, since at  $\psi = 60^\circ$ ,  $\theta = 45^\circ$ , and  $\phi = 90^\circ$  the geometric cross sections of the drops seen by horizontal and vertical polarized waves are almost the same. Only a small amount of cross polarization will be observed.

Now suppose that, while the storm is still in progress, the wind changes its horizontal direction by  $90^\circ$  so that  $\phi = 180^\circ$ . In this case the changes in  $\Delta A$  and  $\Delta \Phi$  become

$$\begin{aligned} \Delta A_H &= 0.52, & \Delta A_V &= -0.52 & \text{dB/km} \\ \Delta \Phi_H &= 0.50, & \Delta \Phi_V &= -0.49 & \text{deg/km} \end{aligned}$$

The actual attenuation and phase shift are

$$\begin{aligned} A'_H &= 30.26, & A'_V &= 24.96 & \text{dB/km} \\ \Phi'_H &= 167.73, & \Phi'_V &= 162.68 & \text{deg/km} \end{aligned}$$

Severe cross polarization will occur between the two orthogonal channels.

In an actual propagation experiment, the depth of the rain cloud is determined from a network of rain gauges, a weather radar, or other auxiliary measurements. For rain gauge measurements empirical curves showing the depth of the rain cloud versus rainfall rate are available [14], [15]. Hence the parameters  $A$  and  $\Phi$  calculated in the example can be readily converted into net decibels of attenuation and total degrees of phase shift. These values can then be used as the input for analyzing various impairments of the signal transmission, such as fading, phase front distortion, group-delay distortion, coherence bandwidth, and depolarization. For a full understanding of the cross-polarization effect due to canting, an extensive study of the terms shown in the last matrix of equation (9) is required. On the other hand, if it is desired only to estimate the cross-polarization isolation level for either linear or circular polarized transmission from the values of  $A$  and  $\Phi$  calculated above, standard formulas [1]-[4], [8], [12], [16] can be applied.

The following discussion will be devoted to the contour patterns of canting on the  $\theta$  versus  $\phi$  plane.

Constant  $D$  contours for  $\psi = 60^\circ$  are shown in Figure 3; the corresponding  $D$  values for the labeled curves are listed in the first two columns of Table 1. For rain rates of 100 and 150 mm/hr with frequencies of 4, 15, and 30 GHz [13], the magnitude of  $\Delta A_H$  and  $\Delta A_V$  is tabulated in Table 1 for each contour. Figures 4a and 4b are complicated contour patterns of

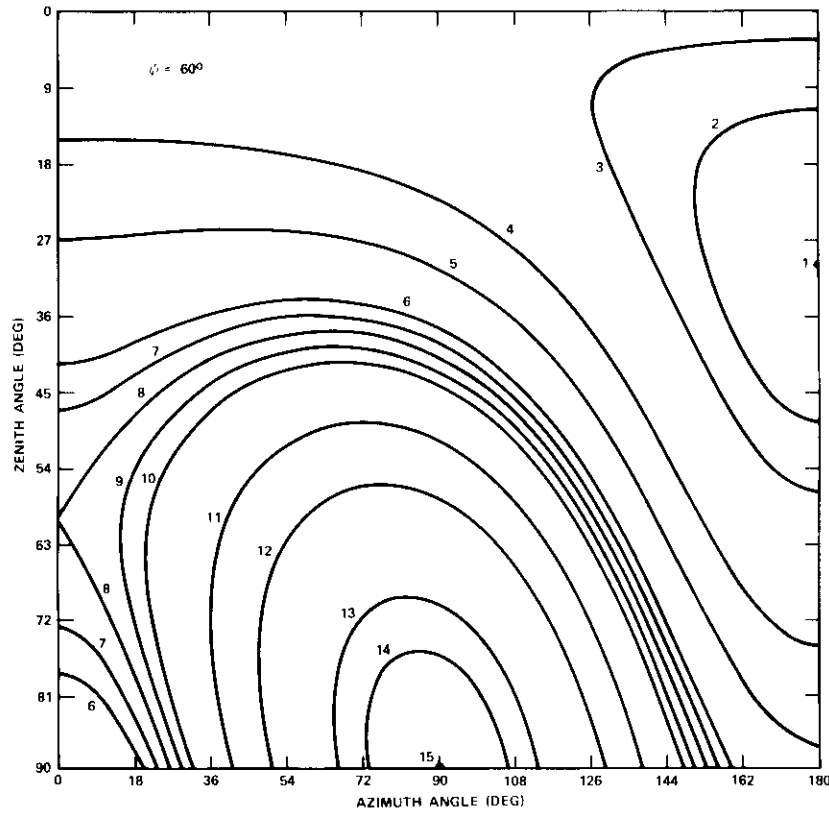


Figure 3. Fifteen Constant Value Contours of  $D$ ,  $\Delta A_H$ ,  $-\Delta A_V$ , or  $F$  (The values of the contours are shown in Table 1.)

$\Delta\Phi_H$  and  $\Delta\Phi_V$ , respectively, for  $\psi = 60^\circ$  at a rain rate of 100 mm/hr and a frequency of 15 GHz. The range of changes in attenuation and phase shift is of the same magnitude as  $A_H(90) - A_V(90)$  and  $\Phi_H(90) - \Phi_V(90)$ , respectively, which are the maximum differences between horizontal and vertical components (Figure 2).

For polarization analysis, the key parameters are the differential attenuation and differential phase shifts. It can be shown that, when canting is taken into consideration,

$$A'_H(\psi) - A'_V(\psi) = [A_H(90) - A_V(90)] F(\theta, \phi, \psi)$$

$$\Phi'_H(\psi) - \Phi'_V(\psi) = [\Phi_H(90) - \Phi_V(90)] F(\theta, \phi, \psi)$$

TABLE 1. VALUES OF  $D$ ,  $\Delta A_H$ ,  $\Delta A_V$ , AND  $F$  FOR VARIOUS CANTING DIRECTIONS SHOWN IN FIGURE 3 AT  $\psi = 60^\circ$

Contour	$D$	$\Delta A_H (-\Delta A_V)$ , dB/km				$F$	
		4 GHz	15 GHz	30 GHz	4 GHz	15 GHz	30 GHz
1	0.125	(0.0354)*	(1.427)*	(3.860)*	(0.0620)*	(2.390)*	(5.680)*
2	0.075	0.004	0.178	0.483	0.008	0.299	0.710
3	0.025	0.003	0.107	0.290	0.065	0.179	0.426
4	-0.125	0.001	0.036	0.097	0.002	0.060	0.142
5	-0.225	-0.004	-0.178	-0.483	-0.008	-0.299	-0.710
6	-0.325	-0.008	-0.321	-0.869	-0.014	-0.538	-1.278
7	-0.35	-0.012	-0.464	-1.255	-0.020	-0.777	-1.846
8	-0.375	-0.012	-0.499	-1.351	-0.022	-0.837	-1.988
9	-0.40	-0.013	-0.535	-1.448	-0.023	-0.896	-2.130
10	-0.425	-0.014	-0.571	-1.544	-0.025	-0.956	-2.272
11	-0.525	-0.015	-0.606	-1.641	-0.026	-1.016	-2.414
12	-0.625	-0.019	-0.749	-2.027	-0.033	-1.255	-2.982
13	-0.775	-0.022	-0.892	-2.413	-0.039	-1.494	-3.550
14	-0.825	-0.027	-1.106	-2.992	-0.048	-1.852	-4.402
15	-0.875	-0.029	-1.177	-3.185	-0.051	-1.972	-4.686
		-0.031	-1.249	-3.378	-0.054	-2.091	-4.970

\*Values of  $A_H(90^\circ) - A_V(90^\circ)$  supplied by Oguchi.

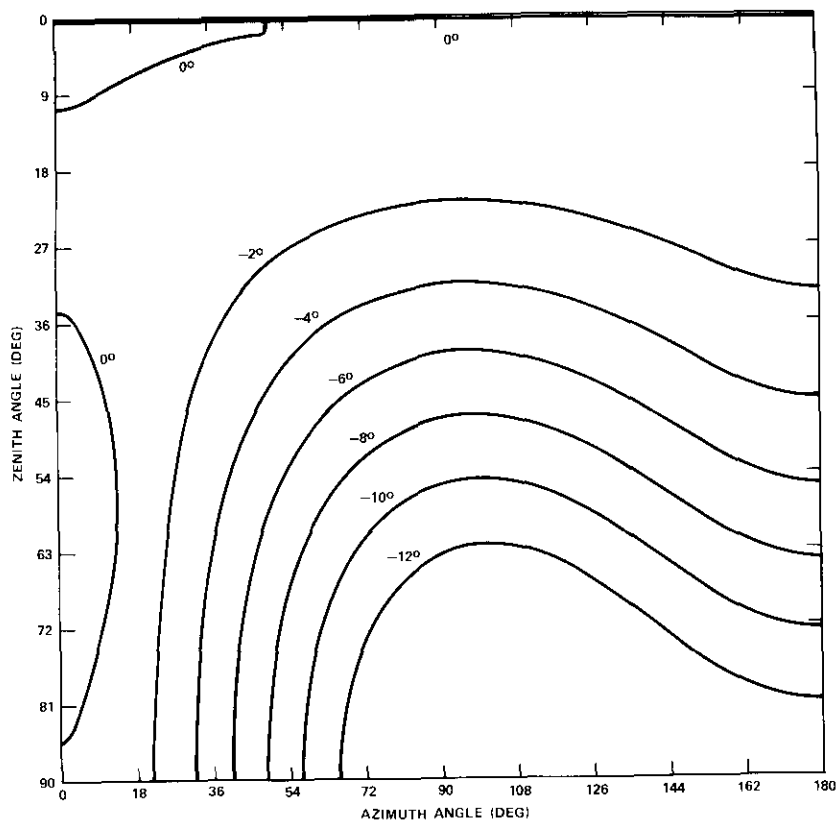


Figure 4a. Contours of Phase Shifts at  $\psi = 60^\circ$  and Rain Rate at 100 mm/hr— $\Delta\Phi_H$  Contours

where  $F(\theta, \phi, \psi) = \sin^2 \psi + 2D(\theta, \phi, \psi)$ . For a known propagation path  $\sin^2 \psi$  is a constant. Therefore,  $F$  contours are essentially the same as the  $D$  contours. For  $\psi = 60^\circ$ , the last column in Table 1 lists the values of  $F$  for each labeled curve in Figure 3. The values range from  $-1$  to  $+1$ .

Intuitively, the difference in attenuation and phase shift between the horizontal and vertical polarizations will yield positive maxima if the horizontal field component sees the largest geometric cross sections while the vertical field component sees the smallest cross section of the raindrops, or vice versa for the case of negative maxima. Furthermore, the difference is minimal if the geometric cross sections viewed by both

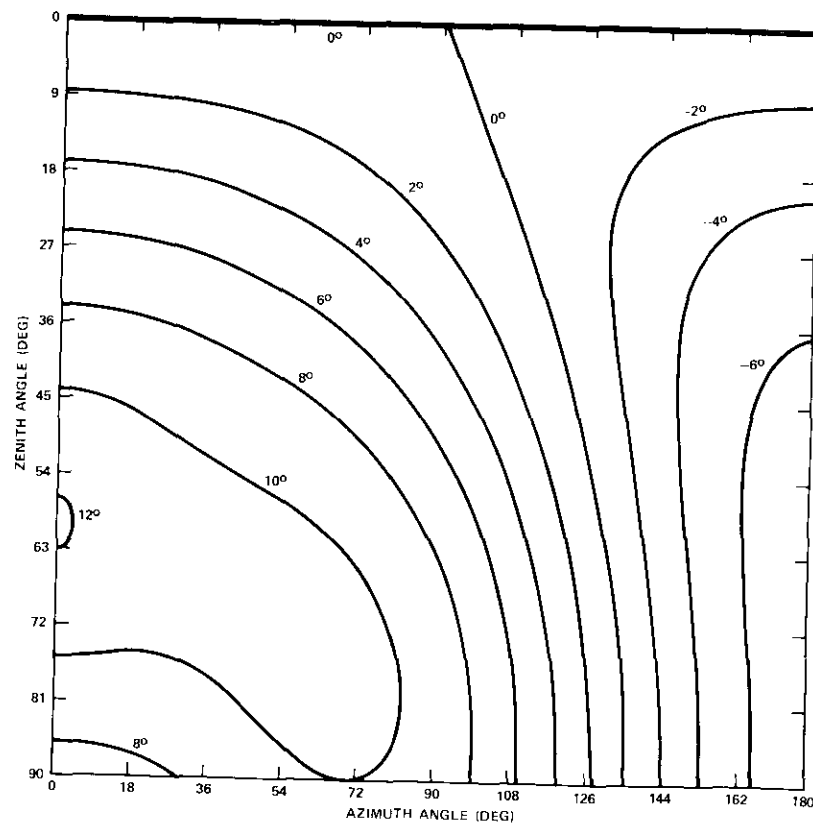
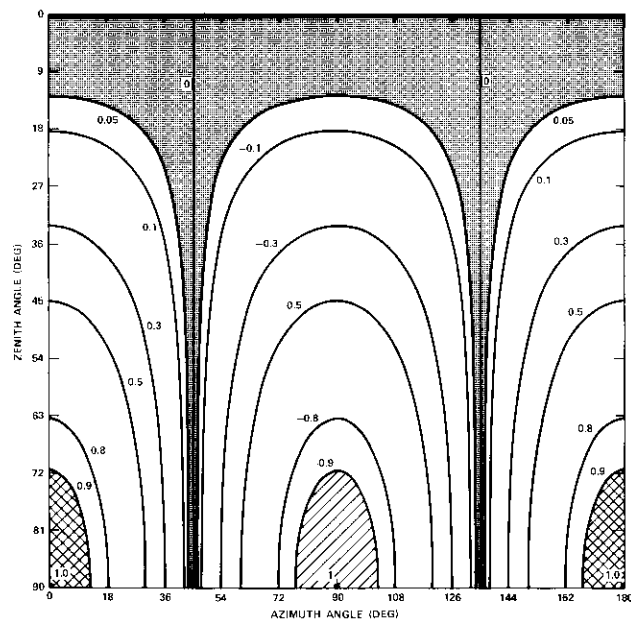


Figure 4b. Contours of Phase Shifts at  $\psi = 60^\circ$  and Rain Rate at 100 mm/hr— $\Delta\Phi_V$  Contours

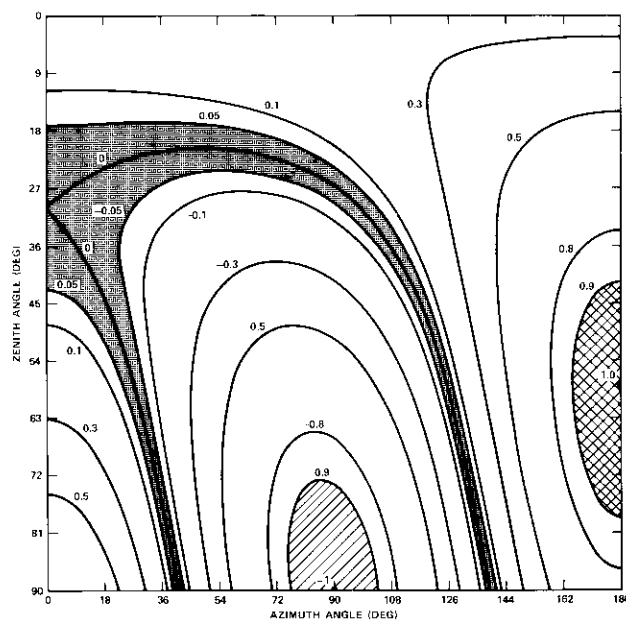
polarizations are the same. This intuitive picture suggests that  $F$  contours (as shown in Figure 3) can be divided into three zones:

- a positive maxima difference zone between contours 1 and 2,  $F \geq 0.9$ ;
- a zero difference zone between contours 7 and 9,  $-0.05 \leq F \leq 0.05$ ;
- a negative maxima difference zone between contours 14 and 15,  $F \leq -0.9$ .

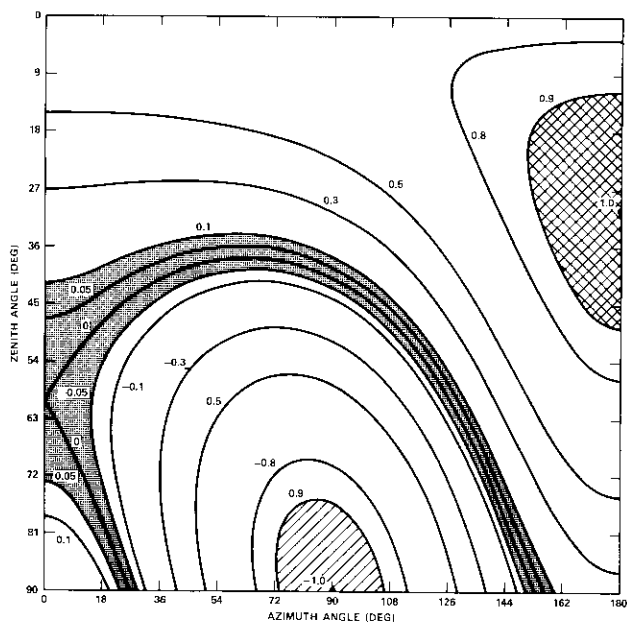
The pattern of zone variations is illustrated in Figure 5.



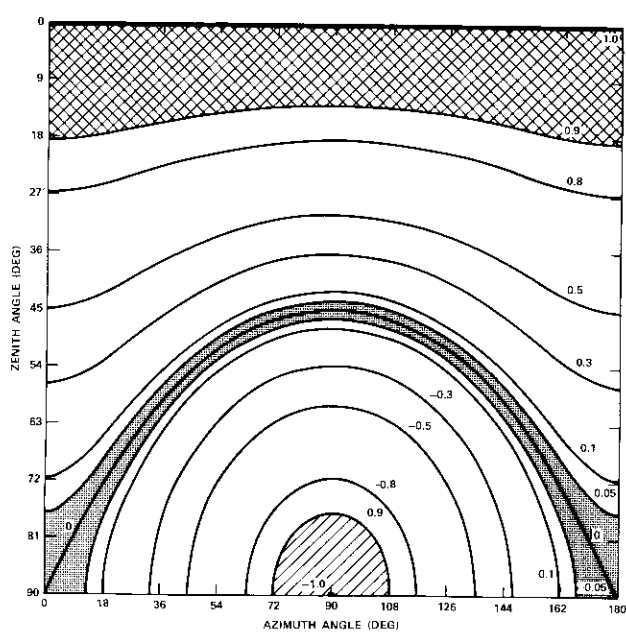
a.  $\psi = 0^\circ$



b.  $\psi = 30^\circ$



c.  $\psi = 60^\circ$



d.  $\psi = 90^\circ$

Figure 5. Pattern of Canting Angle Zones Divided in Accordance with the Difference of Either Amplitude or Phase Between Horizontally and Vertically Polarized Components

The zone pattern changes drastically from  $\psi = 0^\circ$  to  $\psi = 90^\circ$ . This indicates that the common practice of using the terrestrial propagation model ( $\psi = 90^\circ$ ) to analyze satellite-earth propagation ( $0^\circ < \psi < 90^\circ$ ) in the presence of canted raindrops is inadequate. Furthermore, canting is generally analyzed [2]–[4], [8] at the  $\phi = 90^\circ$  plane because it is assumed that the canting behavior of raindrops along the plane will yield the extreme values of attenuation and phase shift. The inadequacy of this assumption is obvious from Figure 5, since the canting behavior at  $\phi \neq 90^\circ$  planes can be markedly different, and the positive maxima difference zone is not always on the  $\phi = 90^\circ$  plane. The  $\phi = 90^\circ$  plane does cover the negative maxima difference zone, which corresponds to the rather rare case in which the wind and turbulence are such that the raindrops are canted horizontally and perpendicular to the propagation path. For this pathological case, the values of attenuation and phase shift for horizontal and vertical polarizations are interchanged.

### Conclusion

The present paper has made three contributions. First, the derivation of equations (11) through (13) has explicitly related propagation parameters to the general canting angle distribution. These equations can be used by engineers to calculate the attenuation and phase shift due to the canting effect in thunderstorms if a canting angle distribution is assumable or available.

Second, the propagation parameters for slant path and terrestrial path propagation have been related. Although theoretical procedures are well documented [5]–[9], there are no practical engineering formulas for evaluating slant path propagation parameters. The relationships presented in equations (14) and (15) serve this purpose.

Third, a first-order study of the effect of canting based on a unique canting direction has been presented. This not only gives credence to the key equations presented herein, but also provides physical insight into the effects of canting. It has been shown that the common assumption that canting is important only on a plane perpendicular to the propagation path is inadequate. Finally, the unsymmetric nature of the canting angle contours plotted in the  $\theta$ - $\phi$  plane reveals that the local wind system and turbulence should be carefully examined before making any detailed characterization of wave propagation in the presence of heavy rainstorms.

### Acknowledgment

Thanks are due to Dr. G. Hyde for his detailed review of the manuscript, to Mr. J. Jih for performing computer calculations, and to Dr. R. Taur for useful discussions.

### References

- [1] M. J. Saunders, "Cross Polarization at 18 and 30 GHz Due to Rain," *IEEE Transactions on Antennas and Propagation*, AP-19, 1971, pp. 273–277.
- [2] D. T. Thomas, "Cross-Polarization Discrimination in Microwave Radio Transmission Due to Rain," *Radio Science*, Vol. 6, No. 10, 1971, pp. 833–839.
- [3] P. A. Watson and M. Arbabi, "Rainfall Cross Polarization at Microwave Frequencies," *Proceedings of IEEE*, Vol. 120, No. 4, 1973, pp. 413–418.
- [4] T. S. Chu, "Rain-Induced Cross-Polarization at Centimeter and Millimeter Wavelengths," *Bell System Technical Journal*, Vol. 53, No. 8, 1974, pp. 1557–1579.
- [5] T. Oguchi, "Attenuation of Electromagnetic Waves Due to Rain with Distorted Raindrops," *Journal of Radio Research Laboratories [Japan]*, Vol. 7, No. 33, 1960, pp. 467–485.
- [6] T. Oguchi, "Attenuation of Electromagnetic Waves Due to Rain with Distorted Raindrops (Part II)," *Journal of Radio Research Laboratories [Japan]*, Vol. 11, No. 53, 1964, pp. 19–44.
- [7] T. Oguchi, "Attenuation and Phase Rotation of Radio Waves Due to Rain: Calculations at 19.3 and 34.8 GHz," *Radio Science*, Vol. 8, No. 1, 1973, pp. 31–38.
- [8] W. J. Vogel, B. M. Fannin, and A. W. Straiton, "Polarization Effects for Millimeter Wave Propagation in Rain," Technical Report No. 73-1, University of Texas, Austin, Texas, December 1973.
- [9] J. A. Morrison and M. J. Cross, "Scattering of a Plane Electromagnetic Wave by Axisymmetric Raindrops," *Bell System Technical Journal*, Vol. 53, No. 6, 1974, pp. 955–1019.
- [10] H. C. Van De Hulst, *Light Scattering by Small Particles*, New York: John Wiley and Sons, 1957.
- [11] T. Oguchi, "Statistical Fluctuation of Amplitude and Phase of Radio Signals Passing Through the Rain," *Journal of Radio Research Laboratories [Japan]*, Vol. 9, No. 41, 1962, pp. 51–72.
- [12] B. G. Evans and J. Troughton, "Calculation of Cross-Polarization Due to Precipitation," *IEE Conference on Propagation of Radio Waves at Frequencies above 10 GHz*, April 1973, Conference Publication No. 98, pp. 162–171.

- [13] T. Oguchi, Private Communications.
- [14] H. W. Evans, "Attenuation on Earth-Space Paths at Frequencies up to 30 GHz," *International Conference on Communication*, Montreal, Canada, June 1971, pp. 27-1 to 27-5.
- [15] L. J. Ippolito, "Earth-Satellite Propagation Above 10 GHz," NASA Report X751-72-208, Greenbelt, Maryland, May 1972, pp. 8-1 to 8-27.
- [16] R. R. Taur, "Rain Depolarization: Theory and Experiment," *COMSAT Technical Review*, Vol. 4, No. 1, Spring 1974, pp. 187-190.



*Dickson J. Fang received his B.S.E.E. in 1962 from Taiwan University, Taipei, China, and his M.S.E.E. and Ph.D. from Stanford University in 1964 and 1967. From 1967 to 1974, he was a radio physicist at Stanford Research Institute, and he authored 17 papers on wave propagations, radio auroras, and ionospheric irregularities. While on leave from Stanford (1969-1970) he was a visiting professor at Taiwan University, where he published a graduate textbook on electromagnetic theory and five articles on the college education system. He joined COMSAT in 1974 and is currently responsible for research on propagation over 10-GHz frequencies.*

Index: multiplexers, earth terminals, traveling wave tubes, waveguide filters

## ***A low-loss multiplexer for satellite earth terminals***

R. W. GRUNER AND A. E. WILLIAMS

(Manuscript received November 8, 1974)

### **Abstract**

A low-loss multiplexer system that improves satellite earth station reliability and efficiency by eliminating the broadband high-power transmitter is described in this paper. Specifically, the 5,925- to 6,425-MHz frequency band is divided into 12 contiguous channels, each with 36-MHz usable bandwidth and operating with a separate air-cooled traveling wave tube amplifier. Channels are added by employing modular units consisting of two 3-dB quadrature hybrids and a matched pair of 4-pole elliptic function waveguide filters. A 3-channel multiplexer with time-delay equalization has been designed, fabricated, and tested. Agreement between calculated and measured results is excellent.

### **Introduction**

Multiplexing or combining a number of separate channels into a single broadband frequency channel is a technique which is widely employed in microwave communications systems. It is particularly important to the successful implementation of satellite earth stations and spacecraft transponders.

During the preliminary design stages of the COMSAT unattended earth terminal (UET), it became apparent that replacing the single broadband high-power amplifier (HPA) with multiple lower power traveling wave tube amplifiers (TWTAs) [1] would result in significant performance advantages. Using 400-W, air-cooled, permanent magnet focused TWTs signif-

icantly improves earth station transmitter reliability. Further, this allows single-carrier-per-amplifier operation with an attendant improvement in efficiency. However, the proposed 5.925- to 6.425-GHz frequency plan of only 10-percent guardbands (4 MHz) and the twelve 36-MHz channels with flat channel group delay and minimum insertion loss imposes stringent design specifications on the transmit multiplexer.

A review of existing multiplexer techniques has indicated that a directional filter concept would be the most appropriate modular design approach for meeting these stringent electrical performance requirements. A subsequent section of this paper demonstrates that this requirement can be met by employing the unique low-loss properties of the optimum amplitude function waveguide filters [2]-[4] developed at COMSAT Laboratories. This section also describes the combination of these filters with 3-dB quadrature hybrids to yield sets of directional filters which exhibit minimum channel loss, low input VSWR, and minimum interaction between adjacent channels.

The design concepts for group-delay equalization are based on the conventional Abele-Wang circular waveguide cavity equalizer [5]. This unit is placed before the TWTs and therefore does not contribute to the loss of the multiplexer.

Three multiplexer units with equalized gain slope and time delay have been designed and fabricated for center frequencies of 6,070, 6,110 and 6,150 MHz. Their electrical performance is presented and shown to agree with theory.

#### Multiplexer design considerations

Compatibility with the existing INTELSAT IV satellite transponder frequency plan required 12 contiguous 36-MHz channels operating with only 4-MHz guardbands to form the 5.925- to 6.425-GHz bandwidth. The small guardband-to-passband ratio imposed stringent specifications on the earth station multiplexer design with insertion loss, group delay, gain slope, and high-power capability the principal considerations.

The following multiplexer designs [6] shown in Figure 1 have been considered:

#### Manifold multiplexer

Separate filters tuned to the center frequency of each channel are coupled into a common waveguide. An analysis of this approach indicates that extremely high selectivity (filter slope) is required for the constituent filters

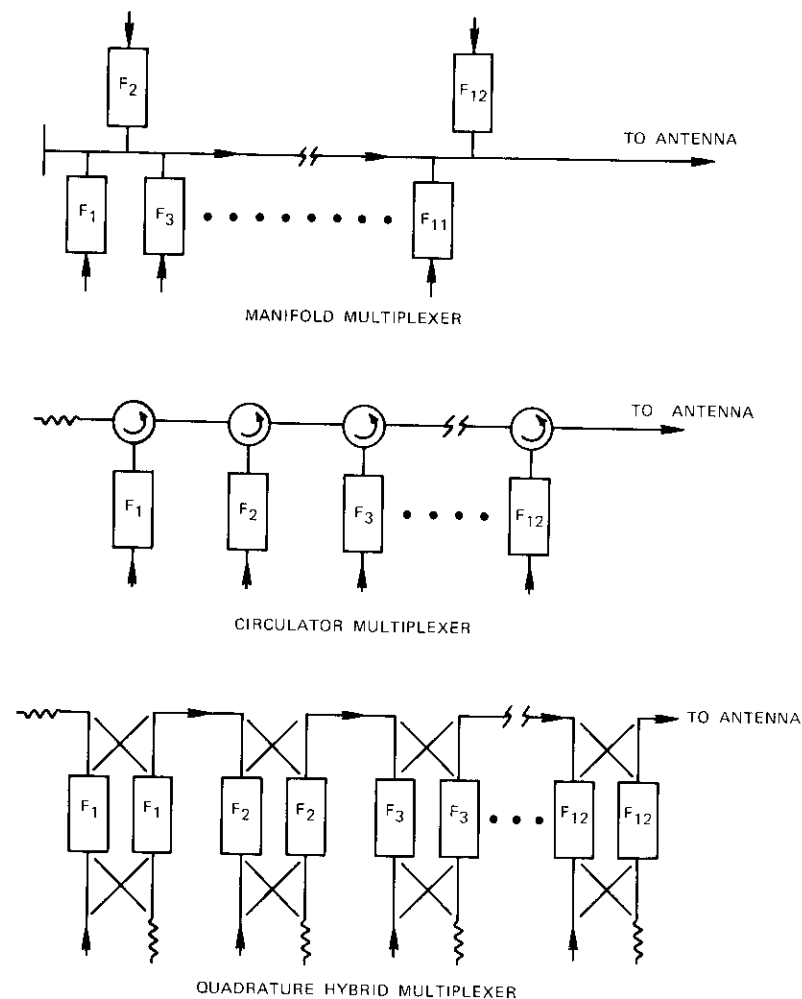


Figure 1. *Multiplexer Design Approaches*

to minimize the interaction and tuning problems. This high selectivity requires a proportionately larger number of filter cavities, resulting in excessive dissipative loss. Because of the extremely narrow guardbands, a 12-channel manifold multiplexer would be extremely difficult to tune and would not be amenable to a modular concept with a flexible frequency plan.

### Circulator multiplexer

The primary advantage of the circulator multiplexer is the directional signal flow. That is, the signals proceed from input to output and do not interact (to a first order), hence allowing a modular concept. The directional nature of the circuit minimizes the required filter selectivity and yields a lower filter loss than the manifold approach. The main disadvantage is that the signals must pass in succession through each circulator, incurring about 0.2-dB loss at each junction.

### Quadrature hybrid multiplexer

The quadrature hybrid multiplexer has the advantages of a directional filter without the disadvantage of high-power circulators.

The specific advantages of the quadrature hybrid multiplexer are, in order of importance:

- Due to the directional nature of the circuit, lower values of filter selectivity can be tolerated. This enables the use of fewer filter cavities and consequently the filter losses are minimized.
- The technique is modular; i.e., TWT amplifiers may be interchanged or turned off without retuning or altering performance.
- Because a smaller number of filter sections are required, the time delay and gain slopes across the passband of the channel are also reduced.
- A very low input VSWR is achieved because the balanced filter mismatches are reflected into the load. This enables high-ripple filters to be used, further reducing the required number of filter sections needed to achieve a prescribed selectivity or slope characteristic.
- The components are passive and ferrite materials are not required.
- The high power from the TWT is split into two separate paths and only one-half flows through each filter. This reduces the voltage breakdown problem and decreases the frequency shift due to thermal heating.
- Third-order intermodulation products generated by the amplifier are reflected by the filters and absorbed by the waveguide loads.

Its disadvantages, also in order of importance, are the following:

- Two identical filters and hybrids must be fabricated for each

multiplexer module. Hence, 24 quadrature hybrids and 24 filters are required for the entire 500-MHz bandwidth.

- The interconnecting line lengths between the quadrature hybrids and filter of an individual module must be precisely balanced to preserve circuit directivity.

- The physical size and weight of the multiplexer are greater than those associated with alternate approaches.

For earth station applications, in which size and weight are relatively unimportant, the quadrature hybrid multiplexer is clearly the best design approach. In the next section the design of the quadrature hybrid multiplexer will be described and its electrical performance characteristics presented.

### Quadrature hybrid multiplexer, design and performance

Figure 2 is a schematic representation of a 12-channel quadrature hybrid multiplexer with TWT amplifiers and equalizers. The equalizers

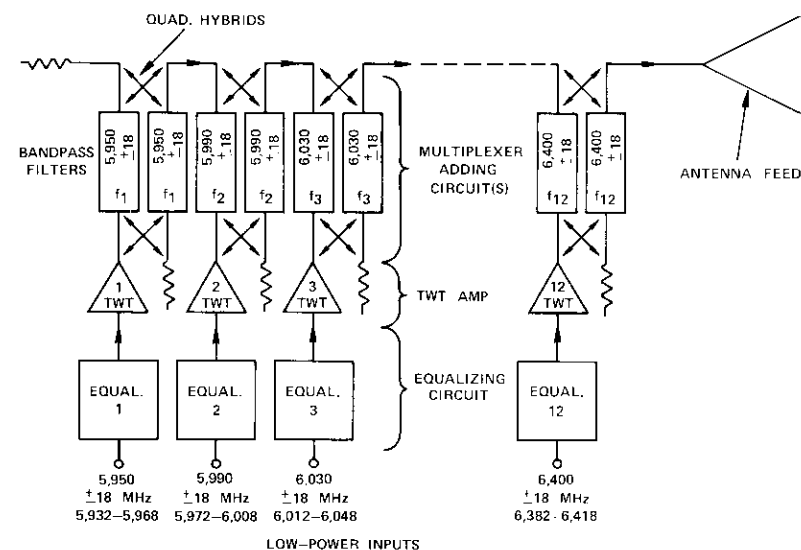


Figure 2. UET Multiplexing System

are placed before the TWT amplifiers so that the equalizer loss will be incurred in the low-power signal path. The equalization can be viewed as a predistortion of the low-power signal. The TWT amplifiers present a linear transformation in the 36-MHz passband. The theoretical operation and measured data for the multiplexer will be presented in this section.

Two cascaded multiplexer modules shown in Figure 3 will be used to discuss the practical limitations leading to the filter tradeoff study. An ideal multiplexer circuit transfers all of the energy at the input (port 1) to the output (port 8); no energy appears in any of the other ports (ports 2, 3, 5, and 6). However, in practice, energy is lost through dissipation within the filter due to finite "Q", and through coupling into unwanted ports due to reflections and imperfect hybrid isolation. If it is assumed that the quadrature hybrid is well matched and has high directivity, the loss from port 1 to port 8 consists of four main contributions: the dissipative loss of the  $f_4$  filter, the reflection or ripple loss of the  $f_4$  filter, the leakage loss of the 6,070- $\pm$ 18-MHz signal through the  $f_5$  filter, and the dissipative loss of the 6,070- $\pm$ 18-MHz signal within the  $f_5$  filter. The specific filter, in-band ripple, selectivity, and number of filter sections are selected to minimize the sum of these four loss components.

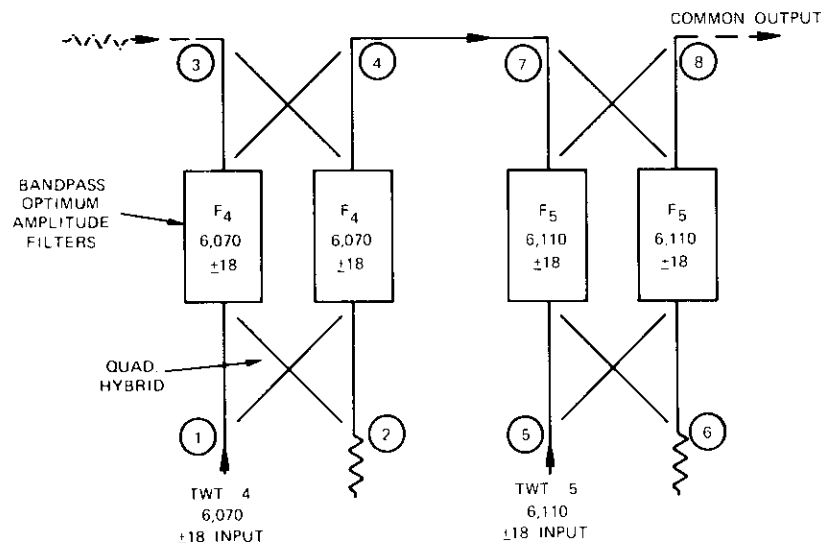


Figure 3. Cascaded Multiplexer Units for Channels 4 and 5

Conventional multiplexer designs are usually based on normal Chebyshev or Butterworth waveguide bandpass filters. For this particular application, in which the guardband-to-passband ratio is exceptionally low, substantial improvement has been realized by using the waveguide optimum amplitude function filters [2]-[4] developed at COMSAT Laboratories. In particular, for an equivalent frequency characteristic, this type of filter has about one-third the loss of conventional filters. Further, it has improved group delay and gain slope so that the time-delay equalization requirements may be relaxed. Each filter cavity is operated in orthogonal polarizations; therefore, two electrical cavities are obtained from one physical cavity. The inherent low loss-high selectivity of this type of filter is fundamental to the success of the multiplexer design. The required filter selectivity, in-band ripple, and number of cavities to minimize the total loss have been carefully studied.

Figure 4 shows the calculated channel losses assuming a  $Q$  of 7,500 for a 4-pole elliptic function filter with a 0.1-dB in-band ripple and a rejection of 13.5 dB at  $\pm 22$  MHz from band center. The center band loss is 0.30 dB and the edge-of-band loss at  $\pm 18$  MHz is 1.10 dB for the path from port 1 to port 4. When the signal reflects off the adjacent channel filter (port 7 to port 8 loss), an asymmetric curve results. The total channel loss, or the sum of these two curves, is given by the  $T_{18}$  curve. The calculated total loss is 0.5 dB at the band center and 1.2 dB and 2.3 dB at the two band edges.

Other multiplexer units are further separated in frequency; therefore, the highly selective filters may be thought of as perfect short circuits reflecting the energy without further dissipation or leakage loss. Consequently, the total loss of a multiplexer channel may be evaluated by adding the transmission loss of the unit under test to the return loss of the adjacent channel unit. The time-delay response of each channel is the sum of the transmission time delay plus the return loss time delay of the adjacent channel. This is also an asymmetric curve and is directly related to the total dissipative loss of the channel.

Figure 4 also shows a calculated loss curve for a multiplexer using a 6-pole filter. The filter has three dual mode physical cavities, a 0.1-dB in-band ripple, and a rejection of 18 dB at  $\pm 22$  MHz from band center. A  $Q$  of 7,500 has again been assumed. The increased selectivity, 18.0 dB versus 13.5 dB in the 4-pole case, results in slightly less leakage loss into the load at port 5. However, the intrinsic filter dissipative loss is increased by the two additional electrical cavities and the net overall loss is higher than that of the 4-pole filter. A thorough tradeoff analysis has shown that the 4-pole

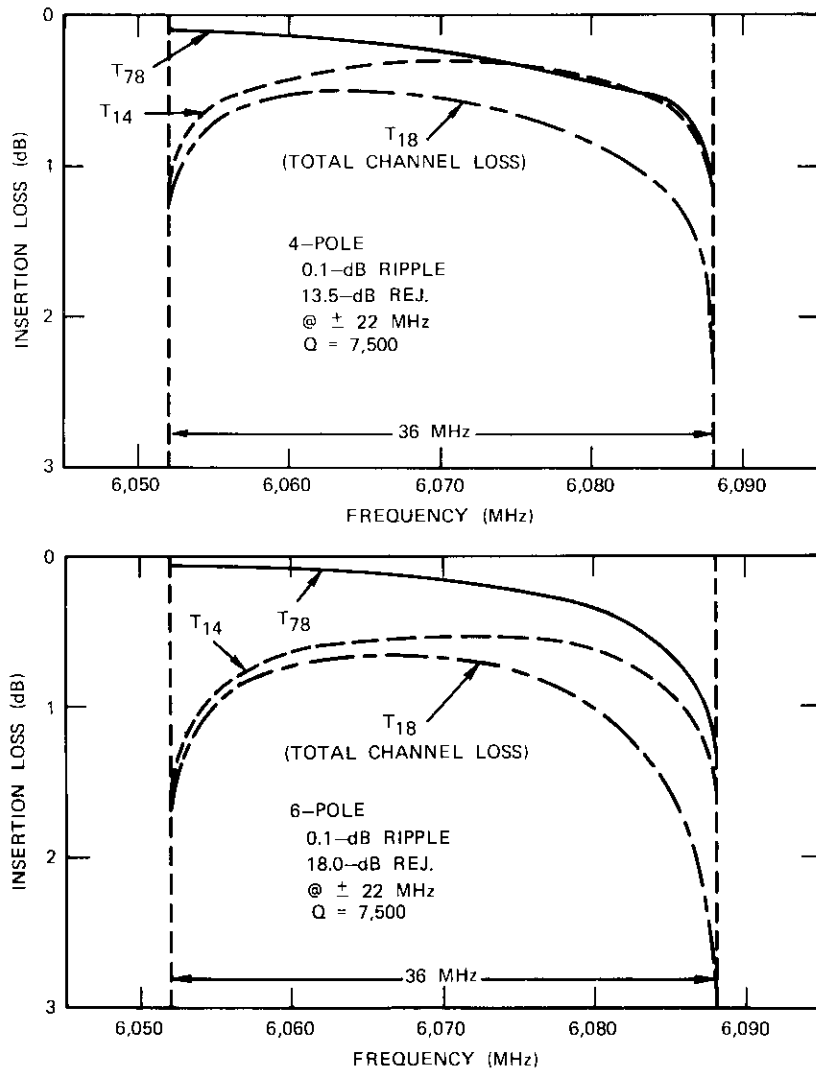


Figure 4. Calculated Channel Losses for 4- and 6-Cavity Filters

filter with 0.1-dB ripple and 13.5-dB rejection at the edge of the guardband yields a multiplexer design with minimum loss. The conclusion of this tradeoff study is that, to minimize the overall insertion loss, the filter should have the smallest number of poles consistent with an acceptable rejection characteristic. This conclusion is also consistent with maintaining

the frequency stability as less RF thermal heating occurs as a result of the reduced filter dissipative loss.

Three directional filter units corresponding to channels 4, 5, and 6 and 6,070-  $\pm 18$ -, 6,110-  $\pm 18$ -, and 6,150-  $\pm 18$ -MHz frequencies were designed and fabricated. Figure 5 shows one of these units. The quadrature hybrids were electroformed to achieve good balance and isolation. The filters were constructed from Invar, plated with silver, and then gold flashed. Invar was used to minimize the frequency shift due to the thermal heating caused by the dissipated high-power RF energy. For a complete 500-MHz-bandwidth transmitting system, 12 of these units would be fabricated and tuned. A complete set of measurements was made for all three units. Although only the data from the channel 4 multiplexing unit are shown, equivalent results were measured for all units.

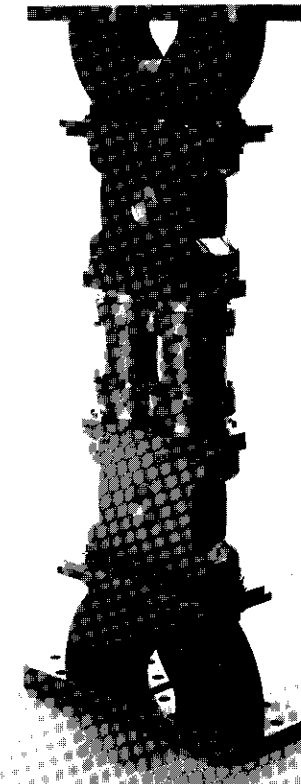


Figure 5. Directional Filter Module

Figure 6 shows the measured transmission loss ( $T_{14}$ ) through the  $f_4$  unit. The loss at band center (6,070 MHz) is 0.3 dB and the loss at the edges of the band (6,052 and 6,088 MHz) is 0.9 dB, as shown on an expanded scale in Figure 7. The measured loss as the 6,070- $\pm$  18-MHz signals reflect off the adjacent channel 5 filter ( $T_{78}$ ) is given in Figure 8. The total transmission loss,  $T_{18}$ , measured with the units connected, is shown in Figure 9. This represents the total loss of the multiplexer chain to the 6,070- $\pm$  18-MHz channel with the exception of the small value of waveguide losses. Figure 10 shows excellent agreement between the calculated and measured losses.

The input VSWR of the  $f_4$  multiplexer, shown in Figure 11, is less than 1.06 over the 6,052- to 6,088-MHz passband. As shown in Figure 12, the transmission loss from port 1 to port 3 is a measure of the directivity of the multiplexer and is in excess of 30 dB within the band. This high value of directivity indicates that there will be minimal interaction between units so that modules may be added or subtracted without retuning. The transmission loss from port 1 to port 2 ( $T_{12}$ ), shown in Figure 13, is the in-band return loss response of the filter. One of the most favorable aspects of this quadrature hybrid approach is that the energy reflected from the filters is

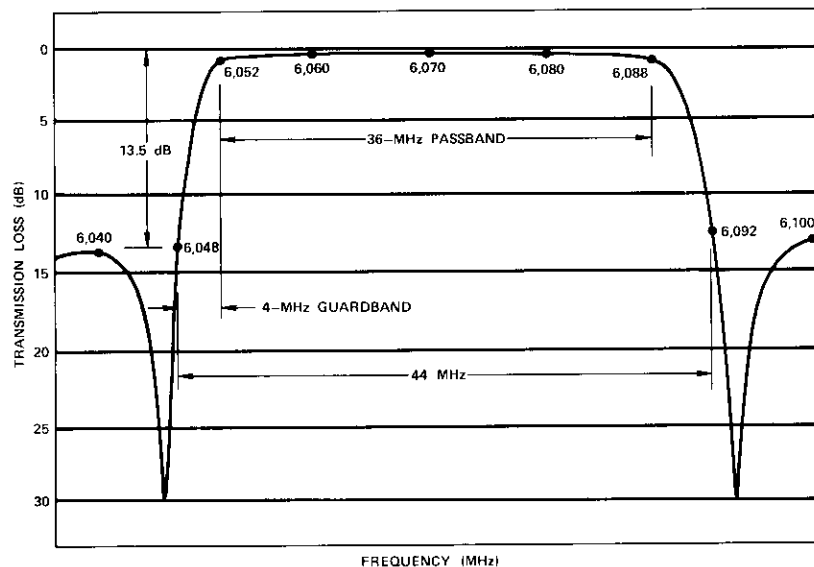


Figure 6. Measured Transmission Loss, Port 1 to Port 4

absorbed by the load and does not represent a mismatch to the TWT amplifier.

The multiplexer was tested with input power levels in excess of 1.5 kW and exhibited no evidence of high-power breakdown. At the operating input power level of 400 W, the filter temperature increases about 50°F above the ambient temperature. Although the temperature increase is small (due to the low loss of the filters), Invar must be used to maintain the frequency stability of the multiplexer unit. The measured frequency shift is less than 0.15 MHz at the 400-W input power level.

The measured time delay for the  $f_4$  multiplexer unit is given in Figure 14. The change in time delay between the band center and edges of the band is about 30 ns. The total time delay when the adjacent channel multiplex is added is shown in Figure 15. Figure 16 shows excellent agreement between measured and calculated time delay. Time-delay equalization is described in the following section.

### Equalizer

To equalize the time delay of the multiplexer channels, an Abele-Wang [5] waveguide equalizer has been chosen. This equalizer consists of a

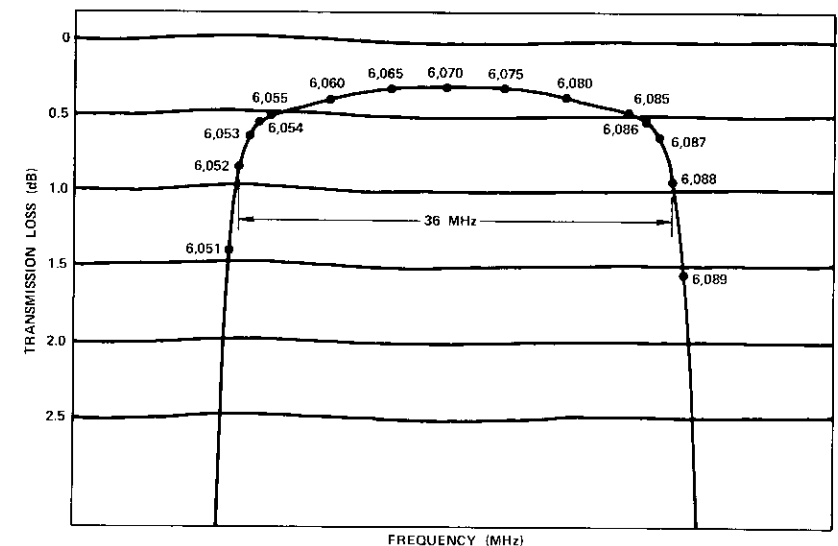


Figure 7. Measured Transmission Loss, Expanded Port 1 to Port 4

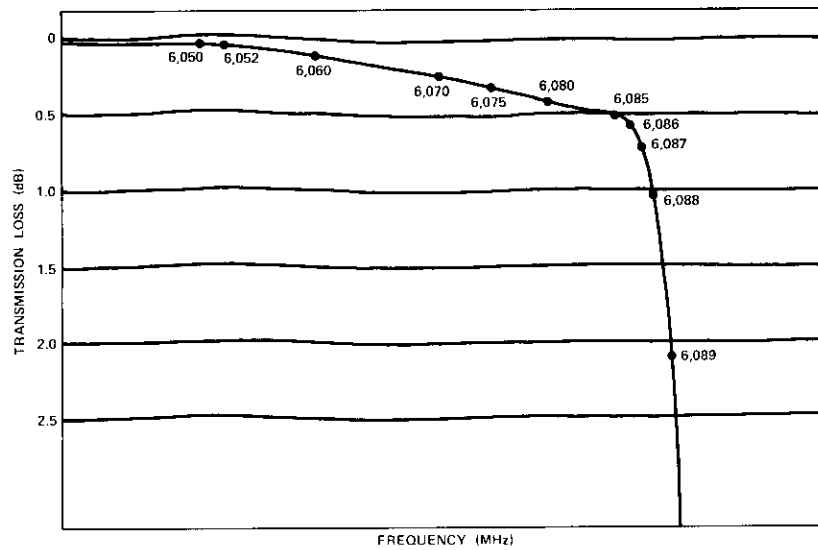


Figure 8. Measured Adjacent Channel Reflection Loss ( $T_{78}$ )

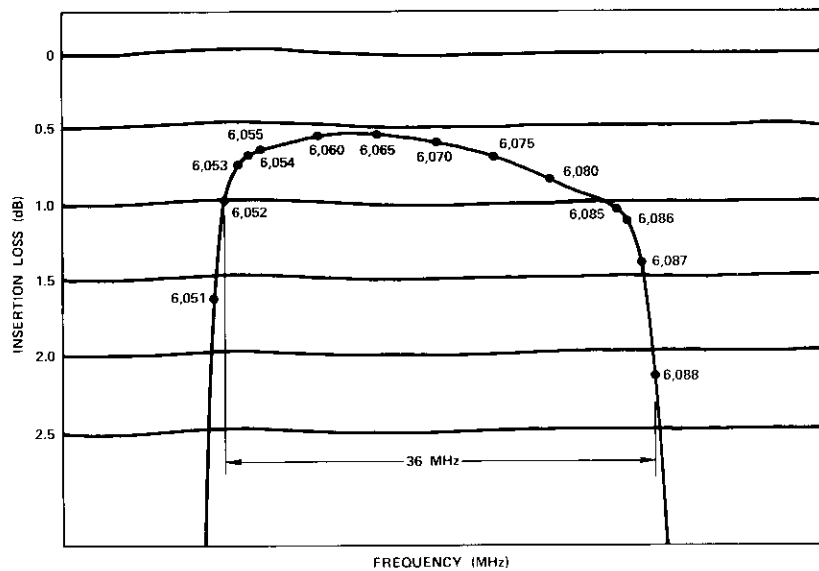


Figure 9. Measured Total Channel Transmission Loss ( $T_{18}$ )

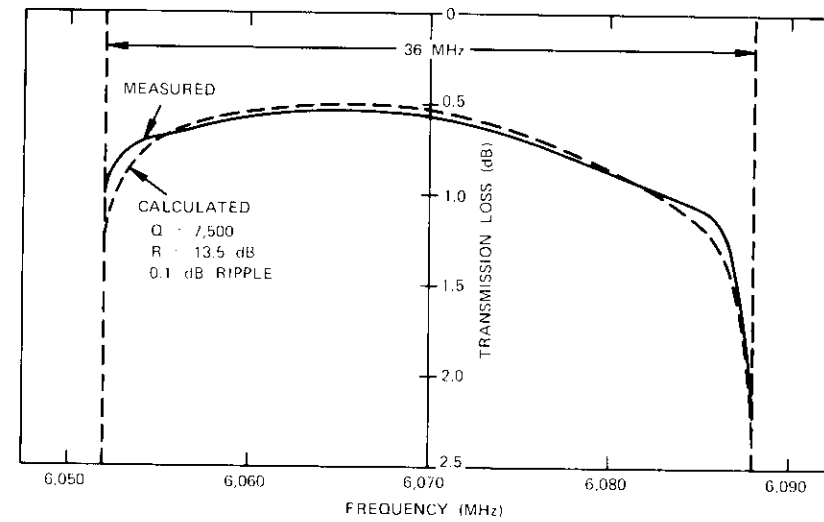


Figure 10. Comparison of Calculated and Measured Total Channel Loss ( $T_{18}$ )

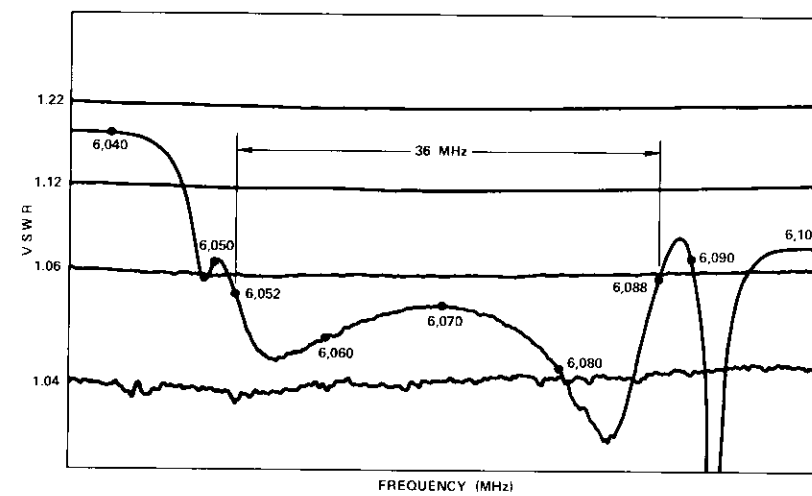


Figure 11. Measured Input VSWR

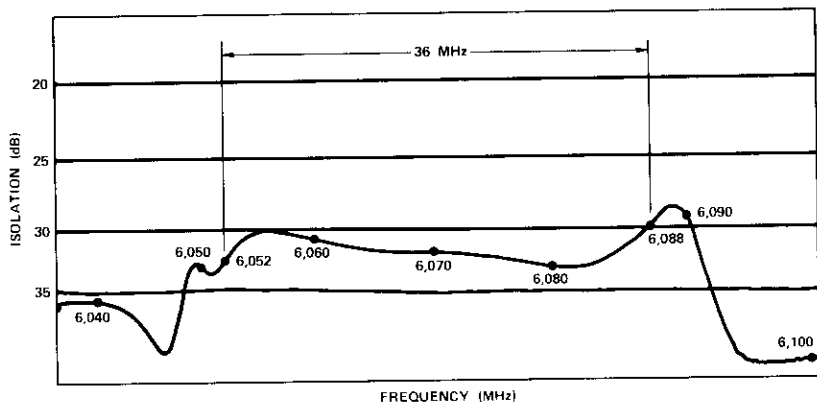


Figure 12. Measured Isolation ( $T_{13}$ )

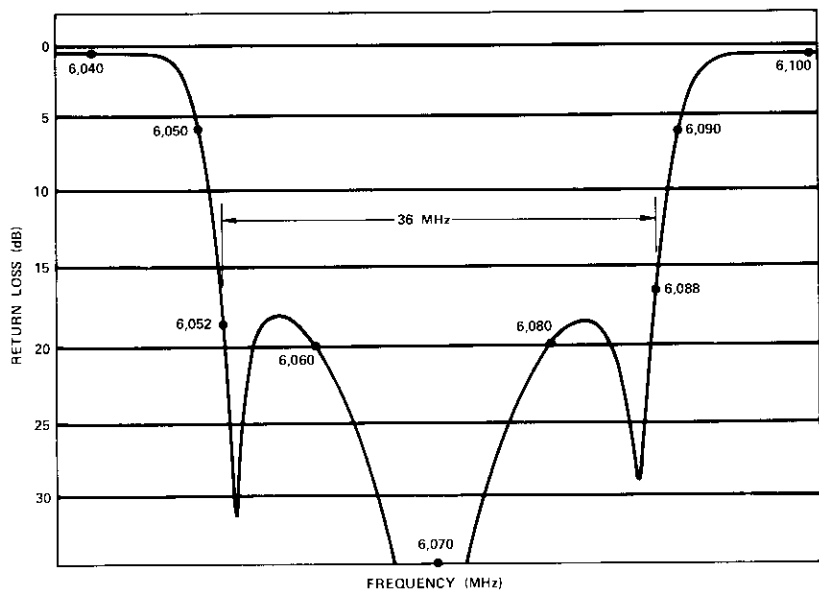


Figure 13. Measured Coupling to Load ( $T_{12}$ )

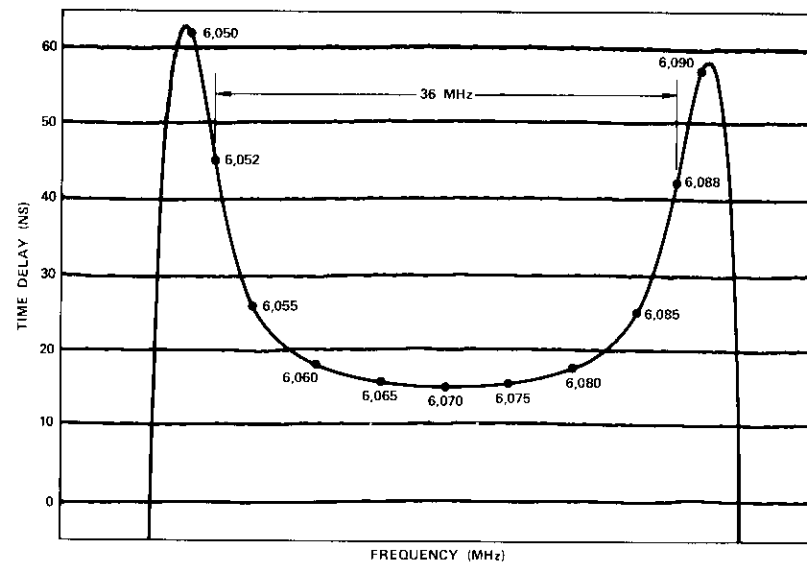


Figure 14. Measured Time Delay, Port 1 to Port 4

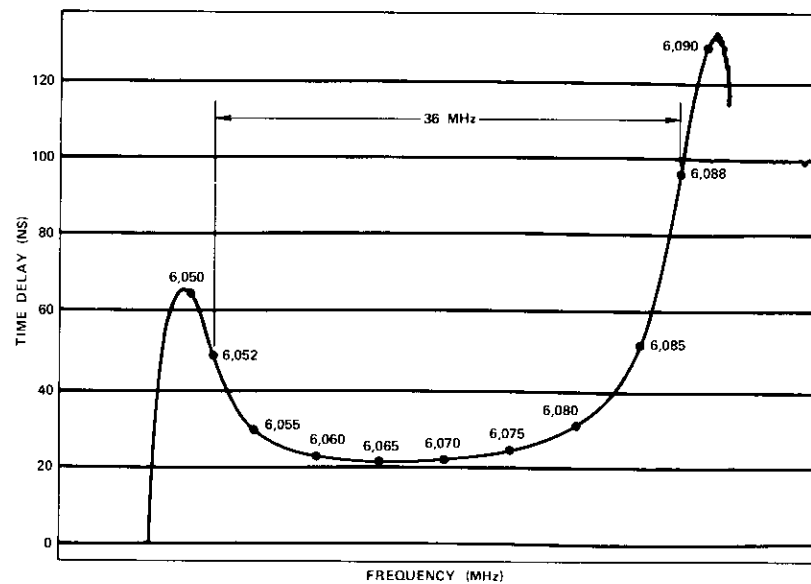


Figure 15. Measured Total Channel Time Delay, Port 1 to Port 8

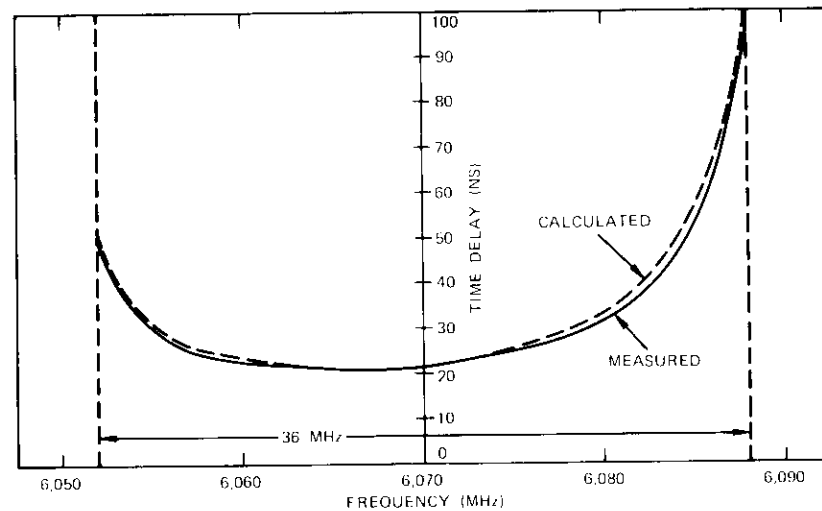


Figure 16. Comparison of Calculated and Measured Time Delay of Channel

circular cavity mounted in an offset position on the broad wall of a waveguide. A circularly polarized resonance is achieved by coupling through a square hole into the cavity in a position at which both the waveguide longitudinal and transverse magnetic fields are equal in magnitude but  $90^\circ$  apart in phase. It can be shown that the narrowband equivalent circuit of this structure approximates an all-pass ladder network exhibiting a single time-delay pole.

The Abele-Wang mathematical model can be used to obtain the relationship between the pole's peak time delay,  $P_d$ , and square coupling slot dimension,  $l$ :

$$P_d = \frac{\{[1 - (1 - S)^2]\} \lambda_g^2}{\{[1 - (1 - S)]^2\} \lambda_0^2 f} \quad (1)$$

where

$$S = \frac{16\pi^2(M')^2 \sin^2(\tan^{-1} \lambda_g/2a)}{3R^2 ab \lambda_g \lambda_{gc}}$$

and the polarization,

$$M' = \frac{0.258 I^3}{[1 - (\lambda_l/\lambda_0)^2] 10 \frac{2.73At}{\lambda_l} \sqrt{1 - (\lambda_l/\lambda_0)^2}} \quad (2)$$

The cavity length,  $l_c$ , is given by

$$l_c = \lambda_{gc}/2 \left\{ 1 - \frac{1}{2\pi} \tan^{-1} \left[ \frac{8\pi M' \sin^2(\tan^{-1} \lambda_g/2a)}{\lambda_g ab} \right] \right\} \quad (3)$$

where  $\lambda_g$  = rectangular guide wavelength

$\lambda_0$  = free space wavelength

$f$  = frequency

$a, b$  = rectangular waveguide dimensions

$\lambda_{gc}$  = circular cavity wavelength

$\lambda_l = 2l - kl$  = resonant length of square slot  
where  $k$  = constant

$A$  = coupling constant

$R$  = radius of cavity

$t$  = wall thickness between cavity and waveguide.

To determine the coupling constant,  $A$ , and the resonant length,  $\lambda_l$ , of the square slot, a single pole of equalization was constructed from WR159 waveguide and a 1.662-in.-diameter circular cavity. Slot length as a function of peak time delay was measured over the frequency range. It was found that, with a tuning screw added below the square slot and in the center of the broad wall, more than 30-dB return loss and a fine adjustment of the peak time delay could easily be achieved. The constant,  $A$ , and resonant length,  $\lambda_l$ , were adjusted until the mathematical model agreed with the experimental results.

To equalize the time-delay response, an optimization and a manual interactive computer program were used to determine the frequencies of the poles and their peak time delay. The channel group delay for three and five poles of equalization is shown in Figure 17. It can be seen that the use of five poles does not lead to a significant improvement in equalization; it was therefore decided that three poles would be used for an initial design.

Since each pole of equalization can be adjusted to realize at least 30-dB return loss, and thus reduce interaction, the three poles can be cascaded on a single waveguide. Spacings greater than a guide wavelength have been used to prevent evanescent mode interaction. Figure 18 is a photograph of the 3-pole equalizer.

The measured equalized time delay of channel 4 is shown in Figure 19. Good agreement with the calculated 3-pole equalization curve of Figure 19

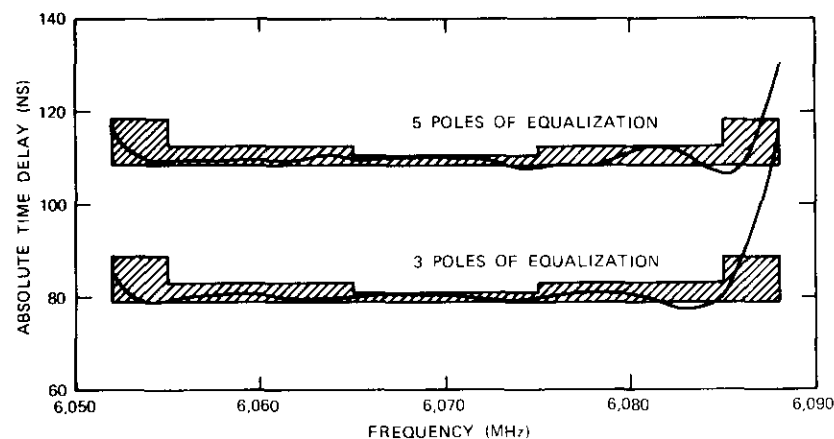


Figure 17. Calculated Time-Delay Response of Equalized Channel 4

is evident; equalization is achieved over at least 34 MHz of the channel passband. If required, this can be increased to 35 MHz by using five poles of time-delay equalization.

The amplitude characteristic of the channel 4 multiplexer and equalizer is given in Figure 20. The amplitude loss of the equalizer is given by curve (*E*) and has a frequency-loss relationship which is the inverse of that of the multiplexer filter. Consequently, the total channel (*E* + *M*) response exhibits significant amplitude equalization and better gain slope than the unequalized amplitude characteristic (Figure 10). It should be noted that the high-power multiplexer loss is equal to the difference between the (*E* + *M*) and (*E*) curves. This is the channel amplitude loss shown in Figure 10.

### Conclusions

Three directional filter and equalization networks for channels 4, 5, and 6 have been designed, fabricated, and extensively tested. Agreement between calculated and measured results is excellent. The overall amplitude performance of the multiplexer is shown in Figure 21. Data from the 3-channel unit may be used to extrapolate to a 12-channel unit.

The multiplexer has a center band loss of less than 0.55 dB, an isolation greater than 30 dB, and an input VSWR less than 1.06. The directional coupler design concept results in a modular approach which allows a

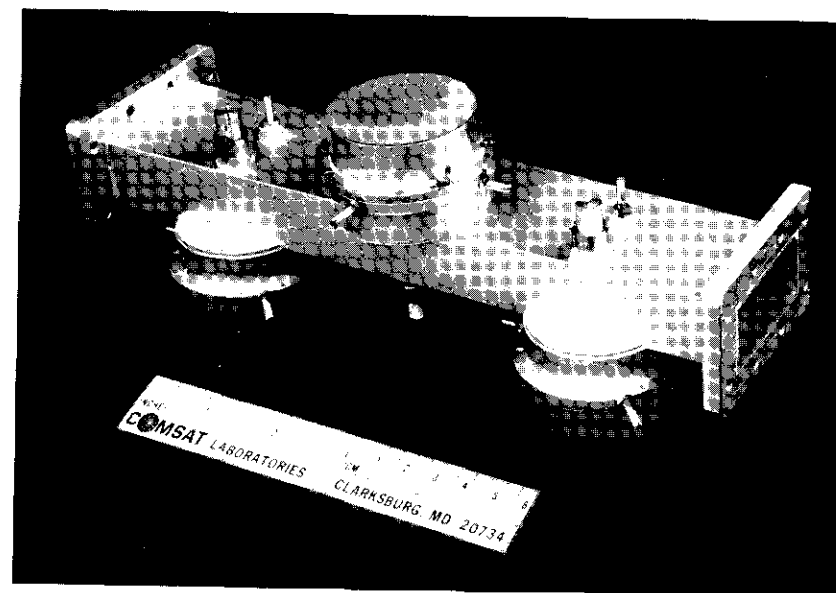


Figure 18. 3-Pole Time-Delay Equalizer

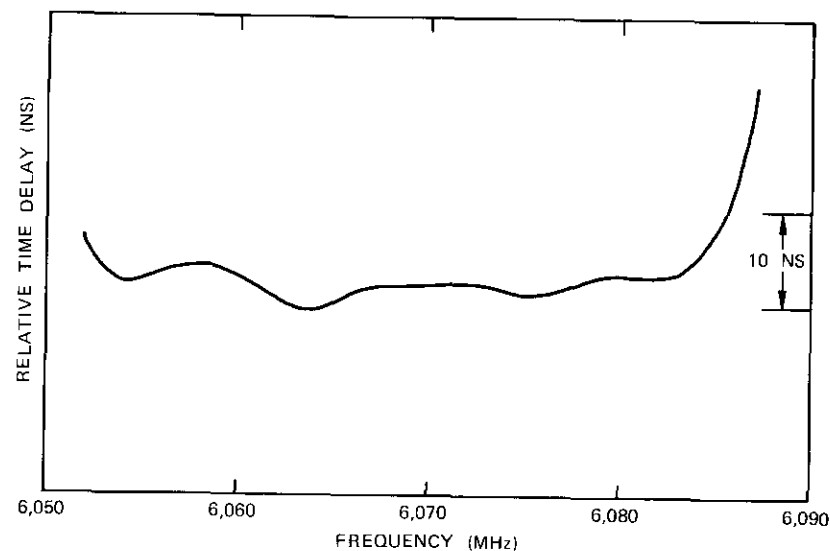


Figure 19. Measured Time-Delay Response of Equalized Channel 4

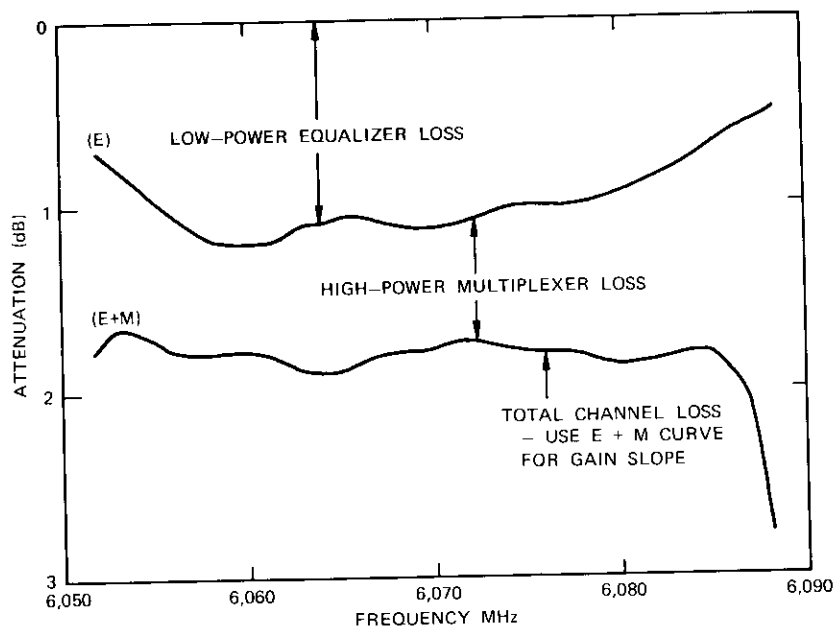


Figure 20. Amplitude Response of Multiplexer and Equalizer

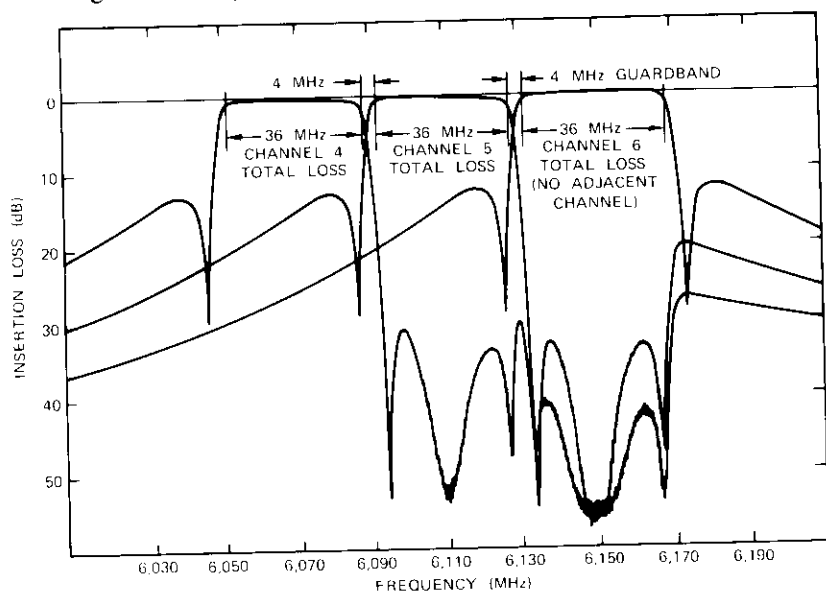


Figure 21. Response of 3-Channel Multiplexers

flexible frequency plan. The time-delay and amplitude responses are corrected with waveguide equalizers placed before the TWT, thereby avoiding the equalizer loss in the high-power TWT output. The multiplexer units have been tested at high power levels and exhibit no voltage breakdown up to 1.5 kW. This is well above the 400-W operational requirement. The multiplexers and equalizers have been in operation for over one year in the UET.

This concept allows the use of narrowband air-cooled TWT amplifiers with attendant improvement in reliability and efficiency. Successful implementation of the multiplexer and equalization circuits has demonstrated the viability of the modular transmitter as an alternative to single, large, high-power transmitters presently used in satellite earth stations.

#### Acknowledgment

The authors wish to acknowledge the support and encouragement of L. Pollack, W. Sones, and R. Kreutel during the course of the UET project. They further acknowledge the assistance of A. E. Atia and W. J. English in the preliminary definition studies.

#### References

- [1] L. Pollack and W. Sones, "An Unattended Earth Terminal for Satellite Communications," *COMSAT Technical Review*, Vol. 4, No. 2, Fall 1974, pp. 205-230.
- [2] A. E. Williams, "A Four-Cavity Elliptic Waveguide Filter," *IEEE Transactions on Microwave Theory and Techniques*, MTT-18, December 1970, pp. 1109-1114.
- [3] A. E. Atia and A. E. Williams, "New Types of Waveguide Bandpass Filters for Satellite Transponders," *COMSAT Technical Review*, Vol. 1, No. 1, Fall 1971, pp. 21-43.
- [4] A. E. Atia and A. E. Williams, "Nonminimum-Phase Optimum-Amplitude Waveguide Filters," *IEEE Transactions on Microwave Theory and Techniques*, MTT-22, April 1974, pp. 425-431.
- [5] T. A. Abele and H. C. Wang, "An Adjustable Narrow Band Microwave Delay Equalizer," *IEEE Transactions on Microwave Theory and Techniques*, MTT-15, October 1967, pp. 566-574.
- [6] G. L. Matthaei, L. Young, and E. M. T. Jones, *Microwave Filters, Impedance-Matching Networks, and Coupling Structures*, New York: McGraw-Hill, 1964, Chapter 16.



components. He is a member of Tau Beta Pi and Eta Kappa Nu.

Robert Gruner received his B.S. in electrical engineering from Northeastern University in 1962. From 1962 to 1969 he was employed by General Telephone and Electronics, where he worked on radar antennas, satellite antennas, and earth station microwave and antenna design. In 1969 he came to COMSAT, where he is presently a member of the Antennas Department of the Microwave Laboratory, working primarily in the area of dual-polarized antennas and associated microwave

Albert E. Williams was born in Albany, Australia. He received a B.E. in electrical engineering from the University of Western Australia, Netherlands, in 1962, and a Ph.D. from University College, London, England, in 1966. From 1966 to 1968 he was a lecturer in the Department of Electrical Engineering, University of Western Australia. Currently, he is a technical staff member of the Antennas Department of the Microwave Laboratory at COMSAT Laboratories, where he is working on antenna and filter theory applicable to future communications satellites. Dr. Williams was a joint recipient of the Institute of Electrical Engineers (London) Sylvanus P. Thompson Premium award in 1966.



Index: suspended substrate stripline, microwave integrated circuits, filters, earth terminals

## Suspended substrate stripline directional filters for receiver demultiplexing at 4 GHz

C. B. COTNER

(Manuscript received August 8, 1974)

### Abstract

Narrow-bandwidth, multiple-pole, directional filters have been developed at 4 GHz to replace the N-way power dividers ordinarily used to route carriers to individual down-converters at an earth terminal. Suspended substrate stripline has been used to achieve the resonator Q's necessary for bandwidths corresponding to those of an INTELSAT IV transponder (approximately 40 MHz). Insertion losses have been reduced, thus improving reliability, by eliminating active devices, and the necessary preselection ahead of the down-converters has been obtained. The advantages of thin film technology have been extended through the achievement of unloaded Q's of 950.

### Introduction

One way to improve reliability in an earth terminal is to minimize system losses which must be offset by using active circuits. A major contributor to receiver loss is the N-way power divider ordinarily used to route down-link carriers to separate down-converters.

In the unattended earth terminal (UET) [1] this power divider has been replaced by a group of directional filters, each with the bandwidth of an INTELSAT IV spacecraft transponder. To ease the individual filter

requirements, a hybrid has been used to provide two isolated outputs, one connected to directional filters for transponders 1, 3, 5, 7, 9, and 11 and the other connected to directional filters for transponders 2, 4, 6, 8, 10, and 12. While the hybrid limits the insertion loss to 3 dB minimum, this technique greatly increases the guardband between adjacent filters. The demultiplexer is shown schematically in Figure 1.

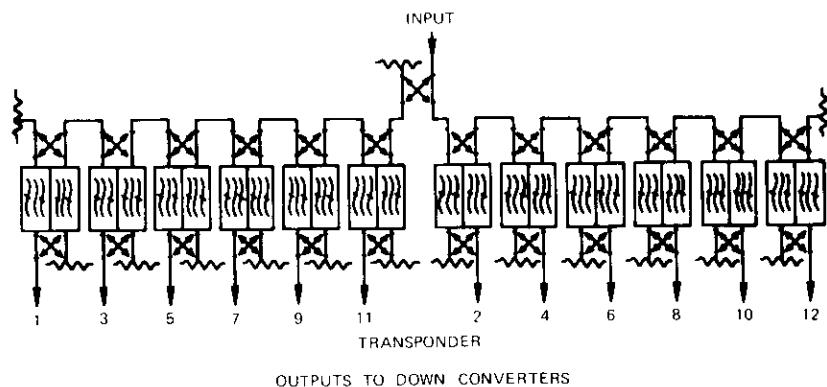


Figure 1. 12-Way Receiver Demultiplexer

Design goals for the demultiplexer, derived from the required communications performance, are listed in Table 1.

TABLE 1. RECEIVER DEMULTIPLEXER DESIGN GOALS

Center Frequency	centered on each INTELSAT IV transponder
Amplitude Response	$\pm 0.1$ dB max. over $f_0 \pm 22$ MHz
Insertion Loss	6 dB max., input to any output
Out-of-Band Rejection	18 dB min. at $f_0 \pm 62$ MHz
Group-Delay Distortion (over each 44 MHz)	
Linear	0.03 ns/MHz
Parabolic	0.2 ns/MHz <sup>2</sup>
Ripple	0.5 ns peak to peak
Return Loss	-20 dB all ports

Initial investigation showed that a 3- or 4-pole filter with a resonator unloaded  $Q$  of about 900 would be needed to meet these specifications. Thin film microstrip technology, with substrates of the usual dimensions, would limit the resonator unloaded  $Q$  to about 200. However, coaxial or

stripline configurations could provide the required performance. The final selection, suspended substrate stripline, demonstrated the combined advantages of an unloaded  $Q$  of 950 measured for half-wave resonators at 4 GHz and the precision associated with thin film technology. A cross section of the suspended substrate stripline is shown in Figure 2.

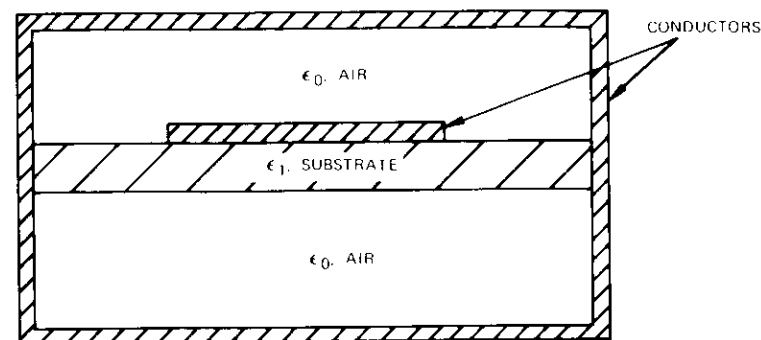


Figure 2. Suspended Substrate Stripline Cross Section

## Filter design considerations

### Low-pass prototype and equivalent circuit

A survey of the literature [2]-[4] was conducted to predict the performance of 3-pole, 0.1-dB-ripple and 4-pole, 0.01-dB-ripple Chebychev low-pass prototypes. The filters were compared for transponder 12 ( $f_0 = 4.175$  GHz), since this represents the smallest fractional bandwidth of interest.

Although either filter would have met the specification, the 3-pole, 0.1-dB-ripple Chebychev low-pass prototype was selected because of lower insertion loss. Lumped element equivalent circuits were computed from Reference 3 for the filters of transponders 5, 6, and 12 ( $f_0 = 3.885$  GHz, 3.925 GHz, and 4.175 GHz, respectively) using half-wave resonators in 50-ohm line with an unloaded  $Q$  of 950 [5]. The equivalent circuit with element values for transponder 5 is shown in Figure 3.

Computer analysis confirmed the suitability of the lumped element equivalent circuit; the worst-case insertion loss (transponder 12) was 1.36 dB. The insertion loss, return loss, and group-delay characteristics of the filter equivalent circuit are shown in Figure 4.

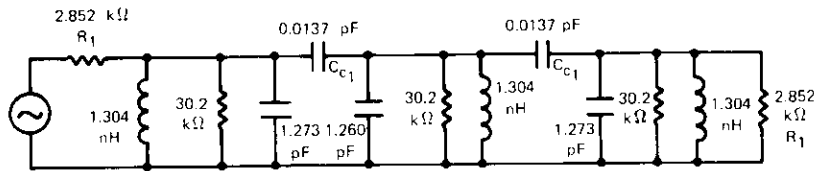


Figure 3. Lumped Element Filter Equivalent Circuit for Analysis

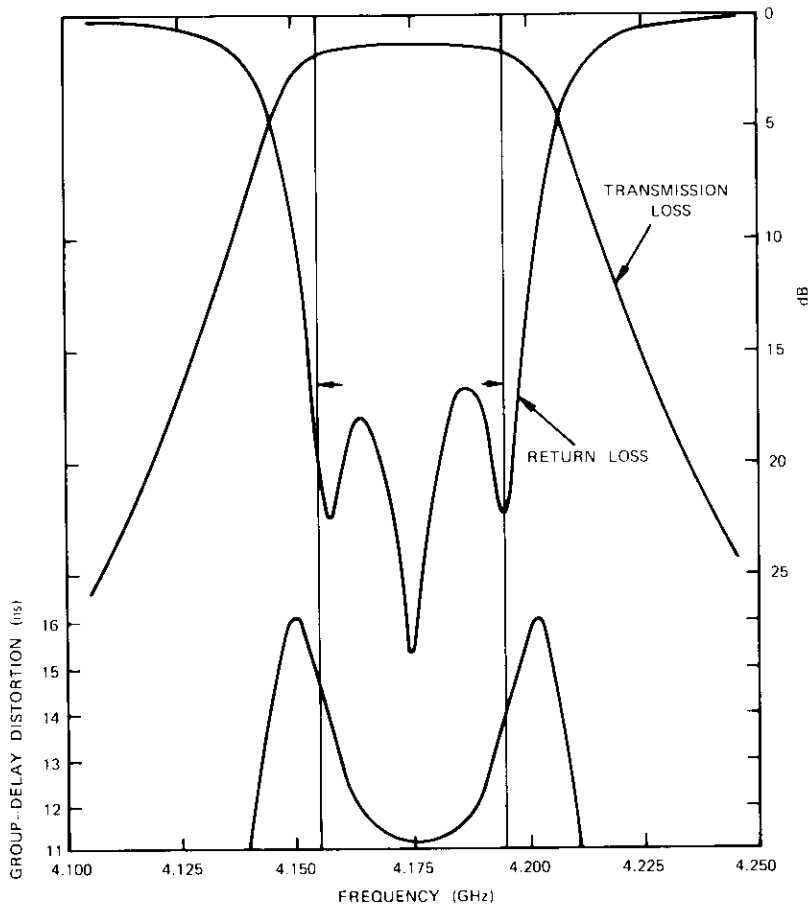


Figure 4. Filter Lumped Equivalent Circuit Performance

**Crosstalk**

The 3-pole prototype filter exhibits adequate selectivity to reject a signal present in transponders once removed from the passband. However, signals in adjacent transponders may not be greatly attenuated and, as shown in Figure 4, they may become heavily amplitude modulated. If there is AM-PM conversion following the filters, but preceding the highly selective IF filters, intelligible crosstalk may result.

The results of Chapman and Millard [6] were used to calculate the crosstalk. One case investigated was that of two 612-channel carriers (see Figure 5); their frequency displacement and other parameters were determined from ICSC-45-13E [7].

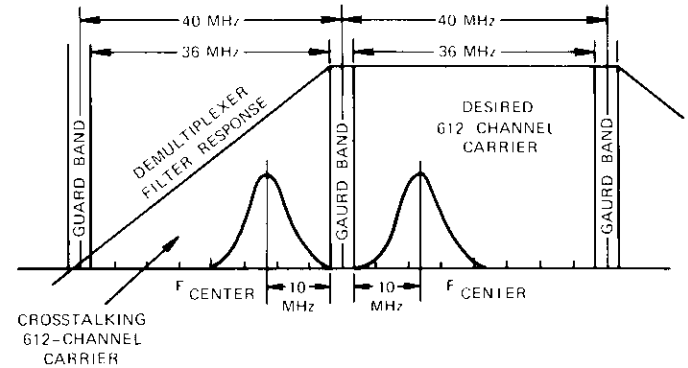


Figure 5. Case of Two 612-Channel Carriers Which May Produce Crosstalk

The data necessary for a crosstalk calculation are the applicable AM-PM conversion, the gain slope producing amplitude modulation on the crosstalking carrier, the top baseband frequency and rms deviation of the carriers of interest, and the relative power of the desired and crosstalking carriers.

In the UET, only the mixer-IF preamplifier is between the receiver demultiplexer and the IF filters; its AM-PM conversion has been measured as 0.05°/dB change in power (maximum). An average loss slope of 0.578 dB/MHz represents the demultiplexer filter skirt in the region of the crosstalking carrier. For the 612-channel carriers the top baseband frequency is 2.54 MHz and the rms deviation is 1.996 MHz.

The desired carrier power may be taken as the integral of a band-limited Gaussian curve whose sigma ( $\sigma$ ) is the rms deviation. The cross-

talking carrier power may be calculated by first weighting the Gaussian distribution with the demultiplexer filter attenuation (from Figure 4). The power densities of the desired and crosstalking carriers are shown in Figure 6. Numerical techniques have been used for the power calculations; the ratio of crosstalking carrier power to total power has been found to be 0.266.

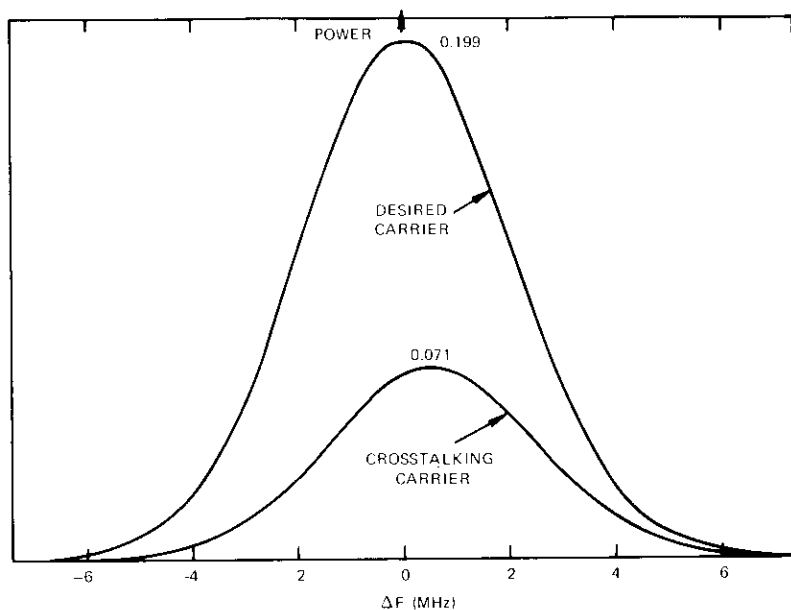


Figure 6. *Desired and Crosstalking Power Densities*

From the preceding, the crosstalk ratio has been calculated as follows:

$$XTLK \text{ (dB)} = 20 \log \frac{2KgF_{\text{top}}}{57.3} \frac{P_1}{P_1 + P_2}$$

where

- $K$  = AM-PM conversion factor (0.05°/dB)
- $g$  = gain slope factor (0.578 dB/MHz)
- $F_{\text{top}}$  = maximum baseband frequency (2.54 MHz)
- $P_1$  = crosstalking carrier power
- $P_2$  = desired carrier power

and

$$\frac{P_1}{P_1 + P_2} = 0.266$$

so that

$$XTLK = -63.3 \text{ dB}$$

Therefore, although the demultiplexer filters do not greatly attenuate signals in the adjacent transponders, the resulting crosstalk is not a problem if the AM-PM conversion following these filters is small.

### Filter design data

#### Filter geometry

The element values for the lumped equivalent circuit of Figure 3 are for half-wave resonators in 50-ohm line. End-coupled geometry has been chosen for this application for several reasons. Since the filter fractional bandwidth is approximately 1 percent, weak coupling is required. High-quality grounds, necessary to maintain the  $Q$  of grounded resonators, are somewhat difficult to construct using etched circuit techniques. With the end-coupled structure, the three resonator filters at 4 GHz will not be inordinately long, and it is unnecessary to generate odd- and even-mode coupling impedance data. Preliminary tests showed that the required resonator  $Q$  can be obtained with cross-sectional dimensions which would not induce moding and cavity problems in the frequency range of interest.

#### Design information

Certain design information is necessary to actually build the filter from the low-pass prototype and lumped equivalent circuit. For example, the phase velocity and the cross-sectional dimensions of the desired line impedance are required. Since the suspended substrate stripline, similar to microstrip, is not homogeneous, the phase velocity will be frequency sensitive because of dispersion. In addition, the unloaded  $Q$  of the resonators must be known as well as the dimensions for the coupling required by the design [5].

One method of analyzing the impedance and approximate phase velocity of an inhomogeneous transmission line is to numerically compute the potential distribution between conductors for a large number of discrete points. The electric field, which is the gradient of the potential, is then computed and Gauss' Law is applied to determine the charge per unit length. The capacitance per unit length follows by definition. An effective

relative dielectric constant and effective phase velocity are calculated by assuming that the line is quasi-homogeneous and supporting a TEM mode only (which is, of course, an approximation).

This finite difference method has been applied to both microstrip [8] and suspended substrate stripline [9] geometries. A Fortran program [10] has been used to predict the dimensions of the desired 50-ohm line. The section of the program which computes the potential distribution uses Liebmann's variation on Richardson's method of iteration [11]. Running time (and thus cost) have been reduced as discussed in References 9 and 11.

Results of the numerical analysis were compared with measurements to confirm the validity of the analysis. The impedance of a line section was measured by plotting the reflection coefficient (with the line terminated in 50 ohms) on a Smith Chart across a sufficiently wide frequency range. The impedance was calculated on the basis of the following relationship [12]:

$$Z_{line} = Z_o(r_1 r_2)^{1/2}$$

where  $Z_o$  = normalization impedance of the chart (50 ohms)  
 $r_1$  and  $r_2$  = normalized resistance circles to which the reflection coefficient is tangent.

The phase velocity was measured using time-domain reflectometry. A typical comparison is shown in Table 2.

TABLE 2. COMPARISON OF CALCULATED AND MEASURED SUSPENDED SUBSTRATE STRIPLINE DATA

Case	Computation	Measurement
Height = 0.262 in. (0.765 cm)		
Half Width = 0.500 in. (1.270 cm)		
Conductor Half Width = 0.125 in. (0.318 cm)		
Top to Conductor = 0.118 in. (0.300 cm)		
Substrate Thickness = 0.05 in. (0.127 cm)	$V_{eff} = 0.7495$	$V_{eff} = 0.737$
Substrate Dielectric Constant = 9.38		
Initial Mesh = 0.0125 in. (0.0318 cm)		

To obtain accurate data, including dispersion for phase velocity at the frequencies of interest, a bar resonator was etched on one of the substrates

to be used, but with the metalization extending over the end of the substrate. Launchers were placed near the midpoint of the sides of the substrate holder, but slightly offset; very weak coupling to the resonator resulted. Each frequency at which resonance occurred was measured using a frequency counter. On the basis of a known physical length and resonant frequencies, the effective phase velocity and relative dielectric constant can be calculated. The data used for the demultiplexer design are shown in Figure 7. The relative phase velocity agrees quite closely with the time-domain reflectometer value of Table 2.

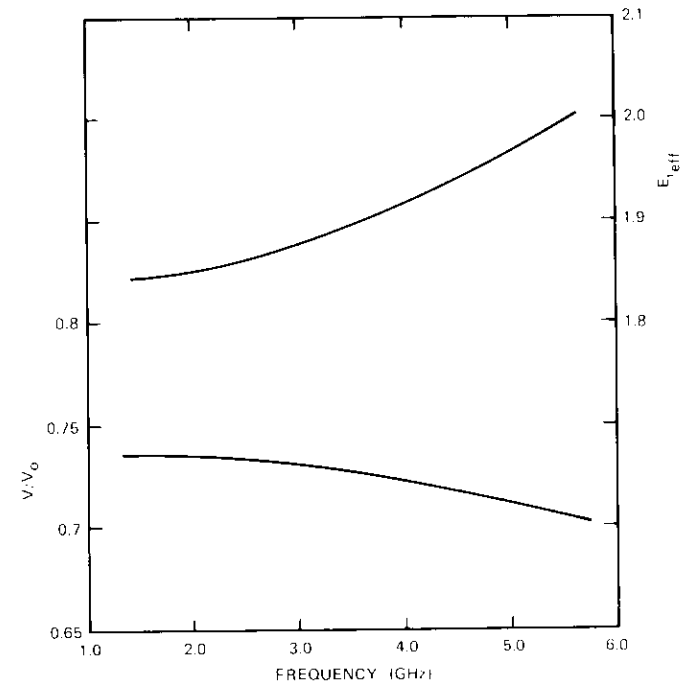


Figure 7. Relative Phase Velocity and Dielectric Constant of Suspended Substrate Stripline

The unloaded  $Q$ , coupling, and end corrections for the suspended substrate stripline resonators were calculated using half-wave resonators coupled to a transmission line at both ends. This method was used instead of measuring a singly loaded quarter-wavelength resonator to avoid the problem of obtaining a high-quality ground. The precision of thin

film techniques made it possible to keep the two coupling gap widths practically identical and thus minimize errors due to asymmetry.

All measurements were performed on the same resonator and substrate, and the gap was opened in steps over the range necessary for the filter design. Prior to each measurement, the gap and resonator dimensions were measured on an optical comparator accurate to within  $\pm 0.0001$  in. ( $\pm 0.00025$  cm). The center frequency, 3-dB bandwidth, and insertion loss were measured for each case. Equations in the literature [5] were then used with these data to calculate the inverter properties of the gaps.

Figure 8 shows an equivalent circuit which may be used to represent coupling gap properties and the equations which relate the various quantities [5]. Since the resonator and gap dimensions are known, the phase velocity and center frequencies measured, and the inverter properties calculated, the values for  $C_1$  and  $C_2$  can be calculated for each gap width. These are the quantities actually used for the filter design and are plotted as a function of gap width in Figure 9.

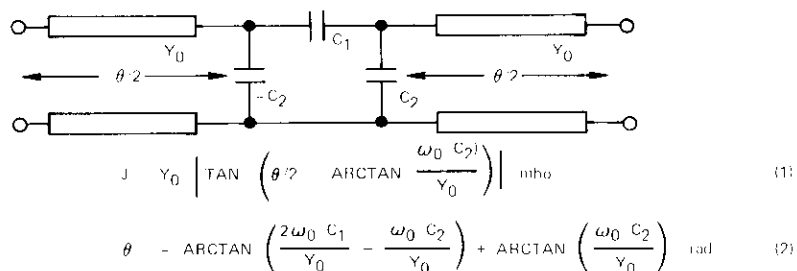


Figure 8. Equivalent Circuit Applied to Transmission Line Gap

Figure 9 shows that, to the left of the crossover point, the magnitude of  $C_1$  is greater than that of  $C_2$ . Since the gap width is selected according to the required value of  $C_1$ , a design with an inverter in this region needs additional negative capacitive susceptance, and hence the gap center-line to gap center-line dimension must be shortened. To the right of the crossover, the magnitude of  $C_2$  is greater; therefore positive capacitive susceptance must be provided by increasing the gap center-line to gap center-line dimension. With  $C_1$  and  $C_2$  known, the required correction to this dimension may be calculated from equation (2) in Figure 8.

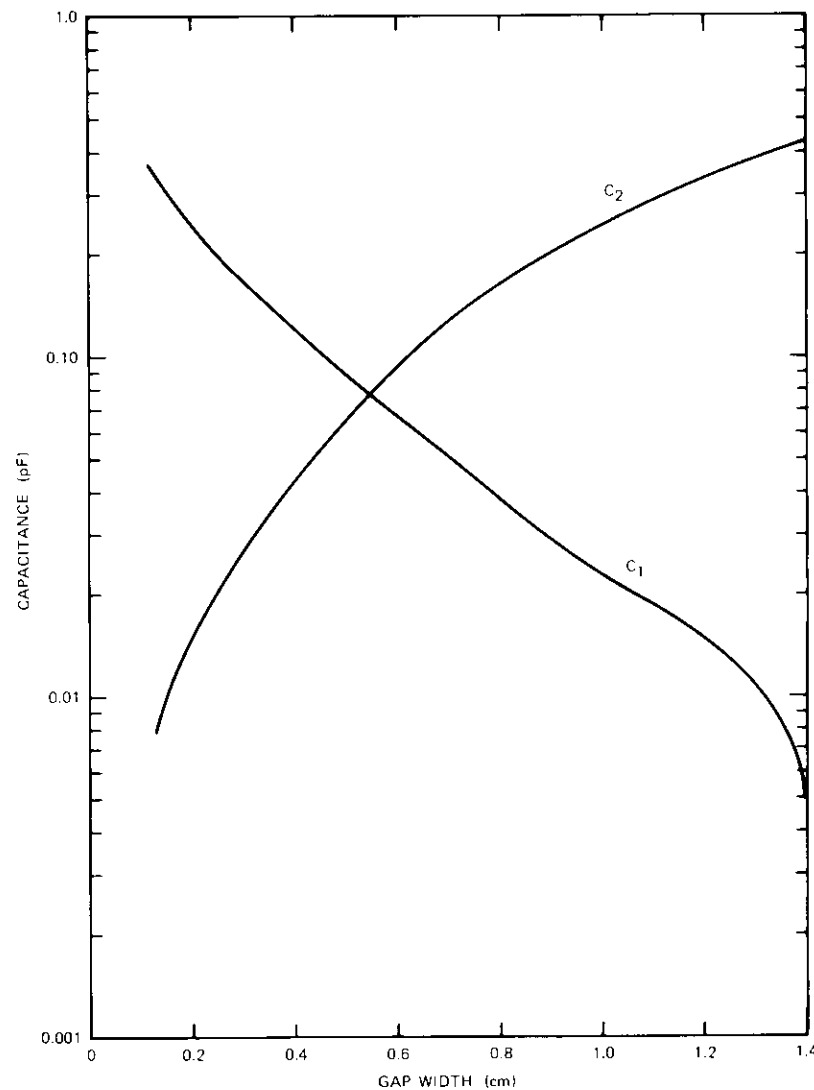


Figure 9. Element Values for the Equivalent Circuit of Figure 7

### Demultiplexer construction and performance

#### Calculation of filter dimension

After the suitability of the lumped element equivalent circuit had been confirmed and the necessary design data assembled, distributed element filters for several transponders were constructed. The conversion of the lumped element equivalent of Figure 3 to a distributed design is shown in Figure 10. In Figure 10a the center inverter sections have been separated

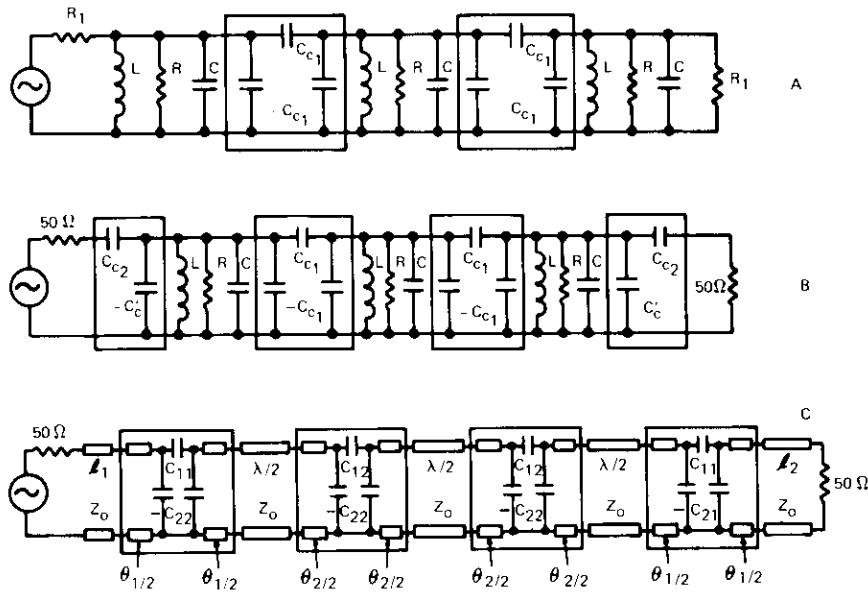


Figure 10. Conversion of Lumped Equivalent Circuit to Distributed Element Design

from the resonator capacitance. To convert the filter to a 50-ohm design, the end resonators must be coupled through suitable inverter sections to the source and load. As shown in the literature [5], these inverters consist of a positive series capacitance,  $C_{c2}$ , and a negative shunt capacitance,  $-C'_{c1}$ , across the end resonators. The values of these capacitances are calculated from the following expressions:

$$C_{c2} = \frac{1}{\omega_o} \left[ \frac{1}{50(R_1 - 50)} \right]^{1/2}$$

$$C'_c = - \frac{C_{c2}}{1 + (50\omega_o C_{c2})^2}$$

Replacing the lumped resonators of Figure 10b with half-wave resonators and substituting the gap equivalent circuit of Figure 8 for the purely capacitive inverter sections result in the distributed element filter of Figure 10c.

As an example, for a lumped element transponder 6 equivalent circuit ( $f_o = 3.925$  GHz),  $R_1 = 2.882$  k $\Omega$ , and  $C_{c1} = 0.0134$  pF. From the curve of  $C_1$  vs width in Figure 9, it can be seen that this value of  $C_{c1}$  corresponds to a gap of 0.489 in. (1.242 cm). From equations (1) and (2) in Figure 8, since  $C_2 = -0.358$  pF,  $\theta$  for the center will be +0.8034 radian.

Substitution in the expression for  $C_{c2}$  gives a required value of 0.1078 pF, and  $C'_c$  must be -0.106 pF. The gap width of 0.173 in. (0.439 cm) for the required  $C_{c2}$  corresponds to -0.051 pF for  $C'_c$ ; hence, an additional negative correction is needed. From the usual expression for a capacitive stub,  $\theta$  is found to be -0.1354 radian. The electrical lengths and gap widths for the transponder 6 filter are shown in Figure 11.

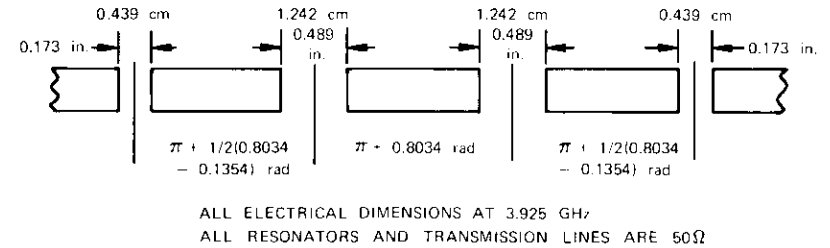


Figure 11. Distributed Element Filter for Transponder 6

The dimensions of Figure 11 produced the response shown in Figure 12. The transmission and return loss versus frequency were compared with predictions using the lumped element equivalent circuit. Similar agreement was obtained for the filters of transponders 5 ( $f_o = 3.885$  GHz) and 12 ( $f_o = 4.175$  GHz). Figure 13 is a photograph of the filter and the hybrids, which will be discussed in the following:

#### The suspended substrate stripline hybrid

The receiver demultiplexer directional filters were formed from basic 3-pole filters with quadrature hybrids at the input and output. Complete

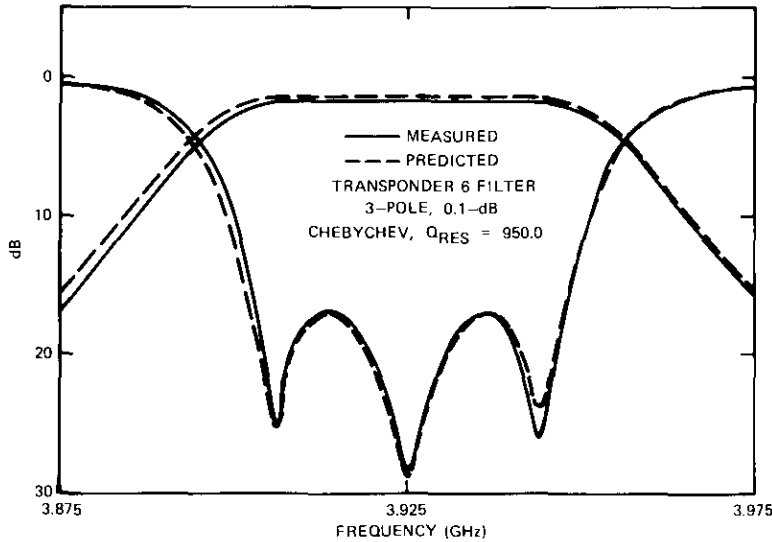


Figure 12. Filter Performance

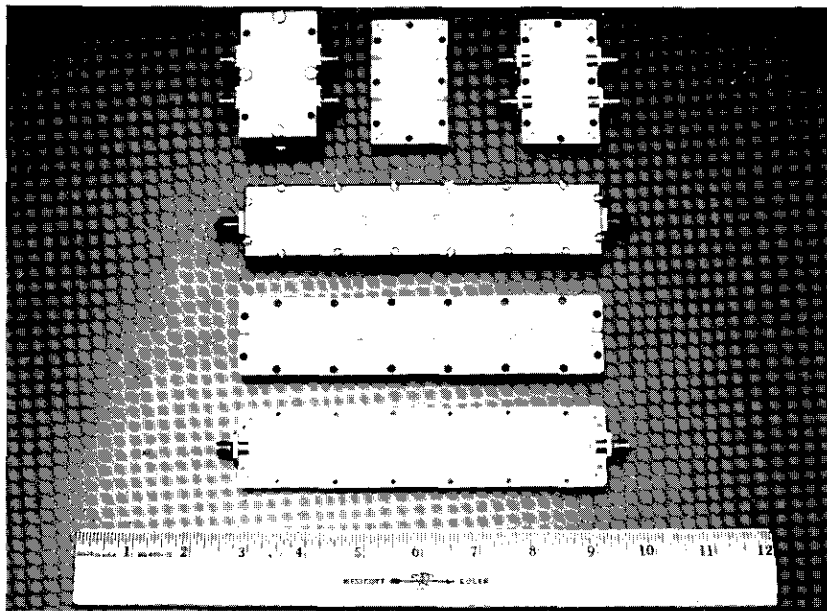


Figure 13. Suspended Substrate Stripline Filters and Hybrids

integration of each directional filter was envisioned; therefore, a suspended substrate stripline quadrature hybrid was built [13]. A cross section of the coupler geometry is shown in Figure 14.

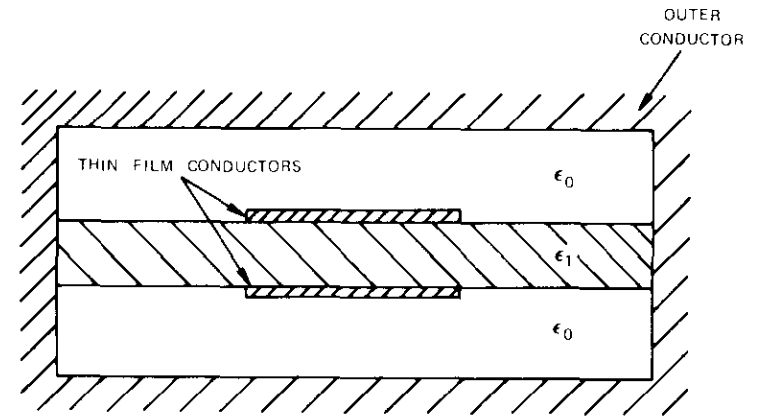


Figure 14. Cross Section of Suspended Substrate Stripline Quadrature Hybrid

The hybrid selected is much simpler to construct than some other designs; its primary limitation is the narrow bandwidth which results from the unequal odd- and even-mode phase velocities. Inspection of the hybrid cross section indicates that the odd-mode electric fields are heavily concentrated in the substrate, while most of the even-mode field is in air. However, the bandwidth of interest is less than 15 percent (3.7–4.2 GHz) so that the simplicity of this hybrid outweighs its bandwidth limitation.

Data from Reference 13 were used for the first hybrid, and the dimensions were adjusted empirically for the dielectric constant of the alumina substrates used ( $\epsilon_r \cong 10.5$ ). The arrangement of the four ports necessitated 50-ohm line sections from the coupled section to the launchers. These sections were dimensioned using the computer program discussed earlier.

The performance of the hybrid is summarized in Figure 15. The additional compensation techniques discussed in Reference 13 have not yet been applied, but would undoubtedly improve the performance.

**Directional filters and demultiplexer assembly**

Directional filters for transponders 5 and 6 were initially required in the Clarksburg UET. The necessary two filter pairs and five hybrids were assembled and tested. Figure 16 is a photograph of one of the directional

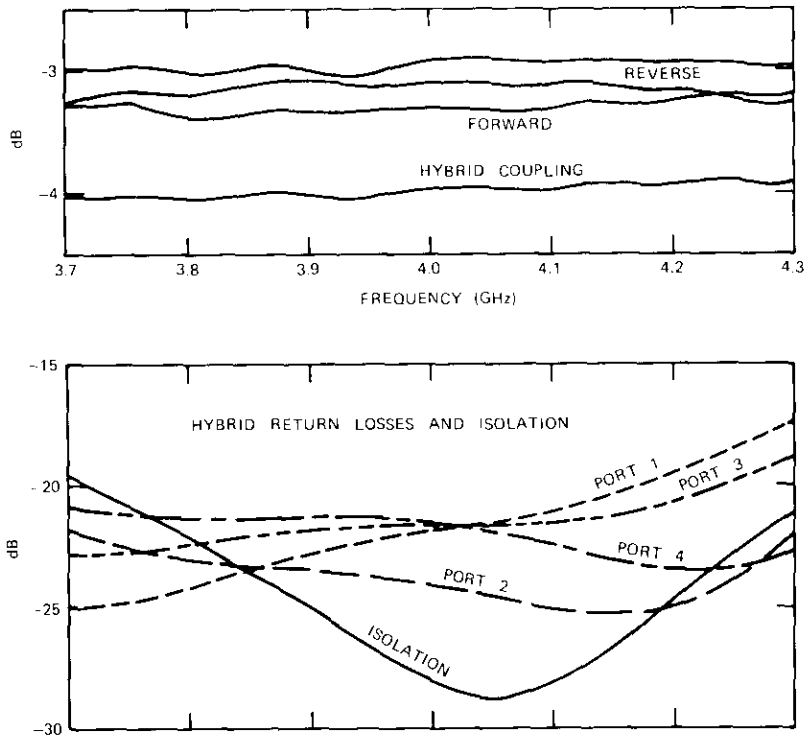


Figure 15. Performance of Suspended Substrate Stripline Hybrid

filter assemblies. Figure 17 is a graph of group-delay distortion versus frequency for the directional filter of transponder 5.

The complete demultiplexer for transponders 5 and 6 was then assembled and tested for transmission and return losses. The results are summarized in Figure 18.

**Conclusion**

Three-pole Chebychev filters with 1-percent bandwidths were successfully designed and fabricated at 4 GHz using thin film technology. The use of suspended substrate stripline techniques made possible an unloaded  $Q$  approaching 1,000 for 50-ohm half-wave resonators.

These filters were combined with suspended substrate stripline hybrids to form directional filters which are now being used for receiver demulti-

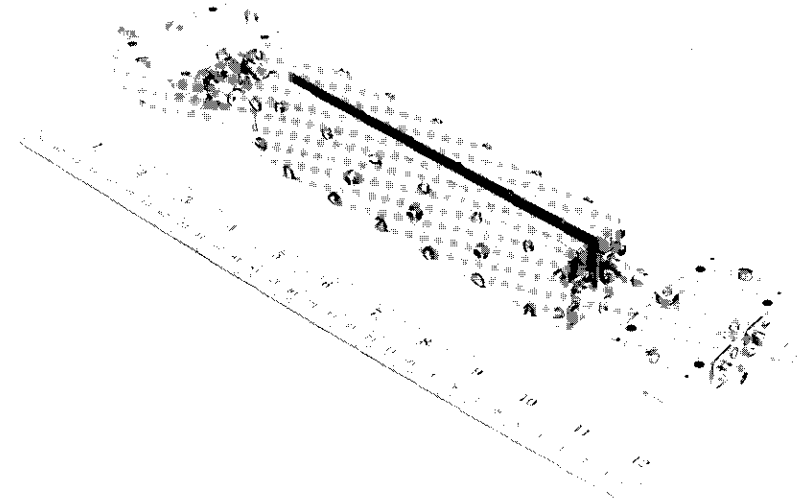


Figure 16. Directional Filter Assembly

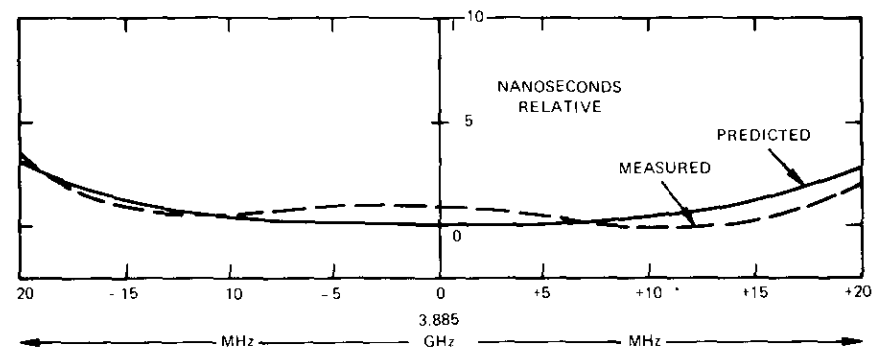


Figure 17. Group-Delay Distortion vs Frequency for Transponder 5 Directional Filter

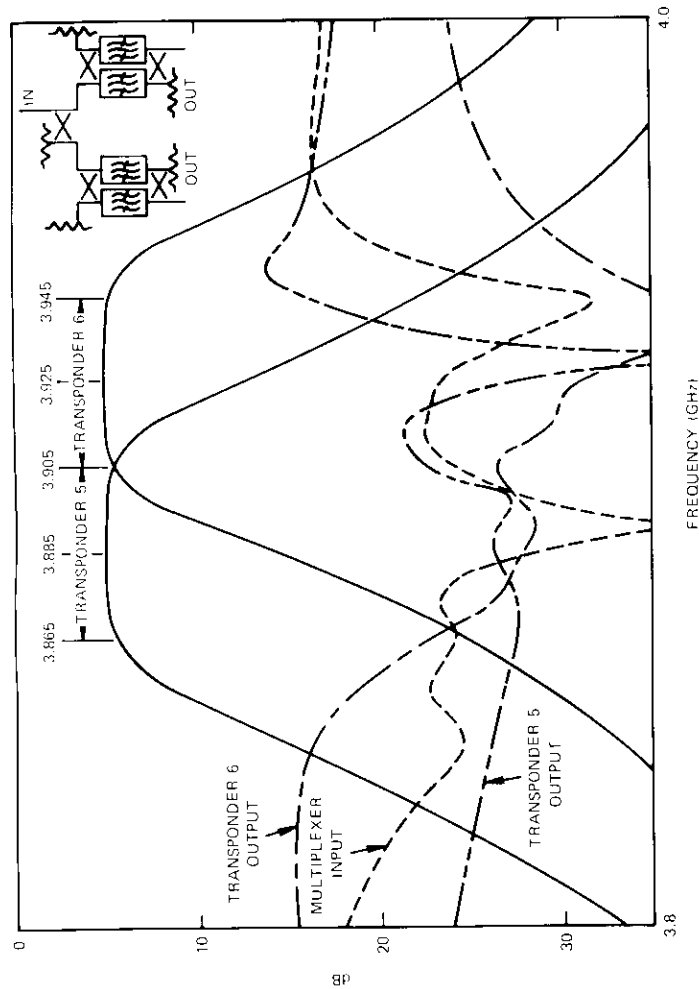


Figure 18. Test Results of Complete Demultiplexer for Transponders 5 and 6

plexing in the COMSAT UET. With an insertion loss of approximately 5 dB, they are at least 7 dB less lossy than the 12-port power dividers which comprise quadrature hybrids. This in turn enhances station reliability by reducing the number of active devices and provides the necessary pre-selection for the down-converters.

### Acknowledgments

The writer wishes to thank Messrs. L. F. Gray and R. L. Sicotte and Dr. W. K. Sones for their technical suggestions, Messrs. Guillermo Arana and Gerardo Mesias for performing much of the measurement and construction, and Messrs. Nils Jespersen and Richard Perry for their work on the computer analysis.

### References

- [1] An Unattended Earth Terminal for Satellite Communications, *COMSAT Technical Review*, Vol. 4, No. 2, Fall 1974, pp. 205-230.
- [2] R. L. Slevin, "Pseudo Exact Bandpass Filter Design Saves Time," *Microwaves*, Pt. 1, August 1968, pp. 38-47; Pt. 3, November 1968, pp. 68-73.
- [3] S. B. Cohn, "Dissipation Loss in Multiple-Coupled Resonator Filters," *Proc. of IRE*, Vol. 47, August 1959, pp. 1342-1348.
- [4] ITT, *Reference Data for Radio Engineers*, 4th Edition, New York: American Book-Stratford Press Inc., 1956, pp. 194, 195, 216, 219.
- [5] G. L. Matthaei, L. Young, and E. M. T. Jones, *Microwave Filters, Impedance Matching Networks, and Coupling Structures*, New York: McGraw-Hill, 1964, pp. 214-217, 434, 438, 514-516, 660-663.
- [6] R. C. Chapman and J. B. Millard, "Intelligible Crosstalk Between Frequency Modulated Carriers Through AM-PM Conversion," *IEEE Transactions on Communication Systems*, CS-12, No. 2, June 1964, pp. 160-166.
- [7] International Telecommunication Satellite Consortium, "Performance Characteristics of Earth Stations in the INTELSAT IV System," ICSC 45-13E W/1/70 (Rev. 1), 23 June 1972.
- [8] Harold E. Stinehelfer, "An Accurate Calculation of Uniform Microstrip Transmission Lines," *IEEE Transactions on Microwave Theory and Techniques*, MTT-16, No. 7, July 1968, pp. 439-444.
- [9] Helmut E. Brenner, "Numerical Solution of TEM-Line Problems Involving Inhomogeneous Media," *IEEE Transactions on Microwave Theory and Techniques*, MTT-15, August 1967, pp. 485-487.
- [10] Helmut E. Brenner, "Use a Computer to Design Suspended Substrate ICs," *Microwaves*, September 1968, pp. 38-45.

- [11] G. N. Lance, *Numerical Methods for High Speed Computers*, London: Iliffe & Sons, Ltd., 1960, pp. 107-110.
- [12] Harry F. Lenzing, "How to Determine Characteristic Impedance," *Electronic Design*, May 10, 1963, pp. 58-61.
- [13] James E. Dalley, "A Strip-Line Directional Coupler Utilizing a Non-Homogeneous Dielectric Medium," *IEEE Transactions on Microwave Theory and Techniques*, MTT-17, No. 9, September 1969, pp. 706-712.



*Calvin B. Cotner received a B.S.E. with honors from Princeton University (1962) and an M.S.E.E. from Cornell University (1964). Before joining COMSAT in 1967, he was a member of the Space Communication Laboratory of IIT Federal Laboratories, Nutley, N.J., and served as the staff signal officer of the 69th Maintenance Battalion in Vietnam.*

*As a member of the Earth Terminals Department of the Microwave Laboratory at COMSAT Laboratories, his assignments have included development of a high-power TWT test facility, a 15-GHz receiving system, MIC equipment for earth terminals, and integration and testing of the unattended earth terminal. He is a mobilization designee with the U.S. Army Communications Command holding the rank of Major.*

## **Translations of abstracts in this issue**

### **Expressions pour calculer la direction topocentrique d'un satellite géostationnaire en fonction du temps**

V. J. SLABINSKI

#### **Sommaire**

On a proposé l'emploi de mécanismes d'entraînement programmés comme méthode simple de commande d'antenne de station terrienne à pinceau fin, permettant de suivre les changements de direction d'un satellite quasi géostationnaire. Les données de pointage d'antenne seraient obtenues à l'aide d'un mini ordinateur à partir d'expressions algébriques simples dans le domaine temporel. Le présent article démontre qu'une expression de pointage adéquate contiendrait: un polynôme quadratique dans le temps, une composante trigonométrique simple dont la période est le jour sidéral, et deux termes de Poisson. Dans une telle expression, l'erreur de pointage sur une période de 28 jours est inférieure à 0,015°. Il suffit que la composante trigonométrique comprenne un sinus et un cosinus dans le cas d'excentricités d'orbite inférieures à 0,005 et d'inclinaisons inférieures à 1°. Pour des intervalles plus brefs, des formes abrégées de l'expression donnent une bonne précision. L'évaluation pratique de l'expression à l'aide du mini ordinateur est également traitée.